Measurement of the Unpolarized $K^+\Lambda$ and $K^+\Sigma^0$ Electroproduction Cross Sections and Interference Terms from the Proton with the CLAS Detector

by

Robert J. Feuerbach

A dissertation submitted in partial fulfillment of the requirements for the degree of

Doctor of Philosophy

in the Department of Physics

Carnegie Mellon University

December 2002

Abstract

Using the CLAS detector, we measure the $K^+\Lambda$ and $K^+\Sigma^0$ electroproduction response functions over the continuous kinematic range from threshold to $W = 2.05\,\mathrm{GeV}$ and for Q^2 between 0.5 and $1.5\,(\mathrm{GeV/c})^2$, with nearly complete angular coverage in the center-of-momentum frame angles. The $\sigma_T + \epsilon\sigma_L$, σ_{TT} and σ_{LT} terms are extracted and compared to recent theoretical calculations based upon a hadrodynamic effective-Lagrangian framework. From examining the W-dependence of the response functions for the $K^+\Lambda$ final state, we find features in the $(\sigma_T + \epsilon\sigma_L)$ term in the $W = 1.75$ to $1.90\,\mathrm{GeV}$ region, similar to features seen in recent photoproduction results. In general, the σ_{TT} and σ_{LT} response-functions for Λ production are of the same order of magnitude as the $(\sigma_T + \epsilon\sigma_L)$ term, suggesting that both σ_T and σ_L contribute significantly. For the $K^+\Sigma^0$ final state the W-dependence of the $(\sigma_T + \epsilon\sigma_L)$ and σ_{TT} terms have large, resonant-like features near $W = 1.9\,\mathrm{GeV}$. Unlike in Λ electroproduction, the σ_{LT} interference term for Σ^0 electroproduction is found to be consistent with zero across nearly the entire kinematic range, while σ_{TT} is comparable in magnitude to the $\sigma_T + \epsilon\sigma_L$ differential cross-section. The models, while achieving some qualitative agreement with the data, fail to both describe the details of the angular distributions and reproduce the resonant-like behavior observed.

Acknowledgments

This measurement was the result of the contributions and hard work of many individuals, to whom I am thankful. I would like to specifically acknowledge the assistance and support offered by the Jefferson Lab staff, the past and present members of the CLAS Collaboration, and by all the members of the CMU Medium Energy group. My financial support was provided by the Department of Energy. Finally, I owe the completion of this project to the emotional support of friends and family.

I would like to thank the Medium Energy Group at CMU for their assistance, support and for maintaining an open and (relatively) stress-free environment in which to work. First, I am grateful to my advisor, Reinhard Schumacher, for his support, council, and shared experience throughout the duration. My also thanks go out to my longtime friend, colleague, and office-mate John McNabb for the relentless discussions and debates, occasional distractions, and overall support. I am indebted to Bob Bradford for his friendship and selfless assistance. Paul Eugenio and Kent Paschke both possessed an inspirational enthusiasm, on the softball field and in the office, that made my graduate-student life and work more enjoyable. My discussions with Professors Curtis Meyer, Gregg Franklin, and Brian Quinn helped broaden my view of nuclear physics beyond my specific experiment, as well as improving the analysis, and are valued as well. I would like to also thank Professors Robert Kraemer and Frank Tabakin for serving on my thesis committee.

I wish to thank Si McAleer and Steve Barrow for their tireless efforts to process the data used in this analysis, as well as for our many discussions. Gabriel Niculescu, with his insight and persistence, played an invaluable part in the measurement for which I am grateful. The weekly discussions with Gabriel Niculescu, Mac Mestayer, and Ken Hicks directed the analysis effort over the last year and improved the quality of the analysis. I wish to thank Professor Daniel Carman for his close scrutiny of this analysis; his feedback has greatly improved the quality of the results. I also thank Richard Thompson for our fruitful discussions as well as the software tools he developed, which then played an important role in this analysis.

Finally, I am deeply indebted to my family for their support and prayers over the years. I am especially grateful to my wife, Jennifer, for her unwavering dedication and support, even in the face of caring for our two children alone through long days. I am very thankful for my children, Elizabeth and Peter, and for their delightful way of correcting my priorities and perspective.

Experiences with CLAS: A Short Narrative

I first became involved in the CLAS collaboration during the Summer of 1997 at the invitation of Professor Reinhard Schumacher, when I participated in the final stages of the Region One drift chamber construction at the University of Pittsburgh. My experience with the drift chambers led to an interest in the CLAS track-reconstruction software. In studying the software, I realized that the geometry for the drift chambers as implemented was quite imperfect, only partially taking into account possible chamber misalignments, having the signal boards for Region One on the wrong side of the detector, etc. Beginning in the Fall of 1997, I rewrote the drift chamber geometry software and modified the tracking code to properly use the wire location and direction information.

Armed with a now "correct" drift chamber geometry, I began to study the relative positions and alignment of the different drift chamber sectors and regions. An optical survey had been previously performed, with the results used in the track reconstruction. However, the reconstructed momentum was of poor quality, and it was determined that the drift chamber alignment was the most likely culprit. From April to October of 1998, I worked to find a technique to measure the alignment, finally succeeding in developing an algorithm and procedure. This technique fits straight tracks from events collected with the main torus off to different combinations of the drift chamber regions. It has been adopted as the standard alignment procedure by the collaboration. Recently, two graduate students have used my code to re-assess and determine the drift chamber alignment after a few sectors had been taken out for repairs. I believe this to be my greatest single contribution to the collaboration.

After determining the drift chamber alignment, there was some concern about the geometry used for the chambers in the GEANT-based model of the CLAS detector, GSIM. Previously, the geometries for the reconstruction and simulation software had been completely separate. During 1999, when my hyperon electroproduction analysis was beginning to mature, I rewrote the drift-chamber portion of GSIM to use the same geometry as the track reconstruction. This was a large step forward to believing the results from our acceptance calculations.

One of the complications of electroproduction measurements was the need to estimate the effects of multi-photon exchange and radiation. To study this correction for the hyperon electroproduction case, I took over a program in 2000 originally written to calculate the radiative effects for eta production. It had been written by Rich Thompson, a graduate student and colleague from the University of Pittsburgh. The program was generalized to produce results for nearly any exclusive electroproduction reaction, and renamed RadGen.

Since the summer of 2000, I have primarily worked on the hyperon electroproduction analysis as part of experiment E93-030. A parallel analysis of the $K^+\Lambda$ and $K^+\Sigma^0$ final states was performed by Gabriel Niculescu for Ohio University, and we have spent the last two years comparing results and techniques, debugging the two

analyses. In November of 2001, the analysis began review by the Structure of the Nucleon working group of the CLAS collaboration. Since then, studies of the systematic errors and further improvements to the analysis have been my primary focus. In the Spring of 2002, the results approached their final form and the work of writing the thesis began.

I have enjoyed being an experimental particle physicist over the past five years, and plan to continue in that role for the foreseeable future.

Contents

Chapter 1

Introduction

The description of the strong nuclear force in the low energy regime remains one of the unsolved problems of particle physics. The strong force has been well described in the high energy regime with quantum chromodynamics (QCD), however for states with energy comparable to or less than the proton and neutron masses, the relevant energy scale for ordinary matter, QCD become intractable. In this experiment, the reactions

$$e + p \rightarrow e' + K^+ + \Lambda$$

$$e + p \rightarrow e' + K^+ + \Sigma^0$$

are measured as part of an effort to study this interaction. While this experiment cannot directly illuminate and solve the workings of the strong interaction, the information it provides will aid in the construction and testing of theoretical models. This chapter lays the groundwork for later discussions of the measurement and its results.

1.1 Theoretical Background

While QCD is well accepted as the correct description for how quarks interact and can be created, calculating its effect in the low energy, non-perturbative kinematic range remains problematic. At high energies the interaction can be calculated with perturbative techniques due to asymptotic freedom; when the energy is lower, around the mass of the proton, these perturbative techniques break down. In fact, the spectrum of baryon and meson masses are stable eigenstates of the strong interaction, unreachable through simple perturbative expansions in α_s. While the direct, brute force approach of lattice QCD is making rapid progress in finding baryon mass states [1, 2], it cannot yet connect directly to more complex observables.

In the meantime, determining how to calculate the effects of QCD in the non-perturbative regime is still a very active field of study. The primary problem is to determine which degrees of freedom are relevant to describe the transitions between QCD eigenstates, *i.e.* the mesons and baryons. At high momentum transfers, the partons (quarks, gluons) are appropriate, but before reaching this scaling region

there is no single clear solution. A number of concepts and models have been proposed: quarks bound by flux tubes which can break, constituent quarks exchanging "massless" Goldstone-bosons, and interacting meson and baryon fields, to list a few. The most commonly used approach when studying kaon electroproduction is with hadrodynamic models, in which the meson and baryon states are treated as the fundamental fields and are used to calculate the interaction amplitudes. A few of these hadrodynamic models will be discussed here, and later compared to the results of the analysis.

For many years, the only data available for the electromagnetic production of strangeness were of limited statistical quality, covering a small angular range. The construction and commissioning of new photo- and electroproduction experimental facilities such as CEBAF, Graal, and SPring-8, promised to provide new, high precision measurements which would greatly improve the available database. This rekindled an interest in many theoretical groups to study how the electromagnetic production of strangeness could be used as a probe of nuclear structure [3, 4, 5, 6, 7]. In 1998, the first high precision kaon photoproduction results were released by the SAPHIR collaboration [8]. Immediately, the new information created a stir in the theoretical community, as interesting features in the differential and total cross-sections pointed to the possibility of the discovery of a new resonance state [9]. With additional results coming shortly from other facilities, we expect the theoretical front to be active and progress, improving our understanding of the strong interaction in the non-perturbative region.

1.1.1 Missing Resonances

One way to study QCD in the low energy region is to look for and study its bound states. Quark model calculations have predicted many baryon resonances, some of which have been seen in pion-scattering data but many others which have not. A recent calculation [10] came to the conclusion that some of these unseen states should couple strongly to both γN and $K\Lambda$ vertices, suggesting a search for these states in strangeness photo- and electroproduction reactions. The KY final state is favorable for looking for high-mass resonant states for a couple of reasons. First, due to the strangeness production threshold being significantly higher than the multi-pion production threshold (1.61 versus 1.23 GeV), high mass N^* or Δ^* states could be seen in a two-body final state as opposed to the more complex multi-pion final state. Second, since the isospin of the Λ (I=0) and Σ^0 (I=1) differ, additional criteria are placed on which resonance states can contribute to their production. The $K\Lambda$ final state is isospin I=$\frac{1}{2}$ and so only N^* can participate in the s-channel. This differs from the $K\Sigma^0$ state which is a superposition of I=$\frac{1}{2}$ and $\frac{3}{2}$ so both N^* and Δ^* resonances can contribute. This additional isospin selectivity can aid in the identification of N^* states.

1.2 Electroproduction Formalism

1.2.1 Kinematics

For a fixed-target electron-scattering experiment such as this one, an electron beam with four-momentum $e_\mu^{lab} = (E, \boldsymbol{e}^{lab})$ in the laboratory reference frame is incident upon a proton target with $p_\mu^{lab} = (\mathrm{M}_p, \mathbf{0})$. The incoming electron, e, is observed to have scattered through an angle θ_e^{lab} to e' (${e'}_\mu^{lab} = (E', \boldsymbol{e'}^{lab})$), with a total momentum transfer of $q_\mu = e_\mu - {e'}_\mu = (q_0, \boldsymbol{q})$. This generates two invariants to characterize the interaction:

$$\begin{aligned} Q^2 &= -(q_\mu)^2 = 4EE' \sin^2 \frac{\theta_e^{lab}}{2}, && (1.1) \\ s &= W^2 = (q_\mu + p_\mu)^2 \\ &= \mathrm{M}_p^2 - Q^2 + 2\mathrm{M}_p(E - E') && (1.2) \end{aligned}$$

where we have neglected the mass of the electron, since $\mathrm{M}_e \ll E$.

In addition, the final state kaon's momentum is measured to be $K_\mu^{lab} = (K_0, \boldsymbol{K}^{lab})$, and so the inferred hyperon momentum Y_μ is

$$Y_\mu = q_\mu + p_\mu - K_\mu \tag{1.3}$$

1.2.2 Electroproduction Cross-section

The exclusive differential cross-section is written in terms of the scattered electron's energy and angles, and the angles of the final state meson. In the laboratory frame, the differential cross-section is then expressed and measured as:

$$\frac{\mathrm{d}^5\sigma}{\mathrm{d}E' \, \mathrm{d}\Omega_{e'}^{lab} \, \mathrm{d}\Omega_K^{lab}}.$$

The center-of-momentum frame for the proton and momentum transfer (q_μ) system is the most useful for examining the interaction and is illustrated in Figure 1.1. This reference frame will also be referred to as the hadronic reaction frame. Under the excellent assumption of single photon exchange [11], where the entire momentum transfer q_μ is given to a single virtual photon, the electron scattering vertex completely determines the photon's properties. The virtual photon is created in the scattering plane defined by the incoming and scattered electron directions, where $\hat{z}$ is along the photon direction, $\hat{y} = \boldsymbol{e} \times \boldsymbol{e'}/|\boldsymbol{e} \times \boldsymbol{e'}|$, and $\hat{x} = \hat{y} \times \hat{z}$. The outgoing K and hyperon define the hadronic reaction plane. In this plane $\hat{z'}$ is still along the photon direction ($\hat{z'} = \hat{z}$), $\hat{y'} = \hat{z'} \times \boldsymbol{K}/\left|\hat{z'} \times \boldsymbol{K}\right|$, and $\hat{x'} = \hat{y'} \times \hat{z'}$. This frame is rotated an angle ϕ_K about the virtual photon's direction with respect to the scattering plane. Finally, θ_K is the angle between the kaon's momentum and the direction of the virtual photon's momentum.

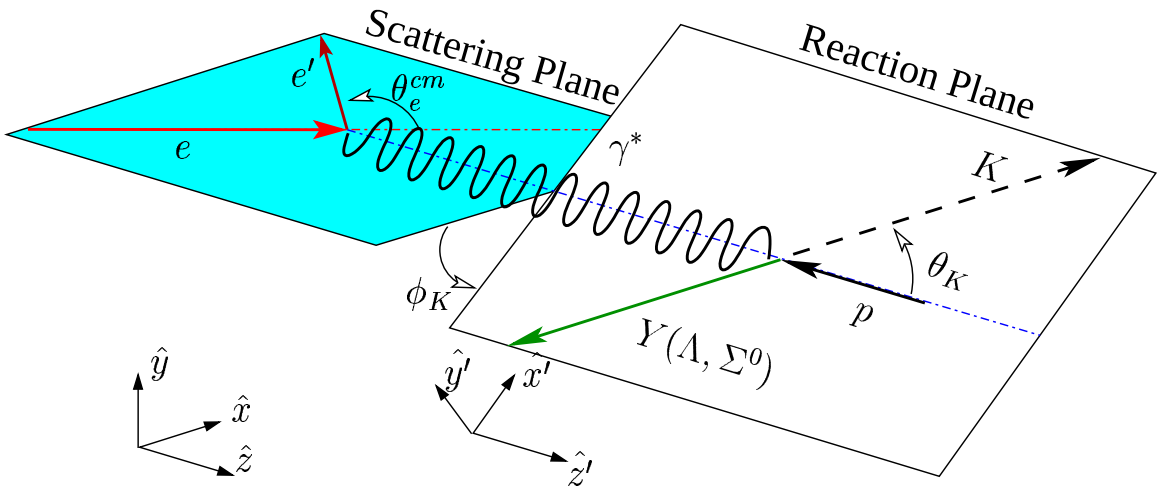

Figure 1.1: The electron scattering and hadronic reaction planes, as viewed from the hadronic ($\gamma^* + p$ or $K + Y$) center-of-momentum frame. Note that ϕ_K is defined to be 0 when the scattered electron (e') and produced kaon (K) travel in roughly the same direction (*i.e.* $\boldsymbol{e'} \cdot \boldsymbol{K} > 0$).

Instead of expressing the cross-section in terms of θ_K, it is often expressed [12] in terms of the Lorentz-invariant Mandelstam variable t. For completeness, the Mandelstam variables are:

$$W^2 = s = (q_\mu + p_\mu)^2 = (K_\mu + Y_\mu)^2 \quad (1.4)$$

$$t = (q_\mu - K_\mu)^2 = (p_\mu - Y_\mu)^2 \quad (1.5)$$

$$u = (q_\mu - Y_\mu)^2 = (p_\mu - K_\mu)^2 \quad (1.6)$$

The variables t and u are directly related to $\cos\theta_K$ when evaluated in the center of momentum frame as:

$$t = -Q^2 + \mathrm{M}_K^2 - 2\sqrt{-Q^2 + |\boldsymbol{q}|^2}\sqrt{\mathrm{M}_K^2 + |\boldsymbol{K}|^2} + 2\,|\boldsymbol{q}|\,|\boldsymbol{K}|\cos\theta_K \quad (1.7)$$

$$u = -Q^2 + \mathrm{M}_Y^2 - 2\sqrt{-Q^2 + |\boldsymbol{q}|^2}\sqrt{\mathrm{M}_Y^2 + |\boldsymbol{K}|^2} - 2\,|\boldsymbol{q}|\,|\boldsymbol{K}|\cos\theta_K. \quad (1.8)$$

Since t is always negative, in the literature $-t$ is often used as the independent variable when discussing cross-sections. Note that both t and u are both always negative, and have their minimum magnitude at opposite ends of the polar angles range: $-t$ is minimum in the forward direction ($\theta_K = 0$), while $-u$ is smallest in the backward ($\theta_K = 180°$) direction.

Unlike a real photon, since a virtual photon is effectively massive it can be polarized along its direction of motion. This is generally referred to as the longitudinal component of the photon's polarization. The virtual photon is actually generated

at the scattering vertex in a polarized state with both transverse and longitudinal components. The polarization is specified by the parameter [11, 12, 13]:

$$\epsilon = \left(1 + 2\frac{|\boldsymbol{q}|^2}{Q^2}\tan^2\frac{\theta_e^{lab}}{2}\right)^{-1}. \tag{1.9}$$

Note that ϵ is invariant under boosts along the photon's momentum direction, and so can be calculated in any frame. In the hadronic reaction frame, the virtual photon's longitudinal polarization component is described by

$$\epsilon_L = \frac{Q^2}{(q_0^{cm})^2}\epsilon \tag{1.10}$$

where q_0^{cm} is the energy of the virtual photon in the center-of-momentum frame. There are a number of different competing conventions for how to calculate the ϵ_L term. Here we have chosen the form suggested by Akerlof [12] and Knocklein [14]. However, throughout the rest of this document only the ϵ term is explicitly used, with the $Q^2/(q_0^{cm})^2$ kinematic factor absorbed into the response functions.

The hadronic center-of-momentum frame can be directly determined from the momentum transfer of the electron. With this and continuing the assumption of single photon exchange, the electroproduction cross-section can be expressed in terms of the kaon center-of-momentum angles and reveals a direct relation to the photo-production cross-section [13, 12, 14]:

$$\frac{\mathrm{d}^5\sigma}{\mathrm{d}E'\,\mathrm{d}\Omega_{e'}^{lab}\,\mathrm{d}\Omega_K} = \Gamma\,\frac{\mathrm{d}\sigma_v}{\mathrm{d}\Omega_K}(W, Q^2, \epsilon, \theta_K, \phi_K) \tag{1.11}$$

where

$$\Gamma = \frac{\alpha}{2\pi^2}\frac{E'}{E}\frac{|\boldsymbol{q}|}{Q^2}\,\frac{1}{1-\epsilon}, \tag{1.12}$$

can be interpreted as the flux of virtual photons in the laboratory frame per electron scattered into $\mathrm{d}E'$ and $\mathrm{d}\Omega_{e'}^{lab}$ [12]. The expression $\frac{\mathrm{d}\sigma_v}{\mathrm{d}\Omega_K}$ is a commonly used shorthand for $\frac{\mathrm{d}^2\sigma}{\mathrm{d}\Omega_K}$, the virtual photoproduction cross-section in the hadronic center of momentum frame; α is the fine-structure constant governing the coupling at the electron-photon vertex; and the electron and photon quantities are evaluated in the laboratory frame.

The electron kinematic variables (E,E', and θ_e^{lab}) can be replaced in the expression for the cross-section with the more physically insightful invariant quantities W, Q^2, and ϵ. The Jacobian relating E', and $\Omega_{e'}^{lab}$ to W and Q^2 is straight forward to compute, and azimuthal angle of the electron is integrated out since only the angular separation of the scattering and reaction planes is meaningful. The cross-section can then be rewritten as

$$\frac{\mathrm{d}^4\sigma}{\mathrm{d}W\mathrm{d}Q^2\mathrm{d}\Omega_K} = 2\pi\,\frac{W}{2EE'\mathrm{M}_p}\Gamma\,\frac{\mathrm{d}\sigma_v}{\mathrm{d}\Omega_K}. \tag{1.13}$$

1.2.3 Virtual Photo-production Cross-section

If the incident electron beam is unpolarized and the polarization of the final state particles is not measured, the virtual photo-production cross-section is [12, 14]

$$\frac{\mathrm{d}\sigma_v}{\mathrm{d}\Omega_K} = \sigma_T + \epsilon\sigma_L + \epsilon\sigma_{TT}\cos 2\phi_K + \sqrt{2\epsilon(\epsilon+1)}\sigma_{LT}\cos\phi_K. \tag{1.14}$$

The different terms correspond to the coupling of the final state to the different polarization components of the virtual photon, and are functions of W, Q^2, and θ_K. The σ_T accounts for the coupling of the transverse polarization components of the photon, and σ_L reflects the longitudinal coupling. The σ_{TT} term is due to the interference between the amplitudes coupling to the two transverse polarization states of the photon. Finally, the σ_{LT} term is due to the interference between the transverse and longitudinal coupling amplitudes.

The literature contains a number of different conventions for expressing $\frac{\mathrm{d}\sigma_v}{\mathrm{d}\Omega_K}$. Another common form is [12]

$$\frac{\mathrm{d}\sigma_v}{\mathrm{d}\Omega_K} = \sigma_T + \epsilon\sigma_P\sin^2\theta_K\cos 2\phi_K + \epsilon\sigma_L + \sqrt{2\epsilon(\epsilon+1)}\sigma_I\sin\theta_K\cos\phi_K \tag{1.15}$$

where some trivial $\sin\theta_K$ factors have been expressed. [1] We have chosen not to express the cross-section in this form since we are not performing a partial wave analysis. When the cross-section is expressed in terms of the CGLN amplitudes [14], many other θ_K dependencies are evident, which cannot be removed without assumptions as to the underlying reaction mechanism. Equation 1.15 explicitly states that σ_{TT} and σ_{LT} must vanish at the very forward and backward directions. This can be explained simply by realizing that the hadronic-reaction plane is not defined in the case where the K and γ^* are co-linear.

In a measurement of the total cross-section, in which the ϕ_K angle is integrated over, only the σ_T and σ_L terms survive. Since separating these two terms requires varying ϵ while keeping W, Q^2 and θ_K constant (accomplished by changing the beam energy) these two terms will often be to referred together as the "unseparated" cross-section:

$$\sigma_U = \sigma_T + \epsilon\sigma_L. \tag{1.16}$$

The unpolarized real photo-production cross-section is sensitive to only the $\sigma_T(Q^2 = 0)$ term. However, there is a connection between the σ_{TT} interference term and the polarization observable, Σ. The linearly polarized photon beam asymmetry is defined as [5]

$$\Sigma = (\frac{\mathrm{d}\sigma}{\mathrm{d}\Omega}^{\perp} - \frac{\mathrm{d}\sigma}{\mathrm{d}\Omega}^{\parallel})/(\frac{\mathrm{d}\sigma}{\mathrm{d}\Omega}^{\perp} + \frac{\mathrm{d}\sigma}{\mathrm{d}\Omega}^{\parallel}) \tag{1.17}$$

[1] In the literature, the σ_T is often written as σ_U, corresponding to the coupling of an "unpolarized" real photon. However, we will use σ_U to refer to the "unseparated" combination of $\sigma_T + \epsilon\sigma_L$.

where $\perp$ ($\parallel$) corresponds to a photon linearly polarized perpendicular (parallel) to the reaction plane. This is related to σ_{TT} by [14]:

$$\Sigma = -\sigma_{TT}(Q^2 = 0)/\sigma_T(Q^2 = 0). \tag{1.18}$$

While we do not directly measure σ_T , the sign of σ_{TT} and its qualitative behavior can be used in comparison to measurements and calculations of the Σ polarization observable in real photon measurements.

Unlike the σ_T and σ_L terms in Equation 1.14, nothing constrains the σ_{TT} and σ_{LT} interference terms to be greater than zero. This is clear when they are expressed in terms of the helicity amplitudes as defined in reference [14]:

$$\begin{aligned}
\sigma_T &= \frac{|\boldsymbol{K}^{cm}|}{q_0^{cm}}\frac{1}{2}\left(|H_1|^2 + |H_2|^2 + |H_3|^2 + |H_4|^2\right), \\
\sigma_L &= \frac{|\boldsymbol{K}^{cm}|}{q_0^{cm}}\frac{\epsilon_L}{\epsilon}\left(|H_5|^2 + |H_6|^2\right), \\
\sigma_{LT} &= \frac{|\boldsymbol{K}^{cm}|}{q_0^{cm}}\sqrt{\frac{\epsilon_L}{\epsilon}}\mathrm{Re}\left\{H_5^* H_1 - H_5^* H_4 + H_6^* H_2 + H_6^* H_3\right\}, \\
\sigma_{TT} &= \frac{|\boldsymbol{K}^{cm}|}{q_0^{cm}}\mathrm{Re}\left\{-H_1^* H_4 + H_2^* H_3\right\}.
\end{aligned}$$

Here σ_T and σ_L come from sum of the magnitudes of the amplitudes, and so are positive definite. However, σ_{TT} and σ_{LT} depend upon the relative phases and magnitudes of the helicity amplitudes, and so can be either positive or negative. While the interference terms do carry the units of a cross-section, referring to them as cross-sections can be misleading. To cope with this, the terms of the virtual photo-production cross-section will be referred to as either "response functions" or, in the case of σ_T and σ_L , as "cross-sections."

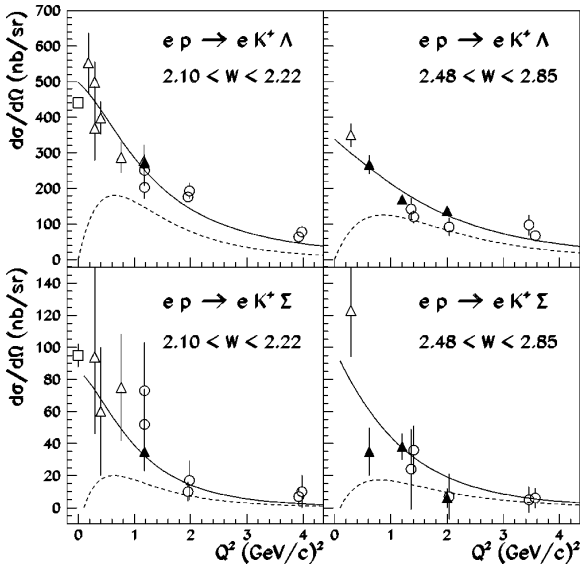

Figure 1.2: The Q^2 dependence of the $ep \to e'K^+\Lambda$ (top) and $ep \to e'K^+\Sigma^0$ (bottom) cross-sections for bins of W, in the forward ($\theta_K < 15°$) region (from [20]). The curves are from the Guidal-Laget model [20], and are explained in Section 1.4.5 and Figure 1.5. The data shown are from (▲) [21], (○) [17], (△) [15]; photoproduction point: (□) [22].

1.3 Prior K^+Y Electroproduction Measurements

The previous kaon electroproduction measurements [15, 16, 17, 18, 19], while precise, were collected with dual-arm spectrometers and so had limited kinematic coverage across the center-of-momentum angles. The majority of the data were collected to study the Q^2 and t dependence of Λ and Σ^0 production at forward angles. Figure 1.2 shows the Q^2 dependence of the previous data for $\theta_K < 15°$, for values of W above the conventional resonance region.

In terms of angular coverage, previous measurements tended to measure the production cross-sections between $0 < \theta_K < 15°$ [15, 16, 21]. Only the 1979 results from DESY [18] covered polar angles greater than 30°, with a range of coverage out to approximately $\theta_K \approx 68°$. Additionally, the data were taken at values of W greater than 2 GeV, above the resonance region. It was not until Jefferson Lab's Hall C came on line and measured the cross-section in the forward direction again, for the purposes of a high-precision extraction of the σ_T and σ_L terms, that a high-quality measurement in the resonance region was made. Our results measured the production cross-section for the first time in the backward hemisphere, and, in contrast to previous measurements, spanned from threshold up to $W = 2.0$ GeV.

The previous measurements, despite limited kinematic coverage, reached a number of conclusions about the production mechanisms. Probably most significant was the

Rosenbluth separation performed by Bebek *et al.* [17], from which they observed that both the transverse and longitudinal components of the cross-section, σ_T and σ_L , contributed significantly to $K^+\Lambda$ electroproduction. They attempted to extract σ_T and σ_L for $K^+\Sigma^0$ production as well with very limited statistics, and came to the conclusion that only the σ_T term was significant for the Σ^0 reaction.

1.4 Hadrodynamic Models

Since non-perturbative QCD (nPQCD) is difficult to calculate directly, phenomenological isobar models have been developed which express the reaction amplitudes in terms of hadronic degrees of freedom. The inherent assumption is that the amplitudes are dominated by the excitation and decay of two-particle resonance states, called isobars [23]. The interactions are then written in terms of an effective Lagrangian, in which the interaction strength is specified in a diagrammatic approach in terms of meson and baryon exchanges and particle couplings. The simplest calculation which could be pursued is then the evaluation of the tree-level diagrams, such as those in Figure 1.3, in which a single hadron is exchanged. Most of the calculations available for investigating kaon electroproduction [6, 7, 24, 25] use this single-channel approach. At the next level of sophistication, the calculations are extended to include re-scattering terms, such that many intermediate states can contribute to the production of the final state of interest; this is the technique used by coupled-channels analyses [26, 27]. The final hadrodynamic-like calculation to be discussed is a Regge-model calculation [20].

The different particle exchanges implemented in the calculations are shown in Figure 1.3. The diagrams are referred to as s-channel, t-channel or u-channel if the intermediate particle is a nucleon($S = 0$), meson, or hyperon($S = -1$), respectively. The names of the different channels correspond to the relevant Mandelstam variable describing the momentum exchanged in a particular diagram. The diagrams in which only one of the initial or final state particles is exchanged are the Born terms, while those which include an excited baryon or meson state are sometimes referred to as the extended-Born terms [6].

When the production amplitude is being calculated, the contribution of a given diagram to is weighted by a term proportional to:

$$\mathcal{A}_X \propto 1/(z^2 - \mathrm{M}_X^2 + \mathrm{i}\mathrm{M}_X\Gamma_X). \tag{1.19}$$

This corresponds to the propagator of the exchanged particle, X, where z is one of (s, t, u) depending upon the diagram, and M_X and Γ_X are the mass and decay-width of X. For the Born terms the particle does not decay, and so the width Γ_X is set to zero. As can be seen from Equation 1.19, the contribution of an s-channel diagram to the production amplitude is maximal when $s = W^2 \approx \mathrm{M}_X^2$. This may create a structure in the cross-section or some other observable. Since both t and u are always negative,

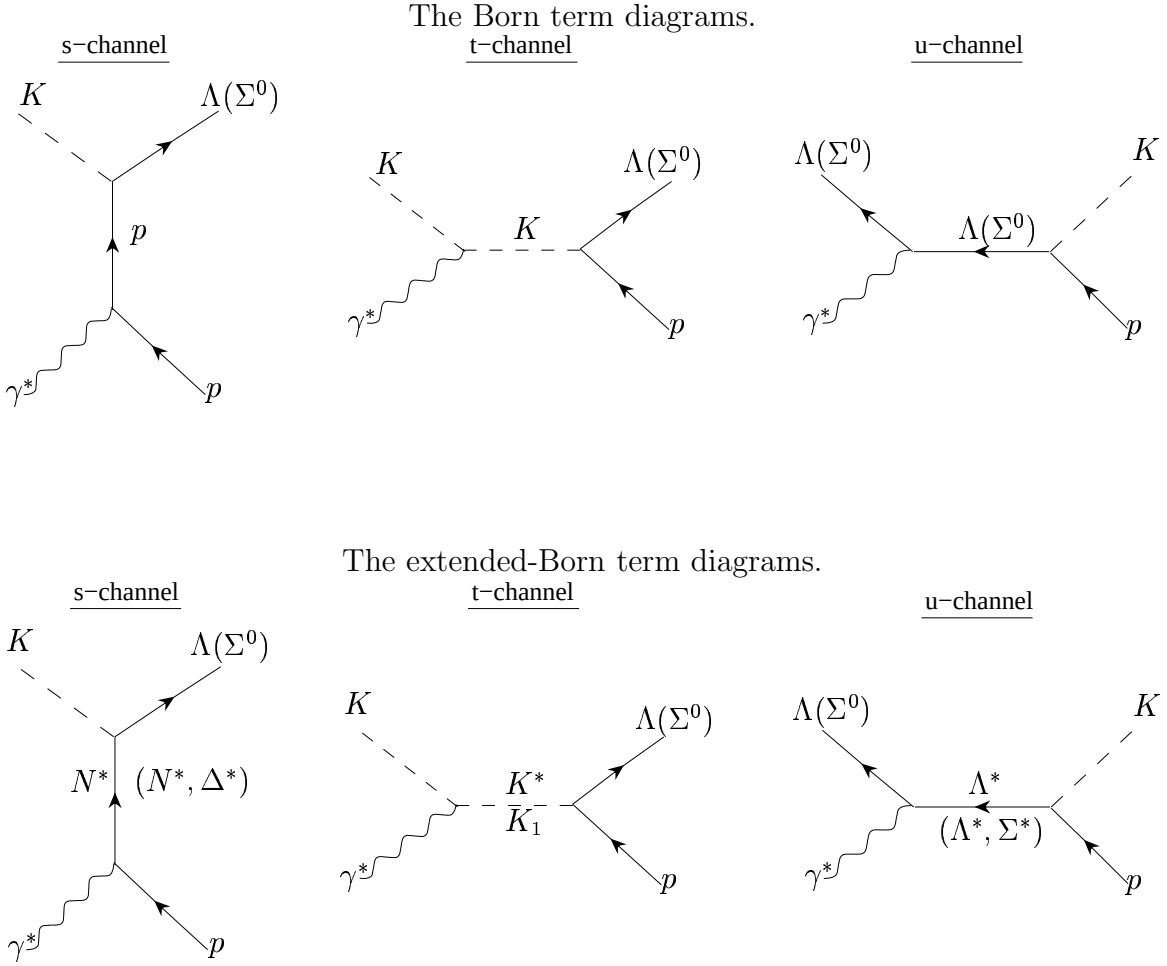

Figure 1.3: The hadrodynamic Born and extended-Born terms for K^+ electroproduction.

they do not exhibit this resonance pole-like peaking behavior. However, since t and u are directly related to $\cos\theta_K$, the $\mathcal{A}$ term moderates their strength, such that their contributions are reflected in different regions of the angular distribution. Processes in the t-channel contribute most strongly in the forward direction (small θ_K) where $|t|$ is minimum, while u-channel processes tend to be strongest in the backward direction (large θ_K). Together with the Born terms, the t- and u-channel terms form the physics background upon which any new s-channel resonance states would be found.

The coupling constants governing the strength of each vertex in the diagrams should reflect the underlying quark-gluon processes. From SU(3) and from measurements of the couplings deduced from pionic reaction processes, one can estimate the range of permissible values for at least the two primary coupling constants, $g_{KN\Lambda}$ and $g_{KN\Sigma}$ [7, 28].

In the case of s-channel production, the intermediate particle's angular momentum is conserved, and is reflected in the orbital angular momentum of the final state KY system.

1.4.1 Single-Channel Isobar Calculations

The data in this thesis are compared with several model calculations. The single-channel isobar calculations each utilized the same basic framework, but different approaches and decisions were made in their development. The first decision was the choice of meson and baryon exchanges to include in the calculation. Since duality relates the s- and t-channel diagrams, one must be careful not to double count contributions when selecting the diagrams to include in the calculation [6]. The next decision was whether to treat the coupling constants at the interaction vertices as free parameters, or to use the ranges given by SU(3). Since the hadronic fields in an effective Lagrangian calculation are not fundamental, the third free choice was how to insert hadronic form factors parameterizing the finite extent of the mesons and baryons. A standard form for this form factor was [24, 29, 30]:

$$F(\Lambda, z^2) = \frac{\Lambda^4}{\Lambda^4 + (z^2 - \mathrm{M}_X^2)^2} \tag{1.20}$$

in which M_X is the mass of the particle being exchanged and $z^2 = s$, t, or u, the four-momentum-squared of the particle. The parameter Λ then determined the effective size and "hardness" of the particle. In the limit where hadrodynamics was exact, the exchanged particles would be fundamental and $\Lambda \to \infty$. For practical purposes, it was considered sufficient to have $\Lambda \gg \mathrm{M}_X$. Since the addition of hadronic form-factors treated each diagram differently, breaking the gauge-invariance they had as a sum, it was necessary to restore gauge-invariance through some technique; this was commonly done by the inclusion of an additional counter-term. Finally, and particular to the electroproduction process, the fourth decision concerned how to implement the electromagnetic form-factors at the photon-meson and photon-baryon vertices. The treatment of these four issues will be discussed for each of the calculations presented.

1.4.2 The Bennhold Model

The most recent model by the collaboration of Mart, Bennhold and colleagues [24, 29, 31] was constructed focusing on dynamics in the s-channel. A goal of the model was to include the minimum set of s-channel resonances required to fit the collected data. The intermediate resonant states were selected by referring to results from recent coupled-channel analyses (such as [26]). Only those states found to decay with a significant branching ratio to the $K\ \Lambda$ and $K\ \Sigma^0$ final states were included, which led to the inclusion of a set of spin 1/2 and 3/2 resonances, and the exclusion of spin 5/2 and higher states. The s-channel states included were the N^* states $S_{11}(1650)$, $P_{11}(1710)$, and $P_{13}(1720)$ for $K\ \Lambda$ production. For $K\ \Sigma^0$ production, the Δ^* $S_{31}(1900)$ and $P_{31}(1910)$ states were also considered, and the $P_{13}(1720)$ state was found to be unnecessary. In addition, $K_1(1270)$ and $K^*(892)$ exchanges were found to be necessary to add to the basic K exchange in the t-channel. The u-channel contained only the Born term diagrams.

An important feature of this model was the use of a novel prescription to restore gauge-invariance [31], which led to a different kind of hadronic form-factor behavior than had been used in previous models(*e.g.* [6]). In contrast to prior techniques, the new prescription permitted the modification of the electric-current contribution by the hadronic form factors to model the finite extent of the hadron; previously this term was forced to be treated as a bare current for a point-like particle. The coupling constants were then determined by a fit to the available differential cross section and recoil polarization data for the $p(\gamma, K^+)\Lambda$ and $p(\gamma, K^+)\Lambda$ photo-production reactions.

In the extension to include electroproduction reactions [24], the electromagnetic form factors used were of a conventional form, similar to those of Reference [6]. An advanced extended vector meson dominance model supplied the hyperon form factors, interpolating between the time-like ($Q^2 < 0$) and high Q^2 ($Q^2 > 0$) couplings. The nucleonic form factor was also of a conventional form, and a monopole parameterization was used for the kaon form factor. When fitting to the recent electroproduction results, the coupling constants were left at their (fitted) photoproduction values while only parameters of the electromagnetic form factors were permitted to vary.

With this model, a possible missing resonance was claimed [9] in the preliminary SAPHIR photoproduction results [8]; these are shown in Figure 1.4. The structure was identified with the $D_{13}(1895)$ state, predicted in a quark model calculation [10]. Without sufficient information to directly identify its quantum numbers, the D_{13} state was assigned to the feature through a comparison of the extracted and predicted strong couplings to the γp and $K^+\Lambda$ states. However, the interpretation of the photoproduction results was not conclusive, as pointed out by Saghai [32], since the shoulder seen in the differential cross-section was also well explained by hyperon resonances in the u-channel.

When the recent Hall C σ_T and σ_L measurements [19] were added to the analysis, Bennhold found it necessary to add a different spin-parity state, such as the D_{13}, to interfere against the resonance states included in the model [24]. In order make a more

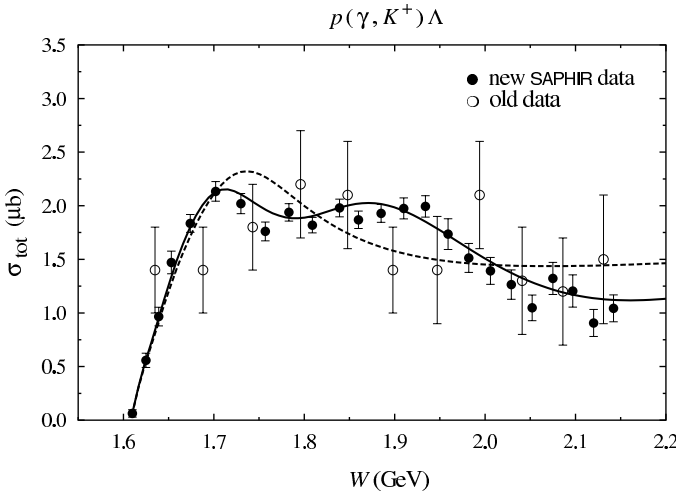

Figure 1.4: The SAPHIR photoproduction results [8] with the calculations from Reference [9] showing the total cross-section with (without) the $D_{13}(1895)$ contribution as a solid (dashed) curve [24].

definitive statement about the state, it was suggested to measure the photon linear-polarization asymmetry, Σ, since the D_{13} was predicted to leave a large signature in this polarization observable [9]. Since Σ is proportional to the σ_{TT} structure function in electroproduction, we hope to shed some light on this debate.

1.4.3 The Janssen Model

The model by Janssen *et al.* [25, 30, 33] was very similar to the Bennhold effective Lagrangian calculation, but with a variation on the hadronic form-factor and the inclusion of u-channel hyperon resonances. Their criticism of the Bennhold model was primarily centered around the use of the hadronic form-factors. First, the terms added to restore gauge invariance contained poles, and were therefore flawed [30]. To improve on this, Janssen used a different prescription that kept the beneficial effects of the form-factor, while not suffering from additional unphysical poles. The second concern focused on the very "soft" form-factors implemented by the Bennhold calculation in order to bring the cross-section down to the level of the data. This caused the form-factor to have a significant impact on the behavior of the cross-sections. Instead, Janssen's model added the $\Lambda^*(1800)$ and $\Lambda^*(1810)$ hyperon resonances to the u-channel for Λ production, which interfered destructively with the Born terms to bring the cross-section down. For Σ^0 production, the $\Lambda^*(1810)$ and $\Sigma^*(1880)$ states were added to the u-channel. In the t-channel, the $K^*(892)$ excited kaon state was included. These contributions then formed the non-resonant background upon which the nucleon resonances were added. The s-channel resonances included in the model were the $S_{11}(1650)$, $P_{11}(1710)$, $P_{13}(1720)$ and $D_{13}(1895)$ N^* states for Λ production,

with the $S_{31}(1900)$ and $P_{31}(1910)$ Δ^* states added as well for Σ^0 production.

The coupling constants were set by a fit to the photoproduction data, notably the recent SAPHIR dataset [8], with values consistent with ranges given by broken-SU(3). When extended to electroproduction, standard forms for the electromagnetic form-factors were applied to each term [34]. With the electroproduction dataset, the parameters describing the Q^2 evolution of the cross-section were optimized. Once again, this was quite similar to the technique followed by the Bennhold calculation [24].

1.4.4 Coupled-Channel Analysis

While the single-channel isobar analyses already mentioned performed well at fitting the data, there was some concern as to how to relate the coupling constants extracted from the models to the "true" coupling strength between hadrons. For example, if a state was formed after many re-scattering processes took place, the coupling constant relating the final state to the intermediate or initial states would inevitably include all the re-scattering processes as well. A recent study at the University of Pittsburgh [27] calculated that in $K\Lambda$ photoproduction, approximately 20% of the production strength came from πN states which re-scattered to the strange final state. This was a significant contribution, bringing into question the validity of comparing the coupling constants extracted from single-channel techniques to those calculated from other approaches. Unfortunately, results from this calculation were not available for the electroproduction reactions.

1.4.5 The Guidal Regge-Model Calculation

Instead of adding more high-spin and high-mass s-channel resonance states as increasing energies were probed, one could instead exploit duality and include more meson-exchange t-channel diagrams. This was done efficiently in Regge model [35] calculations by extending the notion of the exchange of a single particle in the $t-$channel to the exchange of a set of particles, or trajectory. When the internal angular momentum J was plotted versus the mass of the mesons squared (M^2), as shown in the left panel of Figure 1.5, the mesons tended to group onto lines or Regge trajectories. For the kaons, the two sets were the K mesons (S=+1) with un-natural parity (P=$(-1)^{J+1}$) such as the $K(495)$ and $K_1(1270)$, and the K^* mesons with natural parity (P=$(-1)^J$). After using the Born terms as a basis, Regge models then parameterized the t-channel process as the exchange of the entire trajectory. In these calculations the s-channel resonance states cannot explicitly contribute, but instead were averaged over.

The Regge model of Guidal and Laget implemented this standard Regge technique for pion and kaon photoproduction [28] and electroproduction [20] reactions, but with a new approach to restoring gauge invariance. When taken together the Born terms were gauge invariant, however the Regge technique treated the t-channel term

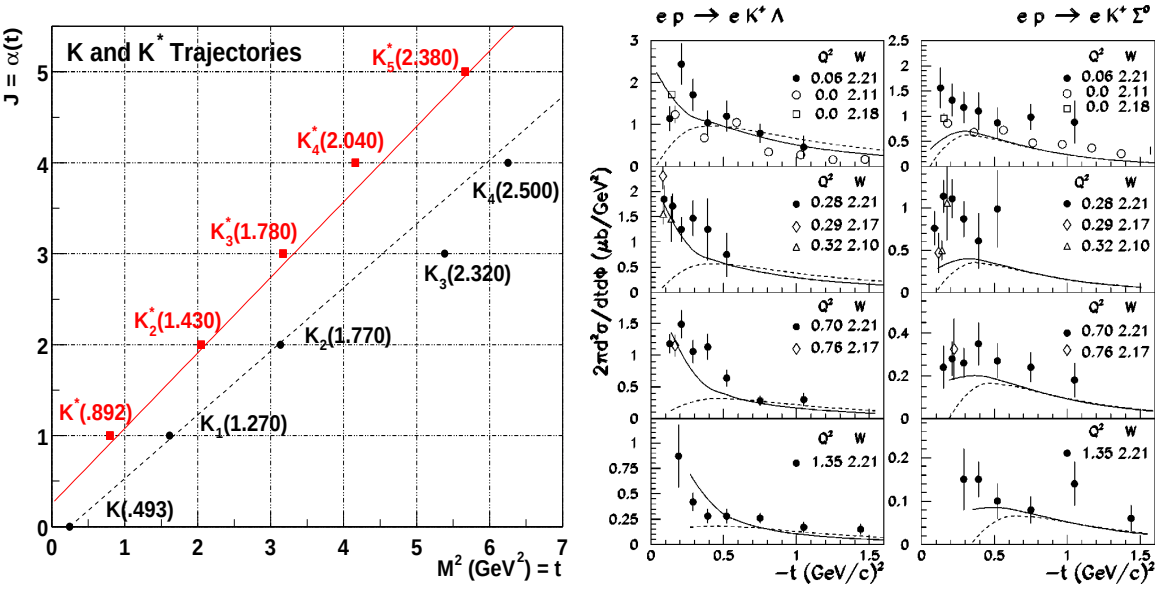

Figure 1.5: The left panel shows Regge-trajectories for K and K^*, with the angular momentum of a particle linearly related to its mass-squared. On the right, the t dependence of $ep \to e'K^+\Lambda$ (left) and $ep \to e'K^+\Sigma^0$ (right) differential cross-sections for different Q^2 values is shown (from [20]). The importance of K^* exchange can be seen by comparing the calculations for $K + K^*$ (solid line) to K^*-only exchange (dashed line). This figure also summarizes well the state of the previous data; electroproduction: (●) [18], (◊) [17], (△) [16]; photoproduction: (○) [8], (□) [22].

differently, which broke their gauge invariance. In contrast, the Guidal-Laget model applied the same factor to the t and s (or u) channel diagrams, maintaining gauge invariance. The coupling constants were determined using constraints from SU(6), measurements of the radiative decay of the K^*, and a fit to high energy ($E_\gamma \geq 5\,\mathrm{GeV}$) photoproduction data. In moving from photo- to electro-production, the K and K^* exchange terms were multiplied by a monopole form factor, including the associated Regge-ized s-channel term. The cutoffs of the electromagnetic form factor were fit to best match the Q^2 dependence of the electroproduction data.

The model found K^* exchange to contribute significantly, as shown in the right side of Figure 1.5. While K exchange dominated at high W and in the forward direction near $-t = 0$, at $-t > .5\,(\mathrm{GeV/c})^2$ the K^*-only curves (dashed) contributed most of the strength in this Regge-exchange picture.

For the purpose of the present study, this model benefits from few free parameters, and is expected to be valid for $W > 2.0\,\mathrm{GeV}$, closer to the diffraction limit and the photoproduction data to which it was fit. Therefore, although we are stretching the range of validity of the model by applying it at these low energies, it will be used as a measure of the average non-resonant behavior expected as one moves beyond the resonance region.

1.5 Summary

The three different calculations each utilized different terms for the non-resonant background and the resonant states to describe the kaon electroproduction process. The models by Bennhold and Janssen are quite similar in that they are isobar calculations of the classic sense, containing the same s-channel resonant states but with very different handling of the non-resonant background. The Regge-model calculation by Guidal could be said to include an average over all resonant states, but only as part of the Regge-ized s-channel Born terms. As such, it will serve as a benchmark, aiding in the identification of new resonance-like behavior.

Chapter 2

Experimental Setup

In this chapter, the configuration and state of the equipment used to make the kaon electroproduction measurement will be briefly described. This includes the CEBAF accelerator as part of the Department of Energy's Thomas Jefferson National Accelerator Facility, and the CLAS spectrometer as configured during the e1c run period[1], when the datasets were collected, between February and March of 1999.

2.1 The CEBAF Accelerator

CEBAF [36] is a superconducting, recirculating electron-beam accelerator utilizing two linear accelerators (linacs) and two bending sections. With energies between 800 MeV and 6 GeV, it can probe the nuclear medium in a transition region where the conventional interaction description changes from baryon-meson exchange to quark-gluon interactions. The superconducting radio-frequency (SRF) cavities permit the accelerator to operate continuously, providing a high duty factor electron beam. This electron beam is well controlled, as evidenced by the low beam energy spread and emittance. The accelerator is also capable of delivering beam to all three experimental halls, satisfying simultaneously the disparate energy and current requirements of multiple experiments.

For an electron beam of this energy, the 100% duty factor is the primary new feature of the CEBAF accelerator. With a continuous electron beam, the instantaneous rate of electrons incident on the target is kept low while maintaining a high luminosity. This permits experiments to detect in coincidence multiple particles produced in a single interaction with little accidental background. The high luminosity aids in the measurement of processes with small cross-sections. Combining these factors, it is now possible to collect large, high quality datasets in a reasonably short period of time, improving greatly upon previous statistically limited measurements.

A schematic of the accelerator can be found in Figure 2.1, which shows the main components of the accelerator: the injector, the north and south linacs, the recircu-

[1]This is also referred to as the e1b run period in the CLAS documentation.

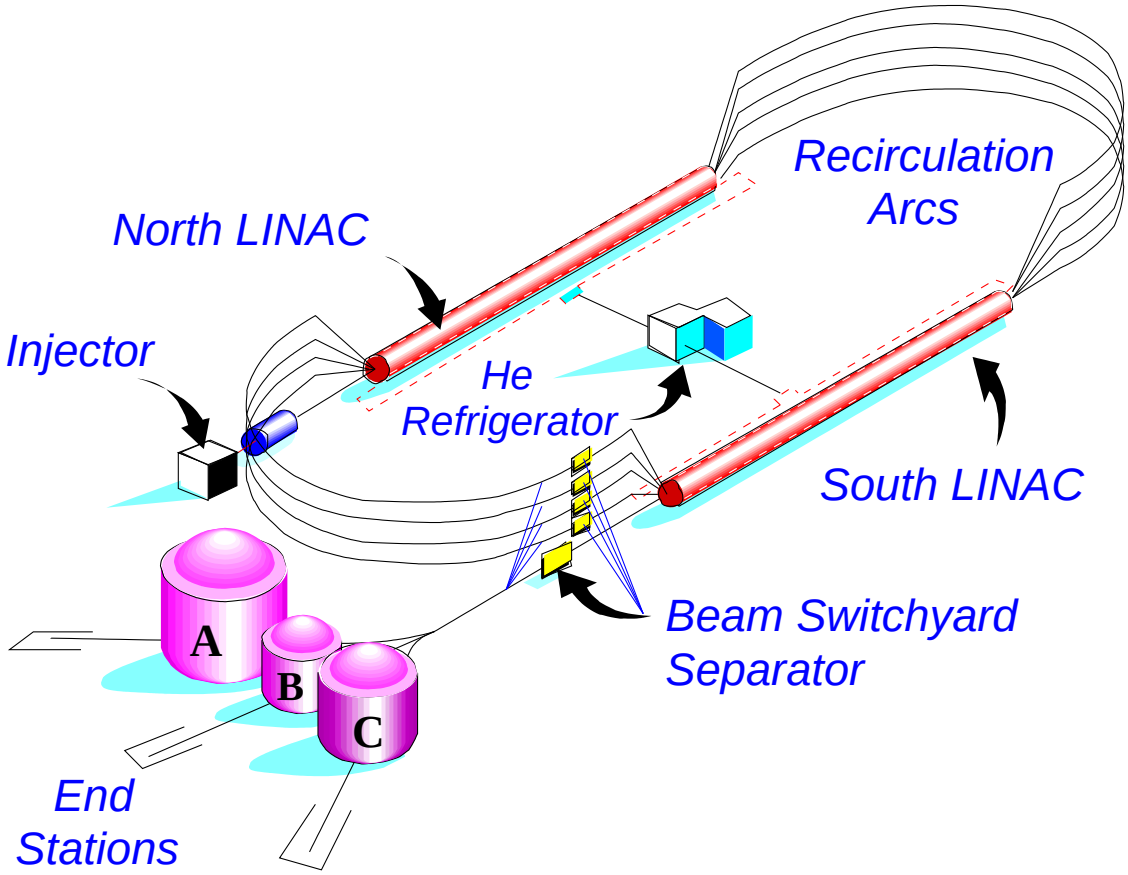

Figure 2.1: The CEBAF accelerator and experimental halls.

lation arcs, and the separator.

The beam began at the injector, where electrons were extracted from a source and prepared for insertion into the main accelerator circuit. Depending upon the needs of the experiments, the electrons could be generated in a polarized spin state from a DC photo-emission gun using GaAs cathodes [37], or an unpolarized state thermionic source. The extracted electrons were then chopped at 499 MHz and bunched into three sets, one for each of the three experimental halls. These bunches had a relative phase of 120°, and were interleaved to form a 1497 MHz electron beam microstructure. Finally, the electron beam was accelerated to relativistic speeds and injected into the north linac with an energy approximately 1% of the maximum accelerator operating energy.

In the linacs, electrons were accelerated until they acquired the desired energy. At the heart of the accelerator were the superconducting radio-frequency (SRF) cavities located in the linac sections. Briefly, an oscillating electro-magnetic field was injected into the cavities with a frequency chosen so that the electric field in the cavity oscillated in time with the motion of the electrons; this is illustrated in Figure 2.2. Since

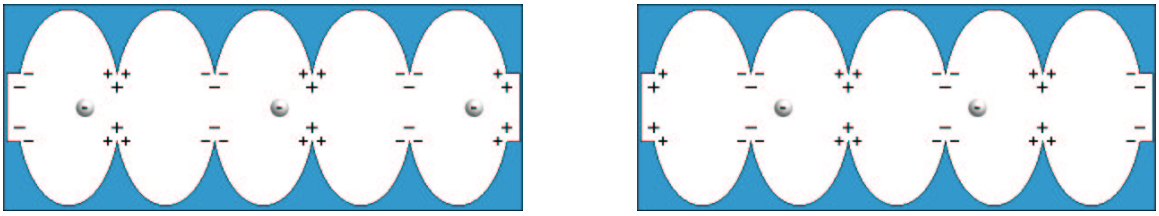

Figure 2.2: As the electrons move to the right in these drawings, the electromagnetic field oscillates, inducing a charge on the interior surface of the cavities, such that the electrons always see a net positive charge in front of them. [38]

the electric field was always anti-parallel to the electron's motion, the electron was continuously accelerated throughout the cavity.

A total of 338 niobium SRF cavities were used in the accelerator. Nominally eight cavities were grouped into a cryomodule, where they were held in a 2.08 K helium bath. Forty-two cryomodules were used in the two linacs, while a one-quarter cryomodule section was used in the injector. Each cavity had an independently regulated 5 W klystron such that it could be individually tuned for optimal performance [39]. The decision to use the relatively young superconducting cavity technology was made in an attempt to limit the power consumption of the machine [36] by substantially reducing the amount of energy lost as heat and to cooling efforts.

The main accelerator was of a recirculating design, where the electron beam was sent through the north and south linacs for up to five passes before delivery to one of the experimental halls. The design called for each linac to accelerate the electron beam by 400 MeV, with a maximum final energy of 4 GeV. The performance of the SRF cavities exceeded the design, and the machine is currently capable of producing a 6 GeV beam, with a plan to upgrade to a maximum $5\frac{1}{2}$-pass beam energy of 12 GeV in motion.

After the south linac, the beam entered the switchyard where each bunch was either recirculated or sent to an experimental hall. A normal-conducting RF separator was used to kick the selected electron bunches of the desired energy toward the appropriate experimental hall. Due to this constraint, only one hall could receive beam from a specific pass except for the full five pass beam, which all halls could receive concurrently.

The electron beam has been shown to be very well controlled and of high quality, with a low emittance (ϵ_{rms} = 1 mm mrad) [40] and an energy stability measured to be better than $3{\times}10^{-5}$ rms [41]. Since the three electron bunches were produced independently at the injector, the beam current supplied to each experimental hall was separately controlled. A common occurrence was for Hall B to receive 100 pA-30 nA, limited by luminosity constraints, while simultaneously ≈130 μA was delivered to Halls A and C where the limitation was due to target cooling requirements [41].

The three experimental halls contain spectrometers specialized for different types of measurements to take advantage of the CEBAF electron beam. Halls A and C both

contain dual-arm spectrometers, while Hall B contains a near-4π large acceptance spectrometer. Hall A houses two optically identical high resolution ($\delta p/p \approx 10^{-4}$) magnetic spectrometers, with a maximum detectable momentum of 4 GeV/c [41]. Each arm was optimized for either electron or hadron detection and identification, and is suited for studying the structure of nuclei as well as the electromagnetic and weak structures of the nucleon. Hall C has a high momentum spectrometer (HMS) with moderate resolution ($\delta p/p \approx 10^{-3}$) and a short-orbit spectrometer (SOS) specialized with a short optical path of 7.4 m to detect short-lived hadrons. The large acceptance spectrometer in Hall B will be discussed in the next section.

2.2 Hall B and the CLAS Detector

The CEBAF Large Acceptance Spectrometer (CLAS) is located in Hall B at Jefferson Laboratory. A schematic of the Hall B beamline is presented in Figure 2.3.

2.2.1 Hall B Beamline

The electron beam in Hall B was monitored and evaluated by numerous devices both before and after it reached the CLAS. These included beam position monitors, halo photomultiplier tubes, a Moller polarimeter, the harps, and the Faraday cup. Here I will only briefly introduce the devices important for the cross-section measurement in this thesis.

2.2.1.1 Nanoamp Beam Position Monitors (BPM)

To monitor the beam position and current non-destructively during data taking, three nanoamp beam position monitors were located in the hall. These were surveyed into position, calibrated to the Faraday cup, and had a position resolution better than $\leq$100 μm [42, 43]. The beam position was read out at a rate of approximately 1 Hz, and was used to provide real-time feedback to the accelerator controls through a software-implemented orbit lock. Figure 2.4 demonstrates how well this feedback system kept the beam position near the target stable during a section of the e1c run period. During data taking, the beam position at the last BPM before the target (2H01) was required to stay within $\pm$50 μm of the specified position.

2.2.1.2 Beam profile and quality monitors

Just in front of the tagger dipole, approximately 22 m upstream of the physics target, was the tagger "harp" and radiator assembly [44]. The harp measured the beam profile by passing a pair of perpendicular 50 μm tungsten wires through the electron beam under the precise control of a calibrated stepper motor [42]. The response of the beam halo monitor photomultiplier tubes were then monitored as a function of

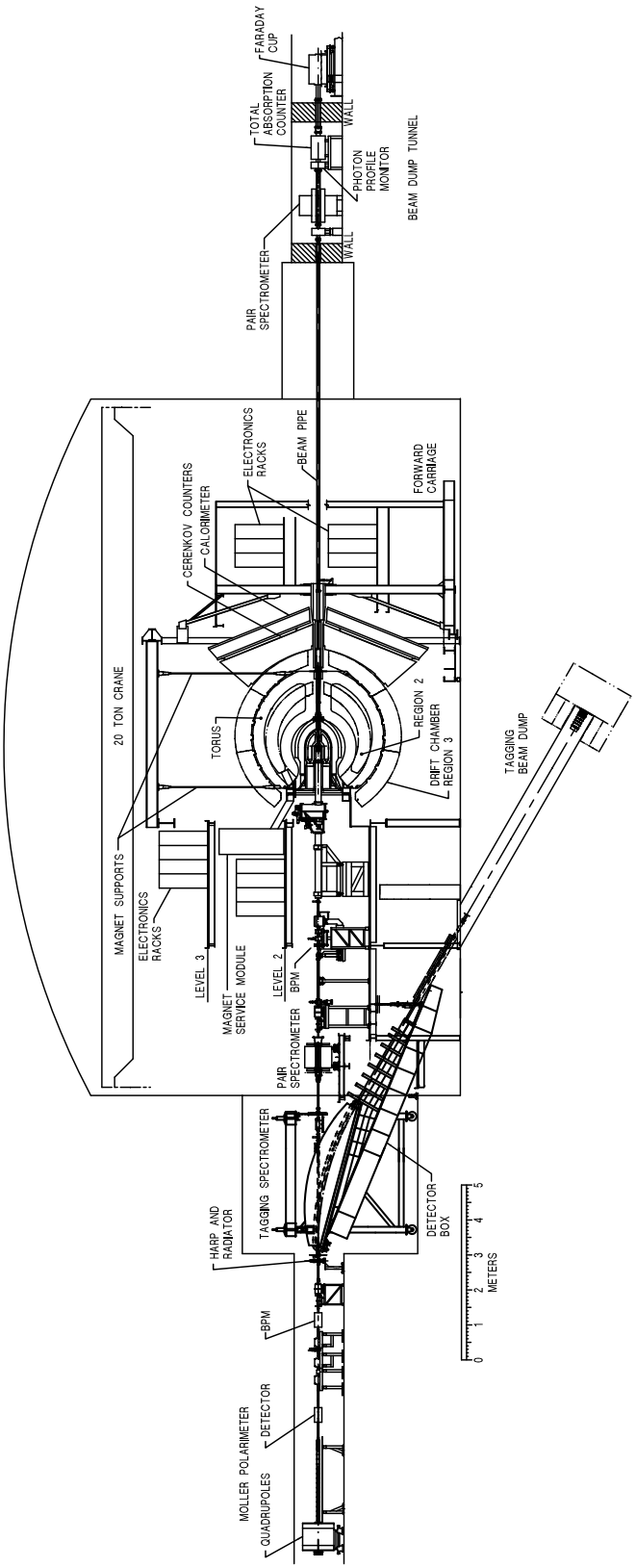

Figure 2.3: A schematic view of the Hall B beamline and the CLAS detector [42].

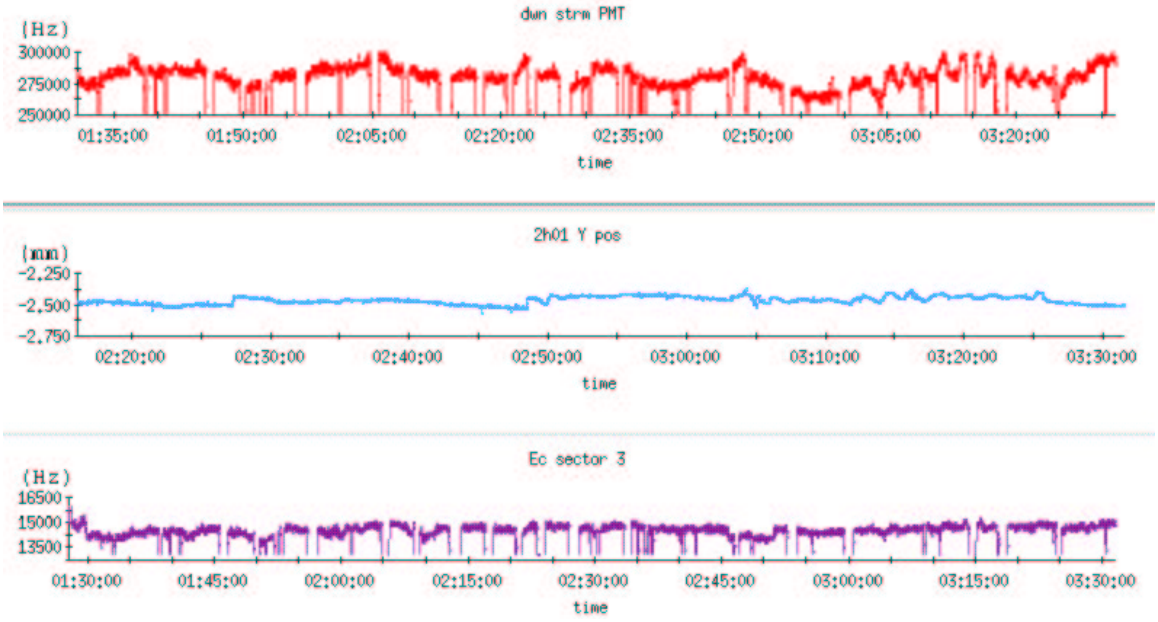

Figure 2.4: The beam monitoring strip-charts, showing a halo monitor(top), beam position from the nA BPM (middle), and the EC scaler rate(bottom) over a two hour period.

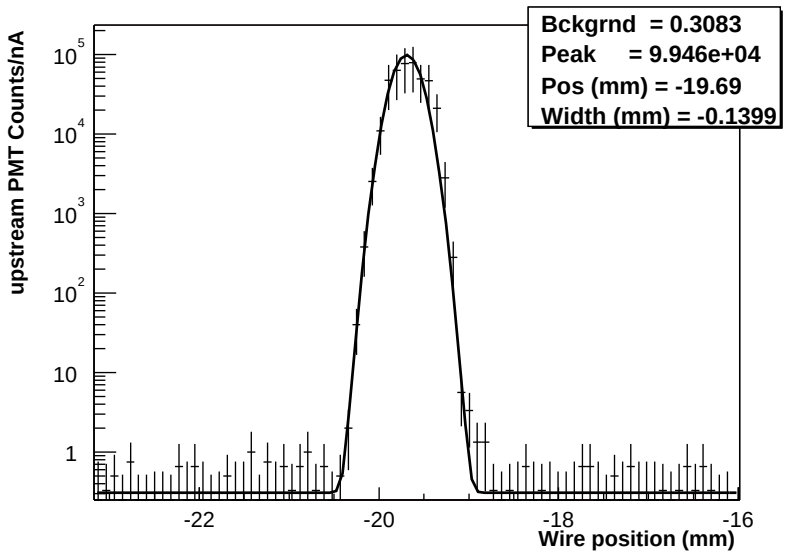

Figure 2.5: The X-profile of the electron beam during a typical harp scan during the e1c run period from a 2.567 GeV, 4 nA electron beam.

the harp position; Figure 2.5 shows a typical beam profile. This permitted the measurement of the beam location and shape, as well as the level of the halo background resulting from beam scraping or the leakage of beam meant for another hall. Typically, the electron beam had a width of $\sigma \leq 200\,\mu$m, with a peak four decades above the background rate. Since the measurement was destructive to the beam, the harp was not used during data taking, but instead used to evaluate the beam tune after a configuration change or when the tune was believed to have degraded.

2.2.1.3 Faraday Cup

Since the beam currents used in Hall B were low, the integrated electron beam flux was directly collected with a Faraday cup. This provided a precise and accurate measurement of the integrated beam current, which was necessary to be able to extract absolute cross-sections. The Faraday cup was made of 4000 kg of lead, over 70 radiation lengths deep, so as to stop the electrons and directly measure the accumulated charge. It was electrically isolated from the environment except through a lead that goes to a current-to-voltage converter, followed by a voltage-to-frequency converter [42]. This signal from the Faraday cup was split, and sent to scalers gated by the state of the data acquisition system. In this way the total charge incident upon the target, the run-gated charge, and the live-gated charge were accumulated and reported. During the e1c running period, the Faraday cup operated at a frequency of 10^{10} counts per Coulomb, typically 40 Hz with a 4 nA beam current. In September 2000, the gain was increased by 10^3 [45] for improved measurements of the beam charge asymmetry when running with a polarized electron beam flipping at 30 Hz.

2.2.1.4 Cryo-Target

A cryogenic liquid hydrogen target provided the protons for this measurement. Target cells of two different designs ("Youri" and "Christo/Saclay") were used during the e1c run period. Both cells were capable of containing and cooling liquid hydrogen and deuterium. The size and specifications of the two cells are given in Table 2.1, and a schematic of the Christo/Saclay cell can be found in Figure 2.6. The target cells were designed to minimize unwanted events from the entrance and exit windows, as well as multiple-scattering from the target structure. The support structures and cooling lines were located upstream of the cell itself so as not to occlude the sensitive region of CLAS. Each target was used to collect approximately 50% of the data for this analysis.

The nominal density of the liquid hydrogen was $0.0695\,\mathrm{g/cm^3}$ at 20 K. However, during the early e1c run period there was difficulty keeping the primary target full. The solution was to super-cool the target to 17 K, which had the effect of increasing the density of the liquid hydrogen by 5%. The temperature and pressure were monitored and recorded to a database throughout the run period, and the corresponding liquid hydrogen density was calculated according to Reference [46].

	Youri (Primary)	Christo/Saclay (Backup)
Length (cm)	4.99	3.98
Radius (mm)	4.86	13.97
Entrance Window Diameter (mm)	4.51	5.00
Al Cell Window Thickness (mm)	0.013	0.015
Kapton Cell Wall Thickness (mm)	0.051	0.127

Table 2.1: The specifications for the target cells used during the e1c run period.

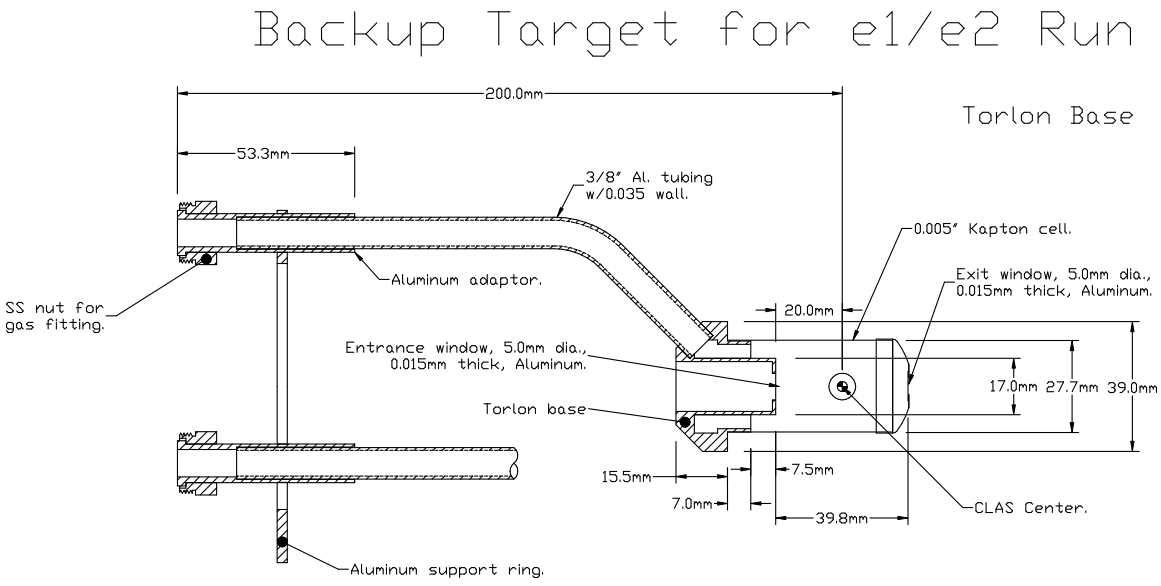

Figure 2.6: Schematic for the Christo/Saclay e1c target.

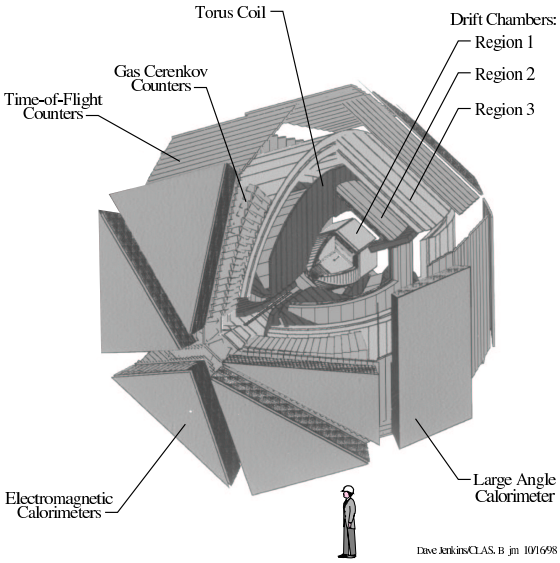

Figure 2.7: A cutaway view of the CLAS, showing the torus and active components. The electron beam enters from the rear-right [49].

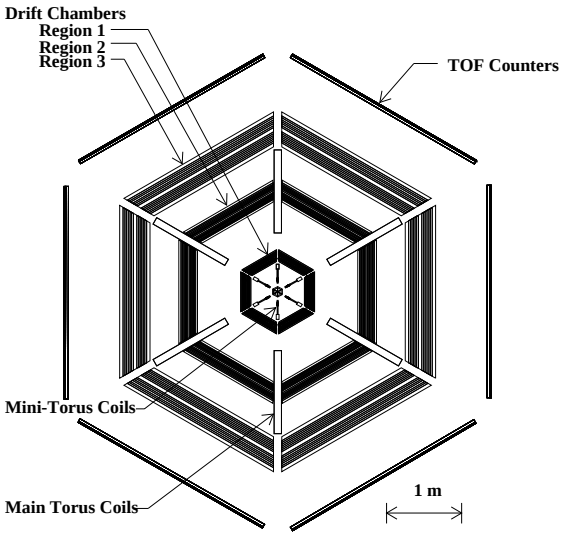

Figure 2.8: A view of the CLAS detector as seen from upstream along the beamline. The torus coils divide CLAS into six sectors. [47]

2.3 The CLAS Spectrometer

A large acceptance spectrometer, CLAS was designed to detect charged particles with momentum greater than 200 MeV/c across a polar angle range from 8° to 140° with up to 80% coverage in the azimuthal angle [47]. It was built around a toroidal magnet, and was divided naturally by the main torus's coils into six independently instrumented and nearly identical sectors, as can be seen in Figures 2.7 and 2.8. In each sector the drift chambers (DC) provided tracking information, scintillating time-of-flight (SC) detectors aided in particle identification, Čerenkov counters (CC) identified electrons, and electromagnetic calorimeters (EC and LAC) aided in electron identification as well as the detection of high energy neutral particles (n, γ). Much more detailed information about the CLAS detector can be found in references [42, 47, 48, 49, 50, 51].

2.3.1 The Toroidal Magnetic Field

The main torus was at the heart of the CLAS spectrometer, permitting the measurement of a charged particle's momentum by inducing a curvature in its path according to the particle's momentum and charge. The torus consisted of six superconducting coils placed about the beam line; the position of the coils with respect to the detectors and beamline can be seen in Figures 2.7 and 2.8. The coils generated a toroidal magnetic field, with the field-lines mostly along the azimuthal ϕ direction, circling

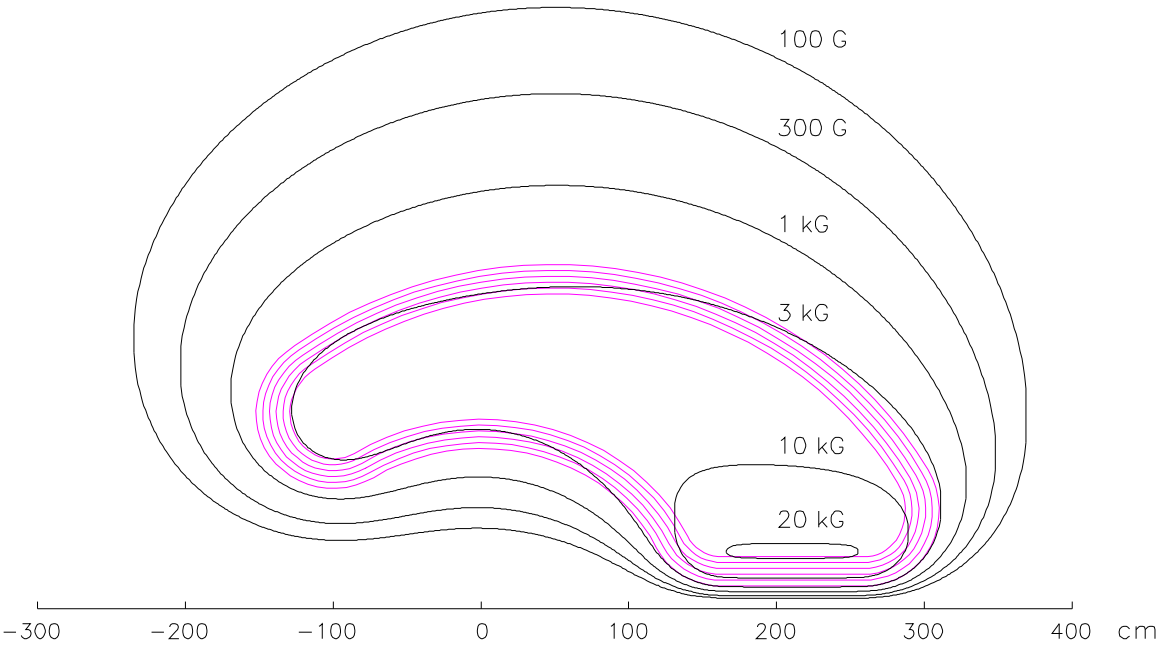

Figure 2.9: The magnetic field contours for the main CLAS torus at the maximum designed current setting of 3860 A [42].

the beam line. This was advantageous since particles originating at the target had momenta perpendicular to the magnetic field lines, and so received the field's maximal effect. This also caused the ϕ angle of a charged particle track to remain nearly constant as it traveled through CLAS, simplifying the track reconstruction.

The main torus was constructed by Oxford Instruments Corporation, and assembled in Hall B. The iron-free coils were each approximately 5 m long and 3 m tall, composed of an aluminum stabilized NbTi/copper conductor and sealed within an aluminum cryostat. The operational temperature of 4.5 K was maintained by a forced flow of supercritical helium through a channel on the inside edge of the windings [51]. The "kidney" shape of the coils was chosen such that the magnetic field was maximal at a low polar angle and decreased as the angle increased, as can be seen in a profile of the magnetic field in Figure 2.9. Under normal operations, the torus's field lines ran counter-clockwise around the beam as viewed from upstream, such that negative (positive) particles bent toward (away from) the beamline. This was optimal for electron scattering experiments since the high momentum forward-going scattered electrons would encounter the strongest magnetic field and bend in toward the forward detectors, optimizing the momentum resolution and maximizing the Q^2 coverage. The magnetic field peaked at 3.5 T [51], with an integral magnetic field of 2.5 T·m in the forward direction when operated at full current [42].

The shape of the magnetic field also minimized the field strength in the region of the target and along the beamline. If the coils were perfectly aligned and centered properly about the beamline, the magnetic field would vanish along the beam's loca-

tion. This would facilitate the use of a polarized target with its own magnetic field. However, since the electron beam was observed to move as a function of the torus current, the coils must not have been at their ideal positions. Much work has been done to try to understand this, and some methods for dealing with the non-ideal magnetic field will be discussed in Section 3.2.2.

During electron running a second toroidal magnet, the mini-torus, was also used to generate a weak magnetic field around the target to protect the drift chambers. Due to interactions of the electron beam and its halo with the hydrogen target and the metal support structures in this region, copious low energy Moller electrons were produced. The mini-torus's field disposed of these electrons by curling them back toward the beamline. Since it generated a magnetic field only 1-5% of that of the main torus at its nominal 6000 A, it had little effect on the higher momentum charged particles analyzed by the main torus.

2.3.2 Drift Chambers (DC)

The drift chambers [47] determined the path a particle took under the influence of the magnetic field by detecting the particle's location at various distances from the target. The three drift chamber regions, situated around the beamline between the radial projections of the torus's coils, measured the charged particle's track within (Region 1), between (Region 2), and outside (Region 3) the coils of the main torus. This permitted the measurement of the initial direction of a particle and its trajectory's curvature, and therefore its momentum.

2.3.2.1 Drift Cells and Layers

The basic unit of a drift chamber is the drift cell, consisting of a positively charge anode (sense wire) at the center, negatively charged field wires about the outside to create the electric field configuration, and the chamber gas. In the CLAS drift chambers, a hexagonal shape for the cell was chosen. Figure 2.10 shows a model of a cell from Region 3 and its electric field lines, with the six field wires on the outer corners and the instrumented sense wire in the center. As a charged particle passed through the cell it ionized the gas, and the freed electrons moved toward the sense wire along the electric field lines. By measuring the time between the passage of the particle through the cell and when the first electrons arrived at the sense wire, the distance of the track from the cell center was calculated. The cells were arranged in layers into a "honeycomb" pattern, as shown in Figure 2.11. Nominally, six layers of cells were placed together into a superlayer, with two superlayers per region. To have a cell's performance independent of its layer, guard wires were placed along the outer edges of a superlayer and held at a voltage to mimic the electric field additional layers would have formed.

The wire directions in superlayers 2, 3, and 5 were axial to the magnetic field, with the wire direction at the midplane perpendicular to both the beam and radial

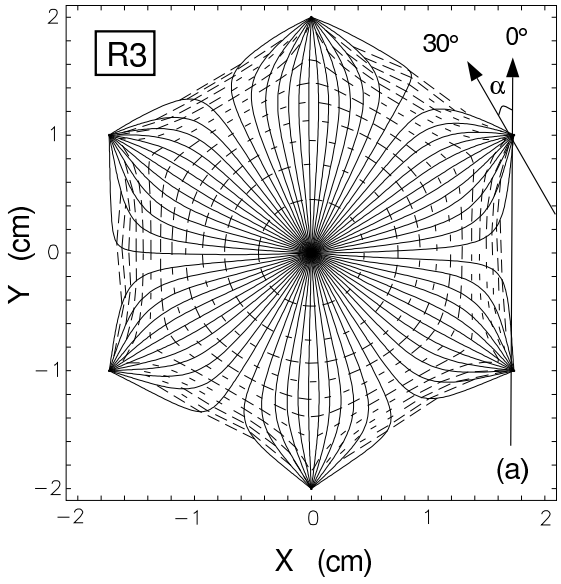

Figure 2.10: The field lines (solid) and isochrones (dashed) of a Region 3 cell.

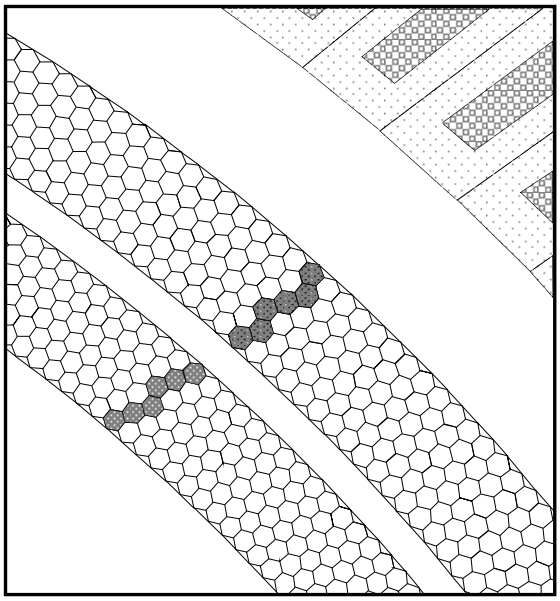

Figure 2.11: The response of the axial (inner) and stereo (outer) Region 3 superlayers to a passing charged particle.

directions. This was nominally perpendicular to the bend plan of the tracks and so was optimized for the momentum measurement. Superlayers 1, 4 and 6 had the wire direction tilted by a stereo angle of 6 ° to the axial direction, providing information about the azimuthal location and momentum components of the tracks.

2.3.2.2 Design and Construction

The open nature of CLAS's geometry required the drift chambers' support structures and electronics to be kept in the shadow of the the torus cryostat. This led to different design considerations for the three regions.

Located less than 1 m from the beamline, the space constraints on Region 1 to keep all inactive material in the cryostat shadow were severe, and required a pair of endplates and the associated electronics to fit within the 3.5 cm space between the sectors. Region 1's aluminum 8 mm endplates were too thin to support the tensional force due to the strung wires. To provide the necessary support, temporary aluminum struts held the endplates at a fixed distance during the stringing process. Later, as the six sectors were integrated into a single unit, the forces were transfered from a compression of the struts to counter-acting tensions across the sectors. These detectors were built at Carnegie Mellon University and the University of Pittsburgh.

The Region 2 drift chambers were situated between the torus's coils, approximately 2 m from the target. Since this was a high magnetic field region, it was designed to withstand a rapid change in magnetic field (in the case of a quench) as well

as the flexing of the cryostat due to the warming and cooling of the superconducting torus [47]. The endplates were constructed from a non-conducting epoxy-fiberglass to avoid forces due to eddy currents which might be generated during a quench. To accommodate for the motion of the cryostat, only the upper endplate was rigidly fixed to the cryostat; the lower endplate was attached via a spring construction that permitted motion only perpendicular to the endplate/cryostat surface. The tensional forces due to the wires were supported by the torus cryostat.

Region 3, being farthest from the beamline at a radial distance of 3 m from the target, was not as spatially constrained in design as the other two regions. Each sector independently supported the tensional forces and was a physically independent device. Carbon struts held the endplates apart during stringing, countering the tension from the wires. The endplates were of a stainless-steel/foam sandwich construction, providing strength with only moderate weight.

The drift cells for all three regions were constructed from the same materials: 20 μm gold-plated tungsten sense wires, 140 μm aluminum field and guard wires, and a 90%/10% mixture of Ar/CO_2 as the chamber gas. The sense wires were chosen to be as small as possible to maximize the electric field at the wire surfaces, and thus to maximize the gain. Tungsten was chosen as the sense wire material due to its durability, and a gold-plating was added to ensure a chemically inert and physically smooth surface. For the field and guard wires, aluminum's long radiation length minimized the effect of multiple-scattering while its low density reduced the required stringing tension necessary to compensate for gravitational sag. The Ar/CO_2 gas mixture was chosen for its non-flammable nature, high saturated drift velocity ($>$ 4 cm/μs), and large operating voltage plateau.

2.3.2.3 Performance

When completed, the drift chambers contained a total of 5862 drift cells per sector. The calibration of the chambers involved two procedures: the x versus t calibration and the determination of the drift chamber alignment. The first procedure determined the relation between the measured drift time and the distance of closest approach of the track which caused the hit [52]. The second procedure, locating the drift chambers and their alignment relative to each other, was developed as part of this thesis project and is discussed in Appendix C. After calibration, the average spatial resolution for a single cell in the optimal middle portion was between 200 and 250 μm and deteriorated close to the sense wire and near the outer edge of the cell, as can be seen in Figure 2.12. For tracks passing close to the sense wire, the extended ionization process lead to a long duration over which the drifting electrons arrived, producing a long but low amplitude signal. The average whole-cell resolutions for the three regions were measured to be 310, 315, and 380 μm for Region One, Two and Three, respectively. Overall, the average efficiency of a single layer was determined to be greater than 98%, again with problems for tracks passing close to the sense wire. During data taking, the luminosity was limited to keep the accidental drift-cell

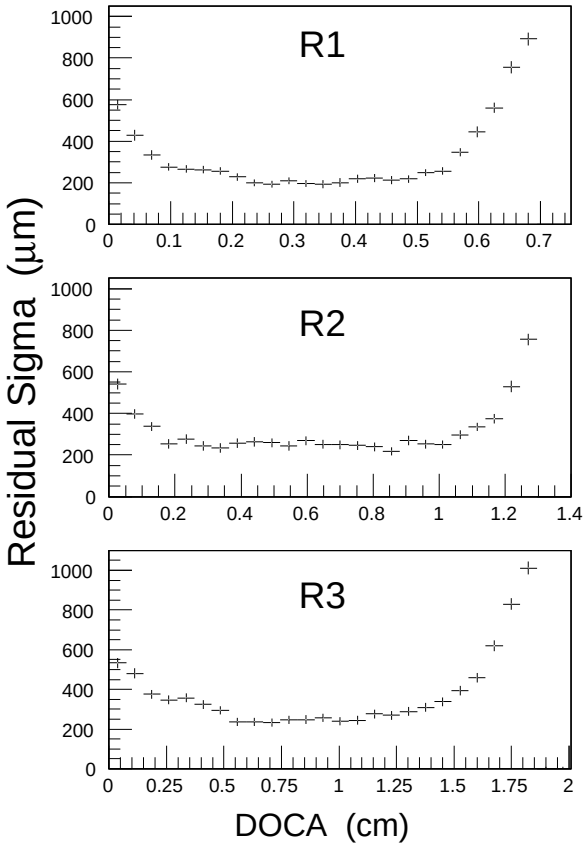

Figure 2.12: The widths of the track-hit residual distributions plotted versus the distance-of-closest-approach (DOCA) for each of the three drift chamber Regions [47].

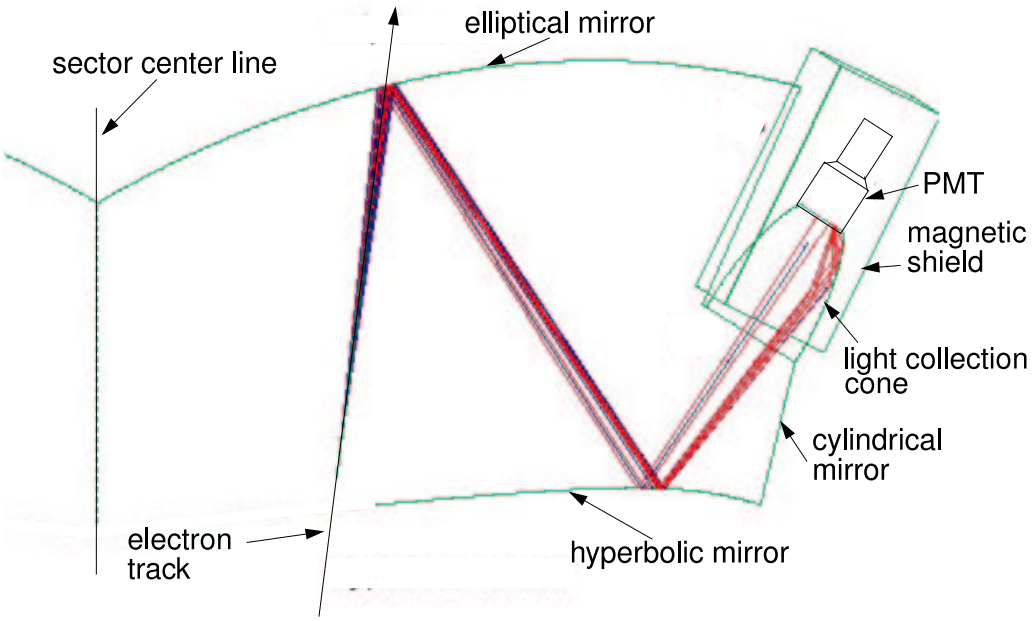

Figure 2.13: The arrangement of a single optical module from the Čerenkov detectors. Each module covers only half the ϕ range of a sector. [48]

occupancy less than 3%, since when the occupancy in Region One was greater than this the track reconstruction efficiency began to suffer [47].

2.3.3 Threshold Čerenkov Counters (CC)

To provide a fast electron trigger and aid in pion/electron separation, CLAS contained a gas threshold Čerenkov detector for each sector. Located on the forward carriage approximately 4 m from the target, the Čerenkov counters spanned out to θ=45° in the laboratory frame. Each Čerenkov was divided optically into 18 units in θ and down the sector midplane, forming 36 optical modules per sector.

Each module, like the one shown in Figure 2.13, consisted of an elliptical mirror at the forward surface, a hyperbolic mirror on the rear surface, and a cylindrical mirror and Winston cone assembly to direct the light into the photo-multiplier tube(PMT). Like the other detector systems, the spatial constraints imposed by the design required the PMTs be located in the torus magnet's shadow. Due to the fringe magnetic fields from the torus, the PMTs were wrapped within a high-μ metal shield. Since the mirrors were in the sensitive region of CLAS, and in front of the time-of-flight detector and electromagnetic calorimeter, it was necessary to minimize the total material used in their construction and support. The mirrors' support was provided by a layered Kevlar and vinyl foam structure. The reflective surface consisted of aluminum vacuum-deposited onto a Lexan sheet, with a layer of MgF_2 added to prevent oxidation [48]. Aluminum was chosen for its high reflectivity through the visible and

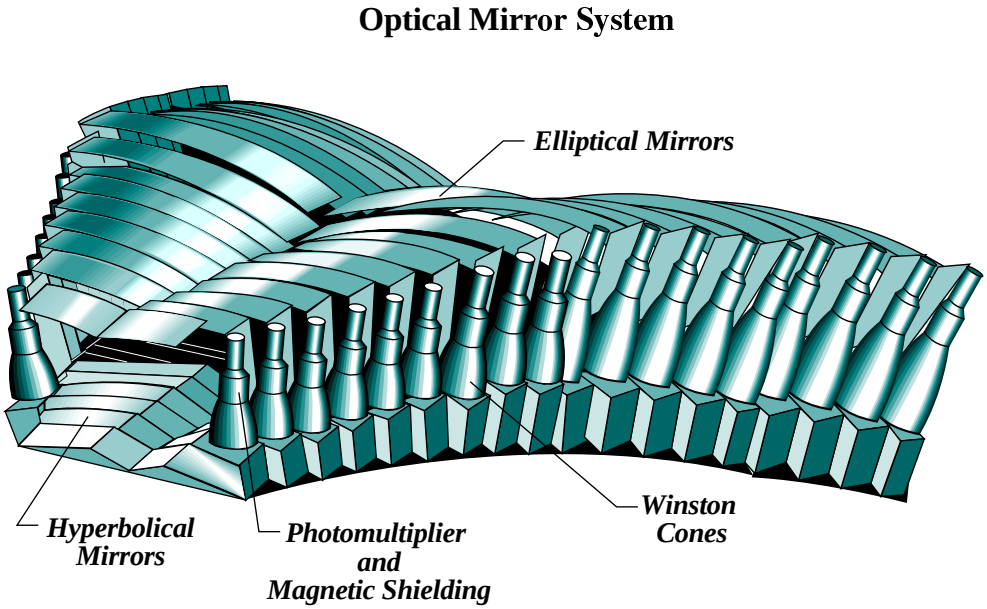

Figure 2.14: A schematic drawing of the 36 modules within a single sector. [48]

into the ultra-violet region. The Čerenkov gas was C_4F_{10} (perflorobutane), with a high index of refraction (n=1.00153) and excellent light transmission properties [48]. This provided electron/pion separation up to a pion momentum of 2.5 GeV/c, or $\beta = 0.9985$.

The Čerenkov detector's trigger electronics were constructed to provide a θ-selective trigger signal. For each sector, the response from each (left/right) module pair was linearly summed into a signal for the segment. The resulting signals from four such adjacent segments were combined into a single group, to account for the spreading of the Čerenkov light across multiple segments. With an overlap of two segments between sequential groups, a total of eight sums were formed from the four segments. These eight sums could then be discriminated at adjustable "high" and "low" thresholds and sent onto the trigger logic, permitting an electron-specific trigger decision to be made, optionally in a θ-sensitive manner. For the measurement in this thesis, an unbiased electron trigger was used.

2.3.4 Scintillating Time-of-Flight Counters (SC)

The CLAS Time-of-Flight scintillating counter (SC) detector [49] provided high resolution timing measurements for determining the flight-time, speed, and eventually mass of a given particle. Located approximately 5 m from the target, it consisted of 57 plastic scintillators per sector divided into 49 channels.

The scintillators within a sector were divided into four panels, as shown in Figure 2.15. They had a uniform thickness of 5.08 cm which provided a large signal for

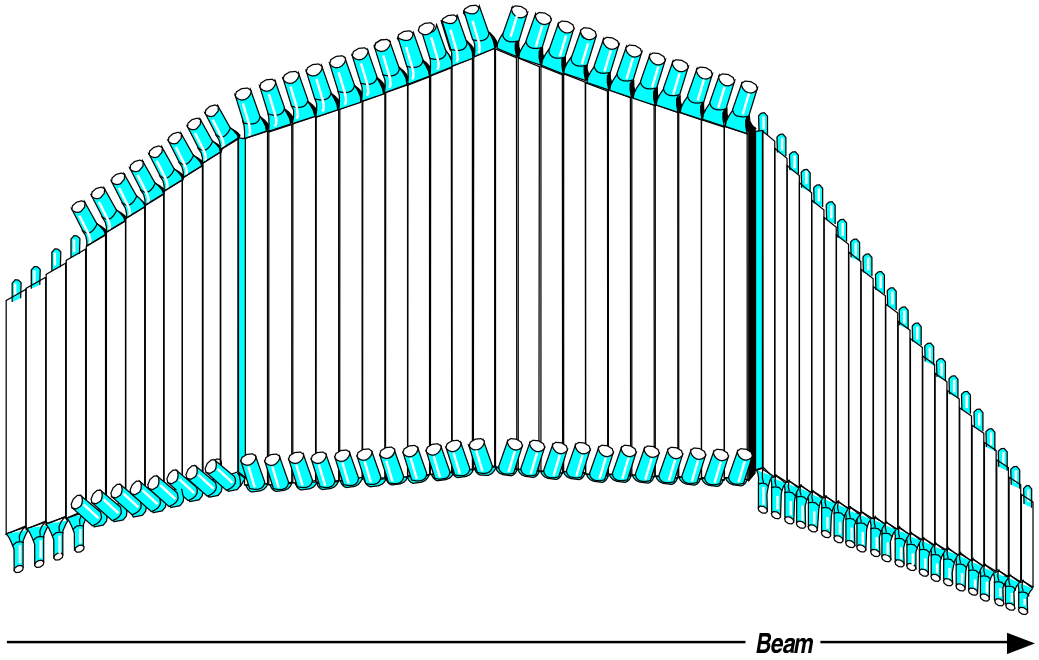

Figure 2.15: The layout of the 57 plastic scintillating counters of the Time-of-Flight Counters for a single sector. The counters are broken into 4 groups (or panels) [49].

minimum-ionizing particles. The first 23 scintillators covered out to 45°, and were mounted on "Panel 1" which is attached to the forward carriage. Due to spatial and rate constraints, these bars were 15 cm wide and coupled to 2 inch PMTs. The remaining scintillators were 22 cm wide and coupled to 3 inch PMTs through bent light guides. The bent light guides were needed in order to fit the photomultiplier tubes in the projected shadow of the torus cryostat. The tapering of the guide, in combination with a bend and twist, brought the photo-tube out of the plane of the scintillator while minimizing light losses and resolution penalties. All the scintillators were read out on both ends with independent PMTs. However, the last 18 bars were paired together and shared photomultiplier tubes, forming 9 logical channels with effective widths of 44 cm. Due to the fringe magnetic field from the torus in the region of the SC system, the PMTs were shielded with a high-μ metal.

The timing resolution of the counters was found to depend upon the length of the scintillators. The intrinsic resolution was measured *in situ* by injecting laser light into the center of each bar and measuring the resulting signal off the PMT, simulating the signal produced by a minimum-ionizing particle; the results are shown in Figure 2.16. The timing resolution for the 15 cm wide bars varied between 65 ps and 140 ps RMS as the length of the bars increased from 25 cm to 350 cm. The wider 22 cm bars, found at lab angles greater than 45°, had an overall average resolution of 100 ps. However, during data taking the timing resolution for electron tracks primarily hitting the shorter scintillators on panel 1 was observed to be approximately 165 ps when

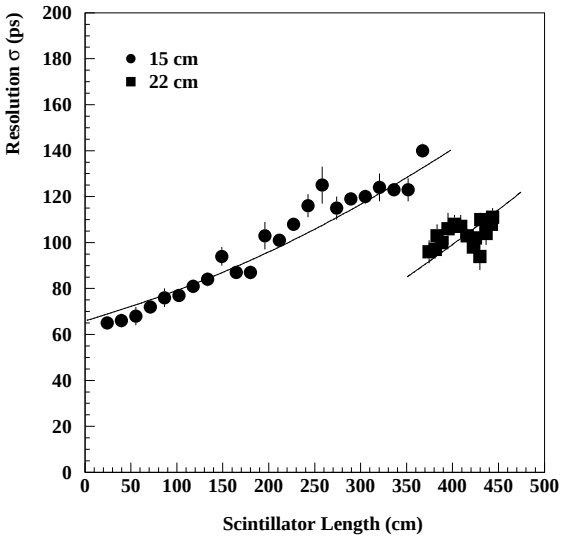

Figure 2.16: The timing resolution of the time-of-flight counters versus scintillator length as measured with the laser calibration system, emulating the signal due to a minimum ionizing particle [49].

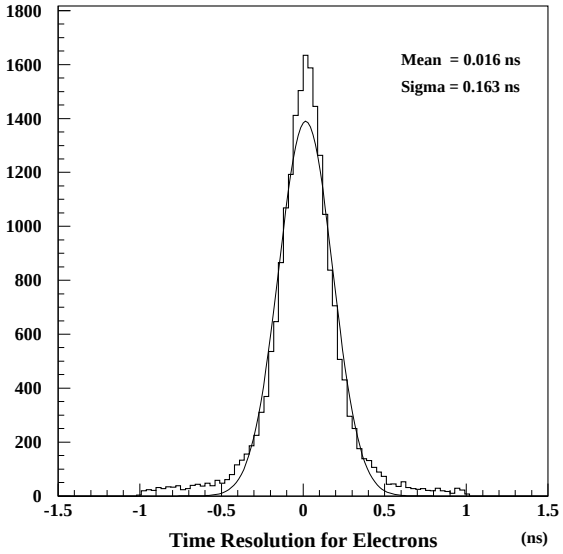

Figure 2.17: The timing resolution for single electron tracks was measured by comparing the calculated start time from the electron track, incorporating both path length estimates and the time from the SC, to the RF signal from the accelerator [49].

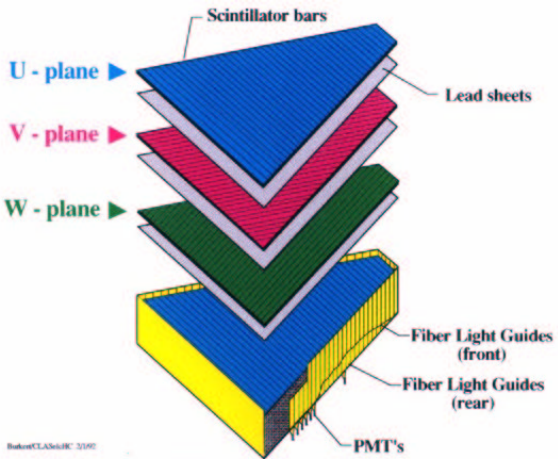

Figure 2.18: The electromagnetic calorimeter construction, showing the layers and three projections (u,v,w) used to provide information about the spatial energy deposition of a hit [50].

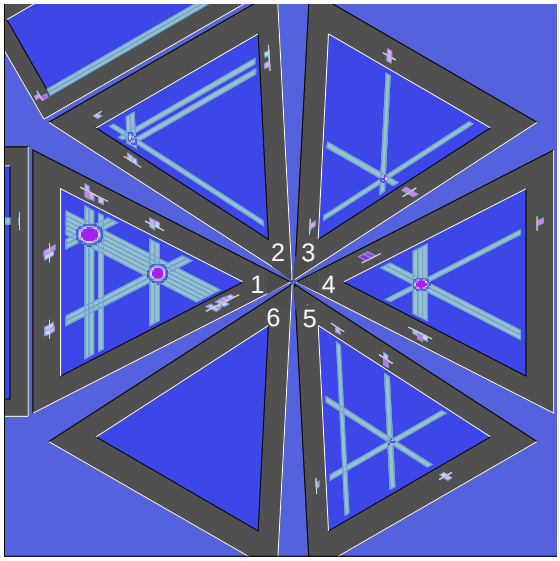

Figure 2.19: A reconstructed event showing hits in the EC. The u,v, and w views for each hit can be seen. The software was designed to identify up to two hits per sector, as shown in sector 1 [42].

measured against a signal from the accelerator marking the arrival of the electrons in the hall.

For use in the trigger, the PMT signals were processed with a customized electronic circuit to provide an angle-selective trigger [49]. The analog outputs from the anode of both PMTs attached to a bar were summed to provide a uniform response across the length of the counter. To account for a single track crossing multiple scintillators, the signals from adjacent bars were then combined into double and triple counter sets. Each of the 32 sets had an independent input to the trigger, permitting the trigger to be tuned to select events according to where on the SC wall hits were found.

2.3.5 Forward Electromagnetic Calorimeter (EC)

The forward electromagnetic calorimeter (EC) [50] served three primary purposes: to provide a fast signal in response to electron-like hits for use in the trigger, to aid in separating electrons from pions, and to detect neutrons and high energy ($P > 200\,\mathrm{MeV}$) photons. Additionally, it was designed to measure the opening angle for two-photon meson decays, as this was critical to be able to directly observe π^0 and η mesons. Located on the forward carriage approximately 5 m from the target, the electromagnetic calorimeter spans the laboratory frame polar angle θ from 8 to 45° with up to 80% coverage in the azimuthal angle.

Like the other CLAS detector systems, the EC was divided into six independent

calorimeters corresponding to the six sectors. Each calorimeter consisted of a lead-scintillator sandwich design of 39 layers, shown in Figure 2.18, with each layer made of a 10 mm thick scintillator followed by a 2.2 mm lead sheet. The lead sheets aided in the electromagnetic shower conversion, contributing over 90% of the calorimeter's 16 radiation length thickness. Each of the scintillator layers was divided into 36 strips parallel to one of the edges, rotating through 120° for each successive layer to form the u, v and w planes. A projective geometry was used such that the solid angle spanned by each layer as viewed from the target was kept constant; this minimized the leakage of the electromagnetic showers out of the edge of the calorimeter. The functional cell size or pixel was then 10 cm, determined by the region of overlap for the three views, optimized between the required position resolution and monetary expense of many photomultiplier tubes. The u,v and w views each contained 13 layers, which were further divided into inner and outer regions 5 and 8 layers deep, respectively. The phototubes, spring-mounted and with optical grease, were connected to the scintillators such that a single PMT collected light from all scintillators of a particular region, strip, and (u,v,w) view. This two region arrangement permitted a measurement of the longitudinal distribution of a shower, to better identify deeply penetrating hadrons from the relatively shallow electron-induced showers. Like in the other outer detectors, each PMT was wrapped in magnetic shielding to ward off fringe fields from the torus. Overall, each sector's EC had a total of 36 strips, three views, and two regions to form 216 channels.

Figure 2.19 shows how these divisions permitted the identification of a hit's position, as well as the measurement of its transverse and longitudinal energy spread. The energy resolution was known to depend primarily upon the number of secondary particle tracks sampled by the calorimeter, generated via electromagnetic showers and ionization processes. The resolution was measured to be $\sigma/e = 11.6\%/\sqrt{E(\,\mathrm{GeV})}$. For electrons with an energy greater than 0.5 GeV, the RMS position resolution on the face of the EC was 2.3 cm. Over the entire detector, the average timing resolution was approximately 200 ps for electrons [42]. To identify neutral particles, the timing information was used to distinguish neutrons from photons for hits that did not correspond to a drift chamber track.

To form the EC's signal for the trigger, the anode signals from the PMT were split, with one line running to the detector's digitization electronics, and the other providing a raw signal to the pre-trigger logic board. The detector's electronics digitized the energy deposition with analog-to-digital converters (ADCs), as well as the hits' timings by passing the signals to low-threshold discriminators and then to time-to-digital converters (TDCs). Since the signal attenuation of a strip depended strongly upon its length, removable resistors were used to equalize the response for each strip prior to processing by the pre-trigger logic [50]. For use in an electron-specific trigger, fast analog sums were created from combinations of the views and inner/outer regions on a sector-by-sector basis. The most useful output, and those finally to form the electron trigger, were the total energy sum across the EC module (EC_{total}) in

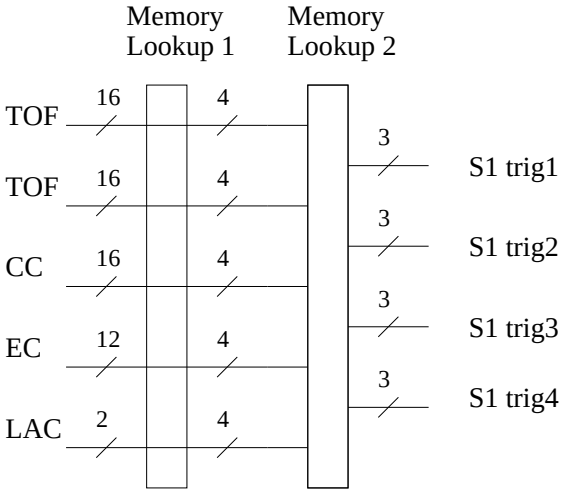

Figure 2.20: Schematic of the Level 1 triggers first stage, where a single sector's forward-carriage detectors' signals (here sector 1) are processed by the MLU to produce four trigger blocks [42].

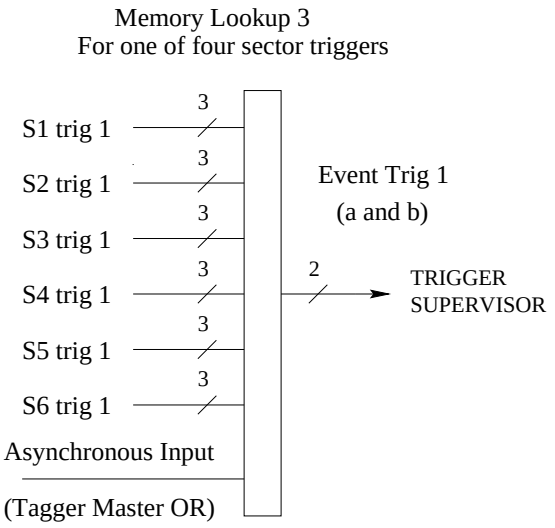

Figure 2.21: Schematic for combining one of the four trigger blocks (here, block 1) from each sector, along with an asynchronous input, to produce the event's Level 1 trigger [42].

coincidence with a sum of the energy deposited across the inner layers (EC_{inner}).

2.3.6 The Trigger and Data Acquisition System (DAQ)

The trigger system for CLAS is built around a two-level system, overseen by the custom Trigger Supervisor electronics. The Level 1 trigger provided a fast signal from selected fast PMT-based detector packages such as the Čerenkov and electromagnetic calorimeter. If an event satisfied the Level 1 trigger, the slower Level 2 system could be initiated to select events with charged particles based upon rudimentary track identification from drift chamber hits. In all cases, signals from both the Level 1 and Level 2 trigger systems were passed to the Trigger Supervisor.

For events which passed the trigger requirements, the data was collected from the FASTBUS and VME crates, properly correlated into events, and recorded, all using the CODA data acquisition system developed at Jefferson Lab.

For this analysis only the Level 1 trigger data were used.

2.3.6.1 The Level 1 Trigger

The Level 1 trigger utilized pipelined memory lookup units (MLUs) to implement a fast, deadtime-free trigger from prompt photomultiplier signals [42]. The configuration of the MLUs could be set to define a trigger from signals from the Čerenkov counter, the Time-of-Flight detector, and the electromagnetic calorimeters. In ad-

Table 2.2: Settings for the primary data-taking trigger during the e1c run period. The Level 1 settings required a coincidence between the detector packages in a single sector, of the form CC $*$ EC_{inner} $*$ EC_{total}. For the EC settings, a 10 mV signal corresponded to an energy deposition of approximately 30 MeV, and in the CC the 20 mV threshold corresponded to less than 0.3 photo-electrons [53].

Beam		Level 1 Configuration (mV)				
Energy (GeV)	Torus (A)	CC	EC_{inner}	EC_{outer}	EC_{total}	Level 2
2.567	1500, 2250	20	60	100	80	Off
4.056	2250, 3375	20	60	100	80	On
4.247	2250, 3375	20	60	100	80	Off
4.462	2250	20	60	60	80	On
4.462	3375	20	60	60	144	Off

dition, information from the tagger system could be used during real-photon data collection. For each sector up to 12 trigger results, broken into four blocks, could be generated in response to a coincidence of hits (*e.g.* CC and EC for an electron). The trigger blocks could then be correlated across the six sectors, in conjunction with an asynchronous input, to provide an event trigger according to a loosely selected event topology. In total, the processing including delays took close to of 90 ns. A total of eight trigger signals were then passed from the Level 1 trigger to the Trigger Supervisor.

2.3.6.2 The Trigger Supervisor

The Trigger Supervisor accepted a total of 12 inputs, eight from the Level 1 trigger and four from various calibration and monitoring sources. The eight Level 1 triggers could be prescaled, such that non-physics detector calibration and/or monitoring purposes data could be taken simultaneously during production running. After a Level 1 trigger was received, the Trigger Supervisor sent out a start-signal to the common start PMT TDCs; a gate to the PMT ADCs to delineate the signal integration; and, after a sufficient delay, a stop-signal to the drift chambers' common stop TDCs. When the Level 2 trigger was required, the Trigger Supervisor would wait approximately 3.2 μs for trigger confirmation. If the Level 2 trigger failed, a fast-clear was sent to the front-end electronics. Otherwise the read-out-controllers (ROCs) were instructed to collect information for the event and push it into the event queue for asynchronous readout.

2.3.6.3 Trigger Configuration for the e1c Run Period

During the e1c run period, the primary trigger was configured to collect electron-like events. The trigger configuration is listed in Table 2.2. The Level 1 trigger required hits in the EC and CC in the same sector, without any additional cuts placed upon

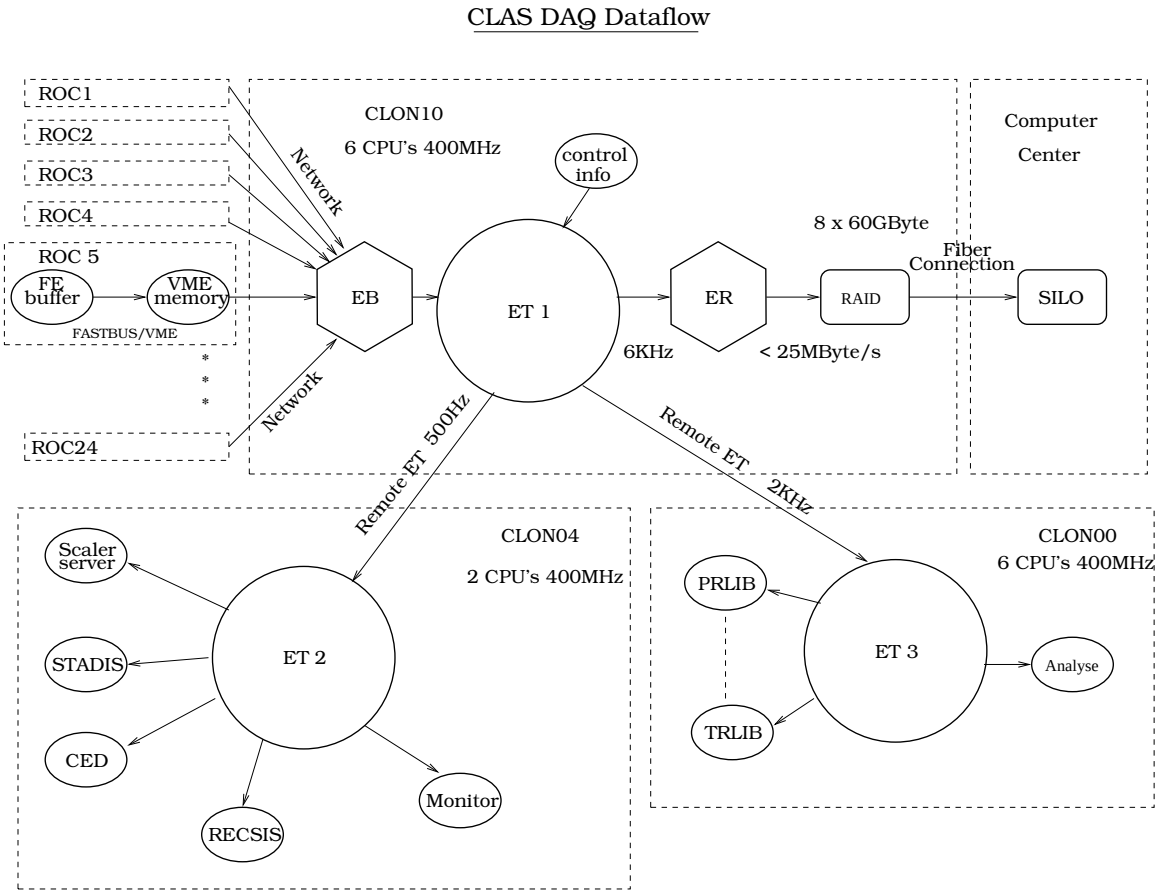

Figure 2.22: A schematic of the data flow for CLAS, from the detectors' read-out-controllers (ROC) to the SILO tape server in the computing center [42].

where in the CC the electron was detected. The EC hit had to satisfy a threshold on both the total energy deposited in the stack, as well as the signal strength from the inner layers. With this trigger configuration, approximately 45% of the events contained electrons.

2.3.6.4 Data Acquisition

A schematic of the data flow for CLAS can be seen in Figure 2.22. After the read-out-controllers received the signal from the Trigger Supervisor to digitize the event, the event fragments under the control of each crate were buffered and sent in bunches using standard TCP/IP protocols over fast ethernet to the CLAS online acquisition computer in the control room. The Event Builder (EB) then collected the fragments and collated them, forming complete events. Additional information, such as event numbers and control signals, was added to the event after which it was passed to the Event Transport (ET) process. The ET system served the events to a flexible set of client processes, such as detector-performance monitors, preliminary event recon-

struction analyzers, and recording processes. From the ET the Event Recorder (ER) collected each event and wrote it to a RAID hard-disk, from where it was eventually be copied to tape for permanent storage.

2.4 Summary

The continuous electron beam provided by the CEBAF accelerator coupled with the large acceptance of the CLAS detector provided an excellent facility for investigating the structure of nuclear matter through observing multi-particle final states. The precise control of the electron beam, the monitoring and stability of the target, and the direct measurement of the electron flux also permitted CLAS to accurately measure cross-sections.

Chapter 3

Analysis of Λ and Σ^0 Electroproduction

We have analyzed the CLAS datasets collected in February and March of 1999, taken with a 2.567 GeV nominal electron beam energy and main CLAS torus current settings of 1500 and 2250 amps. This data will be loosely referred to as the 2.5 GeV datasets. The reactions under study are

$$ep \rightarrow e' K^+ \Lambda(1115) \text{ and}$$

$$ep \rightarrow e' K^+ \Sigma^0(1192).$$

The measured cross-section for each hyperon, as defined in Equation 1.14, is:

$$\frac{\mathrm{d}\sigma_i}{\mathrm{d}W\,\mathrm{d}Q^2\,\mathrm{d}\Omega_K} = \frac{1}{\delta\Omega_K\,\delta Q^2\,\delta W}\,\frac{R_i\,N_i}{\eta_i}\,\frac{1}{N_0\,(\mathrm{A}\,\rho\,t/\mathrm{M_H})} \tag{3.1}$$

where for bin i in W, Q^2, and Ω_K:

N_i is the bin's hyperon yield,

R_i is the radiative correction factor,

η_i is the acceptance;

and for the normalization factor:

N_0 is the live-time corrected incident electron flux,

A is Avogadro's number,

ρ is the target density,

t is the target length, and

$\mathrm{M_H}$ is the molar mass of atomic hydrogen.

To be comparable with photo-production results, the virtual photon flux must be removed from the cross-section. In the one-photon exchange approximation,

$$\frac{\mathrm{d}\sigma_i}{\mathrm{d}W\,\mathrm{d}Q^2\,\mathrm{d}\Omega_K} = \Gamma(Q^2, W)\,\frac{\mathrm{d}\sigma_i}{\mathrm{d}\Omega_K}$$

with

$$\Gamma(Q^2, W) = \frac{\alpha}{4\pi}\,\frac{W}{Q^2\,E^2}\,\frac{W^2 - \mathrm{M}_p^2}{\mathrm{M}_p^2}\,\frac{1}{1-\epsilon}$$

and

$$\epsilon = \left(1 + 2\frac{|\overrightarrow{q}|^2}{Q^2}\tan^2(\frac{\theta_e}{2})\right)^{-1},$$

where E is the incident electron beam energy in the laboratory frame, $\overrightarrow{q}$ is the 3-momentum carried by the virtual photon, and θ_e the scattering angle for the electron. The calculation of ϵ can be carried out in either the lab or center-of-momentum frame since ϵ is invariant under a boost along the virtual photon direction. The virtual photon flux was then integrated across each (Q^2, W) bin and divided out, yielding an average cross-section for the i-th bin of:

$$\frac{\mathrm{d}\sigma_i}{\mathrm{d}\Omega_K} = \frac{1}{\Gamma(Q^2, W)}\frac{1}{\delta\Omega_K\delta Q^2\delta W}\frac{R_i N_i}{\eta_i}\,\frac{1}{N_0\,(\mathrm{A}\,\rho\,t/\mathrm{M}_{\mathrm{H}_2})}.$$

The goal was then to measure the hyperon yields in each kinematic bin, and calculate the correction factors (acceptance, radiative correction, electron flux, etc.) to extract the cross-section.

3.1 Data Reduction

3.1.1 Event Reconstruction

The initial analysis of the dataset was performed with the standard CLAS reconstruction software, using the PROD-1-9 version of the code and calibration constants [54]. As part of the processing effort, the detectors were calibrated (timing, pedestals, drift chamber drift time vs. distance, etc.) so that track reconstruction and a first pass at particle identification could be performed. The tracking software identified tracks from the drift chamber hits, returning a charge, position near the target, 3-momentum vector, and covariance matrix. More information about the track reconstruction can be found in references [55, 56]. Hits in other detector packages were spatially matched with the tracks, to aid in the identification (via time-of-flight measurements, energy loss, Čerenkov light emissions) of the charged particle. Neutral particles (photons and neutrons) were identified by the *lack* of an associated track for a hit in the outer detectors. The primary purpose of the cooking process was to identify the electron

(if any) in a given event and provide a crude identification of the other particles. The criteria used for electron and kaon identification are discussed in Sections 3.3.2.1 and 3.3.2.2.

After processing, the 2.5 GeV datasets contained 212M and 290M electron events for the torus settings of 2250 A and 1500 A, respectively. The raw data and the results of event reconstruction were written in BOS format to the Jefferson Lab tape SILO.

3.1.2 Kaon Filter

After the data was cooked, the events containing candidate K particles were selected. Any positively charged particle with a reconstructed mass, calculated from the momentum and time-of-flight, in the range 0.3 to 0.7 $\mathrm{GeV/c^2}$ was considered to be a possible kaon. In addition, the total energy of the event in the hadronic center-of-momentum frame, W, had to be above 1.5 GeV to discard events far below the strangeness-production threshold.

This event filtering reduced the 2.5 GeV data under study to 1.3M (1.5M) electron-kaon candidate events for the 2250 A(1500 A) torus-setting dataset.

3.1.3 Data Summary Format (DST)

Because even the filtered dataset was too large to handle easily, we went about generating a DST format. The decision to use the CERN open-source analysis package ROOT was made because of its object-oriented design in C++, and the available built-in Lempel-Ziv compression feature. Some of the raw hit information was dropped in this transition. The full results of tracking were kept, but the raw drift chamber hit information was removed. In addition, only SC, CC, and EC hits associated with tracks or consistent with neutral particles were kept. For comparison, the raw data was written in BOS format. In comparing the skimmed file sizes, a bank-filtered BOS-file was 26% the size of the initial file while the ROOT DST was less than 5% of the initial file size.

3.2 Kinematic Corrections

The hyperon mass, determined from the missing mass of the $p(e, e'K)$ system, depended upon the reconstructed track momentum and the initial beam energy. As reported in the first column of Tables 3.1 and 3.2, the uncorrected reconstructed missing mass recoiling off the $e'K$ did not peak at the proper hyperon mass, but instead had a centroid and width that were sector and angle dependent, showing that the determination of the event kinematics was imperfect. This could have been due to a combination of beam energy mis-calibration and momentum mis-measurements. The accuracy of the momentum measurement depended upon the magnetic field generated by the torus and the drift chamber wire geometry, both of which had uncer-

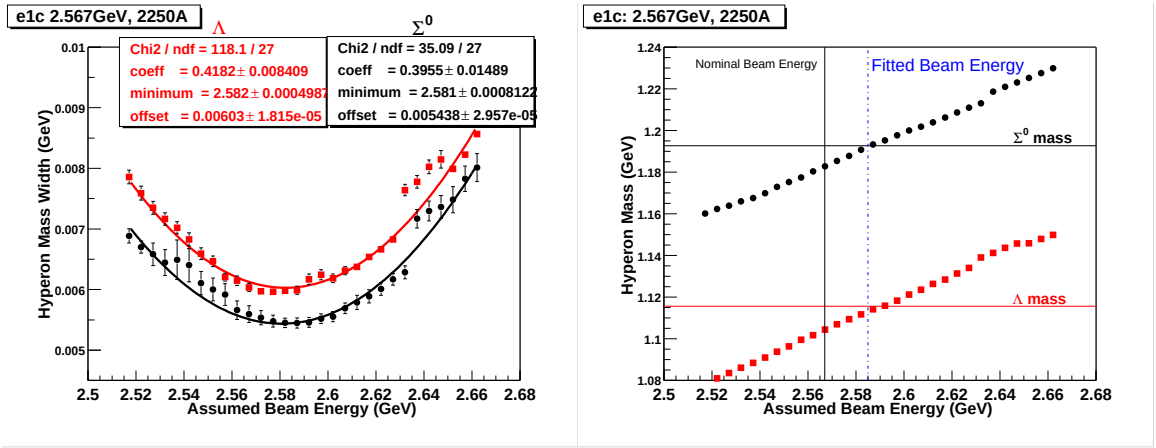

Figure 3.1: The observed Λ and Σ^0 mass peak widths from the data as a function of a trial beam energy. The best fit incoming beam energy, before energy loss corrections, is about 2.581 GeV. Also, the best-fit beam energy provides the most correct values for the observed Λ and Σ^0 masses.

tainties. Unfortunately, it was not possible to completely separate the effects of a mis-calibration of the beam energy from a mis-measurement of the electron momentum.

3.2.1 Correcting the Beam Energy

We initially assumed that to fix the $p(e, e'K^+)$ missing-mass distributions, all the missing energy could be ascribed to having used the incorrect beam energy. This meant only one parameter had to be adjusted. We then measured the electron beam energy by studying the dependence of the $p(e, e'K)$ missing-mass peak widths on the trial beam energy. This dependence can be seen in the left-hand panel of Figure 3.1. The observed hyperon mass widths were determined by fitting the missing mass distributions with a radiated Gaussian function. We supposed that the peak should be most narrow at the true incoming beam energy. The energy loss of the electron and kaon were accounted for by performing the same procedure with the GSIM Monte-Carlo output (described below), and quoted the difference between the "observed" and thrown beam energy as due to energy loss. This energy-loss correction factor came out to be about 4 MeV, resulting in a best fit beam energy of 2.584 GeV. The estimated beam energy was consistent, within 3 MeV, between the 1500 A and 2250 A datasets.

Also, by using the best-fit beam energy we found that the hyperon mass peaks were located at the proper masses, as seen in the right-hand panel of Figure 3.1. While the beam energy fit improved the overall position and width of the sector-summed missing mass peaks, it could not account for mis-measurements of the particle angles or momentum which varied on a sector-to-sector basis.

3.2.2 Momentum Corrections through the Track Curvature

We have used the University of Pittsburgh(U.P.) momentum correction [57] as it was determined for the e1c dataset produced by the PROD-1-9 cooking. The momentum correction is of the form:

$$p' = \frac{qB}{\frac{qB}{p}\left[1 + \beta(\theta, \phi, s)\right] + \alpha(\theta, \phi, s)} \tag{3.2}$$

and captures the mis-measurement of the *curvature* of the tracks. Equation 3.2 separates the constant offset of the curvature $\alpha(\theta, \phi, s)$ due to residual drift chamber misalignment from the term $\beta(\theta, \phi, s)$ parameterizing our ignorance of the magnetic field. The $\alpha(\theta\,\phi\,s)$ and $\beta(\theta\,\phi\,s)$ parameters were measured from e-p elastic scattering, but are generally applicable. The same parameters were determined to be consistent between multiple beam energy and torus setting datasets.

3.2.3 Comparing Kinematic Corrections

We evaluated the quality of the kinematic corrections by looking at the reconstructed mass of the Λ as a function of the kaon and electron angles. The mis-measurement of the particle momentum as a function of sector number and ϕ angle was important to correct for, not only to improve the resolution but also to make it easier to model the detector response. To monitor this, the missing mass of the $p(e, e'\,K)$ system was plotted versus the electron and kaon ϕ angles for the two kinematic correction techniques, which can be seen in Figure 3.2. We see that the University of Pittsburgh momentum correction, shown on the left, removes the majority of the ϕ-angle dependent structure.

Simply looking at the reconstructed missing mass of the Λ, summed over all kinematic bins, suggests that the U.P. momentum correction is the best available choice for a kinematic correction. To compare the effects of the different corrections, Tables 3.1 and 3.2 show the centroids and widths of the Λ peak as fitted from the uncorrected, U.P. corrected, and beam-energy adjusted missing mass distributions for the two 2.5 GeV datasets. The U.P. corrections improved the resolution of all the sectors and moved the missing mass toward the expected value, such that the final resolutions of all the sectors were roughly equivalent.

We chose to use the University of Pittsburgh momentum correction because of its ability to bring the Λ mass of all six sectors to the correct value with the same resolution, while greatly reducing its ϕ dependence.

3.3 Event Selection

The initial missing mass spectrum, created from the Kaon-filtered file, can be seen in Figure 3.3 with a strong signal from the hyperons. Further processing was necessary

Table 3.1: The Λ mass centroid and peak width, in units of (MeV/c^2), for each electron sector for the 2.567 GeV, 1500 A dataset, comparing different types of momentum corrections.

1500 A	No Correction		Beam-Energy Corr		U.Pitt P-Corr	
electron Sector	mass	σ	mass	σ	mass	σ
1	1106.8	8.33	1115.0	8.64	1115.4	7.40
2	1100.5	7.52	1109.2	7.80	1114.7	7.20
3	1108.1	7.78	1116.7	8.04	1114.7	7.48
4	1108.7	7.97	1117.1	8.14	1116.2	7.65
5	1110.0	8.67	1118.4	8.63	1116.7	7.85
6	1109.0	8.41	1117.4	8.46	1116.6	7.60

Table 3.2: The Λ mass centroid and peak width, in units of (MeV/c^2), for each electron sector for the 2.567 GeV, 2250 A dataset, comparing different types of momentum corrections.

2250 A	No Correction		Beam-Energy Corr.		U.Pitt P-Corr	
electron Sector	mass	σ	mass	σ	mass	σ
1	1107.0	6.16	1115.1	6.20	1115.8	5.46
2	1103.5	5.88	1111.9	6.11	1115.7	5.56
3	1108.7	5.82	1116.8	5.86	1115.3	5.35
4	1109.2	6.22	1117.4	6.36	1116.4	5.63
5	1110.4	6.56	1118.6	6.59	1117.0	5.81
6	1108.6	6.47	1116.9	6.38	1116.7	5.60

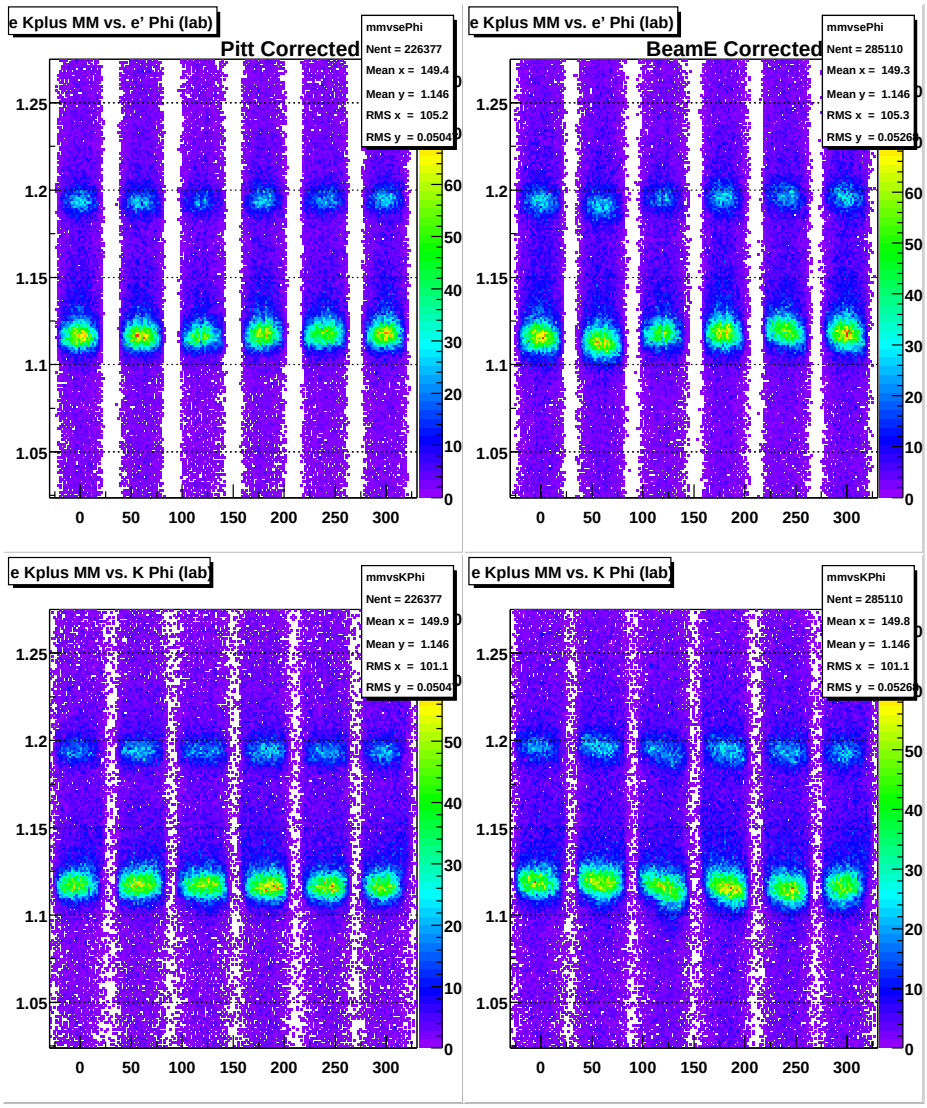

Figure 3.2: The reconstructed missing mass versus the lab azimuthal angle of the electron (top) and kaon (bottom), after kinematic corrections. The left set is after the sophisticated University of Pittsburgh momentum corrections while the right is for the simple Beam Energy adjustment.

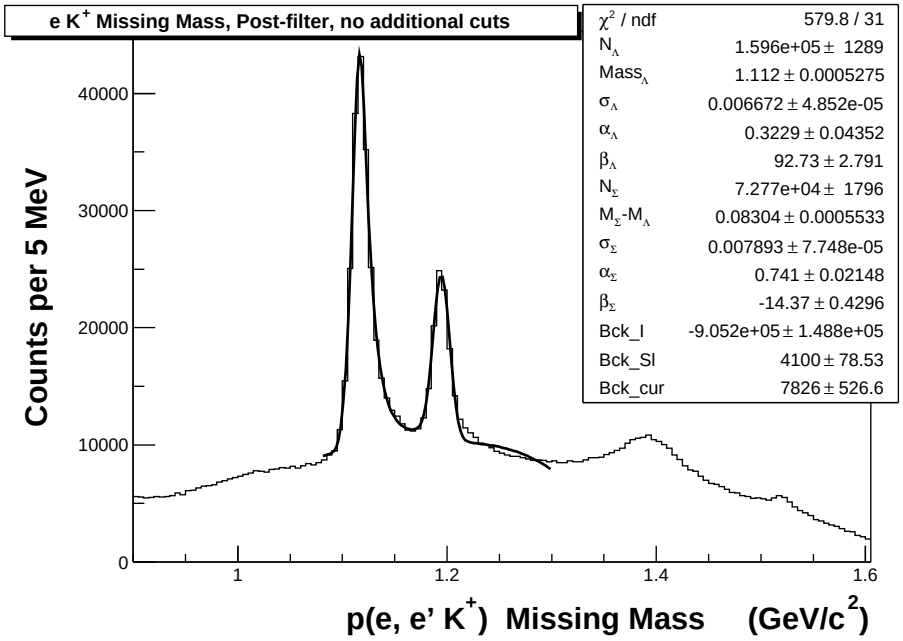

Figure 3.3: The $p(e, e'K)$ missing-mass distribution after the kaon filtering. The U.P. momentum corrections (3.2.2) were applied.

to reduce the background and ensure we could later calculate the acceptance for these events. The overall strategy was to choose the e-K events by identifying the electron (which fired the trigger), the kaon, and verifying that they came from the target region. Both the electron and kaon had to have been observed in regions of the detector that were well understood.

3.3.1 Identifying Poorly-Performing Scintillator Paddles

The K was primarily identified via a time-of-flight measurement, which in turn depended upon properly determining the event start time, T^0. To determine an event's T^0, we made the excellent assumption that the electron was extremely relativistic ($\beta_e \equiv 1$), and used its arrival time (t_e^{sc}) and reconstructed track length(d_e^{sc}) at the SC detectors, to estimate the start time:

$$T_e^0 = t_e^{sc} - \frac{d_e^{sc}}{\beta_e c}. \tag{3.3}$$

By using the RF-structure of the incoming electron beam, a better start time was then determined. The beam arrived in a 2 ps "bucket" every 2.004 ns (τ_{rf}), and T_e^0 was used to pick the closest beam bucket. If the time our reference beam bucket arrived in the hall was t^{rf}, then the i'th bucket after it arrived at $t_i^{rf} = t^{rf} + i * \tau^{rf}$,

and the best bucket was chosen as:

$$T^0_{rf} = t^{rf} + n * \tau^{rf} \text{ such that } \left|T^0_e - T^0_{rf}\right| < \frac{\tau^{rf}}{2}. \tag{3.4}$$

From here on we will define $T^0 \equiv T^0_{rf}$.

The difference between the uncorrected and corrected start times was:

$$\delta t_{rf} = T^0_e - T^0 \tag{3.5}$$

By looking at the distribution of δt_{rf}, collected for each SC paddle the electron hit, we measured empirically the timing resolution of each scintillator, and could identify paddles in the very forward direction that were not functioning properly. The timing-difference distributions can be seen in Figure 3.4. For a good calibration, the peak band was centered about zero and had a width of about 150 ps, which was the expected timing resolution of the SC paddles. While most of the channels were operating properly, there were some (*e.g.* Sector 5 paddle 2) which were not and were therefore rejected. Due to the restricted angular range of the electrons, this technique was only useful out to paddle 17.

The time of flight of the kaon was calculated from the arrival time of the kaon at the SC paddle(t^{scraw}_K) and the event start-time:

$$t^{sc}_K = t^{scraw}_K - T^0 \tag{3.6}$$

By using the measured momentum of the kaon, $p_K \equiv \left|\boldsymbol{K}^{lab}\right|$, and its pathlength, d^{sc}_K, the mass of the kaon was reconstructed as:

$$\beta_K = \frac{d^{sc}_K}{c \cdot t^{sc}_K} \tag{3.7}$$

$$\gamma = \frac{1}{\sqrt{1 - {\beta_K}^2}} \tag{3.8}$$

$$m^{sc}_K = \frac{p_K}{\beta_K \gamma} \tag{3.9}$$

When performing the kaon-filtering of the raw data, cuts were placed upon m^{sc}_K such that only events containing a particle with $0.3 < m^{sc} < 0.7\,\mathrm{GeV/c^2}$ were selected and kept for later analysis.

By looking at this reconstructed mass separately for each SC paddle, it was again possible to identify poorly-functioning paddles. In Figure 3.5 the reconstructed hadron masses using the time-of-flight and momentum measurements is shown. The paddles were required to provide well reconstructed pion, kaon, and proton mass peaks in order to be kept. Additionally, the back-most SC bars were instrumented in pairs, sharing a PMT, such that channels 40–48 each corresponded to two physical scintillating bars. Before the data was cooked, these joined paddles had not been calibrated completely, so they were also discarded in this analysis. The complete list of discarded SC paddles can be found in Table 3.3. Over time, the calibration and gain of the photomultiplier tubes would drift, causing a change in the quality of the response of for a given scintillator. As such, this list was constructed for each dataset.

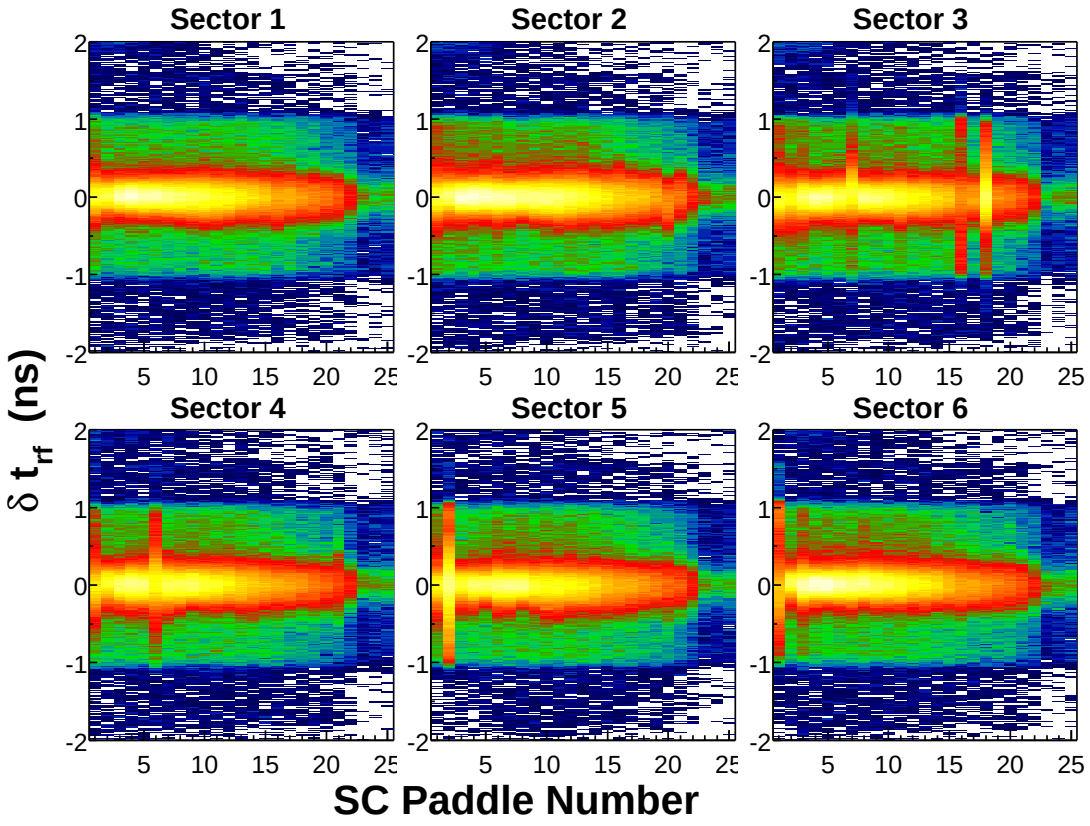

Figure 3.4: The timing correction δt_{rf} versus SC paddle for the 2.5 GeV, 1500 A dataset. The time δt_{rf} is due to a mismatch between the electron beam bucket arrival time and the measured event start time from the scattered electron. Several "bad" SC paddles can be seen. The z-axis runs from blue and green for low occupancy, to red and yellow for the highest occupancy bins.

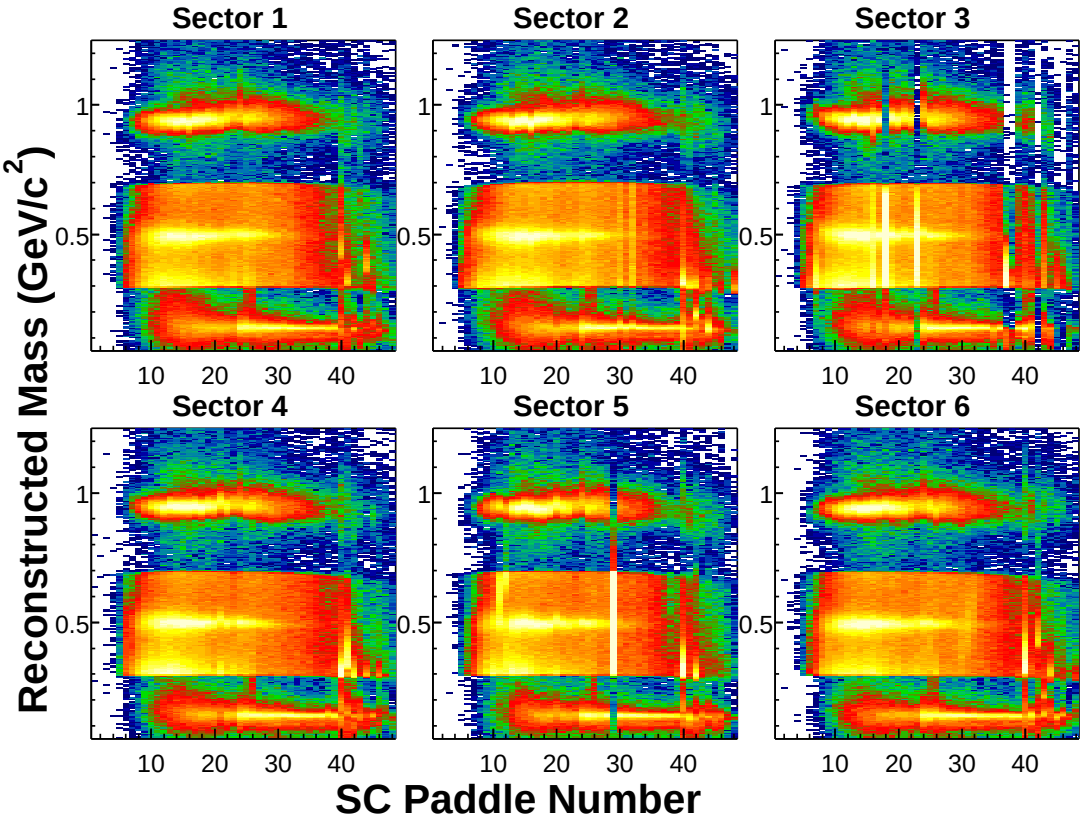

Figure 3.5: The calculated hadron mass m_K^{sc} versus SC paddle for the 2.5 GeV, 1500 A dataset. "Hot" channels (*e.g.* Sector 5, 28), inefficient paddles, and those with a severe calibration problem can be identified. The mass region from 0.3 to 0.7 GeV/c^2 is emphasized due to the Kaon filter. The z-axis range is the same for all sectors.

Table 3.3: The SC paddles removed from the analysis due to poor timing resolution or other problems.

Dataset	Sector	Paddles
2.5 GeV, 1500A	1	40-48
	2	30, 32, 40-48
	3	7, 16, 18, 23, 37, 38, 40-48
	4	6, 40-48
	5	2, 29, 40-48
	6	1, 40-48
2.5 GeV, 2250A	1	16, 40-48
	2	40-48
	3	7, 16, 18, 23, 37, 38, 40-48
	4	40-48
	5	2, 6, 29, 40-48
	6	1, 26, 40-48

3.3.2 Particle Identification

We were concerned not only with identifying any particle that left a track in the drift chamber, but also with reliably ascertaining the efficiency with which that particle would have been detected and identified. Because of this, two kinds of cuts were applied in the name of "identifying" the candidate electrons and kaons for this measurement. First, we cut upon a particle's track (time-of-flight, charge), energy deposition, and Čerenkov light to determine the particle's species. Second, fiducial constraints were applied to ensure that wherever a particle interacted the behavior of the CLAS detector was uniform and well understood.

For this experiment, only an electron and a positively-charged kaon were identified in each event. In cases where more than one electron or kaon candidate passed the cuts, each of the candidates was used in turn.

3.3.2.1 Electron Identification

The hardware trigger during the e1c run-period was an electron-specific trigger, and so the primary concern when identifying an electron in the analysis was that it would have reliably satisfied the trigger requirements. The events with well-identified electrons were selected by the following criteria:

1. Passed Standard Electron identification (PID) – from the CLAS-standard pid software package:
   (a) Negative track in DC
   (b) Matching hits in CC, TOF and EC

(c) $EC_{\text{inner}} > 45\,\text{MeV}$

(d) $-0.26 < (P^{lab} - EC_{\text{total}} * 3.23) < 0.56\,\text{GeV}$

2. The electron candidate was rejected if it hit a poorly performing SC paddle as determined in Section 3.3.1.

3. The electron was required to have $P^{lab} > 420\,\text{MeV/c}$ (trigger enforcement);

4. The estimated efficiency of the Čerenkov detector for the electron's track, as calculated in Ref. [58], had to be greater than 95%.

5. The location of the electron must have been within a fiducial region determined at the face of the electromagnetic calorimeter.

6. The electron's (θ^{lab}, P^{lab}) must have been within a fiducial region of CLAS.

Cut 1: Standard Electron Identification. The basic identification of an electron was performed by requiring a negative track from the drift chamber to have left a signal in the outer detectors consistent with an electron.

Cut 3: Electron Momentum. The electromagnetic calorimeter threshold was set at 80 mV. Using K. Egiyan's study [59] of inclusive inelastic *ep* scattering, it has been shown that a safe cut for the minimum electron energy can be determined from the EC threshold as:

$$EEC(MeV) = 214 + 2.47 * EC_{\text{threshold}}(\text{mV}). \tag{3.10}$$

This yielded a suggested minimum electron momentum of 411 MeV/c, so the higher 420 MeV/c cutoff should have been safe.

Cut 4: Čerenkov detector efficiency. To minimize the uncertainty in the value of the efficiency, the location of the electron's hit must have had an expected $\text{CC}_{\text{eff}} > 95\%$. This value was chosen because the efficiency of the Čerenkov detector dropped rapidly as the number of photoelectrons itself dropped below four; four photoelectrons corresponded to an efficiency of approximately 95%. The efficiency was calculated using the calibrated function provided by A. Vlassov [58].

This technique was chosen, as opposed to a simple cut on the number of observed photoelectrons, because we were concerned about modeling the Čerenkov counter response to a charged particle in the acceptance calculation. The difficulty with placing a cut on the number of photo-electrons is illustrated in Figure 3.6. While the simulated CC response out of GSIM generally had the same features as the data, the details of the distributions, especially for low photo-electrons counts, were quite different. The lower plot is background-free, yet still has a large single photo-electron peak. The two right-hand panels were generated from the identified electron after all the cuts, including the CC efficiency cut, were applied. The plots do not reveal a safe cut on the number of photoelectrons, since it is apparent that at no point are the "real" electrons explicitly separated from the background. So instead, a conservative

fiducial-cut based upon the CC efficiency function was used, which could applied to both the data and the simulated events.

Cut 5: Fiducial hit at EC face. The projected electron track's hit at the EC face had to be more than 10 cm from an edge of the EC, such that the shower would have been completely contained. We found that when looking at the CC efficiency for electrons, with the hits projected onto the EC face, there was an outer "reef" of efficiency as shown in Figure 3.7. This was found to be due to a known effect [48] where electrons and pions directly strike the Čerenkov detector's photomultiplier tubes and their housings. The EC fiducial cuts were tightened to exclude this "reef" region as well.

Cut 6: Fiducial in (θ^{lab}, P^{lab}) While investigating the reproducibility of the active region of CLAS between the data and simulated events, it was found that the coverage was not identical due to the momentum corrections applied to the data. To achieve matching kinematic coverage, fiducial cuts of the electron's (θ^{lab}, P^{lab}) were defined to re-enforce the bad SC paddle knockouts of Cut 2.

There was some possibility of π^-'s being misidentified as electrons, however the exclusive nature of the $e'KY$ final state already served to reduce the effect of this contamination.

3.3.2.2 Kaon Identification

These cuts were placed to minimize the contribution due to misidentified pions which constitute the majority of the background. The events containing a well-identified kaon were selected with the following criteria:

1. The kaon must have had a positive charge and a reconstructed TOF mass between 0.35 and 0.65 $\mathrm{GeV/c^2}$.

2. Only ONE K candidate, defined as satisfying cut 1 may have been present in an event.

3. The kaon candidate was rejected if it hit a poorly-performing SC paddle as determined in Section 3.3.1.

4. The kaon candidate was required to have $p_K > 300\,\mathrm{MeV/c}$.

5. The measured time-of-flight of the candidate K must have been consistent with that of a kaon of the same momentum.

6. The kaon candidate must have satisfied fiducial cuts, which were parameterized in terms of (θ_K^{lab}, p_K) and $(\theta_K^{lab}, \phi_K^{lab})$.

The first three cuts simply placed some loose requirements upon what a kaon event should contain. Cut 1 was a slightly tighter cut on the reconstructed kaon mass than that imposed by the kaon-filtering mentioned earlier. To ensure that the event

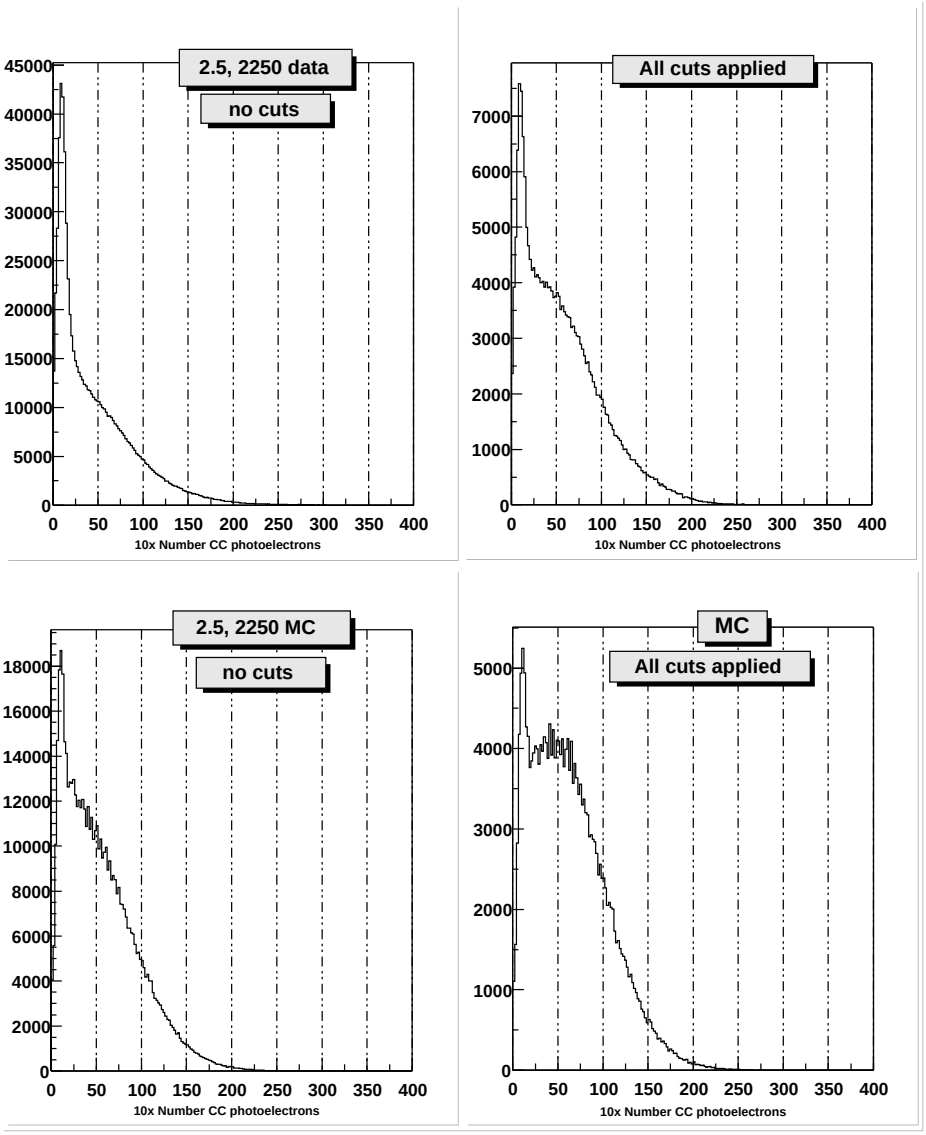

Figure 3.6: The number of photo-electrons reconstructed from the CC hits, as seen in the 2.5 GeV, 2250A dataset (top) and as output from the GSIM detector simulator (bottom), before (left) and after the event cuts (right).

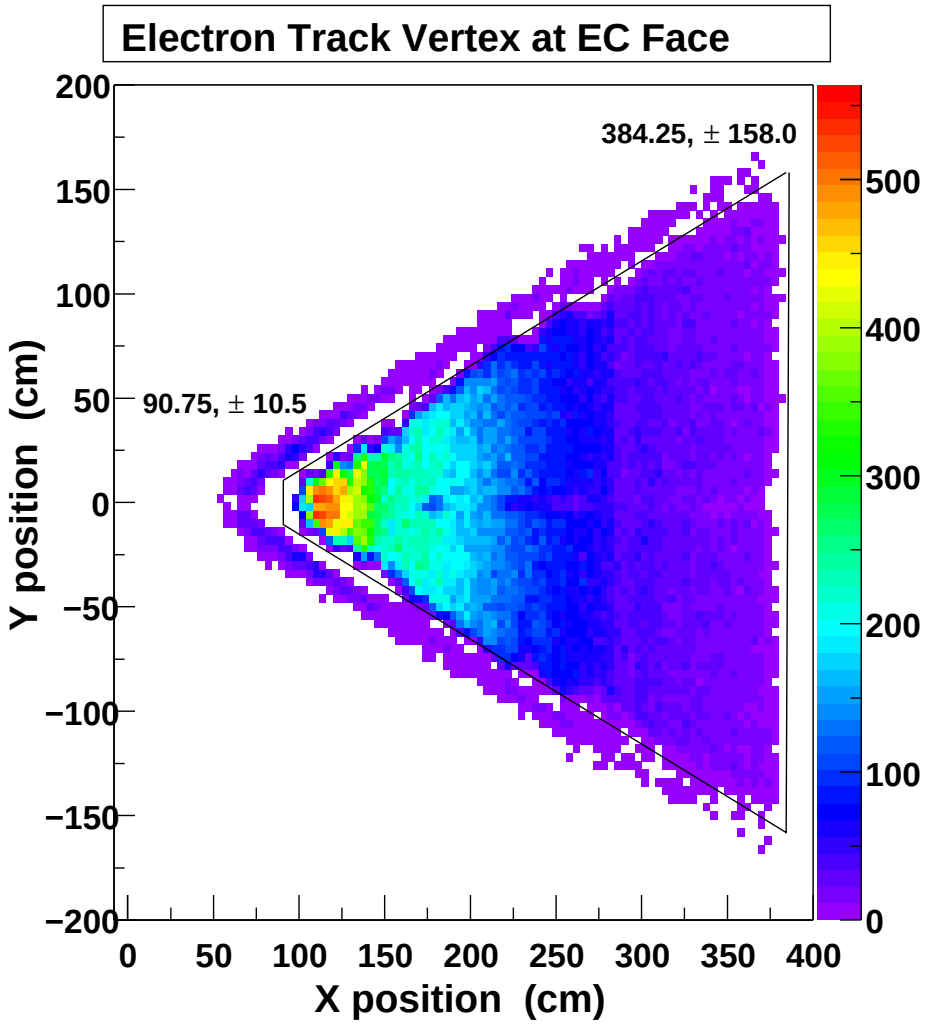

Figure 3.7: Showing the outer "reef" of high CC electron efficiency projected onto the EC face. To limit possible problems with the systematic uncertainty of the electron ID quality, we used the cut shown to select the large contiguous region.

had the correct topology, only one such kaon candidate could be present in an event. This is safe since the only way to get two positive particles in the final state for the reaction was to have the Λ decay to a $\pi^- p$ pair, and the proton's momentum was low enough not to be confused with a kaon. The third cut served both to remove the large number of misidentified particles coming from poorly performing SC paddles, as well as removing those paddles whose behavior it was not possible to properly model.

Figure 3.8 shows the resulting missing-mass distribution as a function of the observed kaon mass after performing these cuts. The Λ, Σ^0, and even higher mass hyperon states are clearly visible, properly centered on the x-axis about the expected kaon mass. The lower edge in missing mass reveals, however, a large source of the background that had to be removed. The feature around a missing-mass of $0.85\,\mathrm{GeV/c^2}$ is due to neutrons in the $\pi^+ n$ final state, where the pion was misidentified as a kaon. The remaining cuts worked to reduce this contamination.

Cut 4: Kaon Momentum. A cut on the kaon momentum was chosen because a kaon with a momentum of 300 MeV/c had a decay length ($\beta\gamma c\tau_0$) of only 225 cm, while the SC paddles were about 400 cm away. Over this distance less than 17% of these kaons survived long enough to be detected. This resulted in the π^+ contamination being very substantial in this very low momentum range. Figure 3.9 shows the reconstructed hyperon-mass versus kaon momentum. Very few hyperons were observed from these low momentum kaons, and this conservatively-placed lower limit simply defined the region of interest in momentum space. It removed the region where few events were collected, the correction for kaon decay was large, and the acceptance could have had a strong dependence upon the kaon track kinematics.

Cut 5: Kaon Timing Cut. The mass cut around the K imposed early in the analysis by the kaon-filter was less than ideal, since at low momentum it tended to admit a large pion background. To improve on this, we choose to look directly at the timing information from the SC detector and compare it to the flight time expected for a kaon. The expected flight time, from rearranging Equation 3.7, is

$$\beta_{K\ Ideal} = \frac{p_K}{\sqrt{\mathrm{M}_K^2 + p_K^2}} \tag{3.11}$$

$$t^{sc}_{K\ Ideal}\left(\boldsymbol{K}^{lab}\right) = \frac{d^{sc}_K}{c\,\beta_{K\ Ideal}}. \tag{3.12}$$

$$\tag{3.13}$$

Then, using the measured momentum and pathlength for a candidate kaon, we examined the difference of flight times:

$$\delta t_K = t^{sc}_K - t^{sc}_{K\ Ideal}. \tag{3.14}$$

Figure 3.10 shows the distribution of δt^{sc}_K from the 2.5 GeV, 1500 A dataset. The outer-edge is due to the cut on the reconstructed mass(cut 1). The central band is due to kaons, while on the lower edge, starting around a momentum of 1 GeV/c, there

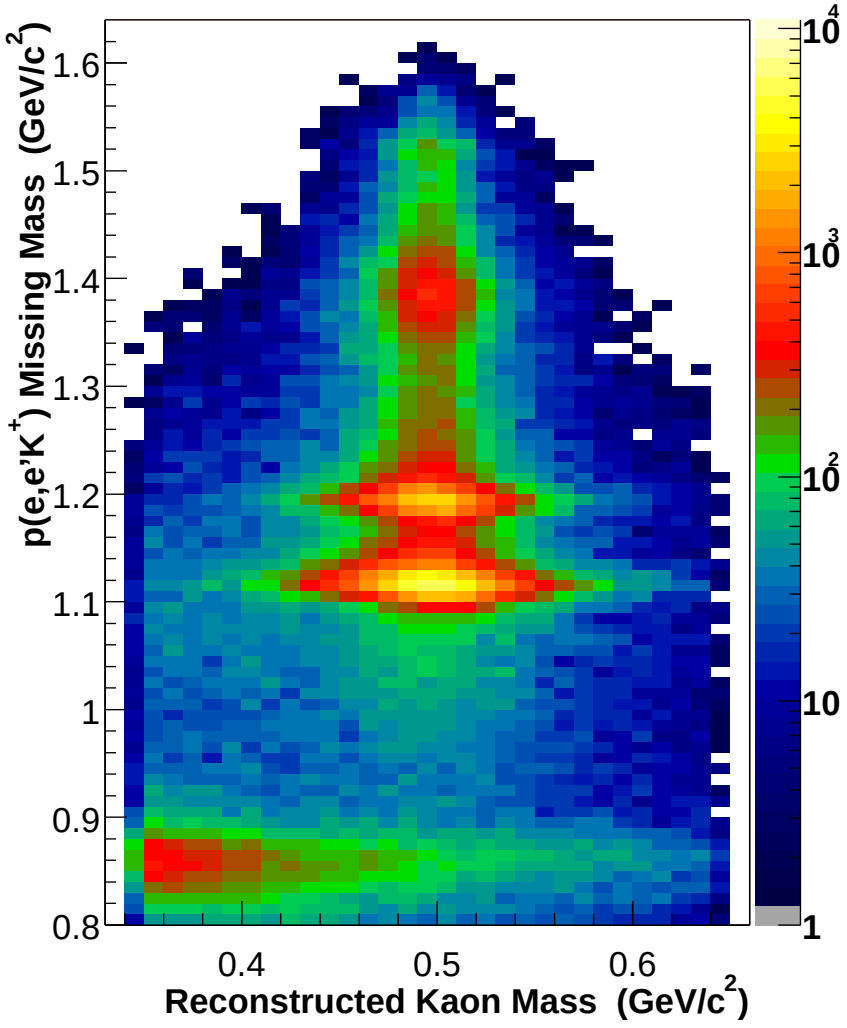

Figure 3.8: The $p(e, e'K^+)$ missing mass plotted versus the kaon candidate's reconstructed mass for the 2.5 GeV, 1500 A dataset. The Λ and Σ^0 peaks (at 1.12 and 1.19 $\mathrm{GeV/c^2}$, respectively) are quite prominent, and the peak around 0.85 $\mathrm{GeV/c^2}$ is due to misidentified π^+ particles and corresponds to the neutron mass.

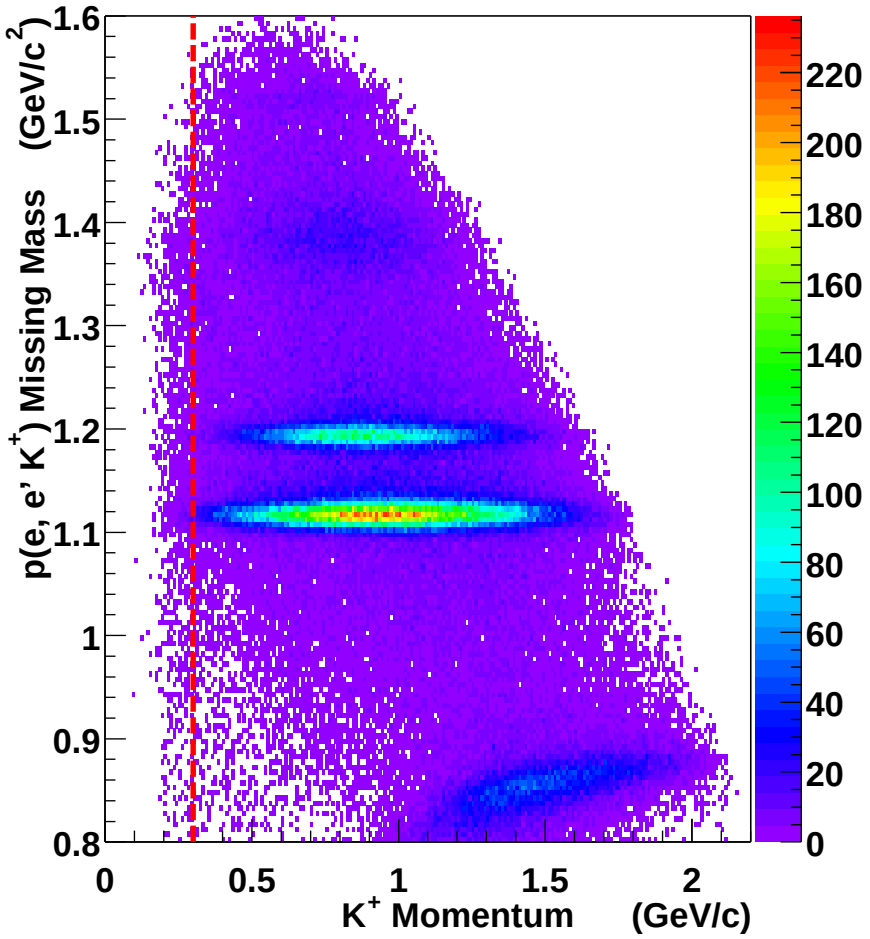

Figure 3.9: The $p(e, e'K^+)$ missing mass distribution versus the kaon momentum for the 2.5 GeV, 1500A dataset. All event-selection cuts except for the kaon momentum cut (shown in red) have been applied.

Table 3.4: The center and width of the δt_K^{sc} distributions for both the real and simulated datasets.

Dataset	Center (ns)	Sigma (ns)
2.5 GeV, 1500 A Data	0.07567	0.2327
2.5 GeV, 1500 A M.C.	0.0031	0.2288
2.5 GeV, 2250 A Data	0.06635	0.2223
2.5 GeV, 2250 A M.C.	0.0091	0.2160

is a faint enhancement due to pions and muons, some from kaon-decay, entering the mass cut.

To determine where to cut on the kaon TOF, the Λ yield was examined as a function of δt_K^{sc}. For each bin of δt_K^{sc}, a missing-mass distribution was collected for kaons with $0.3 < p_K < 1.0\,\mathrm{GeV/c}$. These missing-mass distributions were fit to a Gaussian (representing the Λ yield) plus a linear polynomial (background) in the Λ region. The cut on the kaon TOF was chosen by then fitting the resulting Λ yield as a function of δt_K^{sc} with another Gaussian of width σ_t for each data set. The timing cut was conservatively defined to be $\tau = 3 * \sigma_t$. Table 3.4 lists the centroids and σ_t's describing the δt_K^{sc} distributions for the datasets and simulations (discussed in section 3.3.9).

Cut 6: Kaon Fiducial Cut. When comparing the data to the reconstructed GSIM events, a non-uniformity in the ϕ_K^{lab} kaon distributions was noticed that was not present in the simulated events. The effect was most obvious for sectors 2 and 4, and is presented for the two datasets in Figures 3.11 and 3.12.

Fiducial cuts were created with inspiration from the π^0-analysis [60]. The functional form for edges of the $(\theta_K^{lab}, \phi_K^{lab})$ cuts was:

$$\Phi_{\pm}^{cut}(\theta_K^{lab}) = \phi_{\pm}^{max}\,\left(1. - \exp\left(-b_{\pm}\left(\theta_K^{lab} - c_{\pm}\right)\right)\right) + s * 60^{\circ} \tag{3.15}$$

where the parameters $\phi_{\pm}^{max}$, $b_{\pm}$ and $c_{\pm}$ were determined for each sector (s) and upper/lower limit $(+,-)$ cut independently. The parameters used can be found in Tables 3.5 and 3.6. A kaon was then kept only if $\Phi_{-}^{cut}(\theta_K^{lab}) < \phi_K^{lab} < \Phi_{+}^{cut}(\theta_K^{lab})$.

This non-uniformity is believed to be due to the mini-torus having been slightly rotated out of position and distorted, such that it impinged upon the nominally sensitive region of CLAS. The cuts were independently determined for the two magnetic field settings. Since the mini-torus was located inside the main torus, we expected this effect to be insensitive to the magnetic field setting. In comparing the fiducial regions carved out in Figures 3.11 and 3.12 the cuts were found to be quite similar, with the fiducial region for the 2250 A dataset slightly tighter.

Additionally, when investigating the kaons' (θ_K^{lab}, p_K) distribution, shown in Figures 3.13 and 3.14, we discovered a region in sector 5 corresponding to a problem with the Drift Chambers. Exclusionary cuts parameterized in (θ_K^{lab}, p_K) were placed to isolate the problem. In addition, cuts were defined to map out regions where

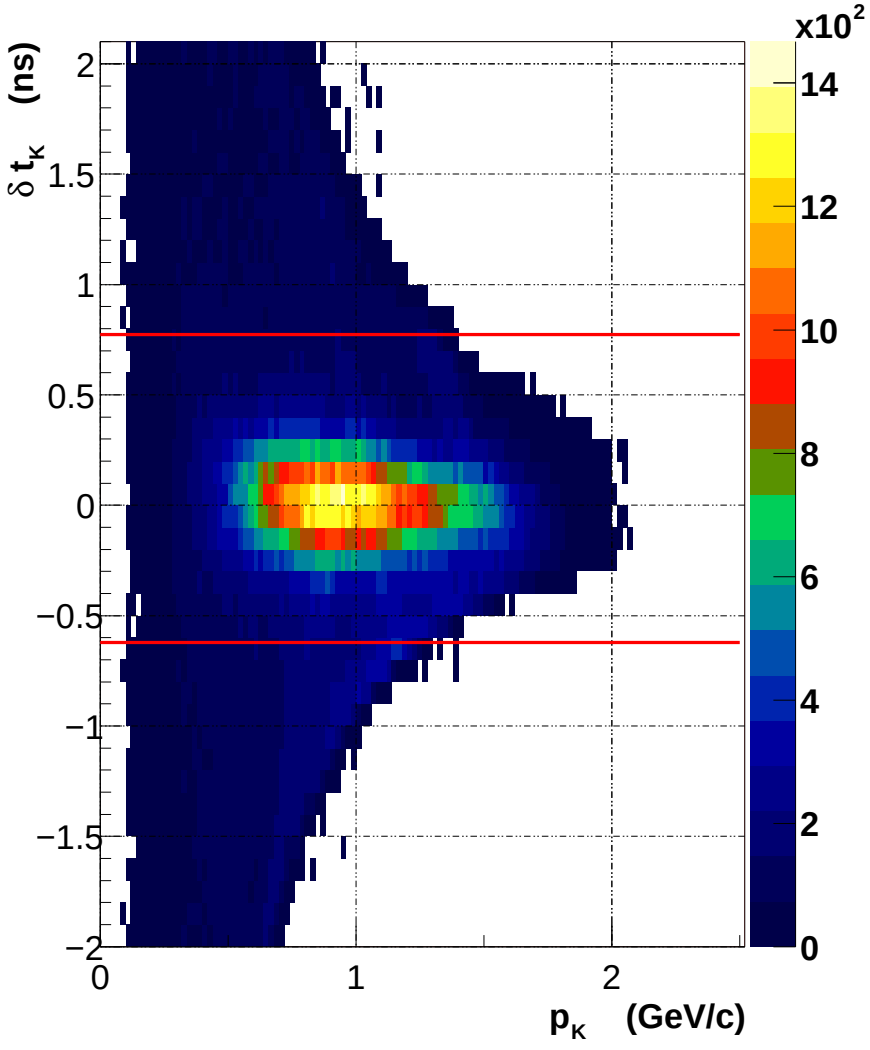

Figure 3.10: The time-of-flight (TOF) difference, δt_K^{sc}, of the observed K candidate and the "ideal" time-of-flight of a K versus the kaon momentum for the 2.5 GeV, 1500 A dataset. The outer contour is determined by the reconstructed mass cut. The final applied timing cut is super-imposed.

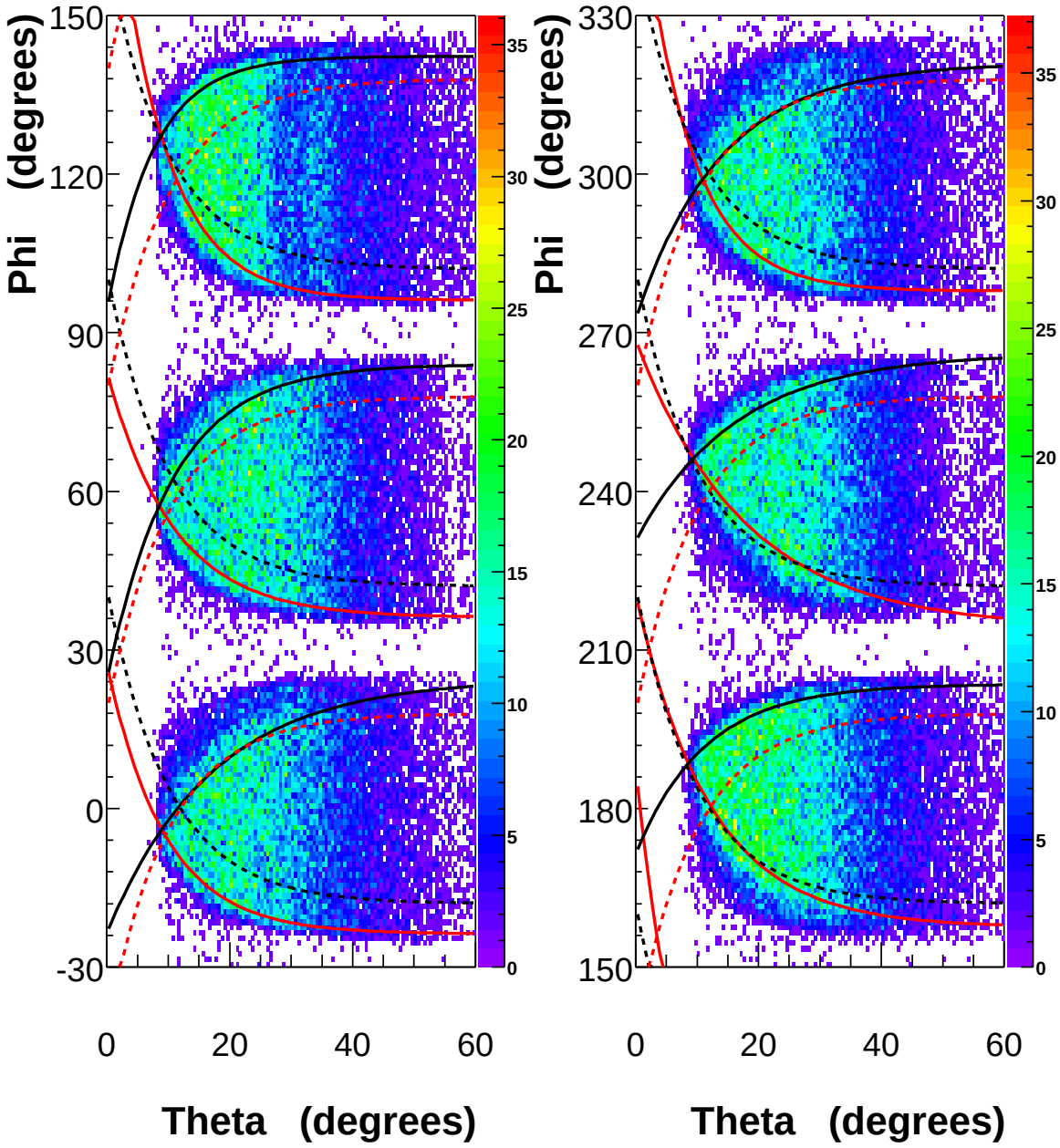

Figure 3.11: The distribution of reconstructed kaon tracks in the lab angles θ_K^{lab} and ϕ_K^{lab} for the 2.5 GeV, 1500 A dataset, showing the six CLAS sectors. The non-uniform regions of low population in the different sectors required the application of fiducial cuts. Two variations on the cuts were used: the nominal cut is shown as the pair of solid lines, and the tighter set of cuts shown with dashed lines.

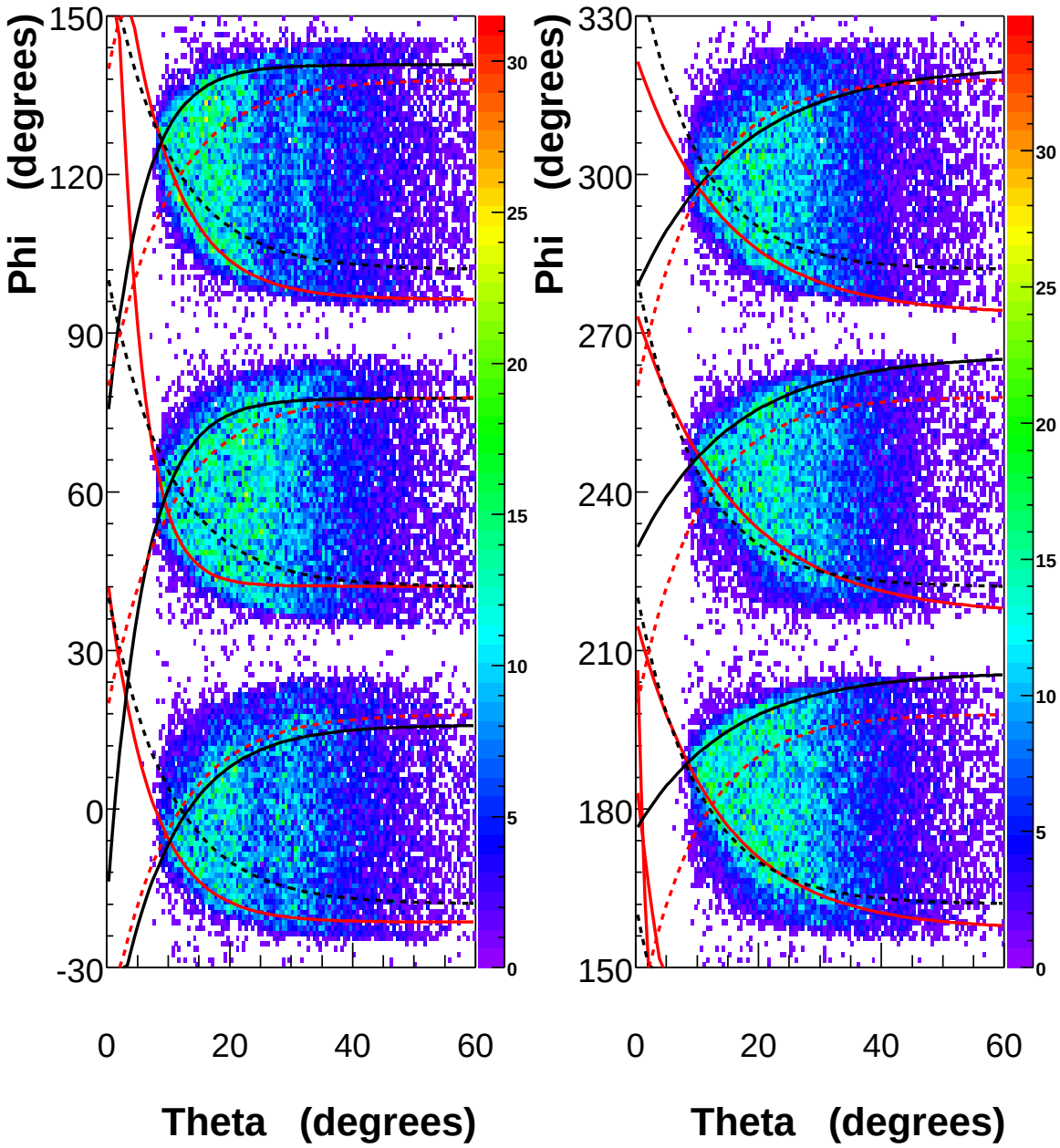

Figure 3.12: The distribution of reconstructed kaon tracks in the lab angles θ_K^{lab} and ϕ_K^{lab} for the 2.5 GeV, 2250 A dataset, showing the six CLAS sectors. Two variations on the cuts were used: the nominal cut is shown as the pair of solid lines, and the tighter set of cuts shown with dashed lines.

Table 3.5: Parameters for the $(\theta_K^{lab}, \phi_K^{lab})$ cuts placed upon the positive hadron tracks for the 2.5 GeV, 1500 A dataset.

2.5 GeV, 1500 A Dataset						
Sector (s)	$\phi_-^{max}(^\circ)$	b_-	c_-	$\phi_+^{max}(^\circ)$	b_+	c_+
S1	-23.7085	0.106172	7.2336	24.583	0.0586046	11.4816
S2	-23.8809	0.0927816	7.21163	24.0469	0.0945943	9.6577
S3	-23.8585	0.122084	10.9964	22.2755	0.132265	5.84134
S4	-22.4689	0.0825928	12.473	23.5381	0.0887164	3.50476
S5	-25.8617	0.0564243	13.2058	26.1265	0.0614132	4.99419
S6	-22.1236	0.125547	10.5562	21.0498	0.0721583	11.5473

Table 3.6: Parameters for the $(\theta_K^{lab}, \phi_K^{lab})$ cuts placed upon the positive hadron tracks for the 2.5 GeV, 2250 A dataset.

2.5 GeV, 2250 A Dataset						
Sector (s)	$\phi_-^{max}(^\circ)$	b_-	c_-	$\phi_+^{max}(^\circ)$	b_+	c_+
S1	-21.4035	0.142903	7.8874	15.8872	0.104407	13.3691
S2	-17.8369	0.255048	9.00191	17.6785	0.17232	9.83127
S3	-23.6124	0.124872	10.7146	20.7714	0.174515	6.85216
S4	-22.8002	0.0729253	12.9601	26.0066	0.0651042	2.20119
S5	-23.3826	0.0628857	14.3577	25.8611	0.0643216	5.58418
S6	-26.4757	0.069321	8.8315	20.5937	0.0604659	11.9187

poorly performing TOF paddles (from cut 3) were located, to assure that the coverage in the laboratory angles and momenta between the data and simulations would be consistent. The same functional form as used before was found to work well:

$$\Theta^{cut}_{s,i,\pm}(p_K) = \theta^{\infty}_{s,i,\pm}\left(1. - \exp\left(-b_{s,i,\pm}(p_K - c_{s,i,\pm})\right)\right) \tag{3.16}$$

with the parameters determined independently for each sector (s), cut (i), and edge ($+,-$). Tables 3.7 and 3.8 contain the parameters used for the analysis. A kaon in sector s with momentum p_K and angle θ^{lab}_K was then rejected if for any cut i, $\Theta^{cut}_{s,i,-}(p_K) < \theta^{lab}_K < \Theta^{cut}_{s,i,+}(p_K)$.

3.3.2.3 Geometric and Kinematic Cuts

1. The reconstructed electron-kaon multi-track vertex (MVRT) must have had a z-position close to the target ($-4 < \mathrm{MVRT}_Z < 3\,\mathrm{cm}$);

2. The event's $W > 1.58\,\mathrm{GeV}$ as determined from the electron, such that the kinematics were proper for hyperon production.

We constructed a "proper" multi-track vertex from covariance matrices for the electron and kaon tracks according to the technique of Reference [56]. The distribution of the z-vertexes, shown in Figure 3.15, was cut to be certain to remove background due to interactions outside of the target region. The cuts did not exclude the target walls, since the vertex resolution was not fine enough to safely remove them. The contribution from the target walls to the Λ and Σ^0 yield is discussed below.

The cut on W was redundant with the implicit requirements on the missing-mass distribution, but served to enforce the cut on the event's W performed by the kaon-filter.

3.3.3 Event Class Cuts

In addition to hits reported directly from the detector systems, control headers and scaler events were inserted into the data stream containing information about the trigger and event type. Two cuts were placed on the event class:

1. The primary data-collection Level 1 trigger had to have fired. This trigger was a coincidence between the a hit in the Čerenkov counter, and the distribution of energy deposited in the EC ($EC_{\mathrm{total}} > 80\,\mathrm{mV}, EC_{\mathrm{inner}} > 60\,\mathrm{mV}$) within a single sector. The trigger is enforced to exclude calibration triggers that were also occasionally in use.

2. To ensure that the incident electron flux was known, only events read in between two consecutive scaler events, in which the accumulated Faraday cup charge as well as livetime information were reported, were kept. Scaler events were inserted into the data stream every 10 seconds.

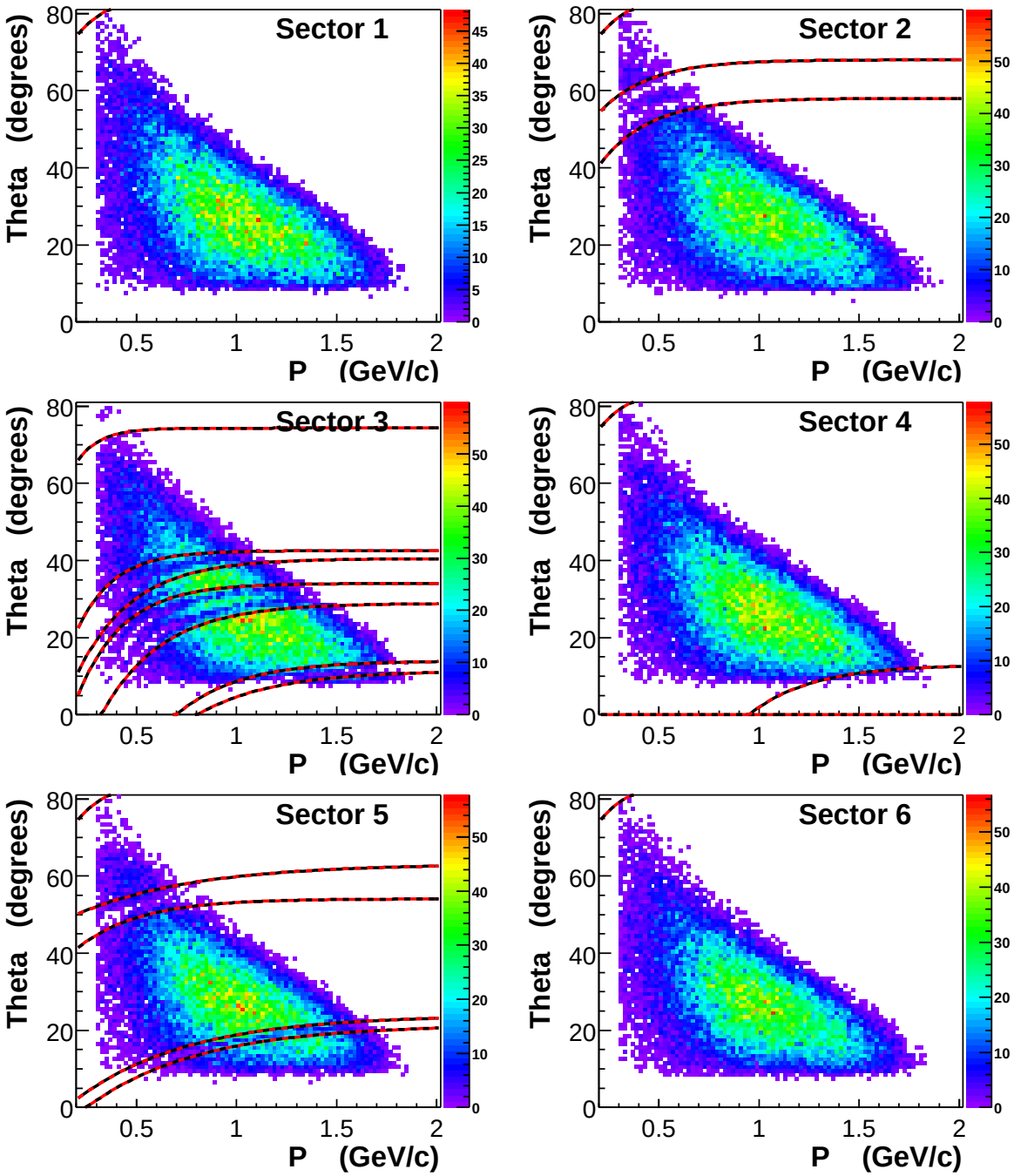

Figure 3.13: The (θ_K^{lab}, p_K) distributions for the kaon candidates from the 2.5 GeV, 1500 A dataset. Cuts (shown in red) were placed to remove the problematic region in sector 5, as well as enforce the bad TOF paddle knockouts.

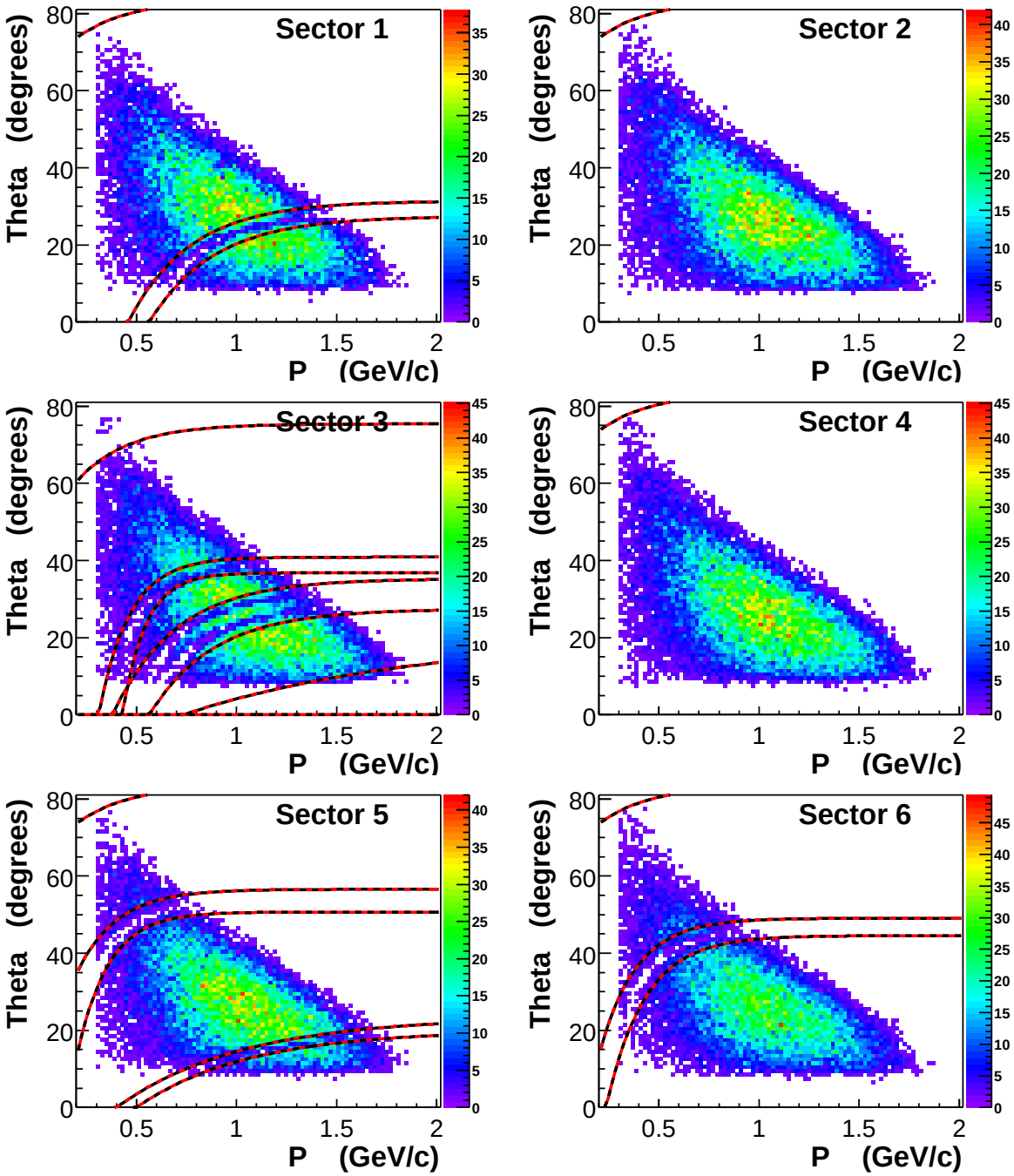

Figure 3.14: The (θ_K^{lab}, p_K) distributions for the kaon candidates from the 2.5 GeV, 2250 A dataset. Cuts (shown in red) were placed to remove the problematic region in sector 5, as well as enforce the bad TOF paddle knockouts.

Table 3.7: Parameters for the θ_K^{lab}, p_K cuts placed upon the positive hadron tracks for the 2.5 GeV, 1500 A dataset.

2.5 GeV, 1500 A						
Sector	θ_-^∞	b_-	c_-	θ_+^∞	b_+	c_+
S1	85.5067	5.79375	-0.146593	180	9999	0
S2	58	4	-0.1	68	4	-0.2
S2	85.5067	5.79375	-0.146593	180	9999	0
S3	11.439	2.64435	0.804644	14	3.2	0.7
S3	28.9005	3.29759	0.324846	34.0578	4.38422	0.171944
S3	40.5	3.6	0.12	42.5296	5.49472	0.0726636
S3	74.3345	8.62152	-0.0453762	180	9999	0
S4	0.	0.	0.	13	3.2	0.95
S4	85.5067	5.79375	-0.146593	180	9999	0
S5	21.5	1.8	0.25	24	1.8	0.15
S5	54.0989	3.27541	-0.234601	63.216	1.70943	-0.716209
S5	85.5067	5.79375	-0.146593	180	9999	0
S6	85.5067	5.79375	-0.146593	180	9999	0

Table 3.8: Parameters for the θ_K^{lab}, p_K cuts placed upon the positive hadron tracks for the 2.5 GeV, 2250 A dataset.

2.5 GeV, 2250 A						
Sector	θ_-^∞	b_-	c_-	θ_+^∞	b_+	c_+
S1	27.4057	3.08509	0.564559	31.3889	3.20291	0.458617
S1	83.7049	3.80072	-0.356417	180	9999	0
S2	83.7049	3.80072	-0.356417	180	9999	0
S3	0	9999	0	20.6104	0.835689	0.733672
S3	27.4057	3.08509	0.564559	35.2719	3.15874	0.381411
S3	75.4337	3.93132	-0.210069	180	9999	0
S3	36.7979	8.42352	0.428333	40.8746	6.47792	0.310806
S4	83.7049	3.80072	-0.356417	180	9999	0
S5	20.	1.8	0.5	23.5	1.6	0.4
S5	50.7003	6.39073	0.155157	56.5828	5.01889	0.0117713
S5	83.7049	3.80072	-0.356417	180	9999	0
S6	44.5508	5.17104	0.235411	49.0721	5.43567	0.140367
S6	83.7049	3.80072	-0.356417	180	9999	0

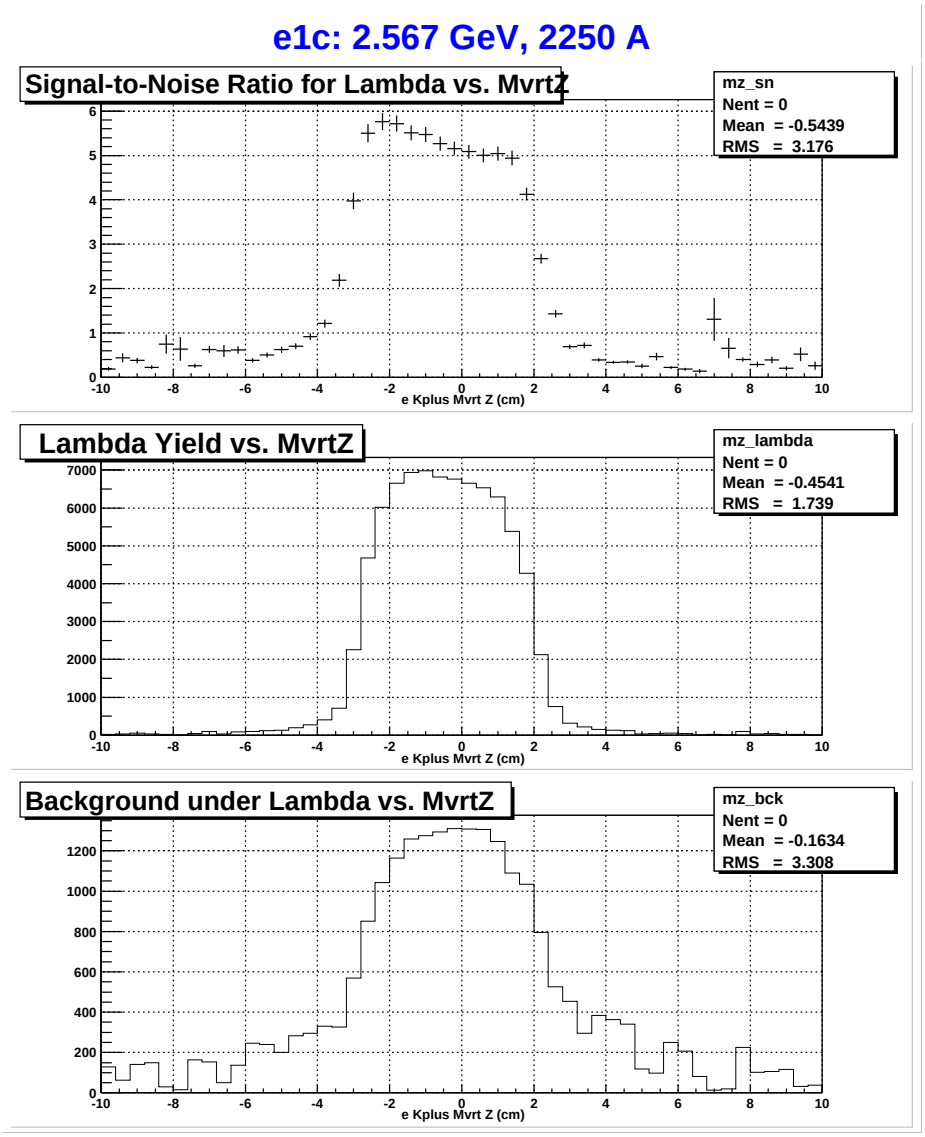

Figure 3.15: The Λ signal-to-noise ratio, yield, and background for different values of the Z-projection of the reconstructed $e\,K$ multi-track vertex. The Λ yield and background were determined by a fitting a missing-mass distribution for each slice of Z to a Gaussian (Λ) and linear polynomial (background). Cuts were placed at -4 and 3 cm. The structures above 6 cm are artifacts of the fitting procedure.

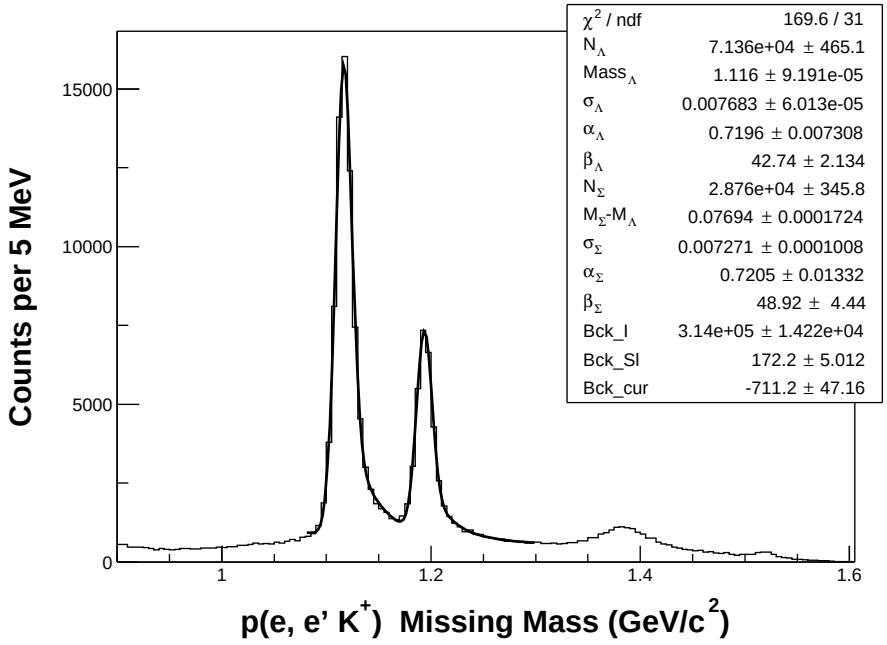

Figure 3.16: The $e\,K$ missing mass distribution for those events which passed the cuts, summed over all kinematics. The level of the background underneath the hyperon peaks has been substantially reduced, compared to Figure 3.3. The rest of the background is believed to be misidentified pions.

3.3.4 Summary of Event and Particle Identification Cuts

For the 2.5 GeV, 1500 A dataset, the effect of each of the cuts, applied in parallel over the complete kinematic range, are shown in Table 3.9; the effects of the cuts on the 2250 A dataset were nearly identical. Most of those desired hyperons which were cut were lost to the electron fiducial cuts 4 and 6, which were chosen for the purposes of defining regions of the CC and EC which could be well modeled by GSIM. Similarly, the next most significant cut was the fiducial cut on the kaon. The final overall missing-mass histogram for the 2.5 GeV, 1500 A dataset can be seen in Figure 3.16, and should be compared with Figure 3.3. The resolution of the hyperon mass peaks has improved, however the level of the background has been greatly reduced. The signal to background ratio of the Λ peak has improved from 5.3 : 1 to 19 : 1, with similar (though lesser) gains for the Σ^0. In addition, the background has become much flatter, with the separation between the hyperon peaks much closer to the known 77 MeV [61].

Table 3.9: The percentage of events, including hyperon estimates, removed from the analysis by the respective cuts summed over all kinematic bins. The cuts were each applied independently.

Cut	Events cut (%)	Λ's cut (%)	Σ^0's cut (%)	Background cut (%)
No Scalar Event	0.1	0.1	0.1	0.1
Wrong trigger	0.0	0.0	0.0	0.0
Failed electron	57.2	39.1	42.2	53.6
Failed K^+	67.0	25.4	24.8	80.7
El(1): No electron	0.0	0.0	0.0	0.0
El(2): Bad SCID	8.0	4.5	4.0	8.5
El(3): low P	16.5	4.1	7.3	10.0
El(4): low CC_{eff}	24.1	21.9	23.1	24.2
El(5): EC vertex cut	22.0	15.2	15.6	24.2
El(6): Non-fiducial	27.8	23.8	23.6	28.3
K^+(1): No kaon	0.0	0.0	0.0	0.0
K^+(2): >1 kaon	1.2	0.5	0.5	1.4
K^+(3): Bad SCID	19.2	2.1	2.5	21.7
K^+(4): low P	11.7	1.0	0.6	14.8
K^+(5): Timing cut	48.9	6.9	7.1	61.6
K^+(6): Non-fiducial	40.0	19.7	20.0	45.7
Event: W cut	6.0	0.0	0.0	0.0
Event: failed $MVRT_Z$	25.2	2.7	3.9	33.2
Failed cuts	86.7	56.9	59.4	94.6
Passed cuts	13.3	41.2	38.7	6.0

Table 3.10: A summary of the number of events used in the analysis.

Dataset	All events	Passed cuts	Final Λ cnt	Final Σ^0 cnt
2.5 GeV, 1500 A	1597874	213188	79688	31971
2.5 GeV, 2250 A	1105516	141392	53117	20184

Table 3.11: The full-target runs from the e1c run period used in this analysis.

2.5 GeV, 1500A: 16507 16508 16509 16510 16513 16514 16515 16516 16517 16518 16519 16527 16528 16529 16530 16531 16532 16543 16544 16545 16546 16547 16558 16559 16560 16561 16565 16566 16567 16569 16576 16577 16581 16582 16584 16585 16586 16587 16588 16589 16590 16595 16597 16598 16600 16601 16602 16604 16605 16606 16607 16608 16609 16610 16611 17135 17136 17137 17138 17146 17147 17148 17150

2.5 GeV 2250A: 16647 16648 16649 16651 16652 16653 16654 16655 16656 16657 16668 16669 16670 16673 16675 16676 16677 16679 16680 16682 16684 16685 16686 16687 16688 16689 16690 16691 16692 16693 16694 16695 16696 16697 16698 16699 16701 16703 16704 16705 16706 16707 16708 16709 16711 16712 16715 16716 16718 16719 16720 16726 16731 16732 17094 17097 17098 17099 17100 17102 17104 17105 17106 17110 17114 17115 17116 17121 17122 17123 17124 17125 17131 17133

3.3.5 Run Selection

To select the runs to be used in the analysis, we studied the number of particles passing the K cuts normalized by the luminosity on a run-by-run basis for each sector. The particle yields for the 2.5 GeV, 1500A and 2250A datasets are shown in Figures 3.17 and 3.18. Ideally, the yield is flat with run-number, and the 1500A dataset matches this rather well. In the 2250A dataset, the first three runs show a distinctly low particle yield in sectors 2 and 5, which was tracked down to problem with the Sector 2 Drift chambers. The list of runs used in the analysis is given in Table 3.11.

3.3.6 Radiative Effects

In general, many photons can be exchanged or radiated in electro-production reactions. A sample case is shown in Figure 3.19. In the figure, an additional virtual photon was exchanged between the incoming and scattered electrons, and a bremsstrahlung photon radiated from the outgoing electron. If the assumption was made that only a single photon was exchanged in this interaction, then the calculated kinematic variables (W, Q^2) to describe the $\gamma^* p \to KY$ process would be inaccurate. The additional photon(s) can mask the "true" kinematics at the reaction vertex of interest or modify the dynamics of the interaction.

One method to deal with this would be to incorporate radiative effects into the theoretical models. While probably the most correct method to handle the problem, it is not conventionally done. Instead, the task is left to the experimentalist to remove the radiative effects.

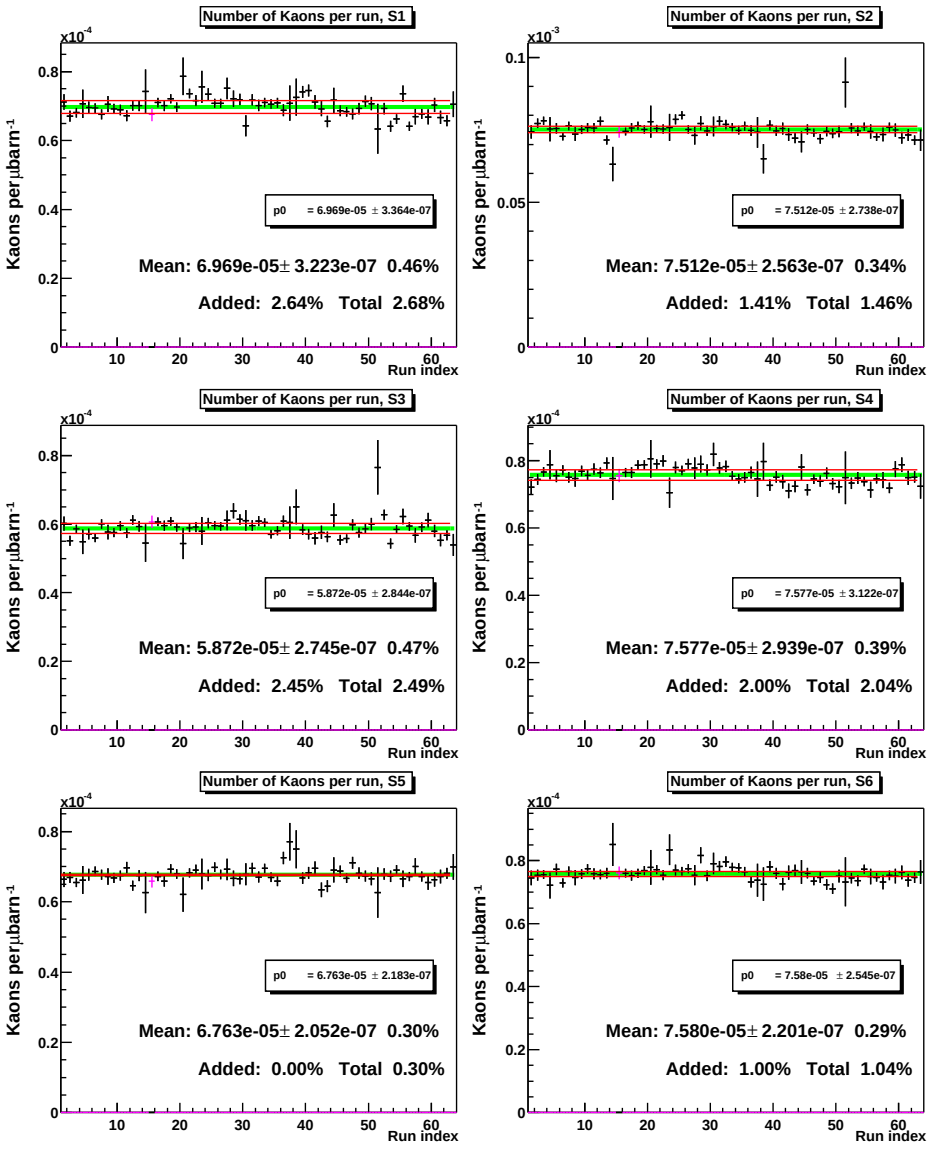

Figure 3.17: The estimated kaon yield per run determined from the 2.5 GeV, 1500 A dataset, normalized by the accumulated luminosity. The inset calculations indicate the relative stability of the extracted yield.

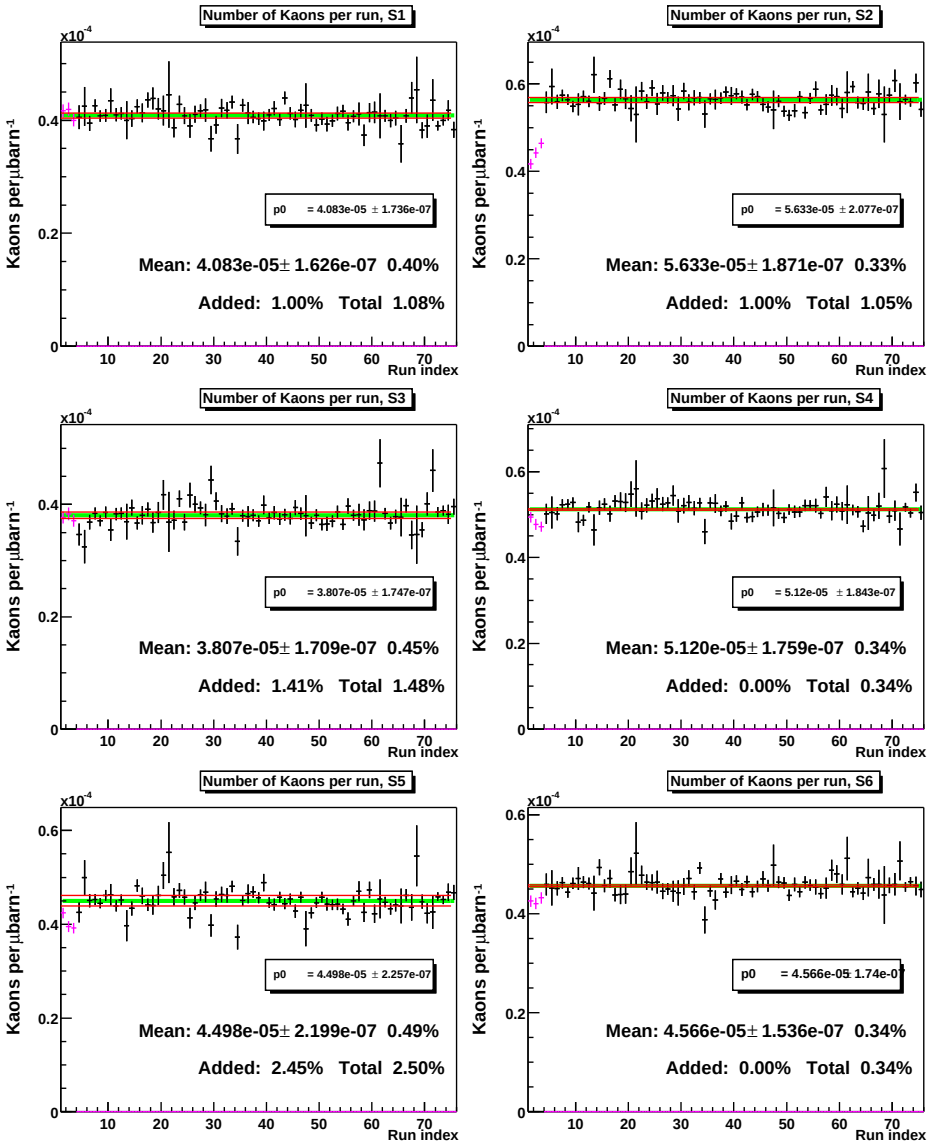

Figure 3.18: The normalized kaon yield per sector from the 2.5 GeV, 2250 A dataset (see Figure 3.17). The first 3 runs show evidence of a problem in Sector 2, and were excluded.

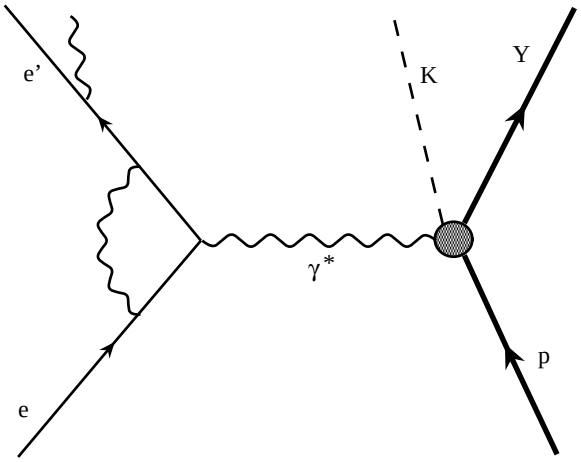

Figure 3.19: An example of multiple photons involved the in electroproduction reaction.

If the radiated and un-radiated cross-sections can be calculated using some reasonable model for a given bin, then the ratio of the cross-sections provide an approximate radiative correction factor for each bin (R_i).

$$\begin{aligned} R_i &= \frac{\sigma_i^{unrad}}{\sigma_i^{rad}} \\ \delta R_i &= \sqrt{\left(\frac{\delta\sigma_i^{unrad}}{\sigma_i^{rad}}\right)^2 + R_i^2 \left(\frac{\delta\sigma_i^{rad}}{\sigma_i^{rad}}\right)^2} \text{ (uncorrelated errors)} \end{aligned} \tag{3.17}$$

The correction factor does contain some model dependence, which can be minimized by ensuring the behavior of the input model for the cross-sections reasonably matches the general features of the data. The uncertainties on the σ^{unrad} and σ^{rad} terms are uncorrelated, since they are determined independently through a statistical technique described below.

3.3.6.1 Radiative Event Generator

An event generator in which radiative effects could be included was written by R. Thompson to study eta electroproduction [62], based upon the calculations of R. Ent [63]. The approach used the peaking-approximation, in which the photons were radiated along one of the particles' momentum direction, to greatly simplify the integration over the secondary photons' directions. The radiative effects then modified the cross-section for each event, based upon the probability of the additional photon exchanges taking place. The calculation was generalized as part of this PhD project to include other reactions, such as kaon electroproduction, and was added to the standard CLAS software as RadGen. RadGen can be easily modified to include

un-radiated models for many $\gamma^* + p \rightarrow Meson + Baryon$ reactions. The program also features the ability to switch the radiative effects on or off easily, mitigating the complications of maintaining two parallel programs. We used RadGen to generate radiated and un-radiated kaon electro-production events for each beam energy according to the WJC [6] model of the Λ and Σ^0 cross-sections.

3.3.6.2 Correction factors

To begin the radiative correction calculation we computed the cross-sections using a Monte-Carlo weighting technique. The kinematic point (W,Q^2,$\cos\theta_K$,ϕ_K) for a single event were generated randomly, and then the numerically evaluated cross-section at that kinematic point, σ_{evt}, determined the probability of the event being kept. Each event was kept with a probability of $P = \frac{\sigma_{evt}}{\sigma_{max}}$, where σ_{max} was a constant factor chosen to be larger than the maximum cross-section in the complete kinematic domain of interest. The events were then binned, with the number of attempted throws into a given bin (T_i) and the number of entries in that bin (N_i) kept. The average cross-section in bin i was then:

$$\sigma_i = \sigma_{max} \frac{N_i}{T_i} \tag{3.18}$$

This technique was used to calculate σ_i^{rad} and σ_i^{unrad} with and without radiative effects enabled, respectively, and finally R_i for each final state.

The uncertainties of σ_i^{rad} and σ_i^{unrad} were calculated differently. Since no bin migration could occur in the un-radiated case, N_i was related via the binomial distribution to T_i and the uncertainty was binomial. For σ_i^{rad}, the events could move between bins. However, since we knew exactly how many events, T_i, were thrown into a given bin, and only the number of observed events, N_i, fluctuated statistically, the errors were calculated by propagating only the uncertainty of the numerator. The uncertainties of the two cross-sections were calculated as:

$$\delta\sigma_i^{unrad} = \sigma_{max} \sqrt{\frac{1}{T_i}\frac{N_i}{T_i}\left(1 - \frac{N_i}{T_i}\right)} \text{ (binomial error)} \tag{3.19}$$

$$\begin{aligned} \delta\sigma_i^{rad} &= \sigma_{max} \frac{\delta N_i}{T_i} \\ &= \sigma_{max} \frac{\sqrt{N_i}}{T_i} \text{ (uncorrelated error in numerator)} \end{aligned} \tag{3.20}$$

A sample of the radiative corrections used can be found in Figure 3.20. The deviation of the radiative correction from unity as ϕ_K varies is quite evident. The radiative corrections for the 2.5 GeV datasets were calculated from "throwing" 290M (45M) radiated and 220M (47M) un-radiated Λ (Σ^0) events. The typical radiative correction

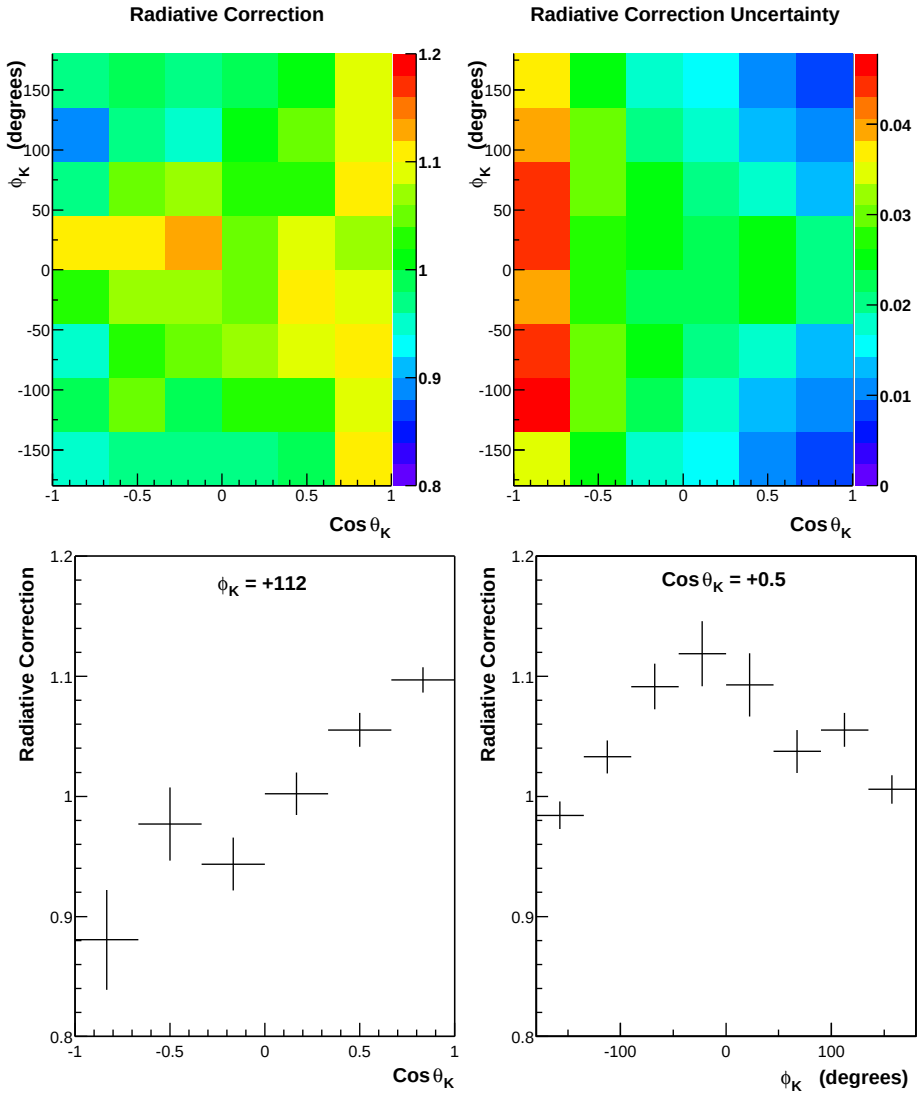

Figure 3.20: The radiative corrections for the Λ Q^2 =0.70 GeV/c^2, W =1.7875 GeV bin. Shown is the multiplicative correction factor (top-left), its statistical uncertainty (top-right), and the factor as a function of $\cos\theta_K$ at fixed ϕ_K and a as a function of ϕ_K for fixed $\cos\theta_K$.

factor was a modification of the cross-section by between +15% and −10 and at the lowest and highest W bins, respectively. On average, the statistical uncertainty on the radiative correction was 5% or less. The uncertainty of the correction was found to be rather insensitive to the details of the model used to calculate the cross-section.

3.3.7 Yield Extraction

To measure the Λ and Σ^0 cross-sections, a $p(e, e'K)$ missing-mass distribution was accumulated from the data for each (Q^2, W, $\cos\theta_K$, ϕ_K) bin. This permitted the background to be measured directly in each kinematic bin. The missing-mass distribution for each bin was fitted to a combination of Λ and Σ^0 hyperon-mass peaks and an analytic background. For this analysis, "templates" were used for the hyperon-mass peaks, and the background was parameterized as a second order polynomial.

The hyperon template shapes were produced from simulated events generated to include radiative effects. These events were passed through a model of the CLAS detector with representative detector responses, and passed through the standard reconstruction software; the details for this procedure are given in the discussion of the acceptance. In this way the template shapes contained contributions from the pure hyperon-mass peak, the radiative tail due to energy loss and multi-photon exchange, and modeled the peak width according to the finite resolution of the detector. Since the shape of the missing-mass peaks was primarily due to the electron arm and its radiative energy loss, the resulting generated Λ and Σ^0 mass distributions were binned in the kinematic variables Q^2 and W determined by the electron and implicitly summed over all kaon angles and momenta. This also best used the statistics of the simulations.

The measured missing mass distributions were fitted, in the range from 1.05 to 1.30 $\mathrm{GeV/c^2}$, to the sum of the shape of the Λ peak and radiative tail, the Σ^0 peak and radiative tail, and a smooth background polynomial.

For many bins, the template hyperon-peaks were seen to be slightly too narrow due to a residual mismatch of the momentum resolution in the simulation and the data. To correct for this, the template shapes were convoluted with a unitary Gaussian of width Δ. We studied the behavior of Δ as a function of the kinematics by including it as a parameter in the yield extraction, however little kinematic dependence was observed. As previously mentioned, this was because the majority of the shape came from the momentum measurement and radiative effects from the electron which were already taken into account. When Δ was permitted to vary with the kaon's kinematics, little effect was observed and it only served to increase the reported uncertainty on the other fit parameters. The distribution of Δ summed over all kinematics is shown in Figure 3.21. Table 3.12 lists the values of Δ chosen for each dataset. The sensitivity of the yields upon Δ was studied, and is discussed later(4.4.2).

The functional form for the hyperon templates used in the fits, including the convoluted Gaussian, was then:

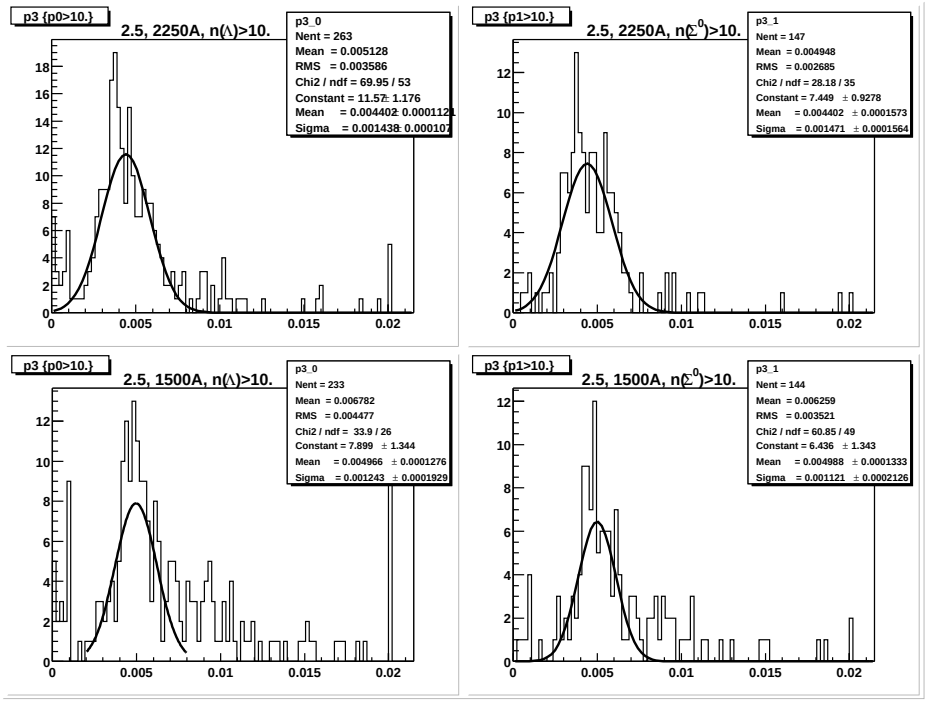

Figure 3.21: The distribution across many fits of the additional-width parameter Δ when it was permitted to float during the yield extraction.

Table 3.12: The values for the additional parameter Δ used to modify the Monte-Carlo hyperon template shapes to aid in fitting to the measured missing mass distributions. Δ was the width of a unitary Gaussian convoluted with the template shapes.

Dataset	Δ (MeV)
2.567 GeV, 1500 A	5.0
2.567 GeV, 2250 A	4.4

$$H^{'}(x_j) = \sum_{i=1}^{nbins} H(x_i) \frac{\delta mm}{\Delta\sqrt{2\pi}} \exp\left(-\frac{1}{2}\left(\frac{x_j - x_i}{\Delta}\right)^2\right) \tag{3.21}$$

where H and $H^{'}$ were respectively the template histograms before and after convolution, x_i was the center and δmm the width of the i'th bin, and Δ was the width of the Gaussian.

The background was parameterized and fit to a quadratic form such that the shape parameters could be fitted separately from the total background integral. The background was limited to be non-negative and to extend only over the kinematically accessible $p(e, e'K^+)$ missing-mass range for each given W bin. These considerations led to the background being parameterized as Legendre polynomials of x', where x' runs from -1 to $+1$ across the fitted region. The final form of the background was:

$$\mathrm{Bck}(x) = \max\left(0, \frac{p_0\,\delta mm}{X_{\max} - X_{\min}} * [\mathcal{P}_0 + p_1\,\mathcal{P}_1(x') + p_2\,\mathcal{P}_2(x')]\right) \tag{3.22}$$

with

$$X_{\min} = 1.05\,\mathrm{GeV/c^2}; \tag{3.23}$$

$$X_{\max} = \min\left(W_{\max} - \mathrm{M}_K, 1.3\,\mathrm{GeV/c^2}\right); \tag{3.24}$$

$$x' = \frac{2}{X_{\max} - X_{\min}}\left(x - \frac{X_{\max} + X_{\min}}{2}\right); \tag{3.25}$$

and $\mathcal{P}_0$, $\mathcal{P}_1$, $\mathcal{P}_2$ as the first three Legendre polynomials. The binsize δmm was set to $5\,\mathrm{MeV/c^2}$. The parameters fitted were p_0, which corresponded to the number of background counts in the distribution, and p_1 and p_2, which parameterized the shape of the background up to quadratic in x.

Since the background was observed to be rather flat, the results were tested against disabling the $\mathcal{P}_2$ term of the background. Also, variations upon fixing the shape parameters p_1 and p_2 as functions of $\cos\theta_K$ and ϕ_K within a (W,Q^2) bin were tested, in an attempt to reduce the number of free parameters in the final yield fits. The final approach was to permit p_1 and p_2 to vary with W, Q^2, and $\cos\theta_K$. The sensitivity of the results upon the background shape is discussed later (4.4.2).

To make best use of the available data, we decided to use a Poisson-statistics fit to the background and hyperon yields, as opposed to a χ^2-fit. This was because the χ^2-minimization technique performs well only if the uncertainty of the histogrammed quantity (the number of counts per bin) is approximately Gaussian, which for practical purposes tends to mean $N_i > 10$ [64]. Bins with contents of zero are ignored by a χ^2-fit, although they do provide information as well. In addition, the χ^2 minimization tends to under-count the area under the fitted curve by a value of χ^2 [65]. In the Poisson-statistics fit, one minimizes [64, 65]:

$$\Xi^2(\boldsymbol{\alpha}) = 2\sum_{i=1}^{n}\left(f_i - N_i - N_i \log\frac{f_i}{N_i}\right) \tag{3.26}$$

to determine the parameters $\boldsymbol{\alpha}$ to match the function $f(\boldsymbol{\alpha})$ to the spectrum of n bins with contents N_i. In contrast to the χ^2 minimization, this form permits all bins to participate in the fit, and assumes a (more proper) Poisson-distribution for the counts in each bin. With a good fit $f_i/N_i \approx 1$ and in the limit of large N_i such that $\delta N_i \approx \sqrt{N_i}$, the natural logarithm term can be expanded as $\log(f_i/N_i) \approx (f_i/N_i - 1) - 1/2\,(f_i/N_i - 1)^2$ and so [65]:

$$\Xi^2(\boldsymbol{\alpha}) \approx \sum_{i=1}^{n} \frac{(N_i - f_i)^2}{N_i} = \chi^2. \tag{3.27}$$

Thus, for a very well populated bin the Poisson-statistics fit approaches the result of the standard least-squares fit.

Two example fits can be found in Figure 3.22. The top panel shows an example of how the Poisson-statistics fit behaved in the case of plentiful statistics, while the lower panel demonstrates the case where the statistics were very limited, but the fit made the best use of the available data.

Another demonstration of the template fitting technique can be found in Figure 3.23. Here, it can be seen that same template shapes fit the data well across the entire kaon angular range. Also, this plot shows how the bin-to-bin statistics varied greatly as a function of $\cos\theta_K$ and ϕ_K.

Finally, as a global measure of how the yield-extraction fits succeeded, a χ^2 distribution assembled from the many Poisson-statistics fits is displayed in Figure 3.24. The left panels shows that overall, the reported χ^2 per degree of freedom distribution (ν) tended to be less than one. The right panel shows how χ^2/ν changed as the number of non-zero bins in the missing-mass distribution increased. Since the minimizations performed to extract the yields was not a χ^2 fit but instead the aforementioned Poisson-statistics fit, we expected χ^2/ν to be different from 1 for small ν. However, as the population of the histogram increased and $\delta N_i \to \sqrt{N_i}$, the Ξ^2 fit approached a χ^2 fit and χ^2/ν should have tended toward 1. This is reflected in the right panel, and reaffirms that the yield extraction fit generally functioned properly.

3.3.7.1 Unified Error Analysis Method

For a number of bins, the hyperon yield determined by the fit was very low, and so the uncertainty reported by the fit under-covered the range of the parent distribution. To handle this, the Unified Error Analysis method [66] was used to determine the appropriate range of uncertainty to report for the extracted points.

Briefly, the Unified Error Analysis method works as follows: The measured yield, N, was from an unknown Poisson parent-distribution with a peak at μ counts. In the limit of many counts, the observed yield, N, with its uncertainty match well to the peak of the parent distribution. However in the case of very few counts, typically less than 10 above the expected background, the Poisson nature of the parent distribution

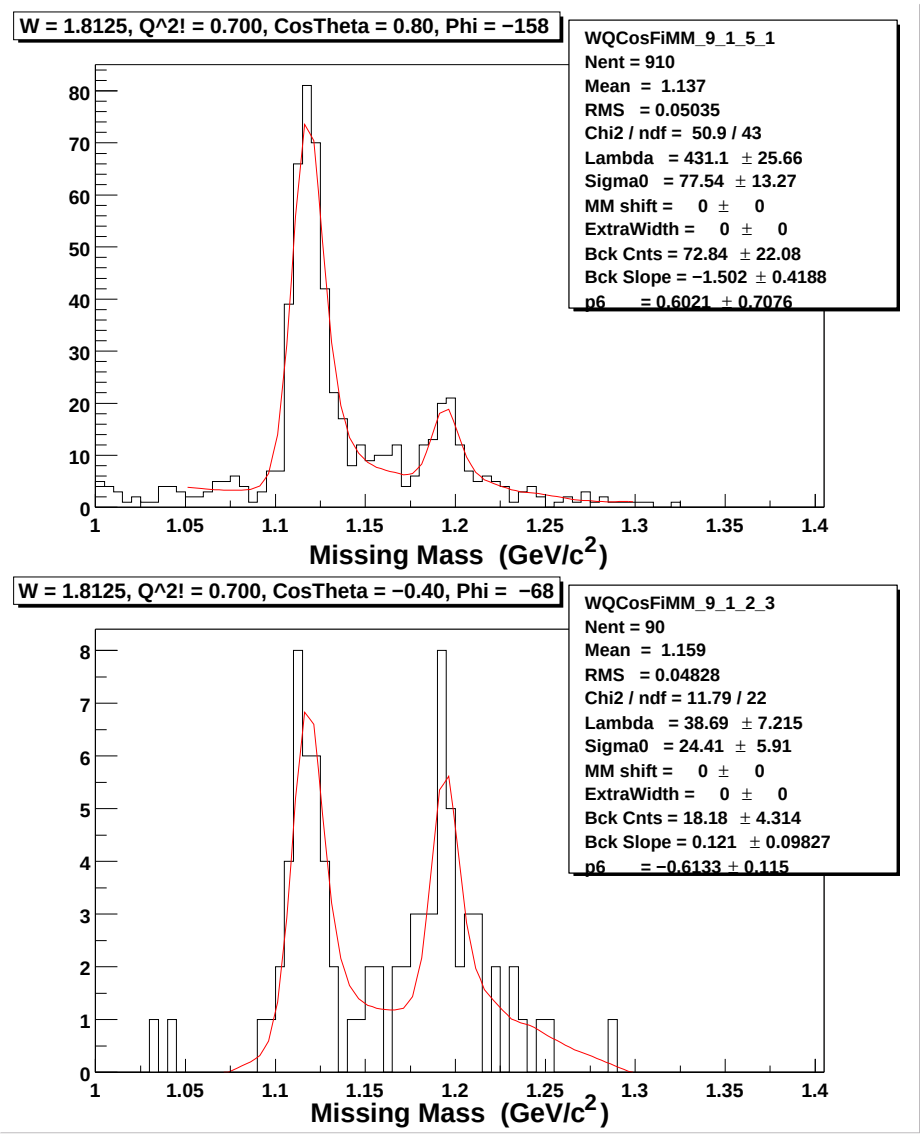

Figure 3.22: Example fits of the observed hyperon spectra using template shapes for the Λ and Σ^0 peaks plus a polynomial background. A Poisson-statistics fit was used to account for the low bin occupancy.

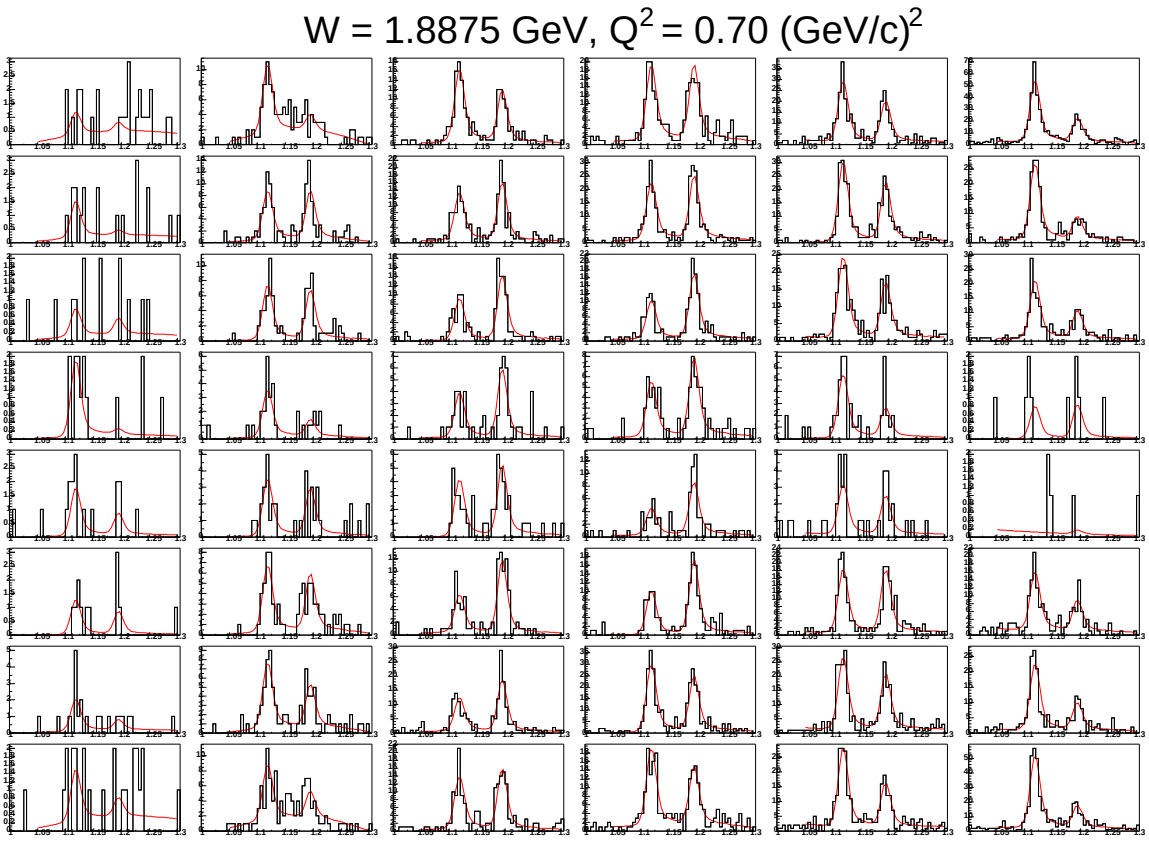

Figure 3.23: The full set of missing mass distributions for one (W, Q^2) bin, shown as the six bins in $\cos\theta_K$ from -1. to +1 (left-to-right), and the eight ϕ_K bins, from -180° (bottom) to +180° (top).

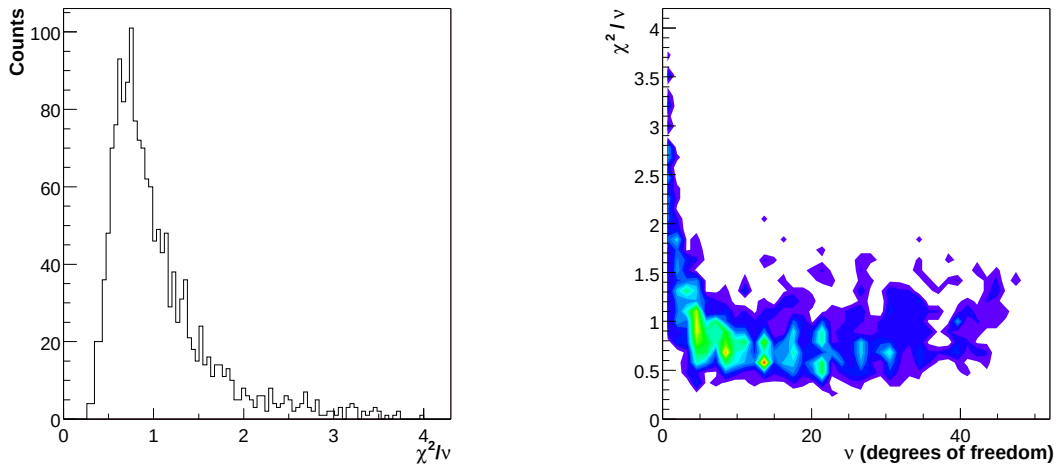

Figure 3.24: The χ^2 per degree of freedom distribution from the yield extraction fit (left), and its trend as more points are added (right). This is from the 2.5 GeV, 1500 A dataset.

guarantee that frequently μ will be outside the range of $N \pm \sqrt{N}$, and so the naively-calculated confidence interval under-covers the span of acceptable values of μ. If instead, we examine the possible values of μ which could produce the observed yield N, the appropriate confidence interval can be determined. This method also has the benefit of permitting the smooth transition from upper-limits to conventional dual-sided error bands.

Using this technique, in general the uncertainty intervals were asymmetric about the central value such that we had N^{+a}_{-b}. The uncertainty then used throughout the rest of the analysis was the larger of the two values, but the central value was left alone. This was done to simplify the later analysis, and since the upper and lower ranges were generally symmetric except when the lower bound was near zero. For example, for the case where the most-likely value was zero but with a finite upper-limit, the yield passed on from the yield fitting procedure was $0 \pm \delta N$. The apparently-included region of negative yield was excluded later in the analysis (see Section 3.3.12).

3.3.7.2 Hyperon and Background Yields

To understand the level of background under the hyperon peaks, the results of the yield-fit were studied as a function of W, Q^2, and $\cos\theta_K$. The distributions are shown in Figure 3.25. The overall level of background in the missing-mass range of 1.05 to 1.3 GeV/c^2, primarily from misidentified π^+ pions, tended to peak toward the forward direction in the center-of-momentum frame, and toward higher W. At no point was the background contribution greater than the hyperon signal, though for W greater than 1.95 GeV, it appeared to have a similar yield to the $K^+\Sigma^0$ final state.

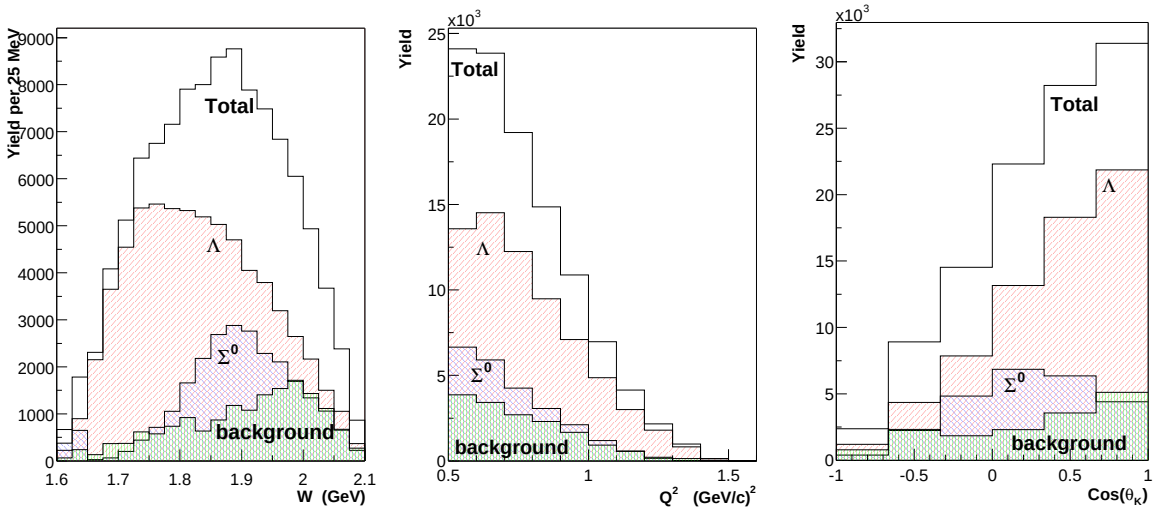

Figure 3.25: The extracted hyperon and background yield, from left to right, versus W, Q^2, and $\cos\theta_K$. The angle ϕ_K and the other two kinematic variables have been summed over. This was collected from the 2.5 GeV, 1500 A dataset.

3.3.8 Removal of Target Wall Contamination

As the electron beam passed through the target, it could interact not only with the liquid hydrogen, but also with the target entrance and exit windows, as well as matter outside of the cell. Since we were studying an exclusive 3-body final state containing long-lived particles off of an initially stationary proton and we detected two particles, our kinematics were very well defined. In the case of kaon production from the more complex aluminum nuclei in the target windows, the Fermi-momentum of the nucleons was around 200 MeV. This Fermi-motion resulted in a broadening of the missing-mass peaks much beyond our instrumental resolution of 5-10 MeV which we saw for the hyperons. Studies with the CLAS collaboration of hyperon photoproduction off of aluminum have shown the Fermi-momentum broadens the missing-mass peaks enough to be unable to separate the Λ and Σ^0 peaks. Therefore, at least to first order the continuous distribution of events from the target walls would be swept into the background function.

Verification for this can be seen in Figure 3.26, where we present the missing-mass distributions for empty target runs. The data was divided according to where the event vertex was located. The events from well inside the target were collected and normalized to get the number of counts in the missing-mass spectra per centimeter of gas in the target. This was compared to the normalized distributions from the target walls. As can be seen, the events from inside the "empty" target very well represent the hyperon signals seen from the target windows. These peaks were actually due to interactions with hydrogen still present inside the warmed target.

The normalized hyperon signal from the empty target runs was approximately

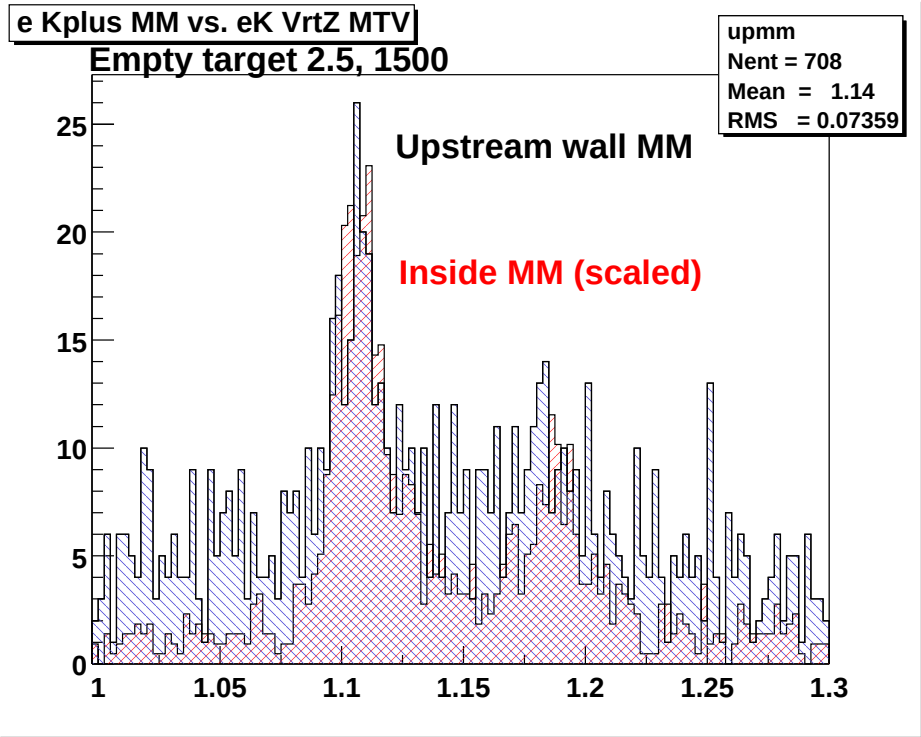

Figure 3.26: Missing mass distributions collected from the 2.5 GeV, 1500 A empty target runs. The distribution from the upstream target window does show peaks corresponding to the Λ and Σ^0 hyperons, however so does the portion from inside the "empty" target. The signal from inside the target was scaled to have the equivalent thickness of the region considered from the upstream entrance window, and it can be seen that the distributions match well.

5% of that from the full target runs. A quick calculation of the density of gaseous hydrogen at the empty target's temperature and pressure (22.6 K,1355 mbar) under the assumption it behaved as an ideal gas yielded a density of $0.0019\,\mathrm{g/cm^3}$, about 3% of the nominal target density. We conclude that the hyperon signal rate from the empty target was consistent with interactions with the hydrogen gas.

3.3.9 Acceptance and Efficiency

The CLAS detector, while a large acceptance device, has large regions of low or zero detection acceptance. In addition, various aspects of the detector systems, such as broken wires in the drift chambers, dead channels in the scintillation detector, and finite timing resolutions, affect the event reconstruction efficiency in non-trivial ways. To understand and correct for these effects, events generated according to distributions similar to the data were processed with a model of the CLAS detector and passed through the standard event reconstruction scheme.

The acceptance for $e\,K$ detection and reconstruction was calculated using radiated events produced with RadGen. The detector response was simulated using GSIM, a GEANT-based [67] model of CLAS. The model included the detector elements, beamline components, and support structures of CLAS. The geometries for the drift chambers and time-of-flight detectors were set to match the configuration during the actual data-taking[1], to best match the simulated and real detectors' responses. GSIM was run in a standard configuration, permitting the particles "swum" through the detector and magnetic field to undergo decay, scatter off the detector's materials, and lose energy due to ionization processes. Hits in the various detector packages were generated, producing responses in the drift chambers, scintillation detectors, and the electromagnetic calorimeter representative of those found in events in the data sample.

After modeling the detector's response, the events were passed onto GPP (GSIM Post Processor) where the trigger and imperfections of the CLAS detector were simulated. First, hits from known dead drift chamber wires were removed. Next, hits in the DC and SC were "smeared" by adding random timing offsets distributed according to a Gaussian representative of the detectors' resolutions. The resolution of the SC was taken from cosmic-ray tests of the scintillators and parameterized as a function of scintillator length [49]. To match the timing resolution for the kaon and electron hits to the data, we found it necessary to apply this additional adjustment with a scale factor of 0.72, suggesting that the timing resolution observed in the data was better than expected. The distribution of applied adjustments to the SC timing is shown in Figure 3.27. The DC effective resolution was determined by parameterizing the distance-of-closest-approach (DOCA) residuals as a function of the DOCA for the different regions [60], and was applied without any additional scale factors.

[1] The geometry and resolution settings for run 16507 were used for the simulation.

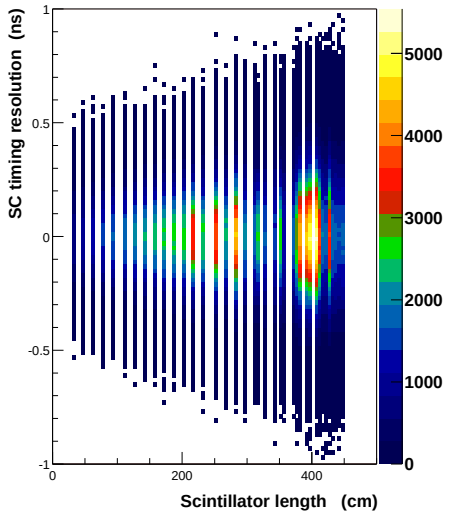

Figure 3.27: The effective timing resolution of the SC paddles as a function of scintillator length, as enforced by GPP.

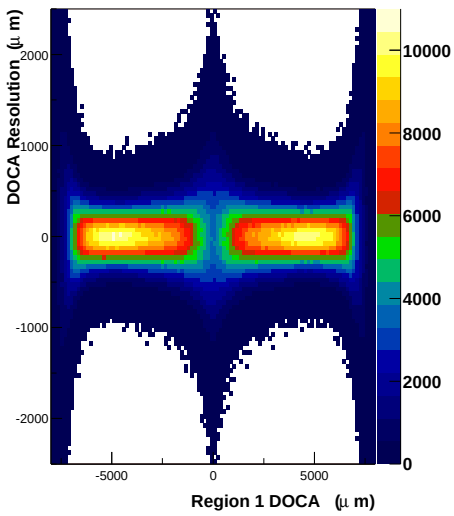

Figure 3.28: The distance of closest approach (DOCA) resolution for Region 1, according to GPP.

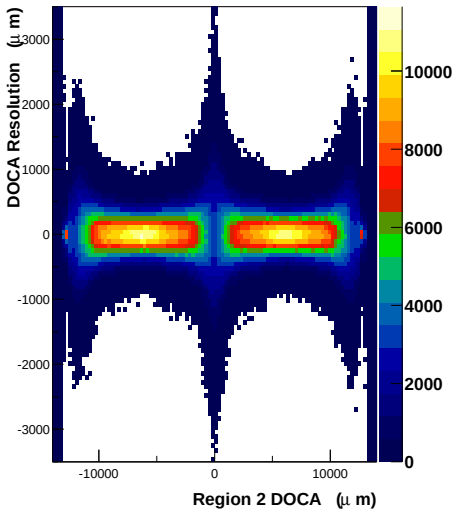

Figure 3.29: The DOCA resolution for Region 2, according to GPP.

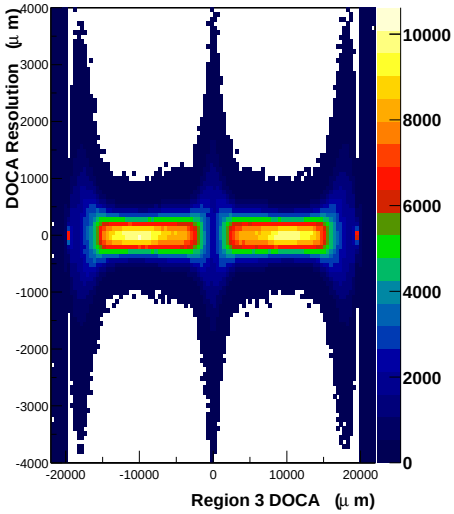

Figure 3.30: The DOCA resolution for Region 3, according to GPP.

Finally, the resulting events were processed with a patched version (prod-1-9-patches) of the PROD-1-9 CLAS event reconstruction software used to cook the original data. The events were then transferred to the ROOT DST format and passed through the same analysis used on the CLAS data.

The same cuts which were applied to the data were applied to the simulated events, with the exception of the Scaler Event-Class cut. In addition, since the model of the Čerenkov detector in GSIM was not complete, electron tracks were identified in the simulated events according to the calculated Čerenkov detector efficiency [58]. The timing cut on the K TOF was independently measured for the Monte-Carlo events, with the same procedure as that used on the data, to verify the timing resolutions matched and to ensure the same percentage of kaons were cut from the simulated events as from the data.

The fitted-template technique was used to determine the yield of observed events in a given bin. During this yield extraction, the background was not permitted to contribute and the additional width (Δ) parameter was set to zero. The acceptance for the bin was the ratio of the yield of reconstructed events observed in that bin to the number of events thrown into the bin. The uncertainty on the ratio was calculated by propagating the uncertainty of the number of reconstructed events in the bin. Since events could migrate from bin-to-bin due to resolution and external radiative effects, the observed yield N_{obs} was not precisely binomially related to the number of events thrown into that bin, N_{thrown}; instead, N_{obs} varied in a normal statistical manner such that $\delta N_{obs} = \sqrt{N_{obs}}$. However N_{thrown} was precisely known, and so for the i-th bin the acceptance and uncertainty were:

$$\eta_i = \frac{N_{obs}}{N_{thrown}} \tag{3.28}$$

$$\delta\eta_i = \frac{\delta N_{obs}}{N_{thrown}}. \tag{3.29}$$

A cutoff on the acceptance was then applied, to remove bins with extremely low acceptance. The cutoff was placed at 10% of the average acceptance over the ϕ_K bins for that particular value of $\cos\theta_K$, with an absolute minimum acceptance of 0.5%.

The total number of hyperons generated and used for creating templates and calculating the acceptance is given in Table 3.13. In comparing with Table 3.10 one sees that between 2.5 and 7 times more simulated Λ and Σ^0 passed the final cuts than were observed in the datasets. This was determined to be adequate simulated statistics such that the final result would not be dominated by the statistical uncertainty of the acceptance.

The acceptance was found to vary strongly with the angle of the kaon in the center-of-momentum frame. The evolution of the acceptance with W for the 2.5 GeV, 1500 A dataset is presented in Figures 3.31,3.32, and 3.33. In all the figure, the acceptance is seen to rise in the forward direction, as the kaons become more energetic and fewer are lost to particle decay. Figure 3.31 shows the acceptance for Λ events between

Table 3.13: The statistics for the simulated events used to calculate the acceptance, summed over all kinematics. This can be compared with Table 3.10.

M.C. Dataset	Λ's generated	Λ's accepted	Σ^0's generated	Σ^0's accepted
2.567 GeV, 1500A	9.84 M	620 k	2.55 M	118 k
2.567 GeV, 2250A	3.37 M	131 k	1.99 M	60 k

$1.65 < W < 1.75\,\mathrm{GeV}, 0.5 < Q^2 < 0.9\,(\mathrm{GeV/c})^2$. There is a marked region of low acceptance near $\phi_K = 0$; this is due to the kaon traveling toward the beam-pipe, as can be seen in Figure 3.34. In Figure 3.34, the lab angles of the kaon for a Λ event are plotted, with the curves marking out the edges of the 10 $\cos\theta_K$ bins of Figure 3.31 and 3.32. The ϕ_K^{lab} angle is for an electron passing through the center of sector 1 at $\phi_e^{lab} = 0$. A marker was placed for each 5° increment of the center-of-momentum angle ϕ_K, with $\phi_K = 0°$ as the point with the lowest θ_K^{lab} angle at $\phi_K^{lab} = 180°$, or at $\phi_K^{lab} = 0°$ when the curve is open. We see that for the forward-most $\cos\theta_K$ bin, spanning from the single marker at $(\theta_K^{lab} = 19°, \phi_K^{lab} = 180°)$ to the innermost curve, a reasonable number of the ϕ_K points would have some coverage. However as $\cos\theta_K$ increases, the points around $\phi_K = 0°$ are at too low a polar angle to be detected in the drift chambers.

In comparing Figures 3.31 and 3.32, two effects due to an increasing W are evident. First, the acceptance increases more sharply in the forward direction with higher W, which is due again to the increased boost of the center-of-momentum frame and the increased momentum in this frame available to the kaon. Second, the hole in the acceptance due to the limited acceptance at small θ_K^{lab} is more focused in the forward direction, almost disappearing at larger θ_K. At these larger angles, the kaons span the entire CLAS detector, as seen in Figure 3.34. This means that the overall acceptance increases, however the sensitivity of the measurement to the modeling of each sector also increases.

3.3.10 Cross-section Normalization

The cross-section normalization factor was determined from the integrated charge of the live-gated Faraday cup, the target density calculated from the target temperature and pressure recorded during the run period [46], and the target lengths [53]. The live-gated electron flux information was kept on a run-by-run basis. The other relevant values for this dataset, such as the target length and nominal density, are summarized in Table 3.14.

During the analysis the livetime calculated from the Faraday cup was compared to the clock- and trigger-based livetimes. When the DAQ system was busy, a gate was generated to reject further events until the digitization was complete. The signals from the Faraday cup and a 10 kHz clock were each sent, both ungated and live-gated, to scalers to provide a measurement of the livetime from each system. Additionally, since

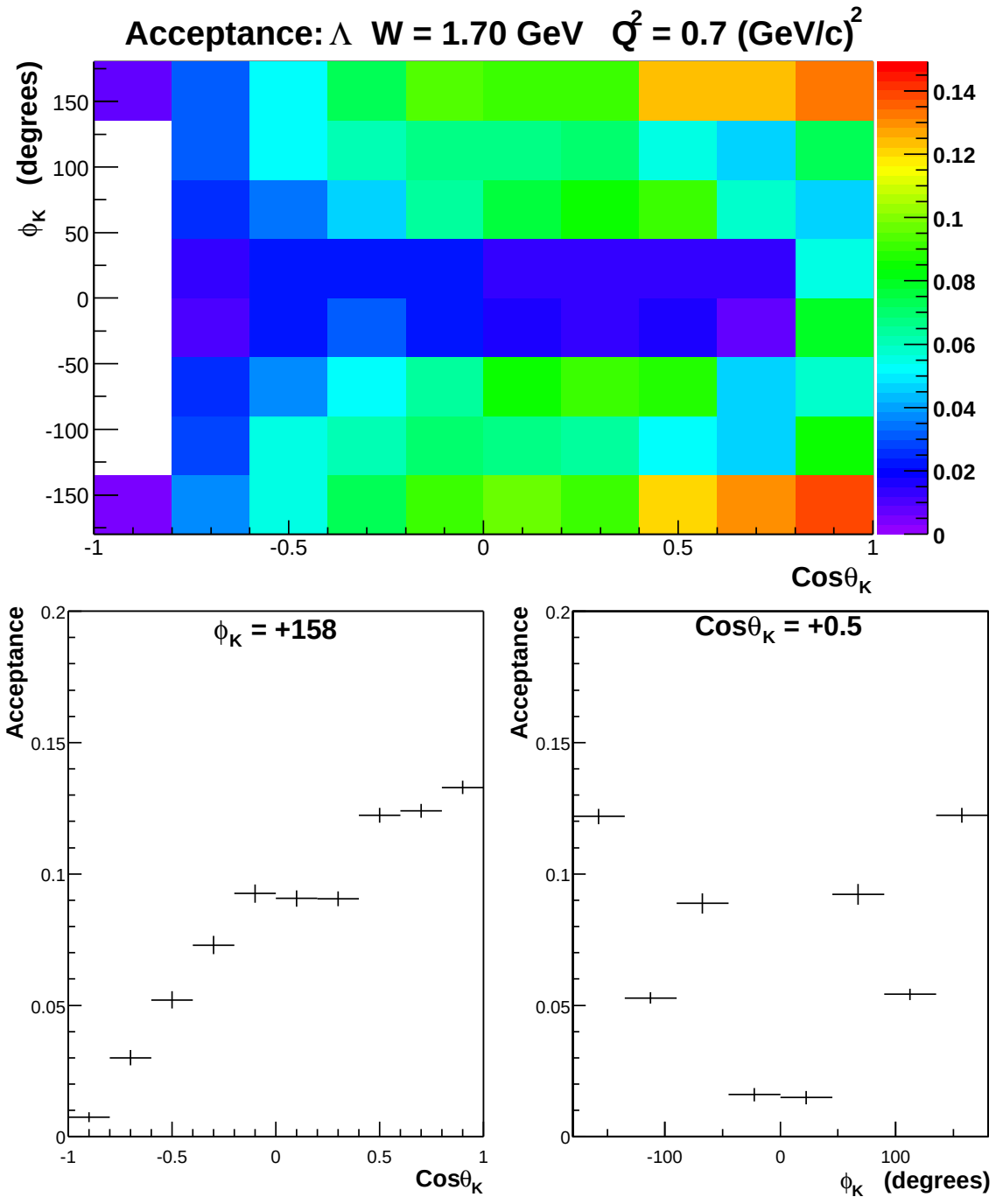

Figure 3.31: The acceptance for a Λ event from the 2.5 GeV, 1500 A dataset, integrated over $1.65 < W < 1.75\,\mathrm{GeV}, 0.5 < Q^2 < 0.9\,(\mathrm{GeV/c})^2$.

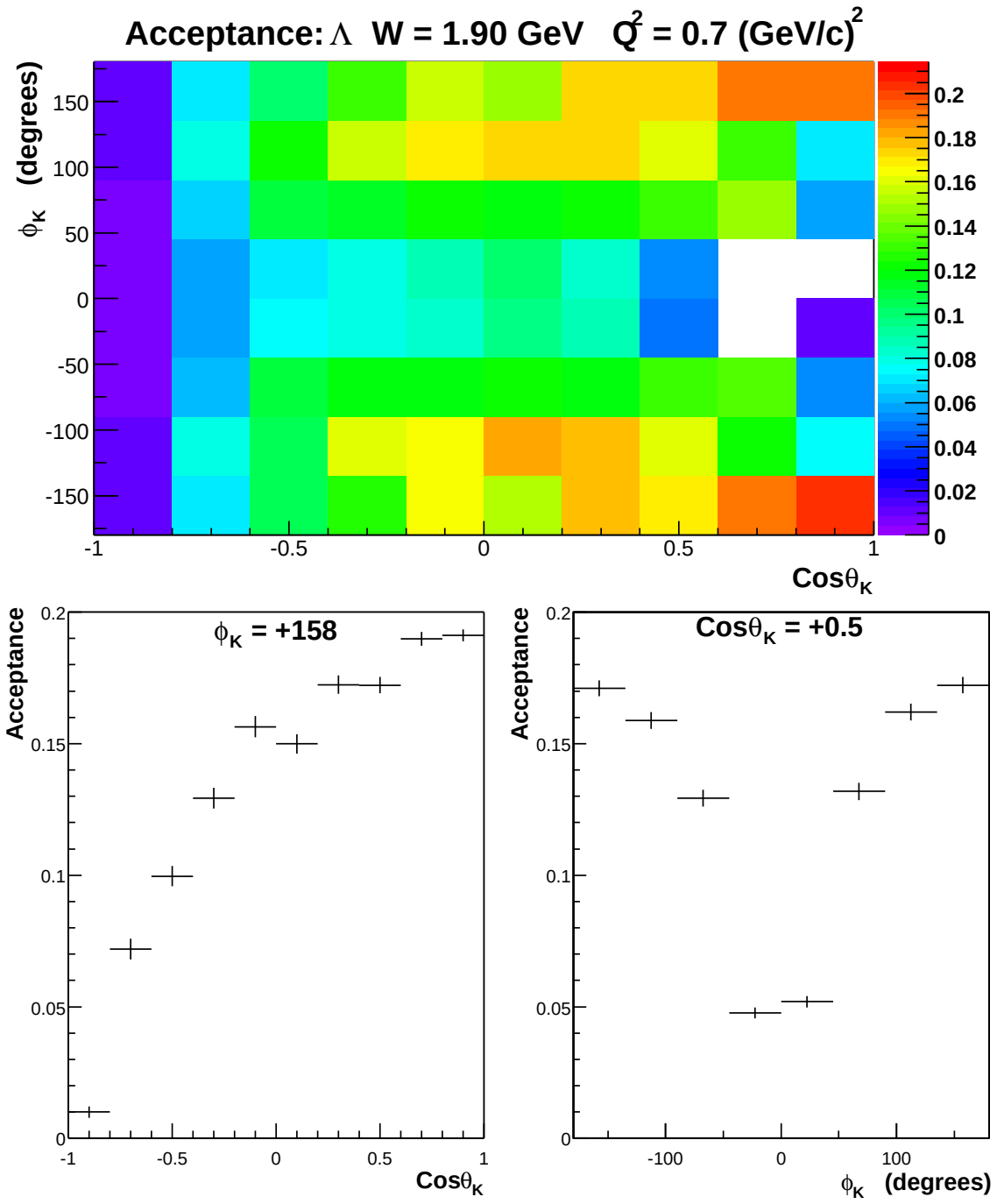

Figure 3.32: The acceptance for a Λ event from the 2.5 GeV, 1500 A dataset, integrated over $1.85 < W < 1.95\,\mathrm{GeV}, 0.5 < Q^2 < 0.9\,(\mathrm{GeV/c})^2$.

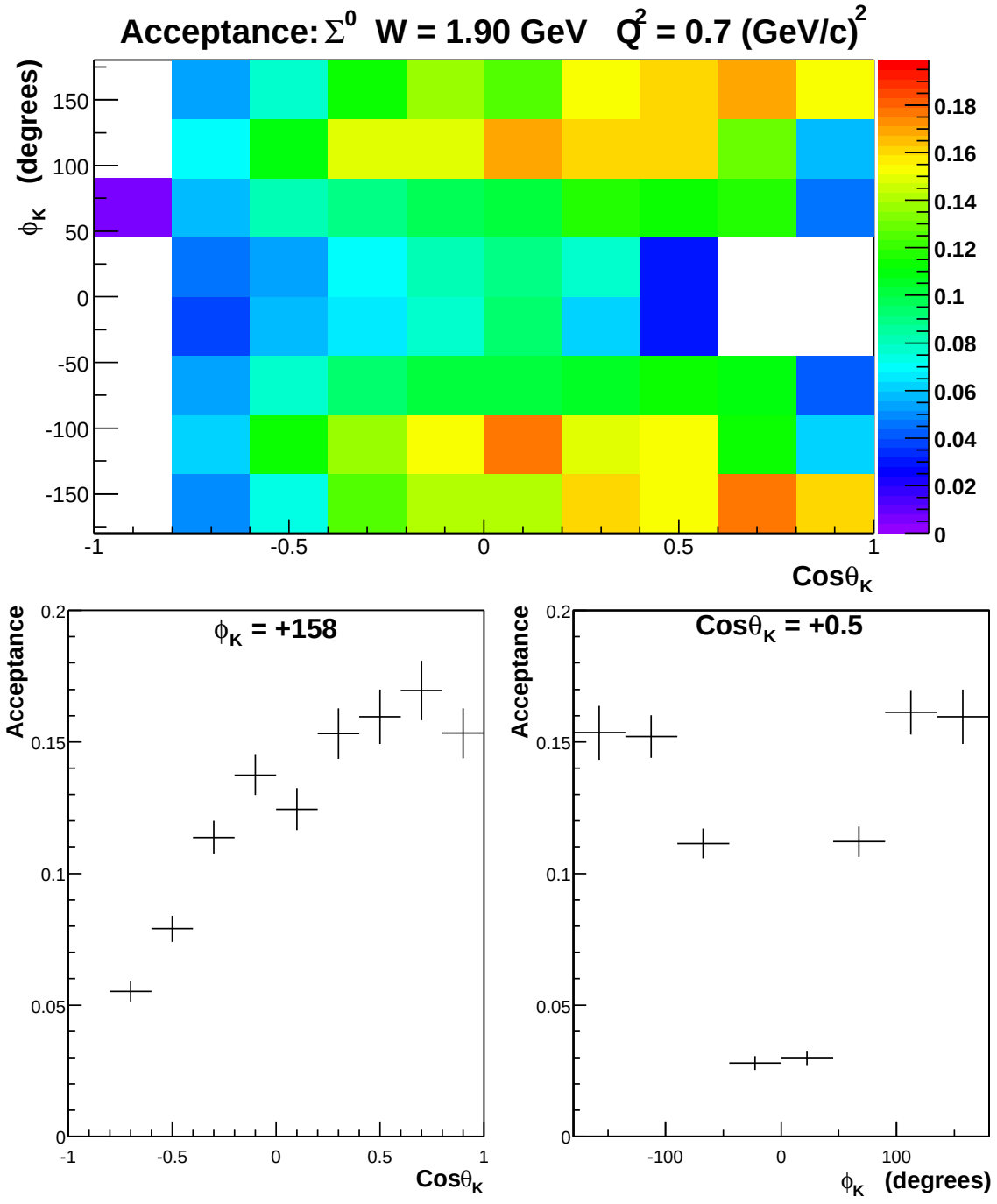

Figure 3.33: The acceptance for a Σ^0 event from the 2.5 GeV, 1500 A dataset, integrated over $1.85 < W < 1.95\,\text{GeV}, 0.5 < Q^2 < 0.9\,(\text{GeV/c})^2$.

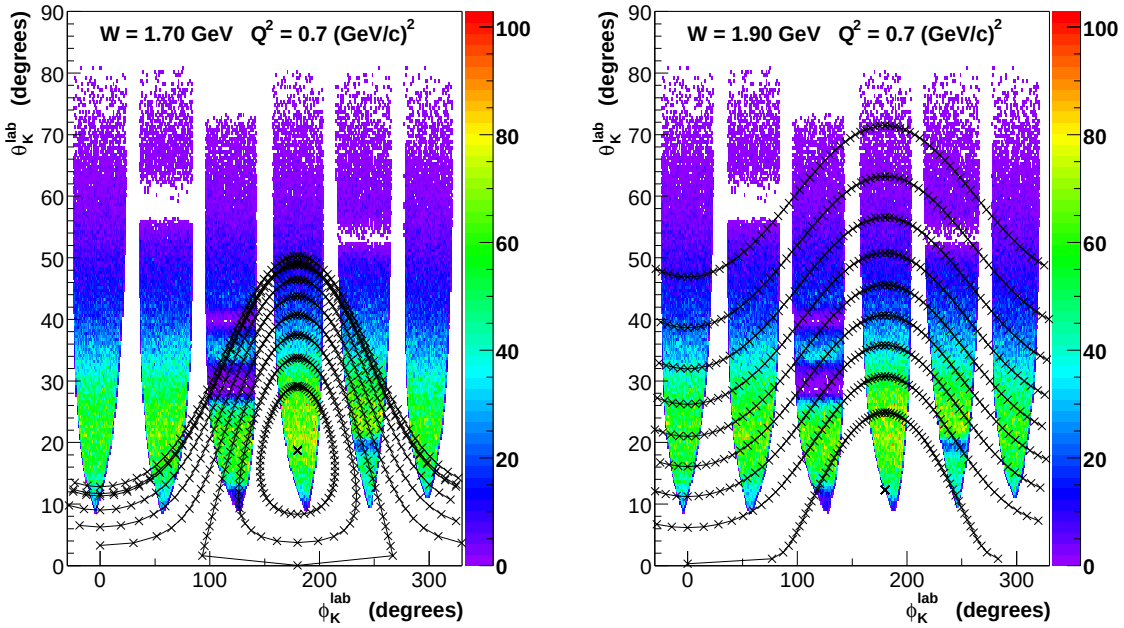

Figure 3.34: The lab polar and azimuthal angle of the kaon from a Λ event when the electron is found in the center of sector 1 ($\phi_e = 0$). The markers denote the edge of the 10 bins in $\cos\theta_K$ as ϕ_K varies from 0 to 180°. Kaons at $\cos\theta_K = \pm 1$ would be seen at the single point at $\phi_K^{lab} = 180$.

Table 3.14: The target conditions during the e1c run period.

		Target		
First run	Last run	Length (mm)	Temperature (K)	H_2 density (g/cm^3)
	16575	50.0	20.5	0.0695
16576	16968	50.0	18	0.0730
16969	17196	38.0	20.5	0.0695

the Level 1 trigger was dead-timeless the number of triggers which were rejected due to the DAQ's busy state were explicitly counted. When these values were compared, the clock- and trigger-based livetimes agreed better to than 0.5%, while the livetime from the Faraday cup was observed to be systematically 3-5% lower. This difference was due to the mismatch of the Faraday cup's slow rate, running nominally at 40 Hz for the 4 nA electron beam for the run period, and the 2 kHz trigger rate at which the livetime signal was switching. To account for this, the live-gated Faraday cup electron flux measurement was increased by 4% before being used to normalize the cross-sections.

3.3.11 Combining the Datasets

The 2.5 GeV, 1500 A and 2250 A datasets, with different main-torus field strengths, had different electron and kaon acceptances leading to slightly different kinematic coverage. This can be seen in Figure 3.35, where the (W,Q^2) coverage, determined by the electron arm, is shown for the two field settings. Overlaid on top of the distributions is a sample binning of dW=25 MeV, dQ^2=0.4 (GeV/c)^2 used to process the data. The lower edge, determined by the minimum electron scattering angle, is markedly higher for the 2250 A dataset since, in the higher magnetic field, these low angle electrons would tend to bend more and miss the Region 3 drift chambers. The binnings were chosen to maximize the coverage of the two datasets.

The low and high torus current setting datasets were combined on a bin-by-bin (W,Q^2,$\cos\theta_K$,ϕ_K) basis, weighted according to their error bars. This was performed after extracting the yields and correcting for acceptance, electron flux, target density, and the scale-free systematic uncertainties (discussed in 4.4), but before the correction for radiative effects (which they share). This resultant set of cross-sections were then used to extract the response functions.

3.3.12 Fitting the ϕ_K Distributions

After determining the cross-section in each Q^2, W, $\cos\theta_K$ and ϕ_K-bin, the different response functions were extracted according to their ϕ_K-dependence. As seen in Equation.1.14, the cross-section was of the form $f(\phi_K) = a + b\cos(\phi_K) + c\cos(2\phi_K)$. Since the bins were of finite size in ϕ_K and rather large, the parameters a, b, and c

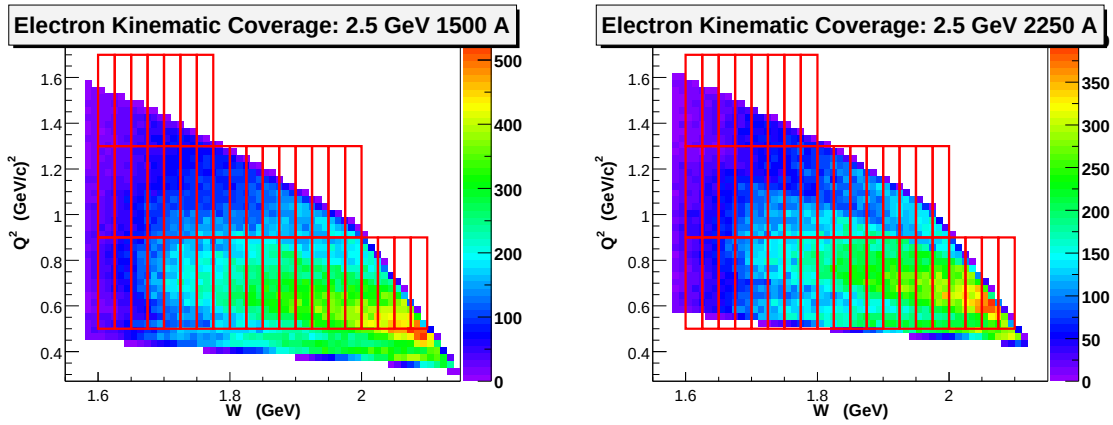

Figure 3.35: The distribution of electrons in W and Q^2 of kaon events, for the 2.5 GeV datasets taken with torus current settings of 1500 A and 2250 A shown in the left and right panels, respectively.

were determined by fitting to the average value of $f(\phi_K)$ across each bin. The χ^2 that was minimized was:

$$\chi^2 = \sum \frac{\left(\frac{d\sigma_i}{d\Omega_K} - \langle f_i \rangle\right)^2}{\delta \frac{d\sigma_i}{d\Omega_K}^2} \tag{3.30}$$

where

$$\langle f_i \rangle = \frac{1}{\phi_{i+1} - \phi_i} \int_{\phi_i}^{\phi_{i+1}} f(\phi) d\phi \tag{3.31}$$

and ϕ_i is the lower edge of the i-th bin. Since a cross-section is a physical measurement of probability, it can never be negative. However, the form of the fitting function $f(\phi_K)$ can become negative for suitable values of a, b and c. To remove the region of negative $f(\phi_K)$ from consideration by the fit, a penalty factor of:

$$\chi^2_{penalty} = \left(-100 * f(\phi_K)|_{extrema-}\right)^2 \tag{3.32}$$

was added to the fit's χ^2 when a bin contained a point where $f(\phi_K)$ went negative. This was found to be quite effective in discouraging the fit from this forbidden region and handling the very low-statistics bins.

Due to the non-trivial propagation of some of the systematic uncertainties onto the terms of the cross-section, with special attention to the ϕ_K-dependent interference terms, the point-to-point systematic uncertainties were added in quadrature to the statistical error of each bin prior to the fit. In this manner, the uncertainties reported by the fit automatically include the estimated systematic errors that could induce changes in the ϕ_K distributions.

Some sample fits to the data can be examined in Figure 3.36. This figure shows the ϕ_K-fits for each magnetic setting separately, and then the results from the combined

datasets. As can be seen, the agreement between the two datasets was very good. For each (W,Q^2) bin the central value of ϵ was calculated. The kinematic prefactors of ϵ and $\sqrt{2\epsilon(\epsilon+1)}$ were then removed to extract $\sigma_T + \epsilon\sigma_L$, σ_{TT} and σ_{LT} .

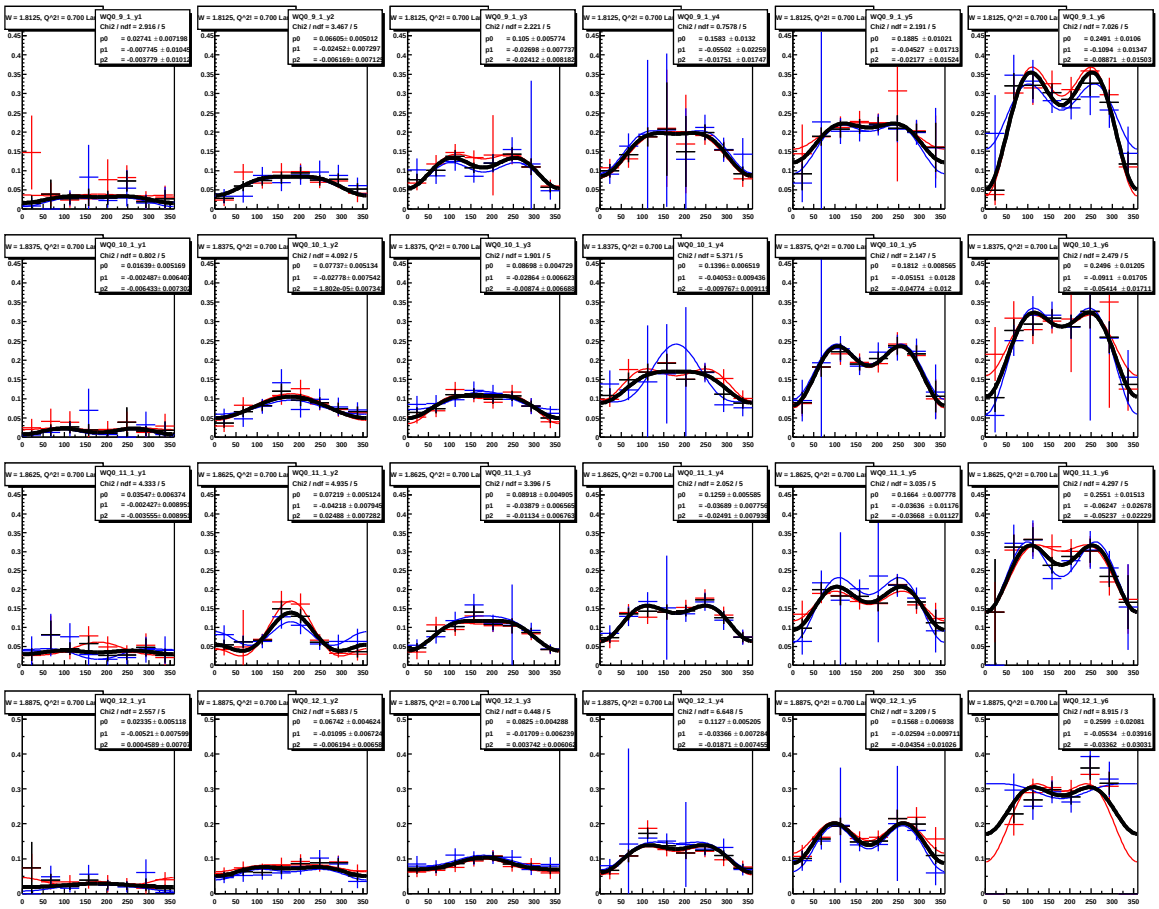

Figure 3.36: The ϕ_K-distributions for Λ production from the W-bins centered at 1.8125 GeV (top) to 1.8875 GeV (bottom), for $0.5 < Q^2 < 0.9\,\mathrm{GeV/c^2}$, and with $\cos\theta_K$ running along the rows from -1 to 1 from left to right. The red (blue) points and curves correspond to the 2.5 GeV, 1500 A (2250 A) dataset. The thick black curve is the fit to the combined datasets.

Chapter 4

Results

In this chapter the final extracted response-functions, according to Equation 1.14, are presented for different binnings of the data. The independent variables are $\cos\theta_K$, W, and Q^2. The horizontal error bars indicate the range over which the average cross-section was measured. The vertical error bars include both statistical and those estimated systematic uncertainties which would affect the shape and trends of the response-functions. The estimation of the systematic uncertainties is also discussed in this chapter.

4.1 Response Functions versus Cos(θ_K)

In order to best observe the angular behavior of the differential cross-section, the data was binned coarsely in W (δW=100 MeV) and Q^2 (δQ^2=0.4 (GeV/c)^2), and finely in $\cos\theta_K$ ($\delta\cos\theta_K$=0.2). This choice of binning emphasized the overall $\cos\theta_K$ dependence of the response functions, as well as indicating their behavior with t.

The resultant terms of the K electro-production cross section are shown in Figures 4.1 and 4.2 for the Λ and Σ^0 hyperons, respectively, according to the form of Equation 1.14. To show the consistency of the results, presented are the extracted values of $\sigma_T + \epsilon\sigma_L$, σ_{TT} , and σ_{LT} after the separate analysis of the high(□) and low(○) magnetic field datasets, along with their combined result(■). The fitted response functions from the combined datasets were not constrained to be the average of the two results, since the fit to extract them was performed after the datasets were averaged together on a bin-by-bin basis. We found the response-functions to be quite consistent between the two datasets, taken with different magnetic fields and acceptances.

The Williams-Ji-Cotanch (WJC) model [6] for kaon electroproduction was used to generate events for the acceptance and radiative corrections, with roughly the correct kinematic behavior. This is shown in the figures as the dashed-curve. While the model did not well match the data quantitatively, it generally had the correct $\cos\theta_K$ dependence for $\sigma_T + \epsilon\sigma_L$.

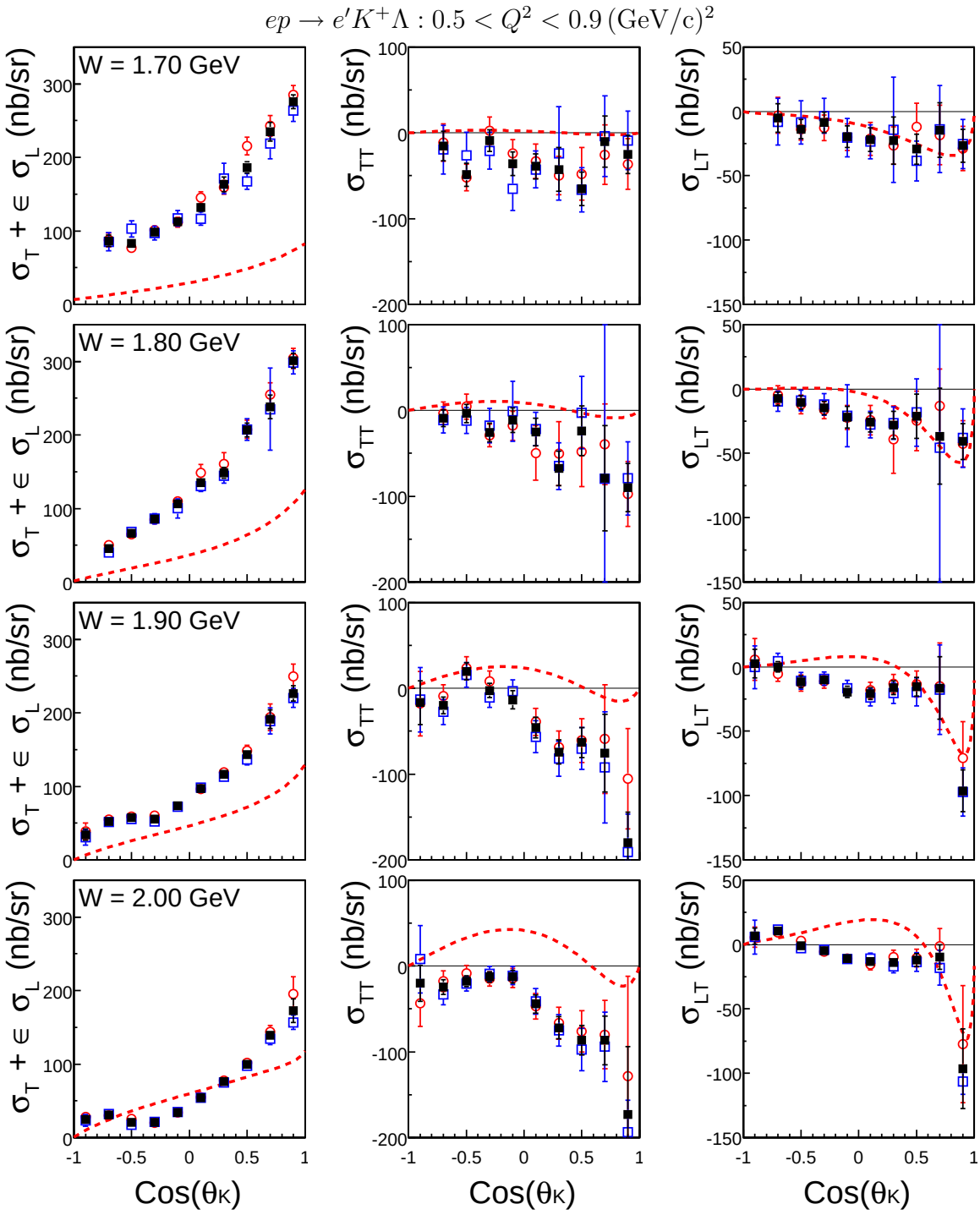

Figure 4.1: The response functions of Λ electroproduction versus $\cos\theta_K$ for 100 MeV wide bins in W and $0.5 < Q^2 < 0.9\,(\mathrm{GeV/c})^2$. Results for the 2.5 GeV, 1500 A (○), 2250 A (□), and combined datasets (■) are presented. The WJC calculation of the differential cross-section is also shown (red, dashed curve).

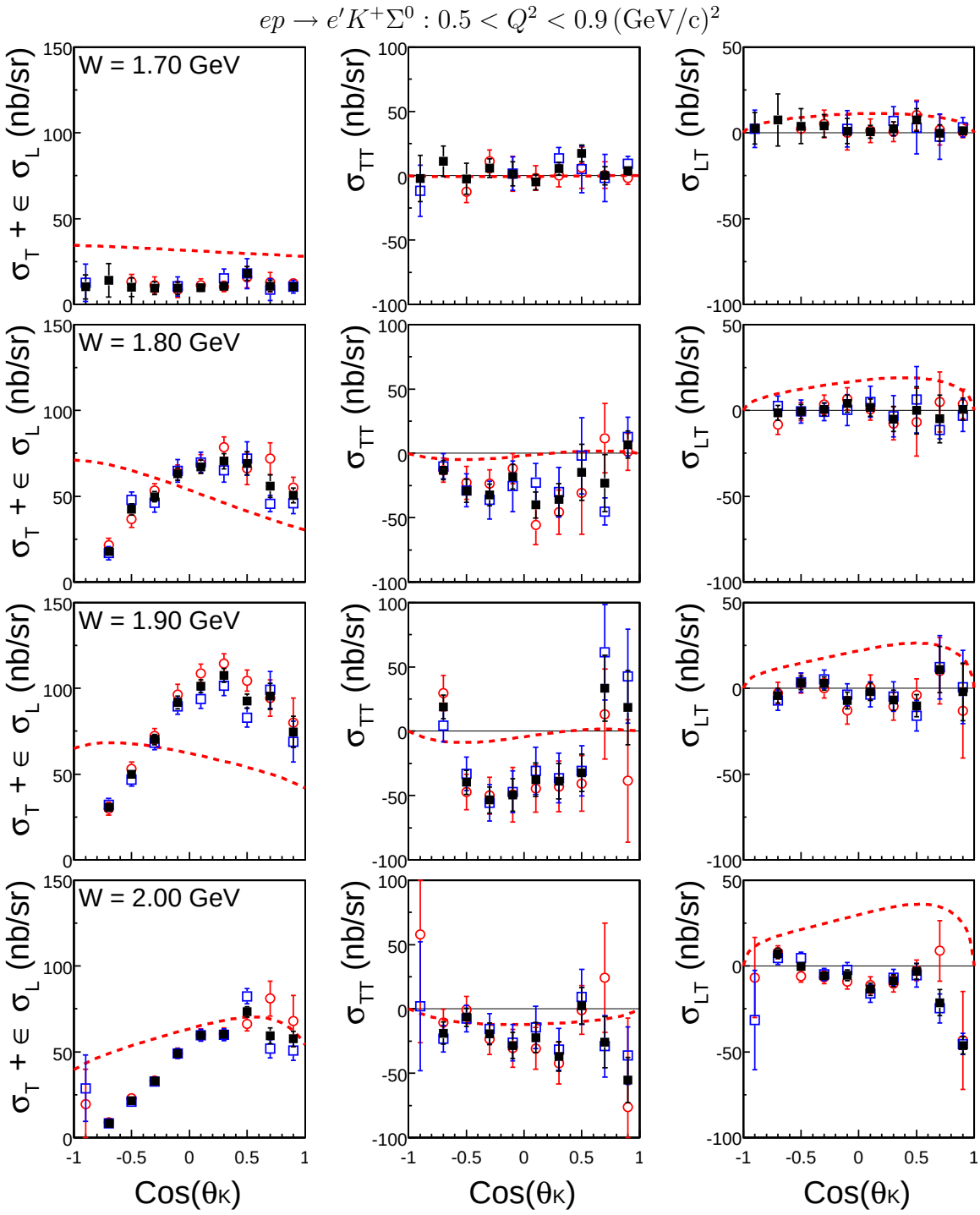

Figure 4.2: The response functions for Σ^0 electroproduction versus $\cos\theta_K$ for 100 MeV wide W bins and $0.5 < Q^2 < 0.9\,(\mathrm{GeV/c})^2$. Results for the 2.5 GeV, 1500 A (○), 2250 A (□), and combined datasets (■) are presented. The WJC calculation of the differential cross-section is also shown (red, dashed curve).

4.2 Response Functions versus W

In looking for evidence for resonant s-channel processes, the signature would be most visible as action in the W-dependence of the response-functions. So, the data was rebinned with narrow 25 MeV bins in W, and wide $\cos\theta_K$ ($\delta\cos\theta_K = \frac{1}{3}$) and Q^2 ($\delta Q^2 = 0.4\,(\mathrm{GeV/c})^2$) bins, presented in Figures 4.3- 4.8. To verify the hyperon-yield extraction was stable against low and changing statistics, the extracted response-functions are also shown for two coarser binnings in W, with δW=50 MeV and 100 MeV denoted by the open squares(□) and open circles(○), respectively. The high-lighted finely binned results are marked as filled squares(■). It should be noted that the systematic uncertainties were studied for the finest-binning results, and extrapolated to the coarser binnings of the data. As such, the error bars for the 25 MeV W-bins are most representative of the systematic and statistical uncertainties of the results, though tests have shown the other binnings have consistent systematic uncertainties. The results from the different binnings are compatible, and also serve to indicate how features could be missed in the case of coarser binning decisions. For example, the $\delta W = 100$ MeV binning, while consistent with the narrower binning choices, failed to capture the interesting behavior of the cross-section seen in the $\delta W = 25$ MeV set at $\theta_K \approx 0°$ and 150° (see Figures 4.3 and 4.7).

As in the case of the $\cos\theta_K$ distributions, the model used to calculate the acceptance and radiative correction is overplotted in the figures. For the Λ, the model's cross-section increased steadily with W while the measured cross-section increased and then dropped off for W greater than 1.8 to 1.9 GeV. In comparing the data and model for the interference terms, the relative agreement was seen to deteriorate as one moved from the forward to backward directions. For the Σ^0, though the model cross-section was incorrect by an overall scale factor, the model did well describe the general rise of the $\sigma_T + \epsilon\sigma_L$ term with W. However, for the interference terms the model performed poorly. These differences led to a large systematic uncertainty in the calculated acceptance, which is discussed below(4.4.3.2).

4.3 Response Functions versus Q^2

The data was rebinned once more to study the Q^2 dependence of the response functions. The binning was chosen to be $0.1\,(\mathrm{GeV/c})^2$ wide bins in Q^2, with 100 MeV bins in W and six bins in $\cos\theta_K$. These results are shown in Figures 4.9-4.13 for particular $\cos\theta_K$ bins of interest for the Λ cross-section, and Figures 4.15-4.19 for the same $\cos\theta_K$ bins for the K^+ Σ^0 hyperon final state. To check the previously mentioned results, which used $0.4\,(\mathrm{GeV/c})^2$ bins in Q^2, overplotted are the values extracted from the widest Q^2 bins.

The two binning schemes presented were compatible, producing consist values for the response functions. In addition, the model used to calculate the correction factors matched well the shape of the Q^2 dependence, if not the absolute magnitude.

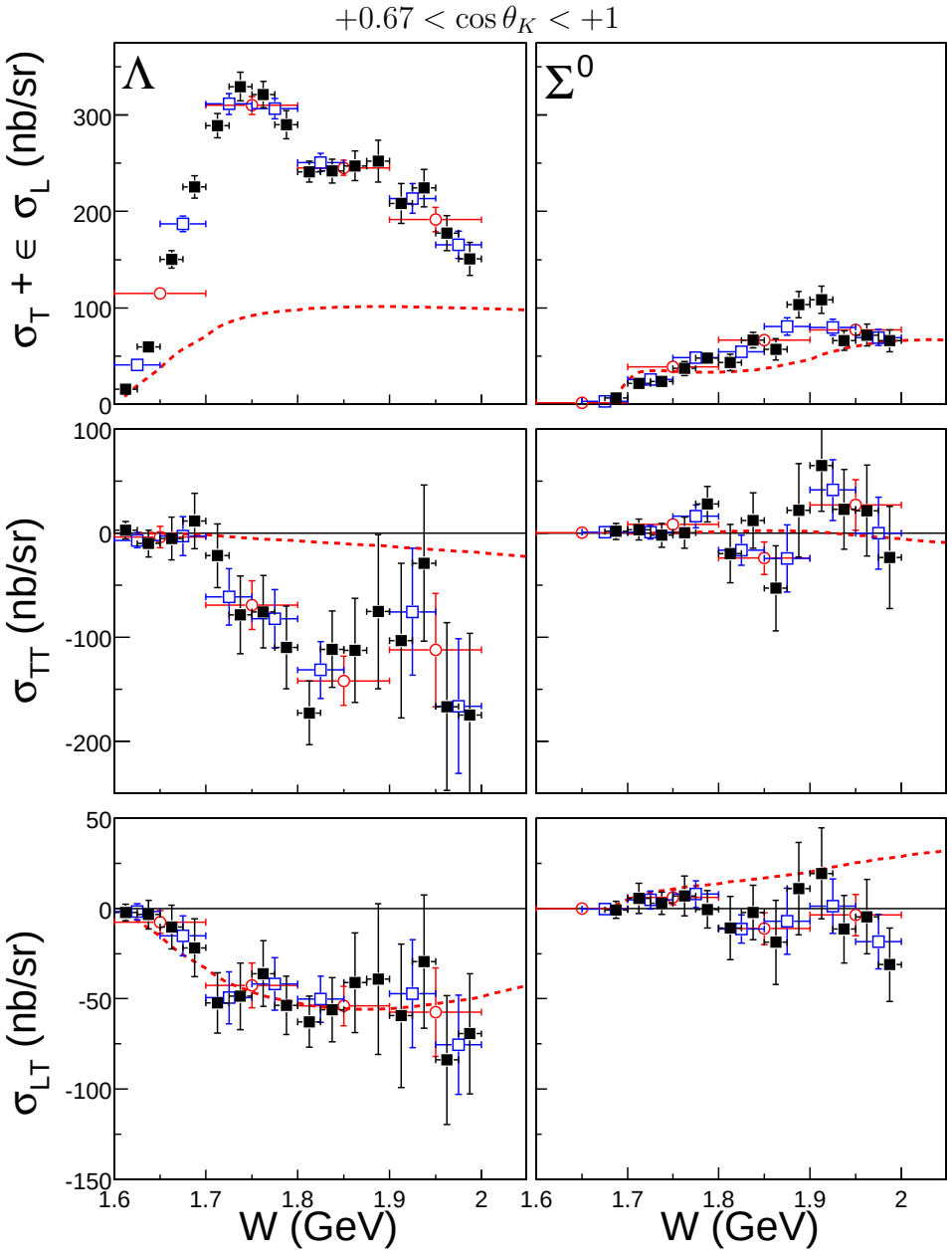

Figure 4.3: The response functions versus W for Λ and Σ^0 electroproduction in the left and right columns, respectively, across $0.67 < \cos\theta_K < 1$ and $0.5 < Q^2 < 0.9\,(\mathrm{GeV/c})^2$. Results for W binnings of 25 MeV (■), 50 MeV (□), and 100 MeV (○) are shown, as well as the results for the WJC calculation of the differential cross-section (red, dashed curve).

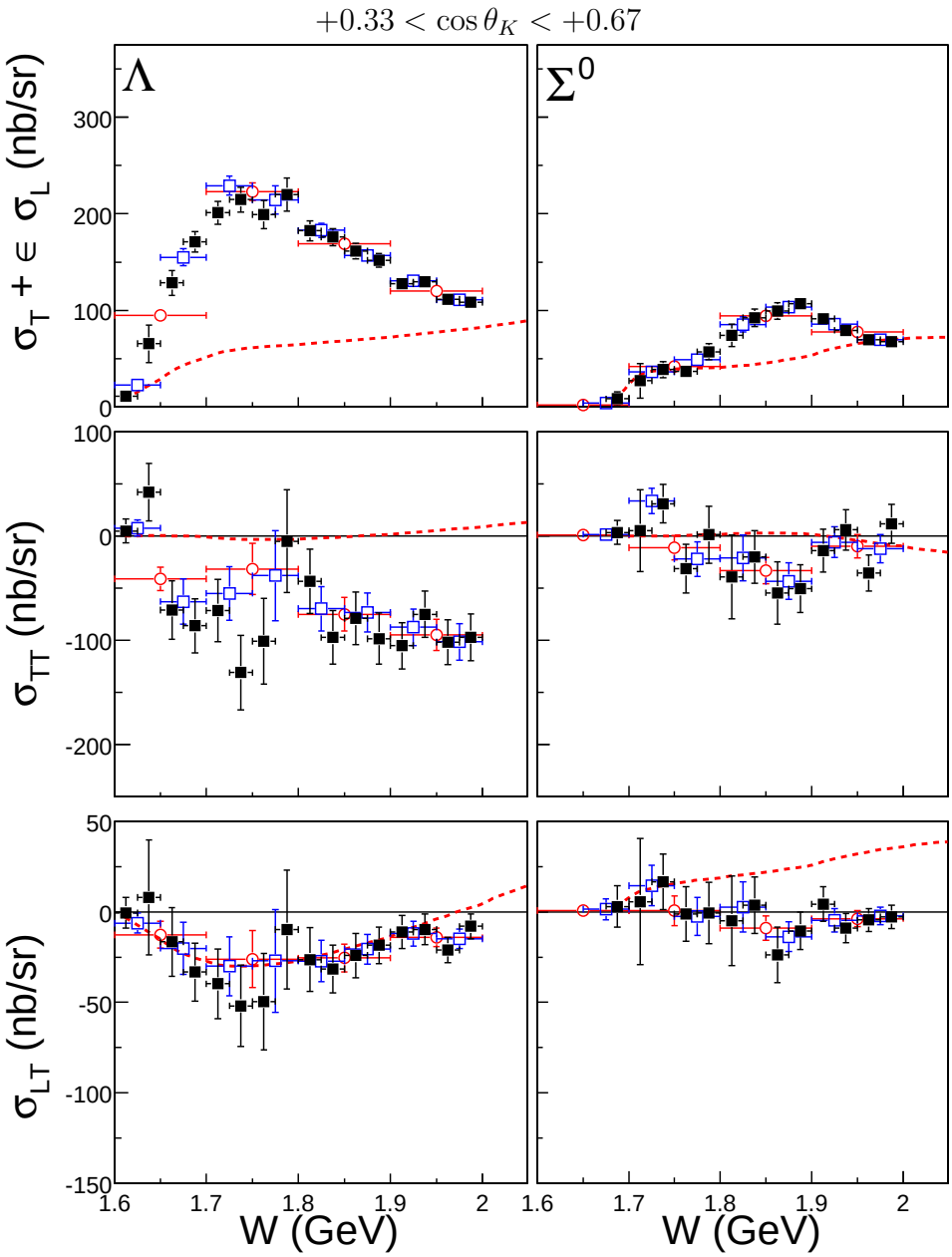

Figure 4.4: The response functions versus W for Λ and Σ^0 electroproduction in the left and right columns, respectively, across $0.33 < \cos\theta_K < 0.67$ and $0.5 < Q^2 < 0.9\,(\mathrm{GeV/c})^2$. Results for W binnings of 25 MeV (■), 50 MeV (□), and 100 MeV (○) are shown, as well as the calculation by the WJC model of the differential cross-section (red, dashed curve).

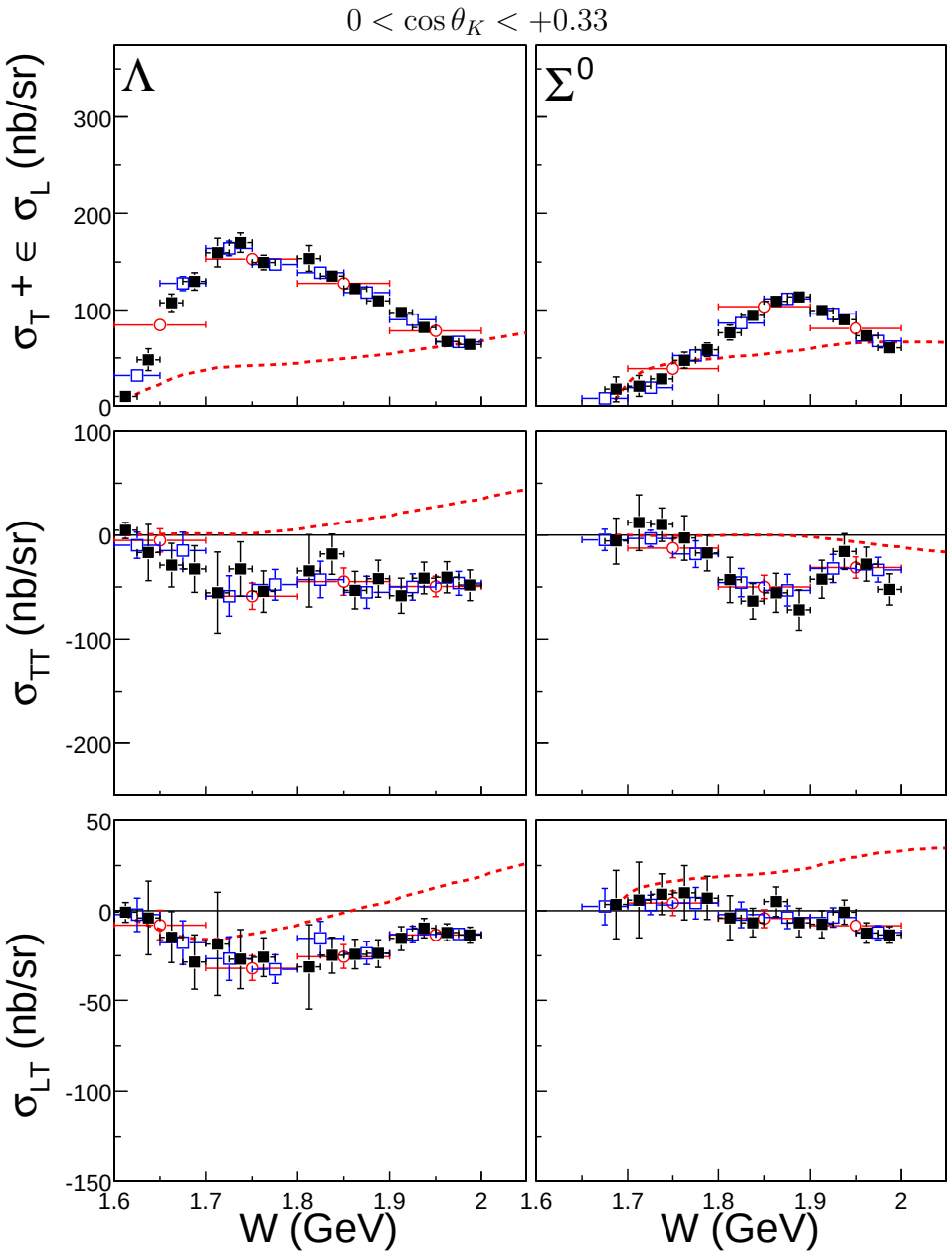

Figure 4.5: The response functions versus W for Λ and Σ^0 electroproduction in the left and right columns, respectively, across $0 < \cos\theta_K < 0.33$ and $0.5 < Q^2 < 0.9\,(\mathrm{GeV/c})^2$. Results for W binnings of 25 MeV (■), 50 MeV (□), and 100 MeV (○) are shown, as well as the calculation by the WJC model of the differential cross-section (red, dashed curve).

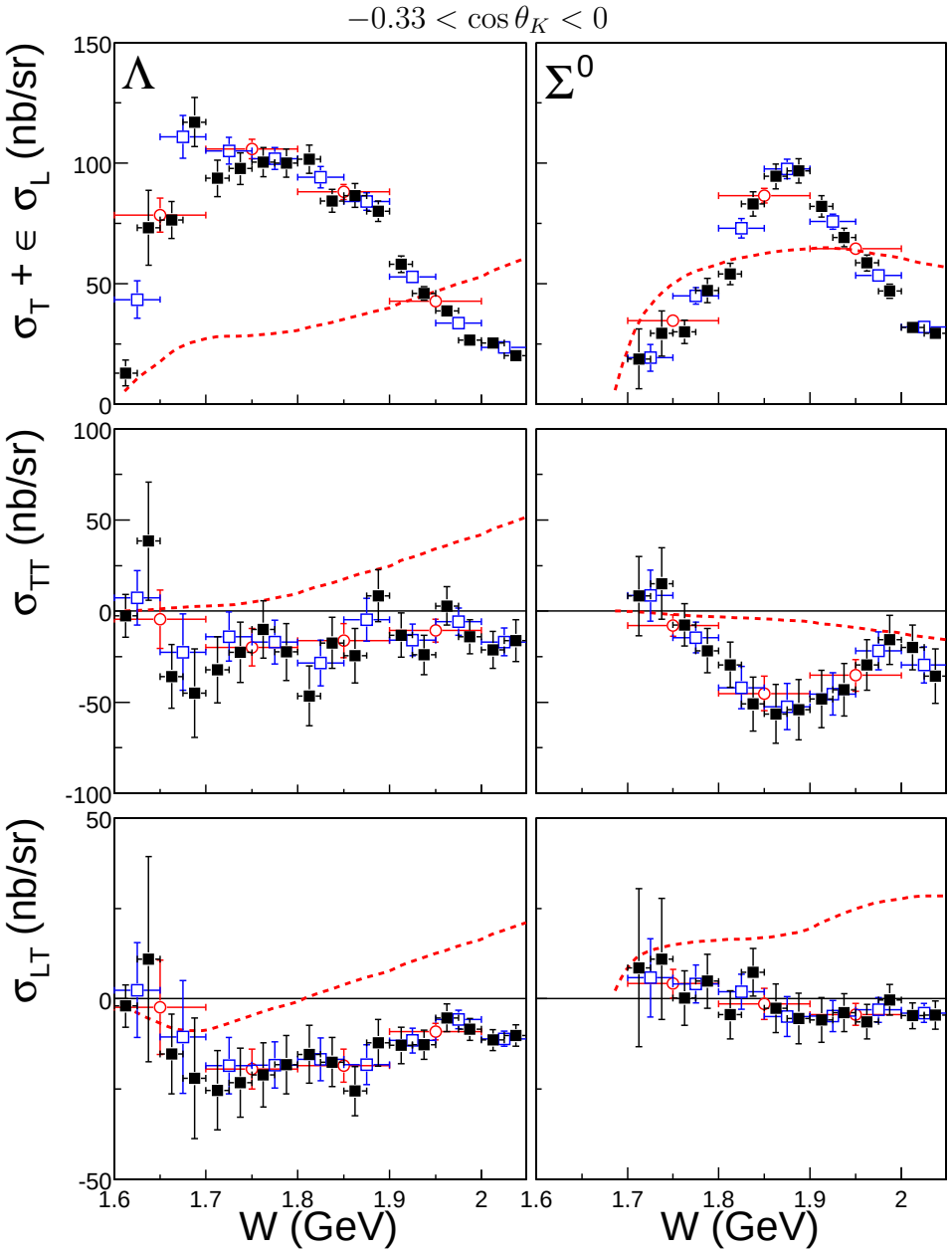

Figure 4.6: The response functions versus W for Λ and Σ^0 electroproduction in the left and right columns, respectively, across $-0.33 < \cos\theta_K < 0.$ and $0.5 < Q^2 < 0.9\,(\mathrm{GeV/c})^2$. Results for W binnings of 25 MeV (■), 50 MeV (□), and 100 MeV (○) are shown, as well as the calculation by the WJC model of the differential cross-section (red, dashed curve).

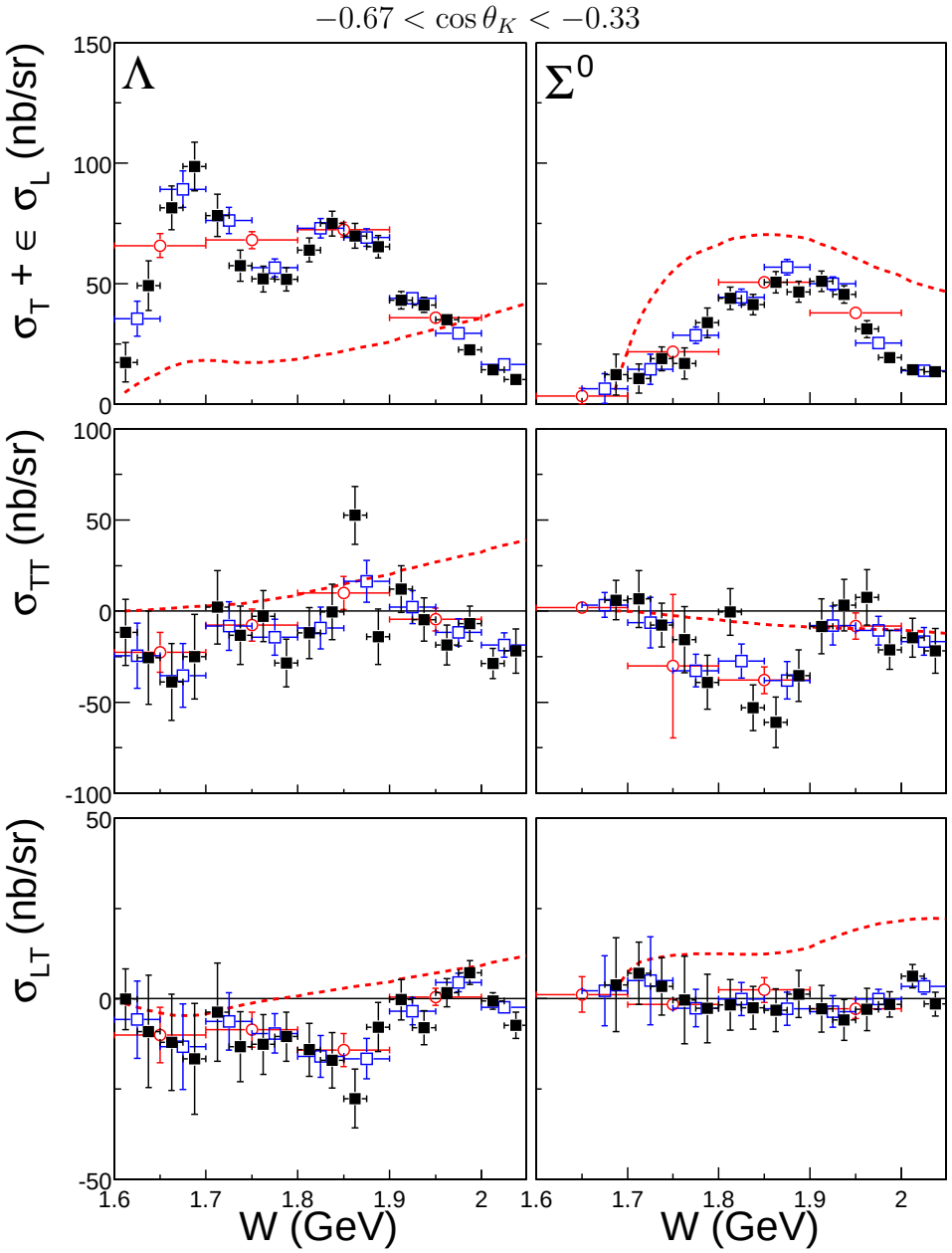

Figure 4.7: The response functions versus W for Λ and Σ^0 electroproduction in the left and right columns, respectively, across $-0.67 < \cos\theta_K < -0.33$ and $0.5 < Q^2 < 0.9\,(\mathrm{GeV/c})^2$. Results for W binnings of 25 MeV (■), 50 MeV (□), and 100 MeV (○) are shown, as well as the calculation by the WJC model of the differential cross-section (red, dashed curve).

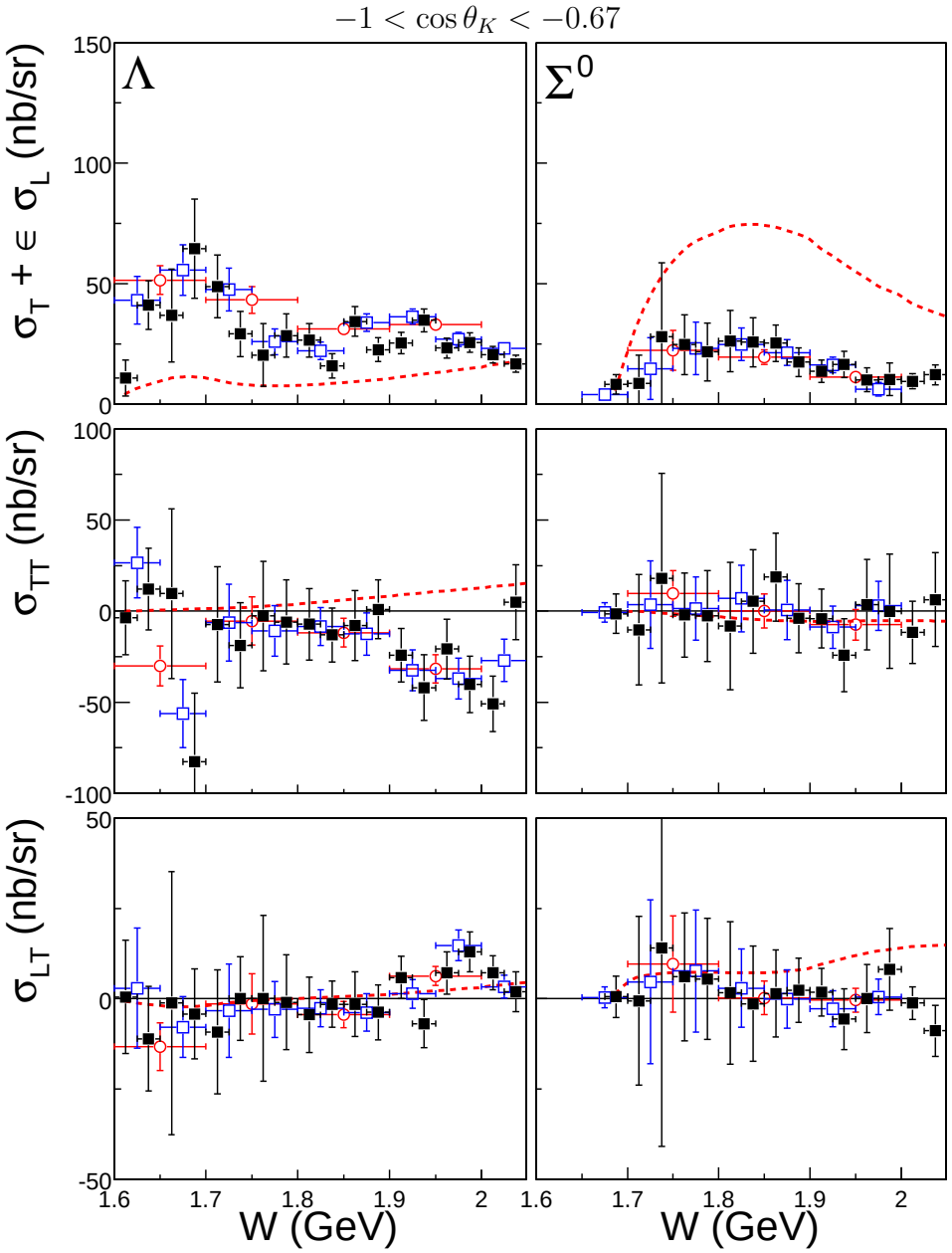

Figure 4.8: The response functions versus W for Λ and Σ^0 electroproduction in the left and right columns, respectively, across $-1 < \cos\theta_K < -0.67$ and $0.5 < Q^2 < 0.9\,(\mathrm{GeV/c})^2$. Results for W binnings of 25 MeV (■), 50 MeV (□), and 100 MeV (○) are shown, as well as the calculation by the WJC model of the differential cross-section (red, dashed curve).

Both the model and data also showed very little action in the interference terms as a function of Q^2. Overall, the variation of the response functions with Q^2 were well under control.

4.4 Evaluation of Systematic Uncertainties

We believed that the extraction of the hyperon yield was the most problematic portion of the analysis, since the quality of a fit often depended upon having sufficient statistics. The different binnings of the data, as mentioned above, were performed as a check of the fitting technique. Overall, the finely-binned and coarsely binned results matched remarkably well.

Unless otherwise noted, the tests were performed with the combined 2.5 GeV, 1500A and 2250A datasets, and the difference between our "best" results and the systematic trial were collected.

4.4.1 Testing Procedures

In general, a cross-section has the form

$$\sigma = \frac{N}{\eta} \tag{4.1}$$

where N is the number of counts in a bin, and η is a correction factor, including all acceptance and normalization factors. The uncertainty of σ is then:

$$(\delta\sigma)^2 = \left(\frac{\delta N}{\eta}\right)^2 + \left(\frac{N}{\eta}\right)^2 \left(\frac{\delta\eta}{\eta}\right)^2 \tag{4.2}$$

$$= \frac{\sigma}{\eta} + \sigma^2 \left(\frac{\delta\eta}{\eta}\right)^2 \tag{4.3}$$

where we have made the normal assumption that $(\delta N)^2 = N$. In testing only the statistical variation of the cross-section based upon the selection of events, we are not interested in the $\delta\eta/\eta$ term, and so use simply $(\delta\sigma)^2 \approx \sigma/\eta$.

To test the effects of different procedures and cuts, a reference set (R) and a trial set (T) were defined, and their difference ($D = R - T$) was examined. When the test tightened a cut made upon the data, the set of trial events was a subset of the original reference set of events. Since all the procedures followed were the same the two sets of results were highly correlated. We then had

$$N_R = N_T + N_X \tag{4.4}$$

where N_R and N_T were the number of events in sets R and T, respectively, and N_X was the number of entries excluded by the tighter cuts. Since the two datasets were

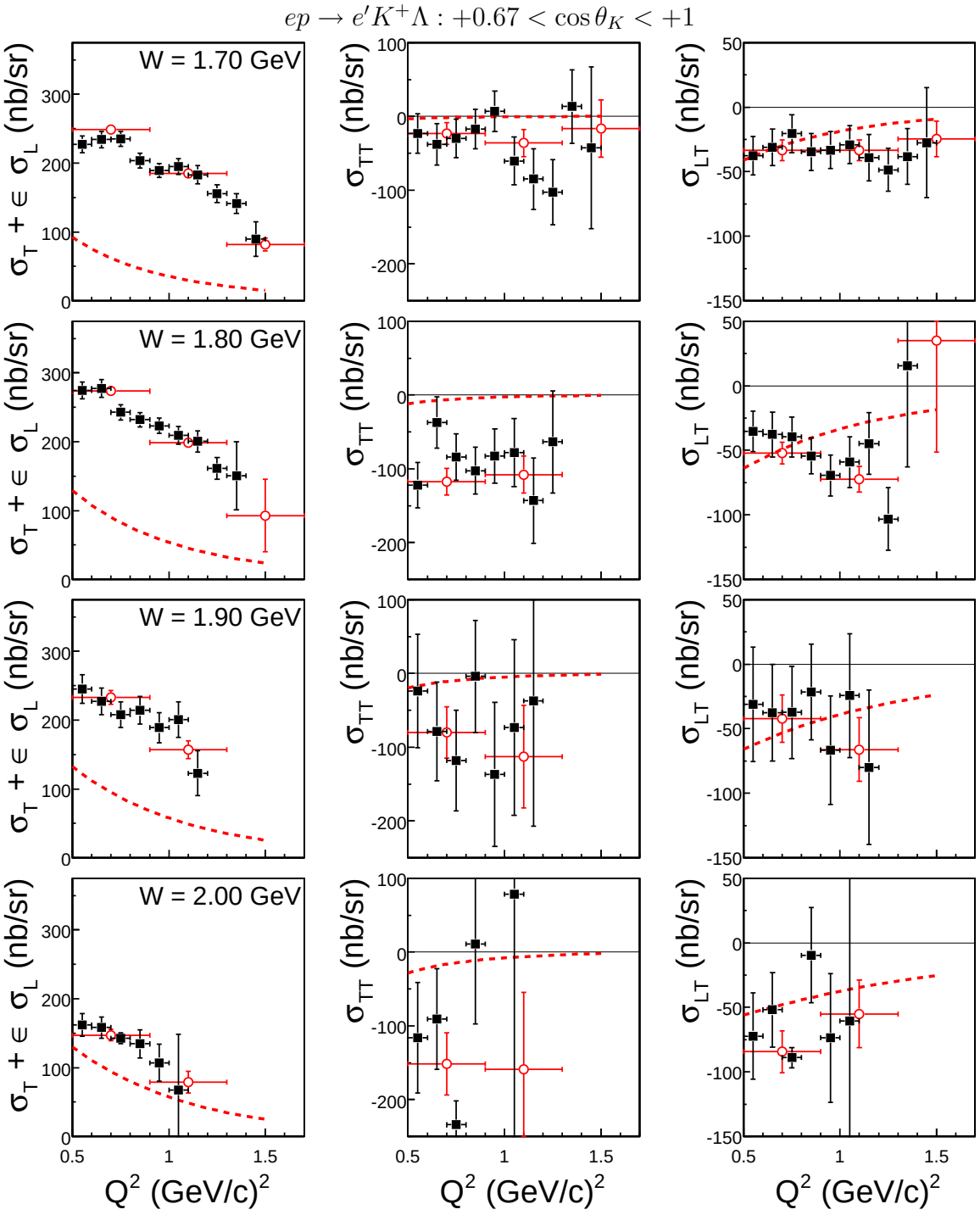

Figure 4.9: The response functions of Λ electroproduction versus Q^2 for $0.67 < \cos\theta_K < 1$, and 100 MeV wide bins in W. Two binnings are shown: δQ^2 =0.1 (■) and 0.4 (GeV/c)^2 (○). The WJC calculation of the differential cross-section is also shown (red, dashed curve).

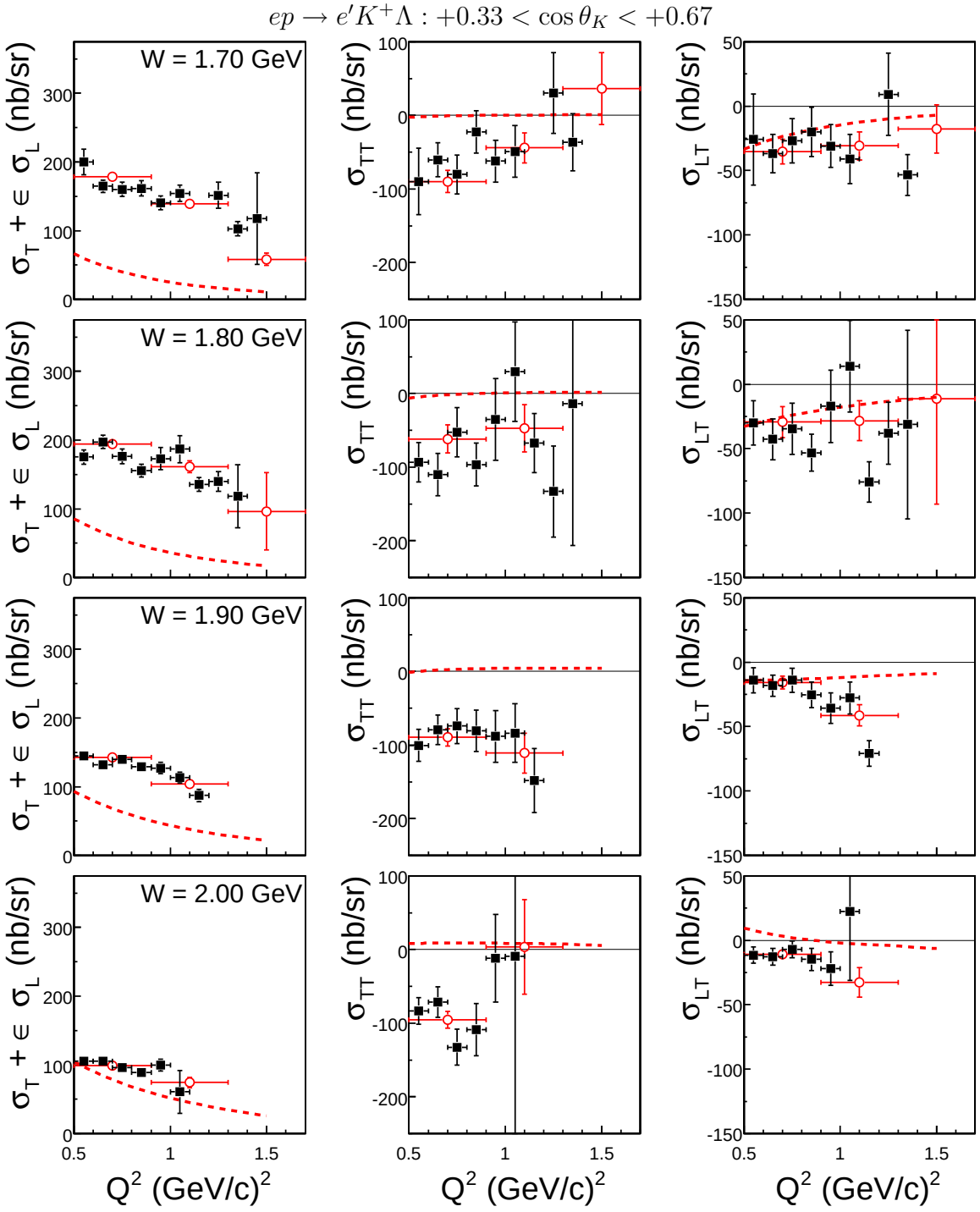

Figure 4.10: The response functions of Λ electroproduction versus Q^2 for $0.33 < \cos\theta_K < 0.67$ and 100 MeV wide bins in W. Two binnings are shown: δQ^2 =0.1 (■) and 0.4 (GeV/c)^2 (○). The WJC calculation of the differential cross-section is also shown (red, dashed curve).

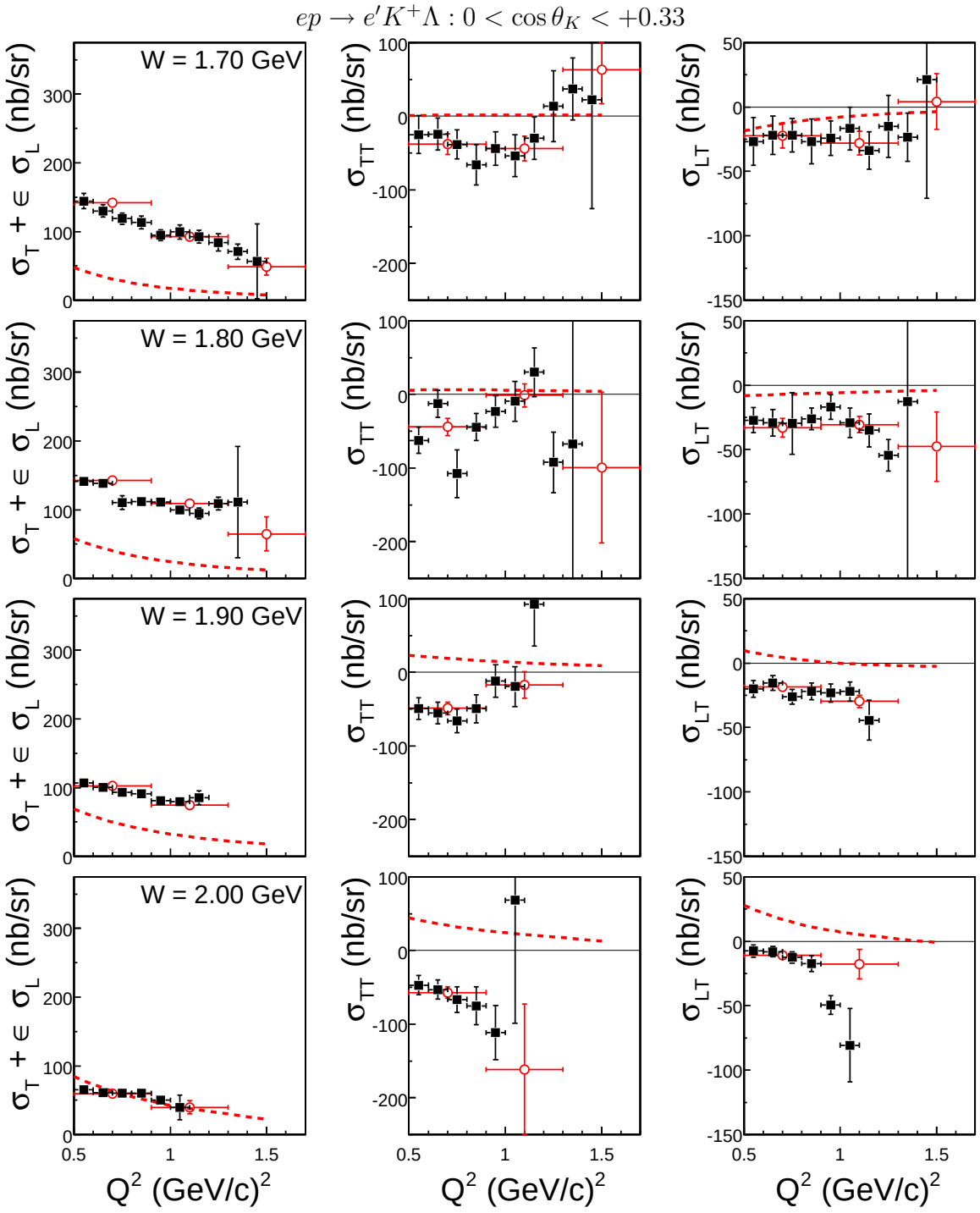

Figure 4.11: The response functions of Λ electroproduction versus Q^2 for $0 < \cos\theta_K < 0.33$ and 100 MeV wide bins in W. Two binnings are shown: δQ^2 =0.1 (■) and 0.4 (GeV/c)^2 (○). The WJC calculation of the differential cross-section is also shown (red, dashed curve).

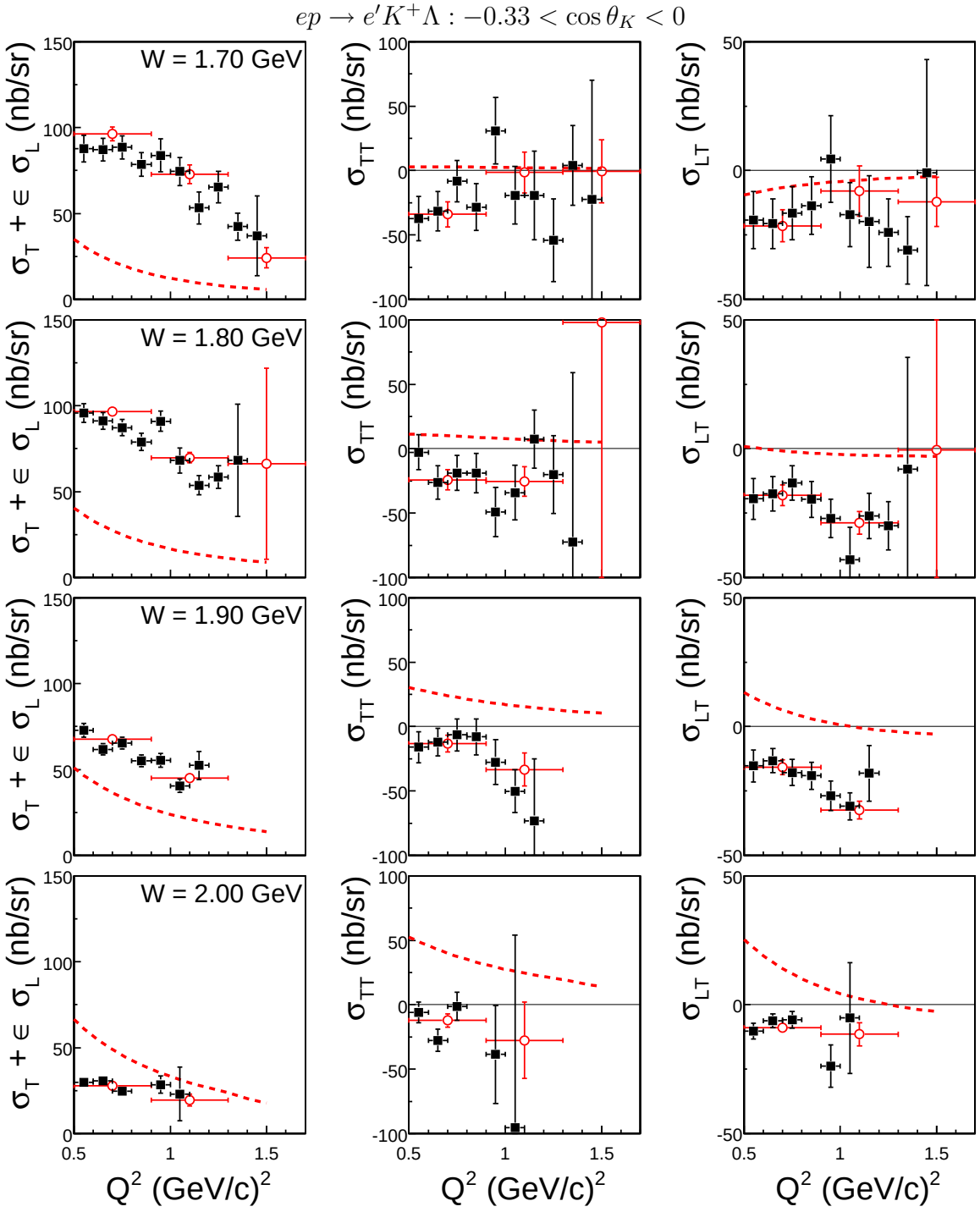

Figure 4.12: The response functions of Λ electroproduction versus Q^2 for $-0.33 < \cos\theta_K < 0$ and 100 MeV wide bins in W. Two binnings are shown: δQ^2 =0.1 (■) and 0.4 (GeV/c)^2 (○). The WJC calculation of the differential cross-section is also shown (red, dashed curve).

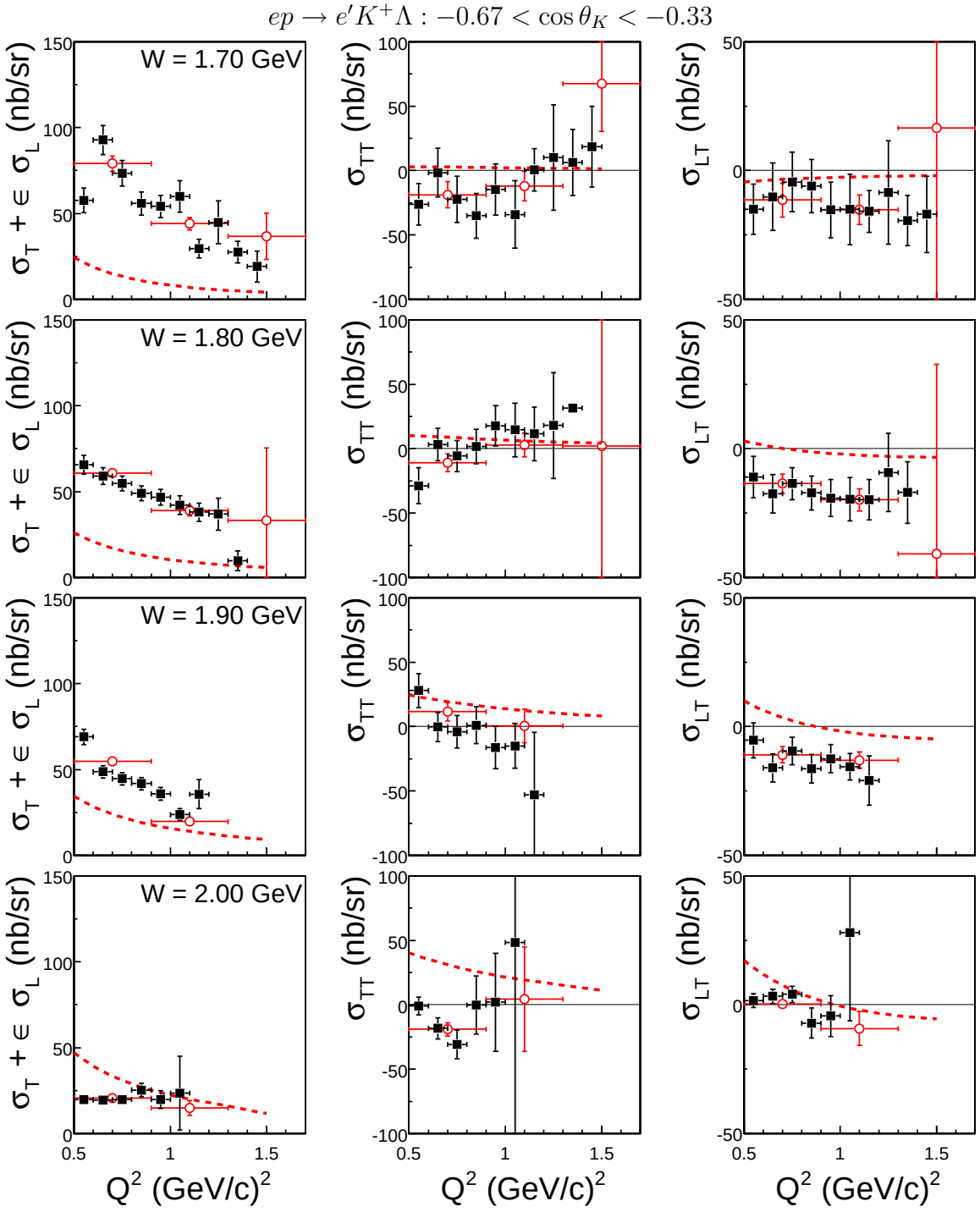

Figure 4.13: The response functions of Λ electroproduction versus Q^2 for $-0.67 < \cos\theta_K < -0.33$ and 100 MeV wide bins in W. Two binnings are shown: δQ^2 =0.1 (■) and 0.4 (GeV/c)^2 (○). The WJC calculation of the differential cross-section is also shown (red, dashed curve).

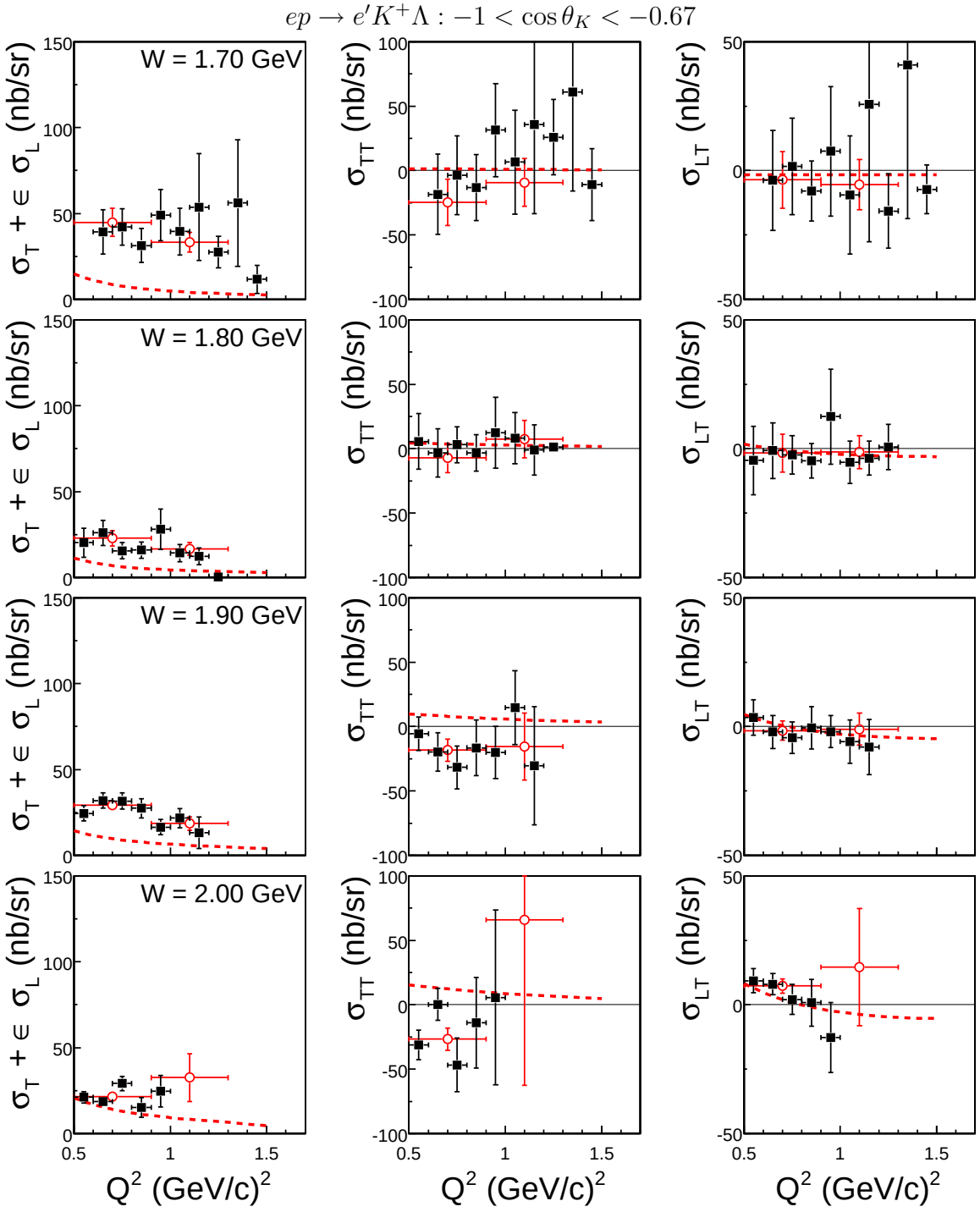

Figure 4.14: The response functions of Λ electroproduction versus Q^2 for $-1 < \cos\theta_K < -0.67$ and 100 MeV wide bins in W. Two binnings are shown: δQ^2 =0.1 (■) and 0.4 (GeV/c)^2 (○). The WJC calculation of the differential cross-section is also shown (red, dashed curve).

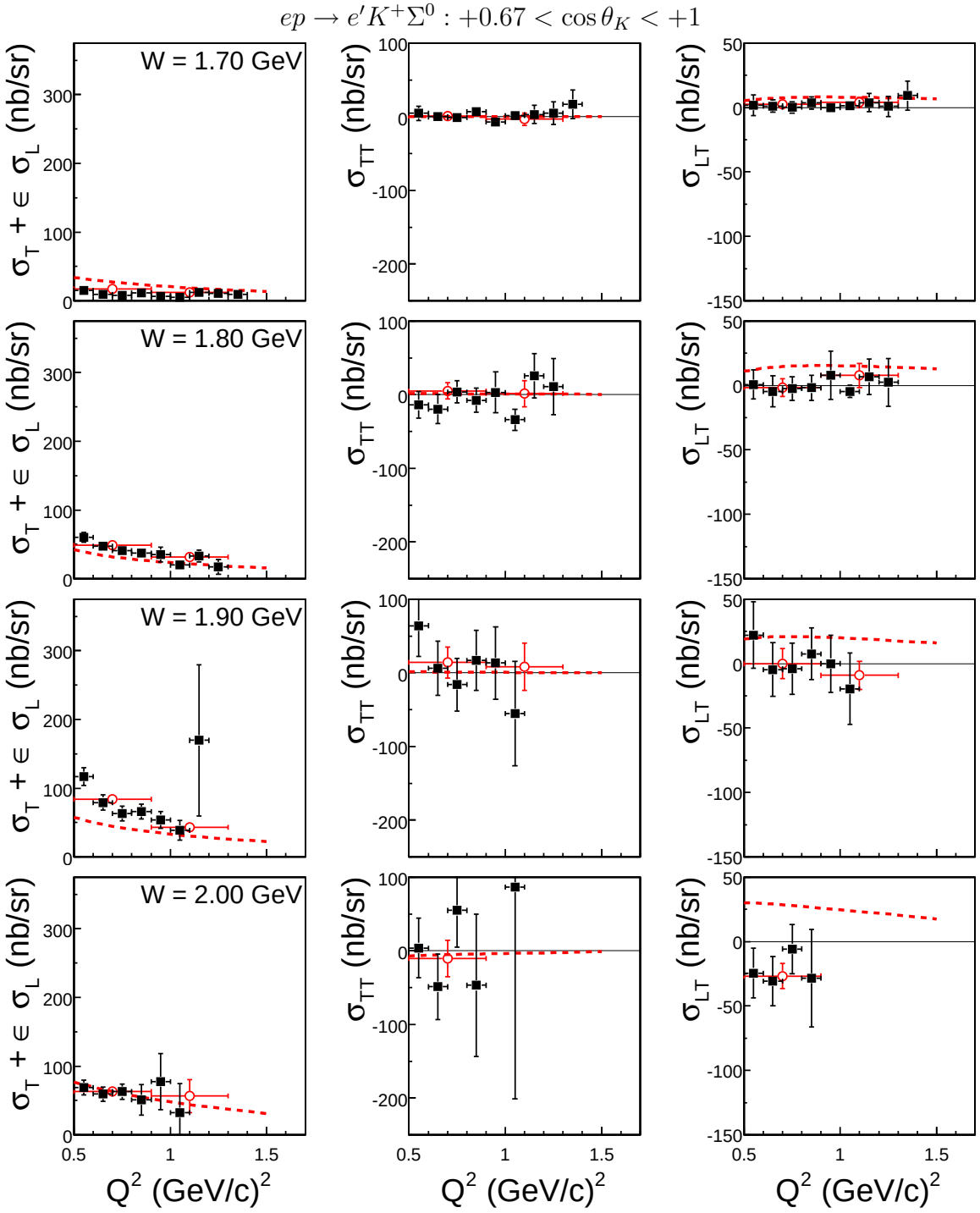

Figure 4.15: The response functions of Σ^0 electroproduction versus Q^2 for $0.67 < \cos\theta_K < 1$ and 100 MeV wide bins in W. Two binnings are shown: δQ^2 =0.1 (■) and 0.4 (GeV/c)^2 (○). The WJC calculation of the differential cross-section is also shown (red, dashed curve).

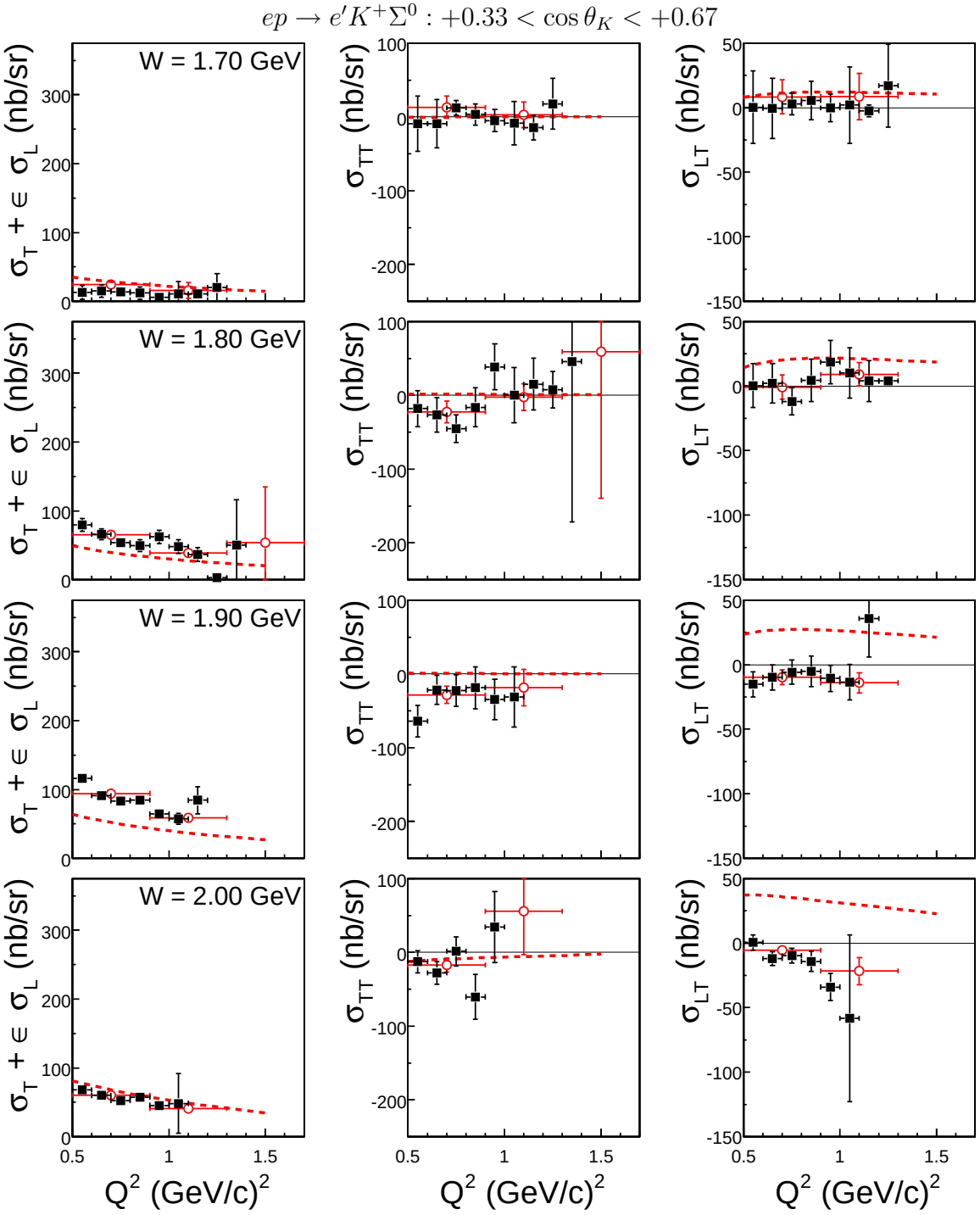

Figure 4.16: The response functions of Σ^0 electroproduction versus Q^2 for $0.33 < \cos\theta_K < 0.67$ and 100 MeV wide bins in W. Two binnings are shown: δQ^2 =0.1 (■) and 0.4 (GeV/c)^2 (○). The WJC calculation of the differential cross-section is also shown (red, dashed curve).

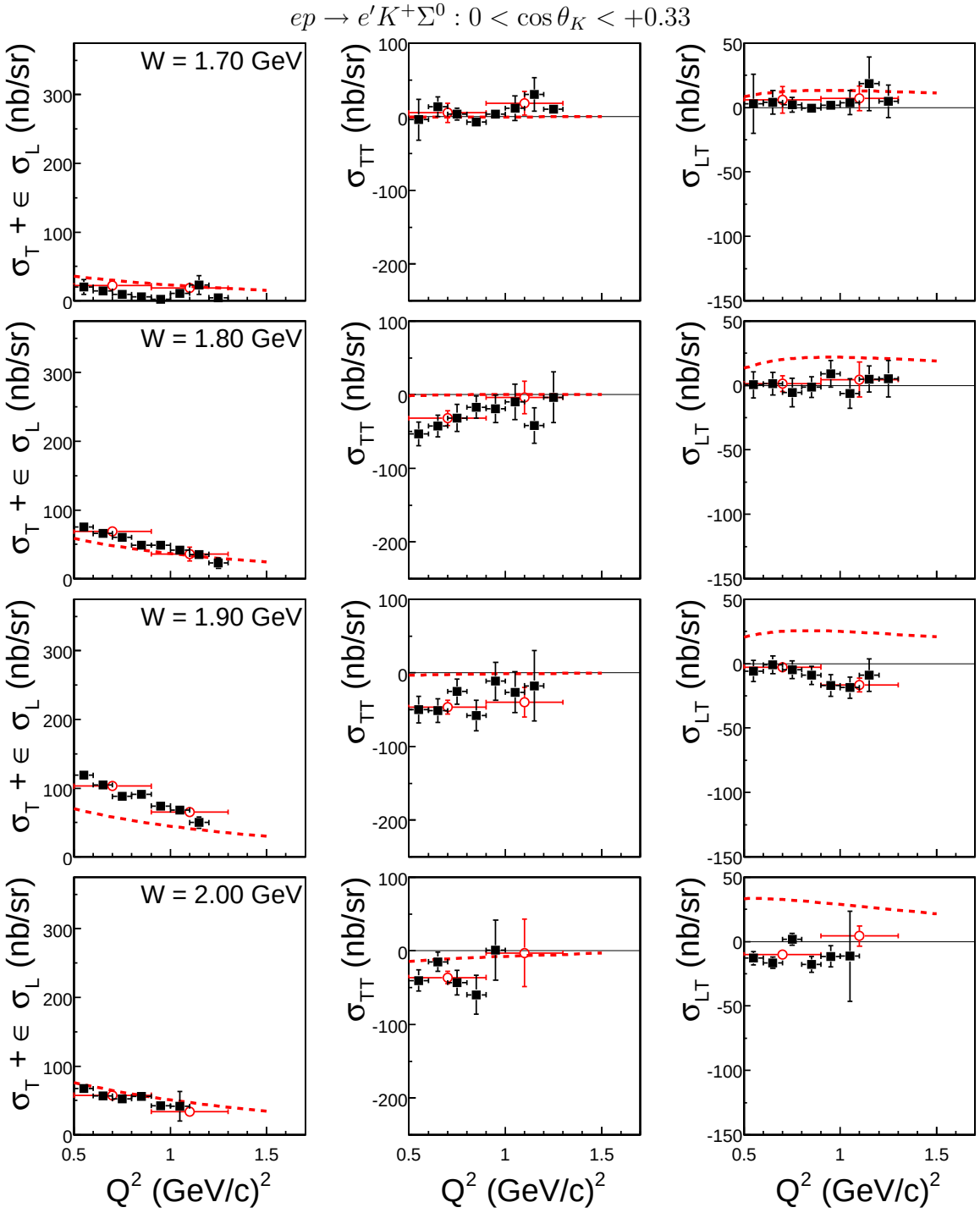

Figure 4.17: The response functions of Σ^0 electroproduction versus Q^2 for $0 < \cos\theta_K < 0.33$ and 100 MeV wide bins in W. Two binnings are shown: δQ^2 =0.1 (■) and 0.4 (GeV/c)^2 (○). The WJC calculation of the differential cross-section is also shown (red, dashed curve).

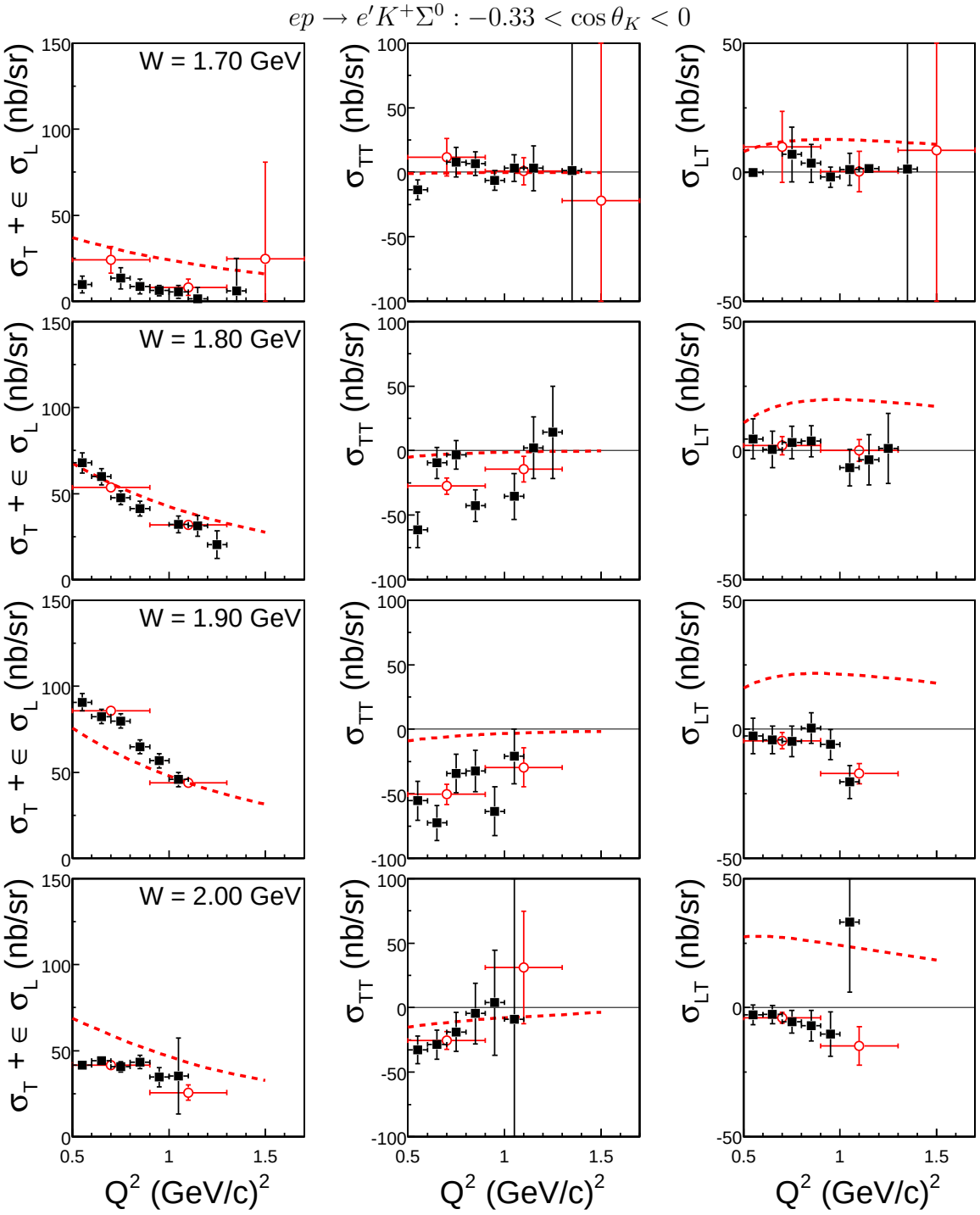

Figure 4.18: The response functions of Σ^0 electroproduction versus Q^2 for $-0.33 < \cos\theta_K < 0$ and 100 MeV wide bins in W. Two binnings are shown: δQ^2 =0.1 (■) and 0.4 (GeV/c)^2 (○). The WJC calculation of the differential cross-section is also shown (red, dashed curve).

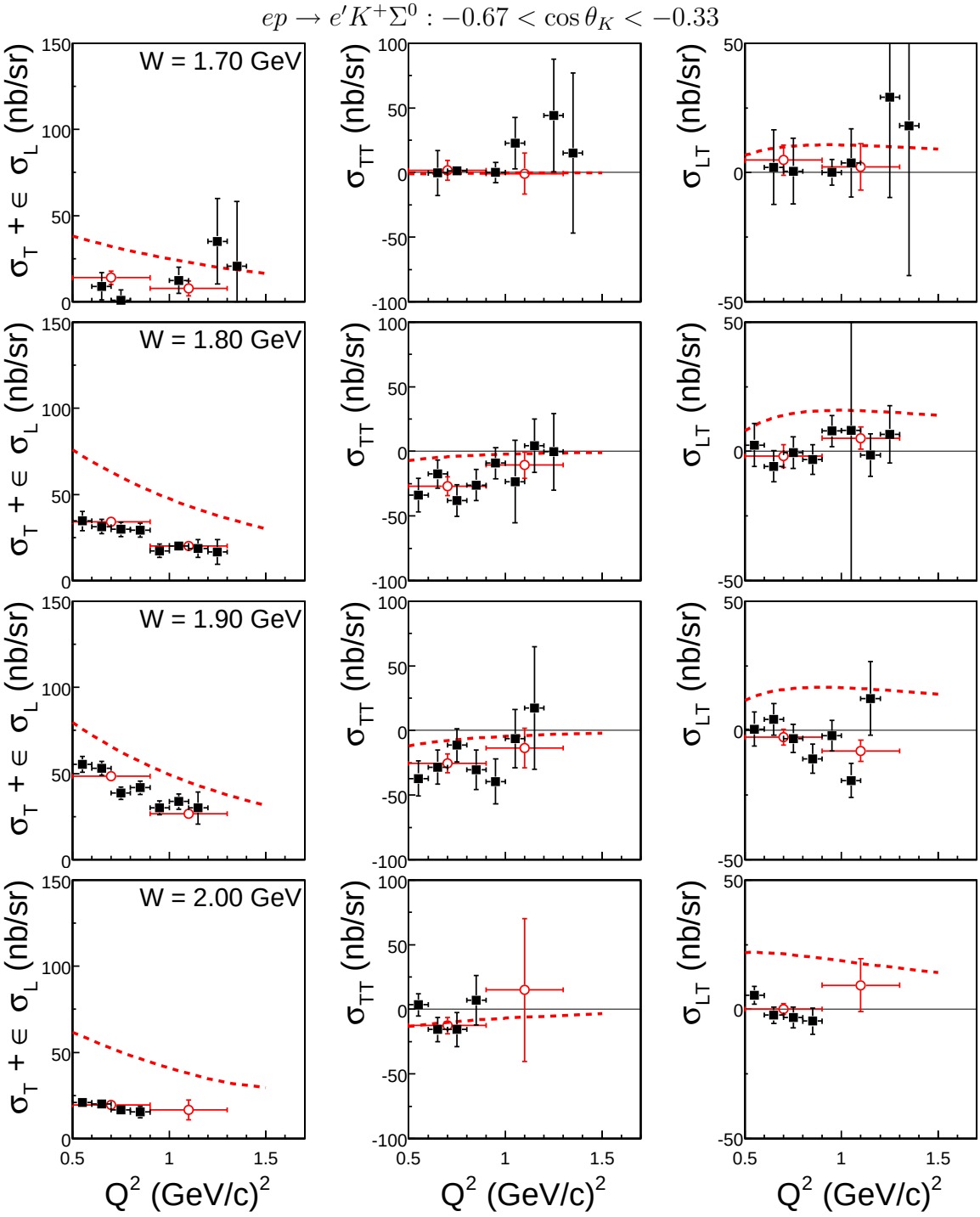

Figure 4.19: The response functions of Σ^0 electroproduction versus Q^2 for $-0.67 < \cos\theta_K < -0.33$ and 100 MeV wide bins in W. Two binnings are shown: δQ^2 =0.1 (■) and 0.4 (GeV/c)^2 (○). The WJC calculation of the differential cross-section is also shown (red, dashed curve).

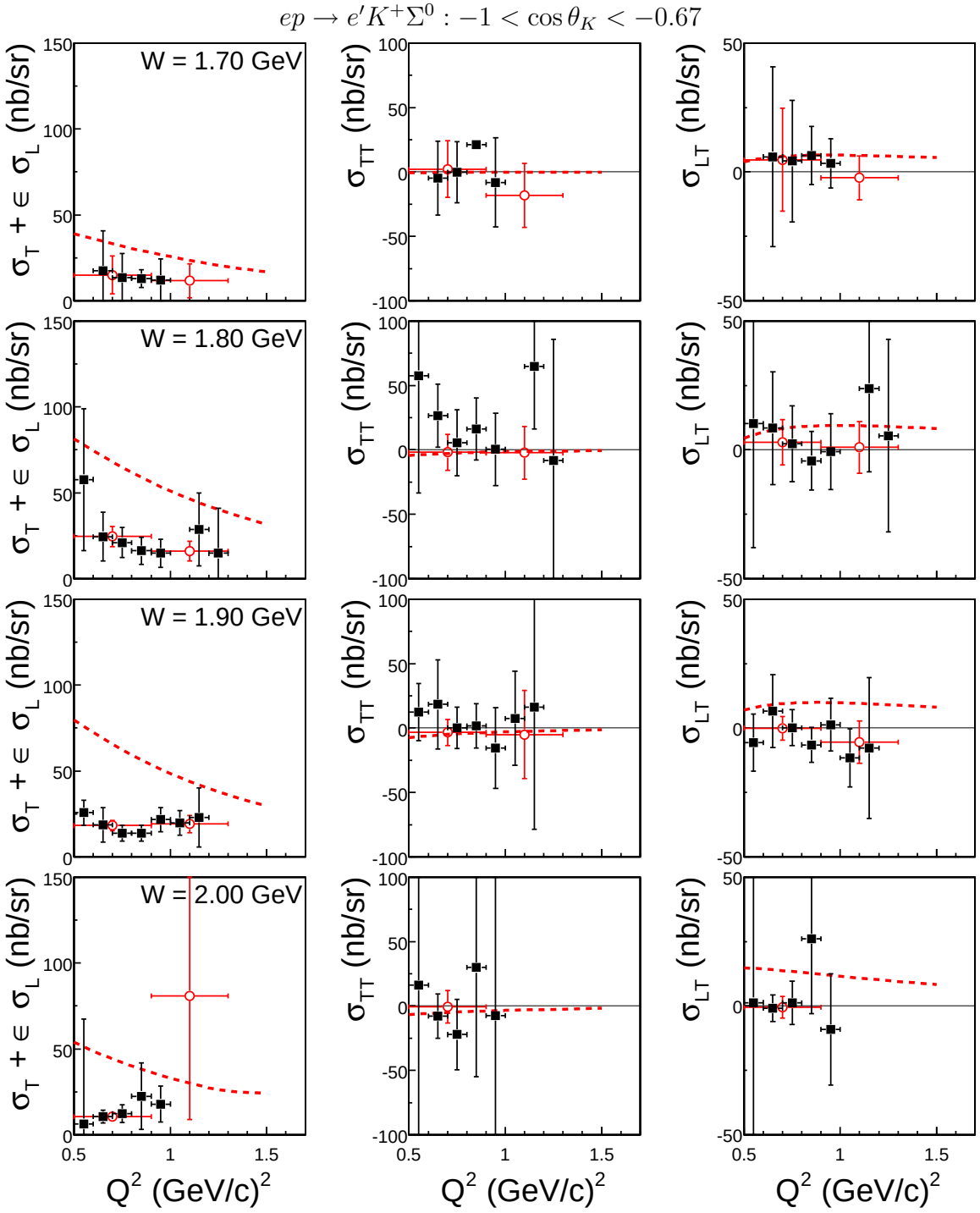

Figure 4.20: The response functions of Σ^0 electroproduction versus Q^2 for $-1 < \cos\theta_K < -0.67$ and 100 MeV wide bins in W. Two binnings are shown: δQ^2 =0.1 (■) and 0.4 (GeV/c)^2 (○). The WJC calculation of the differential cross-section is also shown (red, dashed curve).

so highly correlated, the "normally" computed uncertainty would be an over-estimate of the permitted variation. Instead, the difference $D = (\sigma_R - \sigma_T)$ and its variance $\delta D^2 = [\delta(\sigma_R - \sigma_T)]^2$ between the two datasets was compared. Re-written in terms of the two independently varying quantities, N_T and N_X, the difference was:

$$D = \sigma_R - \sigma_T = \frac{N_R}{\eta_R} - \frac{N_T}{\eta_T} \tag{4.5}$$

$$= \frac{1}{\eta_R}\left(N_X + N_T\left(1 - \frac{\eta_R}{\eta_T}\right)\right). \tag{4.6}$$

The expected statistical variance of D was then:

$$\delta D^2 = [\delta(\sigma_R - \sigma_T)]^2 \tag{4.7}$$

$$= \frac{1}{\eta_R^2}\left[\delta N_X^2 + \delta N_T^2\left(1 - \frac{\eta_R}{\eta_T}\right)^2\right] + \text{non-statistical terms} \tag{4.8}$$

$$\approx \frac{1}{\eta_R^2}\left[(N_X + N_T) - 2N_T\frac{\eta_R}{\eta_T} + N_T\left(\frac{\eta_R}{\eta_T}\right)^2\right] \tag{4.9}$$

$$\approx \frac{\sigma_R}{\eta_R} - 2\frac{\sigma_T}{\eta_R} + \frac{\sigma_T}{\eta_T} \tag{4.10}$$

$$\delta D^2 \approx (\delta\sigma_R)^2 + (\delta\sigma_T)^2 - 2\frac{\sigma_T}{\sigma_R}(\delta\sigma_R)^2. \tag{4.11}$$

In the limiting case where the results from the two data samples were equal, $\sigma_R = \sigma_T$, the permitted statistical variation was just the more intuitive [68]:

$$\delta D^2 = (\delta\sigma_T)^2 - (\delta\sigma_R)^2. \tag{4.12}$$

The distributions of D and δD were then evaluated to test the consistency of the results from the trial and reference sets, by summing over the n data-points and creating a χ^2 function of the form

$$\chi^2 = \sum_{i=1}^{n} \frac{(D_i - C)^2}{\delta D^2 + A^2} \tag{4.13}$$

where C was simply a constant offset shared by all bins. The added A term was varied until $\chi^2/(n-1) \approx 1$. If the difference between the trial and reference results, D, was independent of the kinematics of a given bin, then the estimated systematic uncertainty is shared equally by all bins, and is

$$\delta Sys^2 = A^2 + C^2. \tag{4.14}$$

For these tests, each (W, Q^2, $\cos\theta_K$, ϕ_K) bin was included when evaluating Equation 4.13.

4.4.2 Hyperon Yield

In fitting the missing mass distributions on a bin-by-bin basis we expected some sensitivity of the fit and extracted yield upon the template shape, choice of the background distribution, and number of counts found in the bin.

4.4.2.1 Background Shape

The shape of the background was determined by doing preliminary fits to the missing-mass distributions, summed over various kinematic variables to accommodate for limited statistics. The results of measuring and parameterizing the background shape in three different functional forms have been compared: as a function of the set W, Q^2, θ_K, ϕ_K with poor statistical error bars and fitting probability, W, Q^2, θ_K integrated over ϕ_K, and W, Q^2, ϕ_K with the $\cos\theta_K$ degree of freedom removed. Since the pion-contamination appeared to have the strongest dependence upon the momentum of the kaon candidate and p_K was a function of the set $W, Q^2, \cos\theta_K$, it was decided to use the W, Q^2, θ_K parameterization of the background as the "standard" technique.

While the background-shape parameters were free to vary during the fit, the uncertainties on the hyperon yields reported by the fit included the uncertainty of the background shape. However, after fixing these parameters, this information was lost, and the systematic uncertainty due to the background shape had to be recovered. Since the stability of the fit improved with increased statistics, we wanted to examine the difference between the extracted yields for the unconstrained and W, Q^2, θ_K parameterizations of the background as a function of the statistics in the missing-mass distributions. The relative difference of the cross-sections were then collected in bins of relative statistical uncertainty, and the width of the distributions plotted versus the relative statistical uncertainty. This is shown in Figure 4.21. A correlation between the systematic variance and the statistical error of a point was found, and we used this correlation to parameterize the systematic uncertainty due to the background. In general, the systematic uncertainty of the background was equal to 25% of the statistical error bar reported by the yield extraction fits.

This uncertainty was then incorporated into $(\delta D)^2$ when evaluating Equation 4.13 for each of the subsequent tests, since it denotes the relative stability of the yield extraction fits.

4.4.2.2 Hyperon Peak Shape

We found the initial template widths to be too narrow, so a single additional parameter, Δ, was used to characterize how much wider the observed hyperon peaks were. To test the systematic dependence of the yield extraction upon the choice of Δ, the yield extraction was re-run using other plausible values for Δ: $6\,\mathrm{MeV/c^2}$ and $7\,\mathrm{MeV/c^2}$ for the 2.5 GeV 2250 A and 1500 A datasets, respectively. The value of the parameter Δ had a direct influence upon the magnitude of the cross-section, adjusting

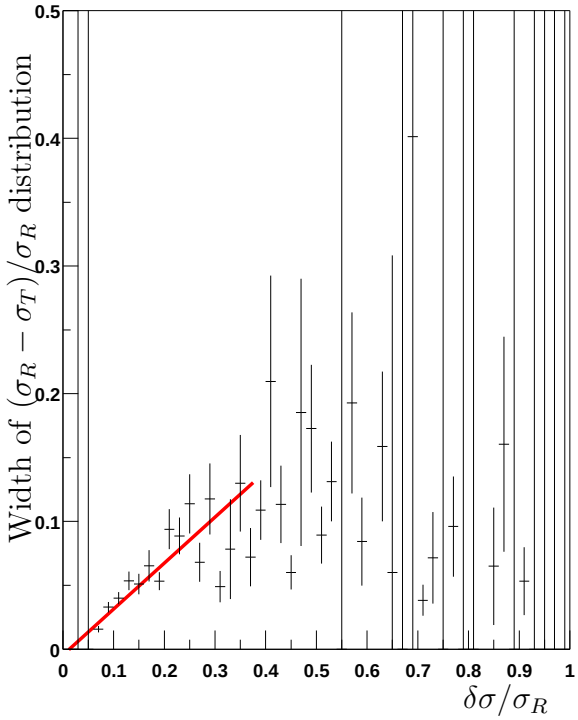

Figure 4.21: A characterization of the relative difference of the cross-sections for variations of the background shape versus the statistical uncertainty, collected from all the $(W, Q^2, \cos\theta_K, \phi_K)$ bins. A correlation between the systematic and statistical uncertainties is shown.

the scale by 3-5%, but introduced a point-to-point variation at the 2% level. Since it might be argued that the proper value of Δ varies with the kinematics, the scale factor it introduced was included in the final quoted systematic uncertainty.

4.4.3 Acceptance and Efficiency

4.4.3.1 Fiducial Cuts

The dependence of the cross-sections on the kaon fiducial cut was tested by changing the fiducial region from nominal values listed in Section 3.3.2.2. Figures 3.11 and 3.12 show the reference fiducial cut and severe-trial fiducial cut with solid and dashed lines, respectively. The differences were evaluated as correlated measurements according to the method discussed above, and the plot used to evaluate Equation 4.13 is shown in Figure 4.22. The horizontal axis is a linearization of the W, $\cos\theta_K$ and ϕ_K bins for a single large bin in Q^2, numbered as:

$$binnumber = W_{\rm bin} * 6 * 8 + \cos\theta_{K\,\rm bin} * 8 + \phi_{K\,\rm bin}.$$

The Λ and Σ^0 final states were assigned the average of the systematic uncertainty measured separately for each channel, since their acceptances were very similar, with final uncertainties of approximately 2%.

4.4.3.2 Model Dependence

The acceptances for different initial thrown distributions of Λ and Σ^0 were computed using a simple fiducial acceptance model which included kaon decays. For the Λ hyperon, the generated event distribution was varied from the WJC model [6] to one with a W and Q^2 dependence according to the virtual photon flux and flat in $\cos\theta_K$ and ϕ_K. The acceptance was found to vary by 8% on average when computed using the two different event distributions. This was compatible with an estimate [69] of the model dependence of the acceptance when comparing the distributions from the WJC model and a calculation by T.Mart [70], performed with the complete GSIM model of the CLAS detector. The resulting distribution of the ratio of the acceptances can be found in Figure 4.23. Not shown in this plot is the angular dependence of the ratio, which is weak for the mid-range of θ_K, but demonstrates a systematic upward shift of 5% at forward and backward angles.

The Σ^0 acceptance was calculated with events thrown according to the WJC model, and compared to an acceptance calculated with an earlier model, described in Reference [71], which had an angular distribution similar to that observed in this analysis. The variation of the acceptance between the two calculations was found to be approximately 7% and uniform across the kinematic range.

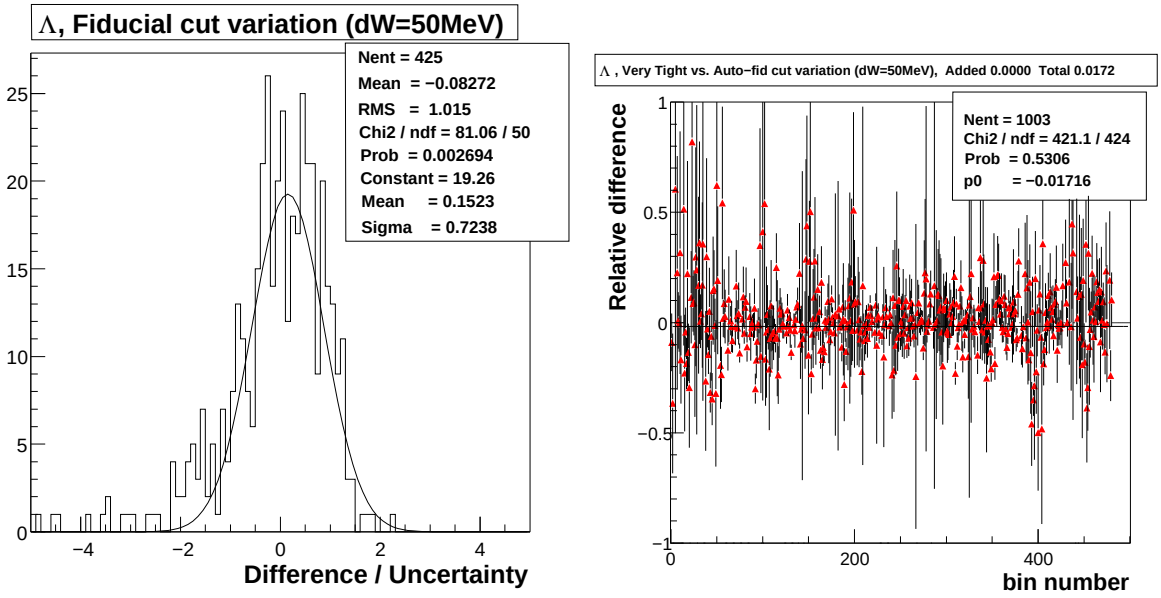

Figure 4.22: An illustration of the method used to determined the systematic uncertainty for the variation of a cut: in this case, the two fiducial cuts. The left panel shows the difference in cross-section measurements normalized to the permitted variance (from Equation. 4.11). In the right panel the relative difference of the cross-section for the variations is shown versus a linearization of the bin. The error bars indicate the permitted variance. See text for further explanation.

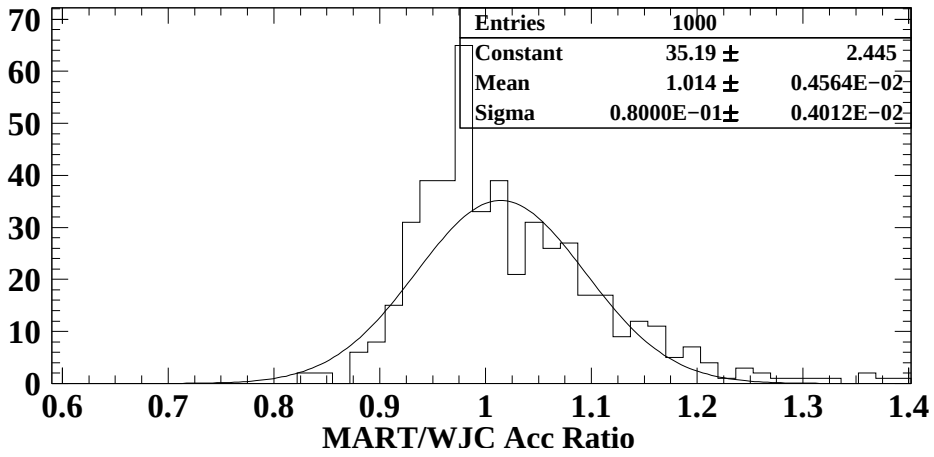

Figure 4.23: A comparison of the acceptances for the $K^+\Lambda$ final state, determined for the 2.5 GeV, 1500 A dataset. The comparison is between the WJC [6] model, which was used to calculate the acceptance correction in detail, and the T.Mart [70] model. The distribution was for a sum over all bins [69].

4.4.3.3 Kaon Identification

While investigating the appropriate timing resolution of the SC paddles for processing Monte Carlo events with GPP, we found that modeling the timing resolution well was critical. As can be seen in Figure 4.24, kaons that decayed had an associated time of flight less than those kaons which did not decay before the TOF paddles. This was because the daughter particles of the kaon decay traveled faster than the kaon, due to the momentum gained from the decay. If the difference of the timing resolution between the data and simulated data was large, then the number of decayed kaons accepted in the real and simulated data would be different, and could affect the cross-section by more than 5%. By matching the timing resolution to better than 3%, this was minimized.

To test the sensitivity to this effect on the final cross-sections, we varied the size of the timing cut, described in Section 3.3.2.2, between 2.5σ and 3.5σ, as opposed to the nominal 3σ. The results differed by less than 1.5%.

4.4.4 Normalization

4.4.4.1 Livetime

The livetime was measured by three different sets of signal generators and gated scalers during the data-taking: a signal from the Faraday cup which ran at approximately 40 Hz, a 10 kHz clock, and the trigger logic. As stated in Section 3.3.10, the clock and trigger-based livetimes were determined to be the more correct measurement and agreed to better than 0.5%.

4.4.4.2 Overall Stability

From looking at Figures 3.17 and 3.18, we see that kaon yield per sector does vary slightly with time. To compute the level of stability for the number of kaons identified per unit luminosity, we examined the kaon yield normalized to the livetime-corrected luminosity on a run-by-run basis, summed over all six sectors. The χ^2 test of Equation 4.13 was used determine the relative stability of the combined Faraday cup and CLAS system for kaon identification. This factor would include the livetime calculation, different target configurations, and the quality of the detector calibrations. The value was determined to be 1.43% for both datasets.

4.4.4.3 Absolute Electron Flux

From the analysis of $e\,p$ elastic scattering [60], the absolute accuracy of the Faraday cup system has been verified to the 3% level.

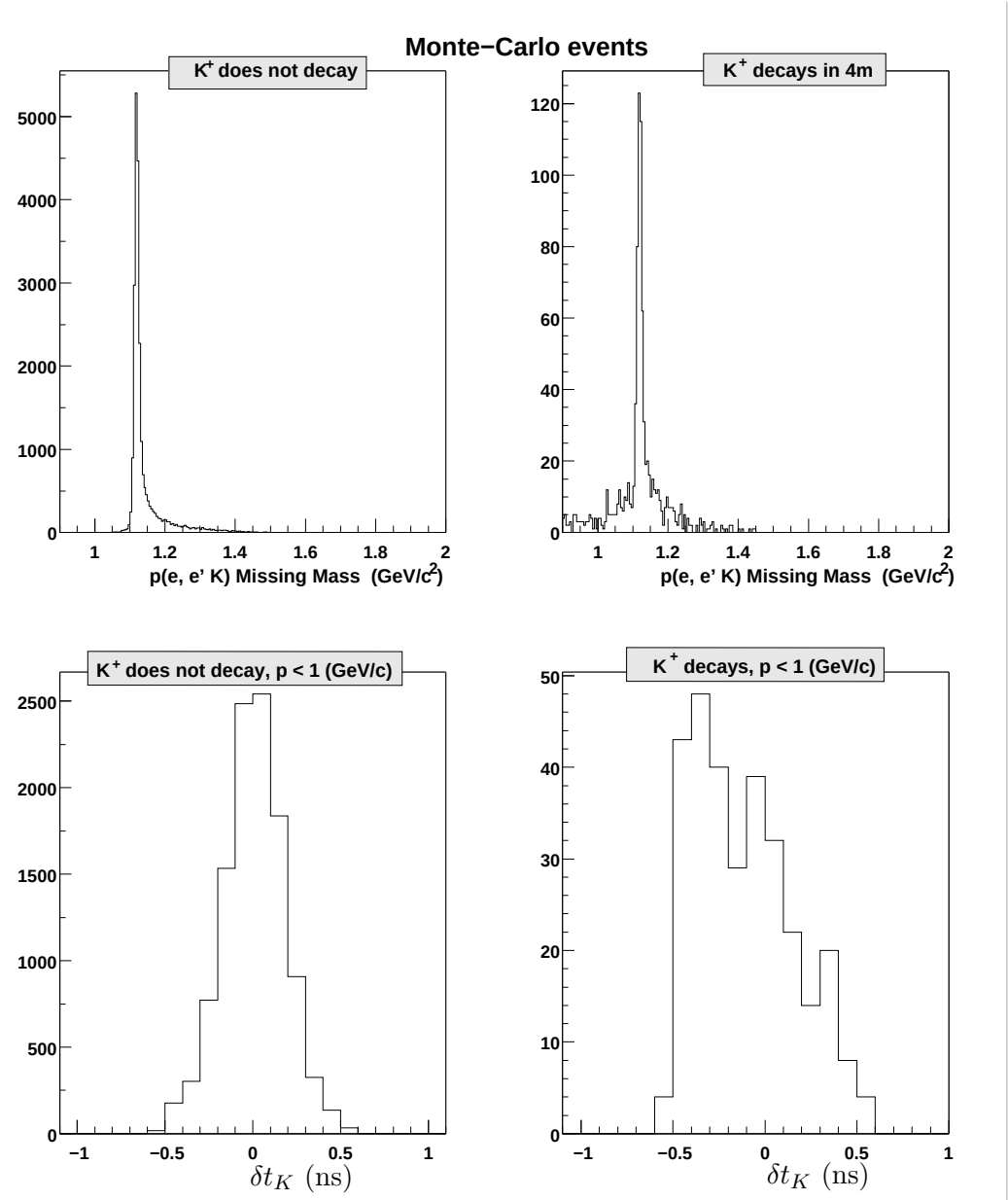

Figure 4.24: The reconstructed missing mass (top) and $\delta t_K = t_K - t_{K\,Ideal}$ (bottom) from simulated GSIM events. The left panels are for kaons that did not decay, and the right for those that did decay within 4 m of the target. Note the skew of the timing distribution for the decayed kaons toward a shorter time-of-flight.

4.4.5 Error Budget

Summaries of the reported contributions to the systematic errors are given in Tables 4.1 and 4.2. On average, the uncertainty on each $(W, Q^2, \cos\theta_K, \phi_K)$ point for each dataset was approximately $15\%(stat) \pm 10\%(sys)$ with a global 3.3% scale uncertainty. After the datasets were combined, the effective uncertainty on each point was approximately 15%. The extraction of $\sigma_T + \epsilon\sigma_L$, σ_{TT} and σ_{LT} included these uncertainties during the fit, and so they are reflected in the error bars of the response functions.

4.4.6 Systematic Checks

4.4.6.1 Results from the Two Magnetic Field Settings

Since the two datasets were taken with different magnetic fields, particles with the same momenta and angles at the target traversed different regions of CLAS, providing a tool to study the degree of uncertainty which the experimental setup could introduce. To evaluate the agreement between the independent datasets, a χ^2 quantity was constructed from the measured cross-sections they had in common. When the narrow W-bin data-sets were combined after the systematic errors have been applied, the resulting χ^2/ν was 1613/2689. If instead the systematic error estimates were *not* added we found χ^2/ν to be 2569/2689. While this means the systematic uncertainty for the yield extraction and acceptance were probably over-estimated, the datasets did agree well within the accepted quoted uncertainties.

4.4.6.2 Results from the ϕ_K-Distribution Fits

After combining the datasets, the fits to the ϕ_K distributions to extract the response functions were performed. For each fit, the resulting χ^2 was kept, and collected according to the number of ϕ_K bins which participated in the fit. The χ^2 distribution for the $(W, Q^2, \cos\theta_K)$ bins where all eight ϕ_K points were present is shown in Figure 4.25. Overplotted on in this figure is also the expected χ^2-distribution for five degrees of freedom. The observed distribution matches the expected shape rather well, with perhaps an overall lower average χ^2 than predicted. This was attributed to the addition of the systematic uncertainties to the cross-sections prior to extracting the response functions.

4.5 Summary

The final results of the analysis have been presented with a discussion of the systematic uncertainties. The results for different binnings and datasets, analyzed completely independently, were quite consistent providing assurance that systematics effects were under control. Statistically, it appeared that the systematic uncertainties

Table 4.1: The estimated systematic errors for the 2.5 GeV, 1500 A dataset. Systematic uncertainties which could cause a point-to-point variation were applied at the ϕ_K-bin level (prior to the ϕ_K fits); those which caused a general scale shift are given at the bottom.

Source of Error	Description of Error; Size of the Effect	Contribution of Uncertainty to Cross-Sections
Yield Extraction	Reported Statistical (fine W binning)	stat: 13-20% (typical)
	Background shape Fixed vs. Constrained	sys: $0.25 * \sigma_{stat}$ (4% typical)
	Hyperon Peak shape $\Delta = 5$ vs. 7 MeV	sys: 4.6% (Λ), sys: 5.9% (Σ^0)
e′ K Acceptance	Geometrical Acceptance and Efficiencies Λ: 0.5 to 20% ave: 8.0% ± 1.2%	stat: 8%
	K Fiducial cuts	sys: 2.2%
	Event Generator V.Photon Flux (Cotanch) vs. WJC for Λ (Σ^0)	sys: 8% (Λ) sys: 6.7% (Σ^0)
	Timing Resolution	sys: 1.5%
Radiative Corrections	Correction of cross-section by -20% to +40%	stat: 5%
	Theoretical Uncertainty 5% of correction	sys: 2% (typical)
Total Systematic Uncertainty	Point-by-point	$9.6 + 0.25 * \sigma_{stat}$% ($\Lambda$) $9.3 + 0.25 * \sigma_{stat}$% ($\Sigma^0$)
Stability and Normalization	Livetime (85-95%)	sys: 0.5%
	Kaon ID Stability (includes livetime)	sys: 1.43%
	Absolute Electron Flux from elastic cross-section measurement	sys: 3.0%
Total Systematic Uncertainty	Overall scale	3.3%

Table 4.2: The estimated systematic errors for the 2.5 GeV, 2250 A dataset. Systematic uncertainties which can cause a point-to-point variation are applied at the ϕ_K-bin level (prior to the ϕ_K fits); those which caused a general scale shift are given at the bottom.

Source of Error	Description of Error; Size of the Effect	Contribution of Uncertainty to Cross-Sections
Yield Extraction	Reported Statistical (fine W binning)	stat: 14-22% (typical)
	Background shape Fixed vs. Constrained	sys: $0.25 * \sigma_{stat}$ (4% typical)
	Hyperon Peak shape $\Delta = 4.4$ vs. 6 MeV	sys: 3%
e' K Acceptance	Geometrical Acceptance and Efficiencies Λ: 0.5 to 22% ave: 7 % $\pm$ 1.8%	stat: 10%
	K Fiducial cuts	sys: 1.7%
	Event Generator V.Photon Flux (Cotanch) vs. WJC for Λ (Σ^0)	sys: 8% (Λ) sys: 7% (Σ^0)
	Timing Resolution	sys: 1.0%
Radiative Corrections	Correction of cross-section by -20% to +40%	stat: 5%
	Theoretical Uncertainty 5% of correction	sys: 2% (typical)
Total Systematic Uncertainty	Point-by-point	$8.7 + 0.25 * \sigma_{stat}$% ($\Lambda$) $7.9 + 0.25 * \sigma_{stat}$% ($\Sigma^0$)
Stability and Normalization	Livetime (85-95%)	sys: 0.5%
	Kaon ID Stability (includes livetime)	sys: 1.43%
	Absolute Electron Flux from elastic cross-section measurement	sys: 3.0%
Total Systematic Uncertainty	Overall scale	3.3%

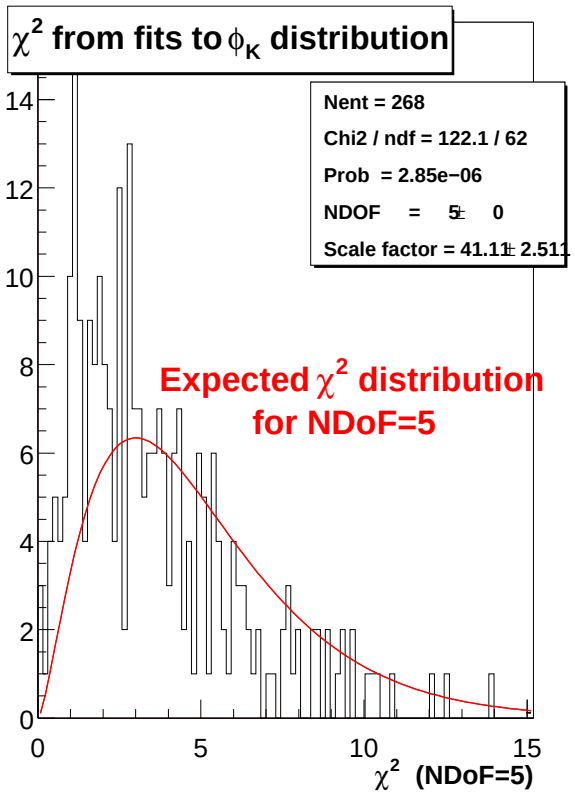

Figure 4.25: The distribution of the χ^2 values after the fits to the ϕ_K distributions, when there were five degrees of freedom in the fit. The solid line is the expected distribution for NDoF=5.

were correlated between the datasets and perhaps slightly over-estimated. By incorporating the uncertainties early in the analysis, they were automatically reflected in the error bars for the results of the fits to the ϕ_K-angle dependence..

Chapter 5

Discussion of the Results

In this chapter, the final extracted response functions will be presented again, this time compared with the theoretical calculations mentioned in Section 1.1.

Please note that to compare the results of this experiment directly to previous measurements, it would be necessary to match the three kinematic variables $(W, Q^2, \cos\theta_K)$ but also the virtual photon polarization factor, ϵ. However, the kinematic coverage of this experiment was quite different from prior measurements and so this was not possible. Instead, the Guidal and Laget calculation [20] was used as a proxy for the older data since it fit the Q^2 and $\cos\theta_K$ (and therefore t) behavior of the Λ cross-sections very well, as previously shown in Figures 1.2 and 1.5.

For clarification, the theoretical curves to be shown are an average of the calculation over each finite bin, weighted by the virtual photon flux. This is as opposed to simply using the value of the model calculated at the bin centers. This was important since in the three different binning schemes, two of the dimensions spanned by the bin could be considered large compared to the variation of the models.

5.1 Cos(θ_K) Dependence of the Λ Response-Functions

The measured results of the response functions for the $ep \rightarrow e'K^+\Lambda$ reaction are shown in Figure 5.1, as a function of $\cos\theta_K$, for different bins of W. In looking at the $(\sigma_T + \epsilon\sigma_L)$ term, we see that the Λ production cross-section is strongly forward peaked, even around $W = 1.70\,\text{GeV}$, near threshold, where the production mechanism has been described as primarily S-wave in photoproduction [29]; this assumption is reflected in the Bennhold curve(solid). As the energy in the center of momentum frame increases, however, the data and all the models qualitatively agree that this forward-peaking of the cross-section is increasingly significant, suggesting the naturally forward-peaking t-channel exchange as the primary production mechanism. The Janssen calculation (dot-dashed curves), with its inclusion of the u-channel excited hyperon states, has too much strength in the backward direction. Whether this is due

to an improper distribution of the production strength between the u- and t-channel exchanges will have to be determined by a new fit to the data within that model. By $W \approx 2.00\,\mathrm{GeV}$, close to where previous measurements were made to which the hadrodynamic models were fitted, our $(\sigma_T + \epsilon\sigma_L)$ term is 30% lower than predicted. This is due to the virtual photon polarization, $\epsilon = 0.354$, being much lower than that of the previous measurement ($\epsilon \approx 0.8$) taken near this Q^2 point [18]. Since ϵ is so different, the transverse and longitudinal components of the cross-section are in a different combination. Our results suggest that the σ_L term plays a larger role in Λ production near $W = 2.0\,\mathrm{GeV}$, $Q^2 = 0.7\,(\mathrm{GeV/c})^2$ than previously expected.

To examine the roles that K and K^* exchange might play in Λ production, an alternative version of the calculation provided by Michel Guidal [72] is shown (dotted curves). This calculation contains the same Regge-K exchange, but the K^* term has been turned off. From this, we can gather that in the very forward direction, the production mechanism is predicted to consist primarily of t-channel K exchange. However, as one moves to larger θ_K and higher W the K^* term is predicted to play a larger role. Of course as s- and u-channel states are added, as is done for the Bennhold and Janssen models, they too can provide strength in the middle and backward angles. The $(\sigma_T + \epsilon\sigma_L)$ data are insufficient to better determine the underlying reaction channels without a more sophisticated analysis.

The σ_{TT} and σ_{LT} interference terms, since they are different combinations of the helicity amplitudes which produced $\sigma_T + \epsilon\sigma_L$, provide additional information as to the relative importance of the longitudinal and transverse coupling of the virtual photon to the $K^+\Lambda$ state. First, we note that σ_{TT} and σ_{LT} are decidedly finite and non-zero over most of the kinematic range, and are of magnitude comparable to $\sigma_T + \epsilon\sigma_L$; this is the first time these terms have been definitively measured, with previous measurements yielding results consistent with zero [16, 18]. Since both σ_{TT} and σ_{LT} are finite, we can say that both the longitudinal and transverse couplings of the virtual photon to the $K^+\Lambda$ state are important and play a significant role. This is consistent with a prior measurement in which a full Rosenbluth separation of the σ_T and σ_L terms was performed at forward angles [17]. When comparing the theoretical curves to the interference terms, we observe that the full Regge-model calculation describes the response-functions' behavior remarkably well. This is somewhat surprising, since the Regge calculation was designed to explain the forward-angle, high-energy limit, yet it appears to be working well in this measurement for large θ_K and at low W. Another interesting note is that the Bennhold model produces a σ_{TT} term with the inverse sign of the data and other calculations, including the similar Janssen calculation.

From the $\cos\theta_K$ distributions we conclude that Λ-production can be well described via K-exchange in the very forward direction, with some strength for the backward angles coming from K^* exchange, and u- or s-channel exchange processes.

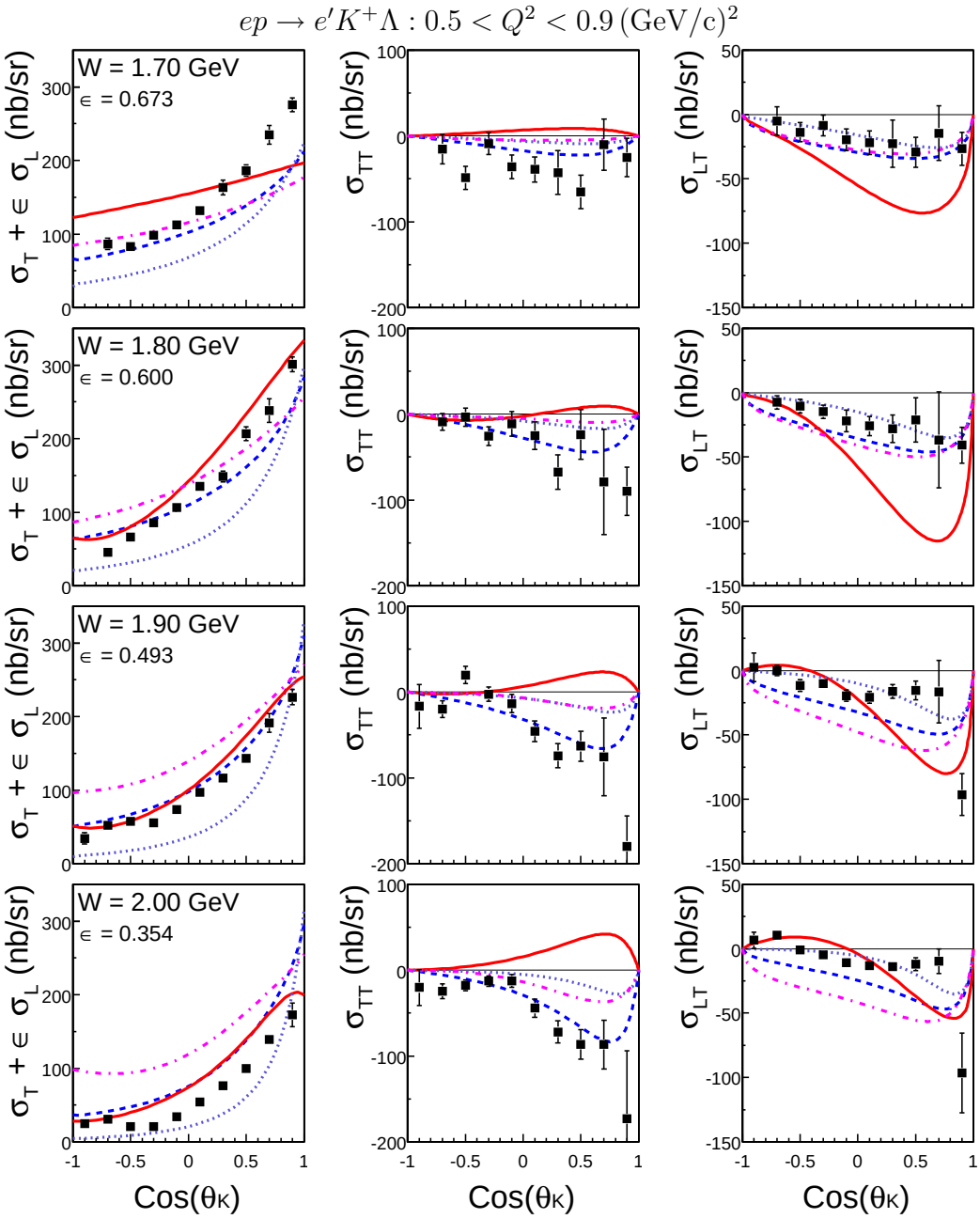

Figure 5.1: The response functions of Λ electroproduction for 100 MeV wide bins in W and $0.5 < Q^2 < 0.9\,(\mathrm{GeV/c})^2$, versus $\cos\theta_K$. The theoretical curves are from the Bennhold [24] (solid, red), Janssen [73] (dot-dashed, magenta), and Guidal [20] (dashed, blue) calculations. A version of the Guidal calculation excluding K^* exchange [72] (dotted, blue) is shown as well.

5.2 Cos(θ_K) Dependence of the Σ^0 Response-Functions

The measurements of the response functions for the $ep \to e'K^+\Sigma^0$ reaction are shown in Figure 5.2 as a function of $\cos\theta_K$ for different bins of W. In contrast to Λ production, the Σ^0 unseparated cross-sections, $\sigma_T + \epsilon\sigma_L$, are not forward peaked, but instead tend to peak in the mid-forward angle region. At first glance, this suggests that the primary production mechanism is not primarily via t-channel exchange, but instead perhaps through s-channel processes. This might be expected, since the $K^+\Sigma^0$ state has isospin $\frac{3}{2}$ components such that Δ states could also contribute to the s-channel production mechanism. The models do not fit the response-functions well, except for the near identically-zero σ_{LT} term. With little previous electroproduction data on the Σ^0 except at very forward angles, this is not very surprising. In fact, in the very forward direction as $\cos\theta_K \to 1$, the calculations do reasonably well in predicting the Σ^0's unseparated cross-section. The exception is near $W = 1.9\,\mathrm{GeV}$, where the models significantly under-predict the $(\sigma_T + \epsilon\sigma_L)$ term. This is in the region where a number of Δ^* resonances have been observed in pion-scattering measurements, and the Janssen and Bennhold effective Lagrangian models both contain the Δ^* $S_{31}(1900)$ and $P_{31}(1910)$ states. The miss by the models might very well be due to inaccurate electromagnetic form factors for these states. This measurement then provides key information as to the internal structure of these Δ^* states. This region of W will be further discussed below.

As already noted, the σ_{LT} term for Σ^0 production is consistent with zero. Since σ_{TT} is finite and of the same order as $(\sigma_T + \epsilon\sigma_L)$, we suggest that, unlike Λ production, only coupling to the transverse polarization of the virtual photon contributes significantly to Σ^0 production. This statement is consistent with the conclusion of a prior measurement in which a Rosenbluth separation of the σ_T and σ_L terms was performed, albeit with extremely poor statistics, for the Σ^0 state [17].

5.3 W Dependence of Λ and Σ^0 Production

Figures 5.3-5.8 present the $K^+\Lambda$ and $K^+\Sigma^0$ response functions as a function of the total energy in the center of momentum frame, W, from forward to backward bins in $\cos\theta_K$. By examining the response functions directly as a function of W, we can more easily recognize features which might be due to s-channel resonant states.

In the forward-most $\cos\theta_K$ bin shown in Figure 5.3, a number of features in the K^+ Λ final states are visible. The cross-section rises sharply with increasing W to a broad peak at 1.75 GeV, then drops off slowly as W increases further. In comparing $(\sigma_T + \epsilon\sigma_L)$ to the prediction of the Bennhold calculation, the sharp rise is due the N^* $S_{11}(1650)$ contributing strongly at threshold. Features in the σ_{TT} and σ_{LT} interference terms for the Λ are also visible near threshold. The σ_{TT} response

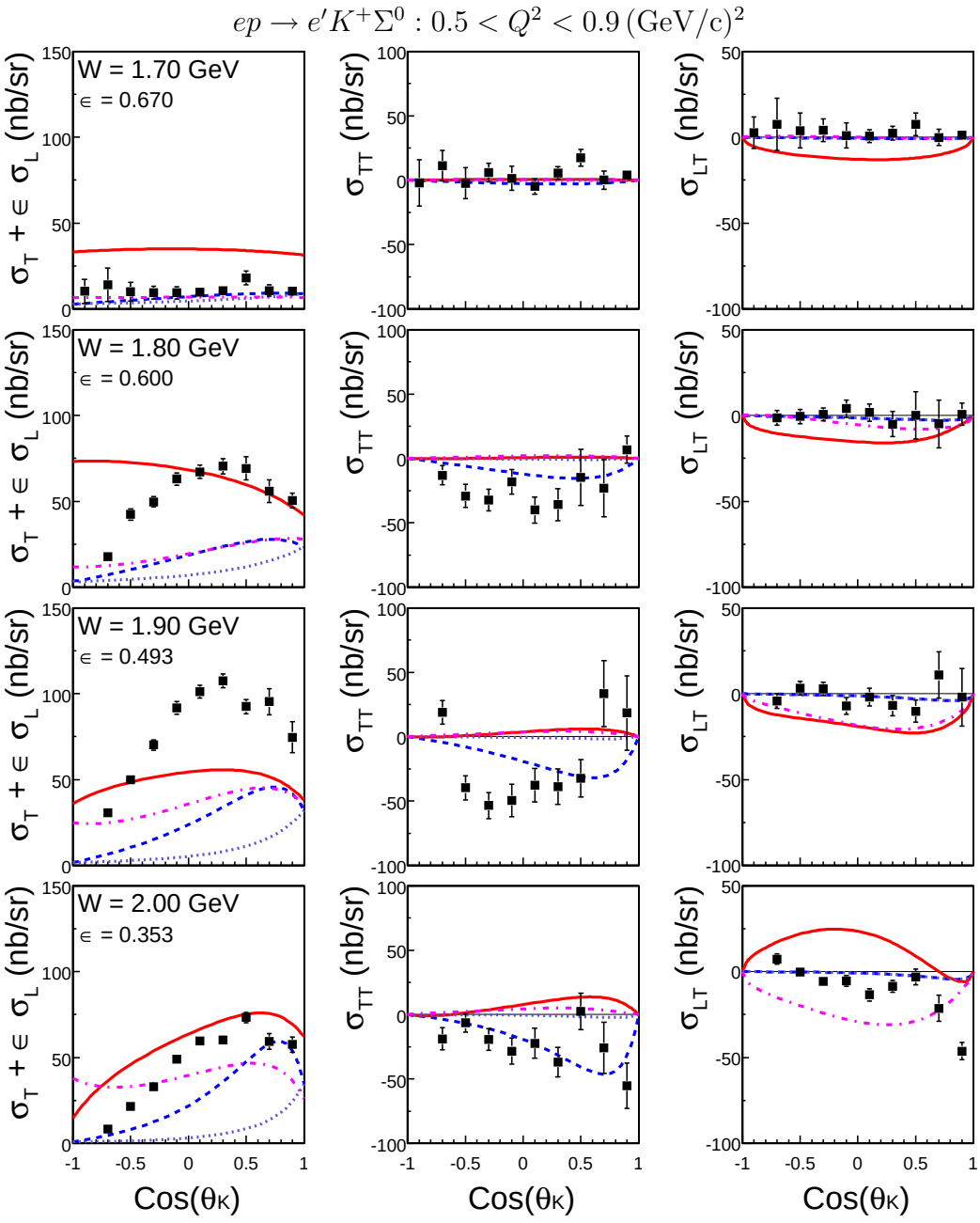

Figure 5.2: The response functions of Σ^0 electroproduction for 100 MeV wide bins in W, $0.5 < Q^2 < 0.9\,(\mathrm{GeV/c})^2$, versus $\cos\theta_K$. The theoretical curves are described in Figure 5.1.

function appears to be nearly zero until $W = 1.75\,\mathrm{GeV}$, when it suddenly drops and then stays approximately constant near a value of $-100\,\mathrm{nb/sr}$. Likewise, σ_{LT} appears to drop slowly until it reaches a plateau in the same region of W. It should be noted that the threshold for $K^+\Sigma^0$ production is 1.71 GeV, so these effects could be due to channel coupling between the $K^+\Lambda$ and $K^+\Sigma^0$ final states. In the region between 1.85 and 1.90 GeV, the $(\sigma_T + \epsilon\sigma_L)$ term has slight shoulder before decreasing further. This is in the region of the hypothesized $D_{13}(1895)$ resonant state [24].

Figures 5.4-5.6 show that as θ_K increases and we move out of the t-channel dominated forward region, the features of the $K^+\Lambda$ response functions change. The shoulder visible at forward angles has vanished, but instead the cross-section drops off more rapidly at higher W than predicted by the models. In Figure 5.7, in the $\cos\theta_K$ bin centered about -0.5 a "dip and bump" structure is revealed. The depletion, centered about $W = 1.75\,\mathrm{GeV}$, is at the same location as the peak in the most forward $\cos\theta_K$ bin, while the rise is centered at $W = 1.85\,\mathrm{GeV}$. The recent photoproduction data [8] had a similar feature near this energy which was proposed to be a missing D_{13} resonant state with a mass and width of $1895\,\mathrm{MeV/c^2}$ and 372 MeV, respectively [9]. This state is included in the Janssen calculation (dot-dash), and its very slight predicted influence can be seen in the curve. From comparing the calculation to the $\sigma_T + \epsilon\sigma_L$ term, however, it is evident that the proposed state is far too wide to simply explain the 100 MeV wide "bump" in the data. The D_{13} was also predicted to have a large signature in the linear polarized beam asymmetry photo-production observable, Σ, so we would expect to see a feature in the closely-related σ_{TT} interference term; however little variation of σ_{TT} is seen which could correspond to such a wide resonance. It should be noted that the two calculations which include the proposed D_{13} state also do not predict a significant feature. We believe a more sophisticated partial-wave analysis will be necessary to conclusively identify the physics behind these features.

The $K^+\Sigma^0$ response functions, shown in the right panels on the same vertical scale, show an overall rise of $\sigma_T + \epsilon\sigma_L$ up to $W = 1.9\,\mathrm{GeV}$, where it too begins to slowly drop off. As seen in the $\cos\theta_K$ distributions, the Σ^0 production cross-section is not forward peaked, and so as we move to larger θ_K (smaller $\cos\theta_K$) in Figures 5.4 and 5.5, we see the $(\sigma_T + \epsilon\sigma_L)$ term increase slightly. However, the Σ^0's production response functions have a very similar shape across all the $\cos\theta_K$ bins. The σ_{TT} interference function appears to go through a minimum near $W = 1.85\,\mathrm{GeV}$. This is seen most clearly in the backward-hemisphere bins. Figures 5.6 and 5.7, corresponding to $\cos\theta_K \approx -0.17$ and -0.50, respectively, have a large feature in the σ_{TT} interference term between W =1.7 and 1.9 GeV. The full width of the feature is approximately 150 MeV, the same as the rise and fall of the $(\sigma_T + \epsilon\sigma_L)$ term, and consistent with the width of a resonance in this region. This feature suggests that K^+ Σ^0 electroproduction is dominated by s-channel processes.

As previously stated, the Bennhold and Janssen models do contain Δ^* states in this energy range, the $S_{31}(1900)$ and $P_{31}(1910)$, however neither model predicts the structures present in the data. It is interesting to note that a previous partial

wave analysis of the $\pi^+ p \to \Sigma^+ K^+$ reaction could determine only upper limits of the partial widths for the $S_{31}(1900)$ and $P_{31}(1910)$ states to the $K\Sigma$ final state, but a finite (greater than 3σ) coupling of the $P_{33}(1920)$ to the $K\Sigma$ final state [74]. The $P_{33}(1920)$ is a three-star resonance, with a mass and width quoted as between 1900 and 1970 MeV, and 150 to 300 MeV, respectively [75]. This is certainly consistent with the features we see in $(\sigma_T + \epsilon\sigma_L)$ for $K^+\Sigma^0$ production, and the interference of the $P_{33}(1920)$ with other Δ^*'s could be reflected in the σ_{TT} response function.

5.4 Q^2 Dependence of Λ and Σ^0 Production

Figures 5.9 through 5.20 show the measurements of the Q^2 dependence of $K^+\Lambda$ and $K^+\Sigma^0$ electroproduction. These results contain the same data shown in the previous sections, but with smaller bins in Q^2 and wider bins in $\cos\theta_K$ and W. Please note the suppressed $Q^2 = 0\,(\mathrm{GeV/c})^2$ point on the x-axis; the Q^2 dependence is displayed only over the region where this data was taken. Also shown in each figure are curves for the theoretical calculations mentioned previously: the Bennhold effective-Lagrangian model (solid), the Janssen model (dot-dash), and the Guidal Regge-trajectory model with the full t-channel exchange (dashed) and with only K^+ exchange (dotted).

In comparing the $K^+\Lambda$ results to the theoretical curves, we find that, as before, none of the curves represent the data well. In the forward direction, the $(\sigma_T + \epsilon\sigma_L)$ term is predicted to be 30% smaller than observed around $W = 1.7$ GeV, but approximately 30% larger than observed for the $W = 2.0$ GeV bin. As previously mentioned, the results of this experiment are for a lower range of ϵ than prior measurements, and so an error in the predicted value of σ_L could cause this kind of effect. Closer to the midplane, for $\cos\theta_K = 0$, the $(\sigma_T + \epsilon\sigma_L)$ results match the magnitude and shape of the Guidal Regge-model calculation quite well, where the K^* exchange, according to the calculation, is becoming more significant.

An interesting feature seen in the $K^+\Sigma^0$ results as a function of Q^2 is the much larger than predicted cross-section in the $W = 1.9$ GeV bin. In the forward bins, across the entire range of Q^2 to which the experiment was sensitive, we find the $(\sigma_T + \epsilon\sigma_L)$ term to be 50 to 100% higher than the closest model prediction. In general, the models did not perform well in calculating the magnitude of $K^+\Sigma^0$ production. Only the Bennhold calculation approached the size of the $(\sigma_T + \epsilon\sigma_L)$ term, however it also predicted a very significant σ_{LT} term which is not seen in the data.

In comparing the Q^2 dependence of the $K^+\Lambda$ and $K^+\Sigma^0$ reactions, it does appear the Σ^0's production falls off more quickly with increasing Q^2 than that of the Λ, if only around $W = 1.9$ GeV. This can be seen in the $0 < \cos\theta_K < +0.33$ bins (Figures 5.11 and 5.17). In these bins, $\sigma_T + \epsilon\sigma_L$ for the Σ^0 drops by approximately 30% between Q^2 =0.5 and 1.0 $(\mathrm{GeV/c})^2$, while at this same kinematic point the $(\sigma_T + \epsilon\sigma_L)$ term for Λ production drops by only 10 to 20%. However, away from the $W = 1.9$ GeV region where we saw s-channel-like structures, the Q^2 dependence of the two hyperons appear to be rather similar.

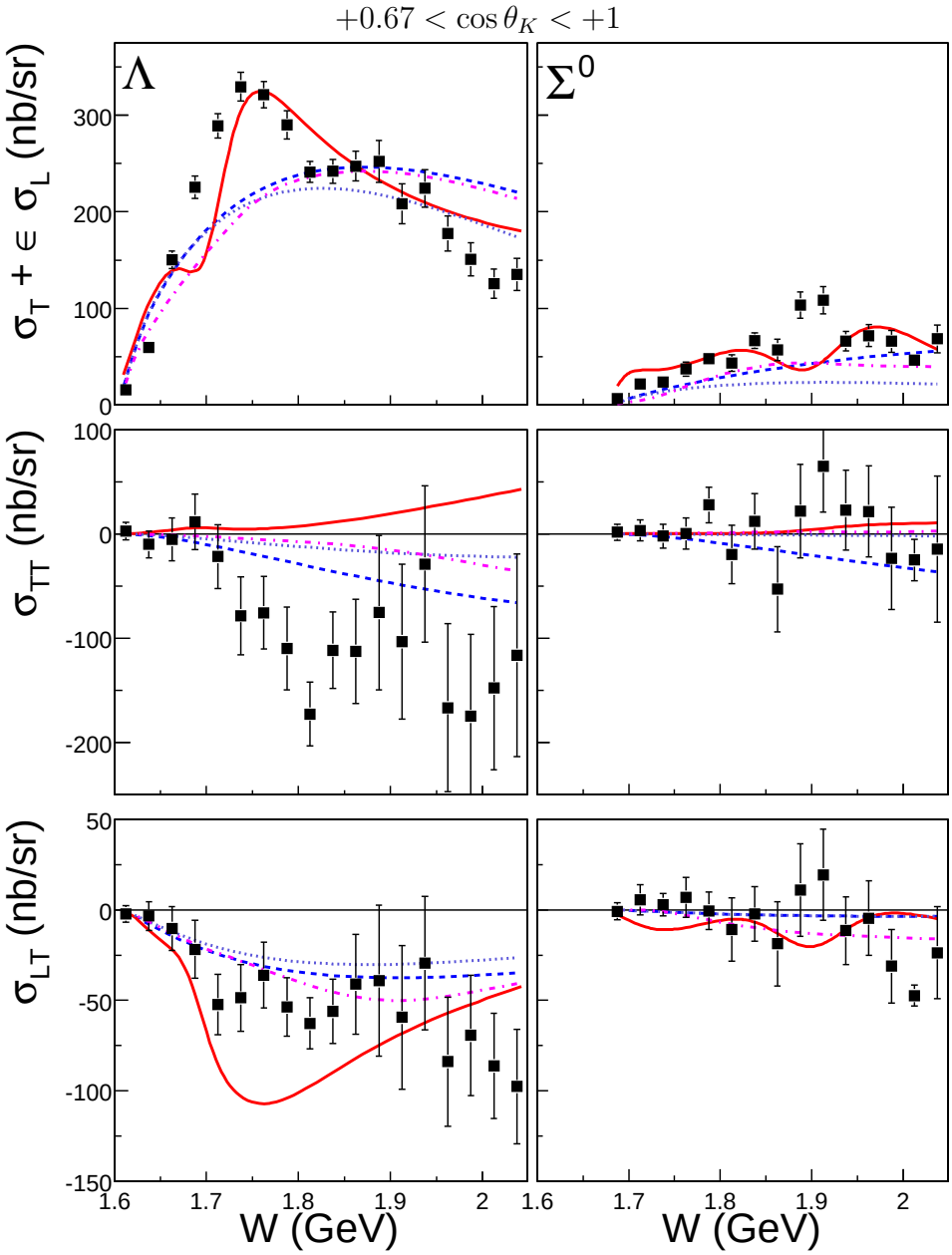

Figure 5.3: The response functions versus W for Λ and Σ^0 electroproduction in the left and right columns, respectively, for $0.67 < \cos\theta_K < 1$ and $0.5 < Q^2 < 0.9\,(\mathrm{GeV/c})^2$. The theoretical curves are from the Bennhold [24] (solid, red), Janssen [73] (dot-dashed, magenta), and Guidal [20] (dashed, blue) calculations. A calculation by Guidal excluding K^* exchange [72] (dotted, blue) is shown as well.

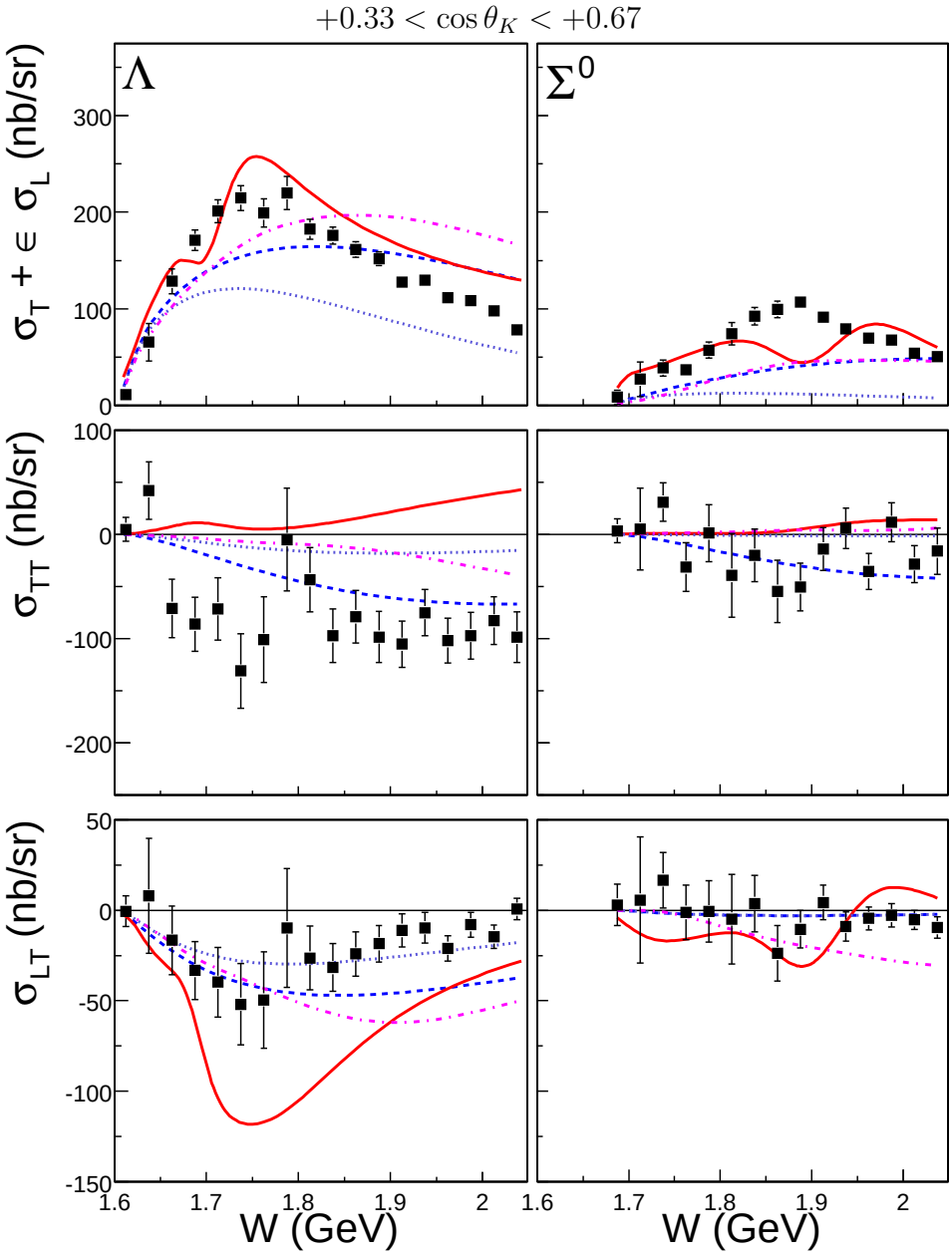

Figure 5.4: The response functions versus W for Λ and Σ^0 electroproduction in the left and right columns, respectively, for $0.33 < \cos\theta_K < 0.67$ and $0.5 < Q^2 < 0.9\,(\mathrm{GeV/c})^2$. See Figure 5.3 for a description of the curves.

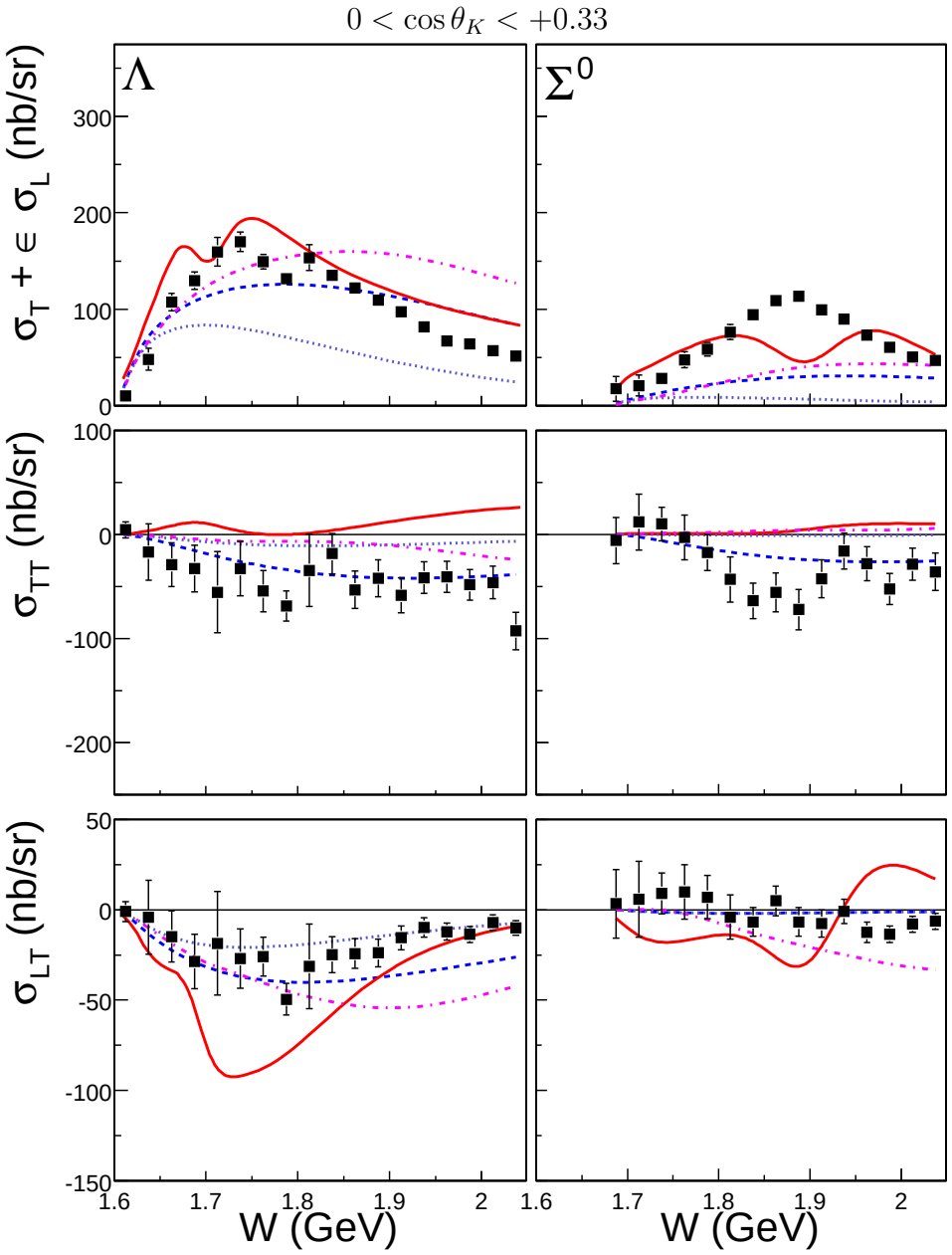

Figure 5.5: The response functions versus W for Λ and Σ^0 electroproduction in the left and right columns, respectively, for $0 < \cos\theta_K < 0.33$ and $0.5 < Q^2 < 0.9\,(\mathrm{GeV/c})^2$. See Figure 5.3 for a description of the curves.

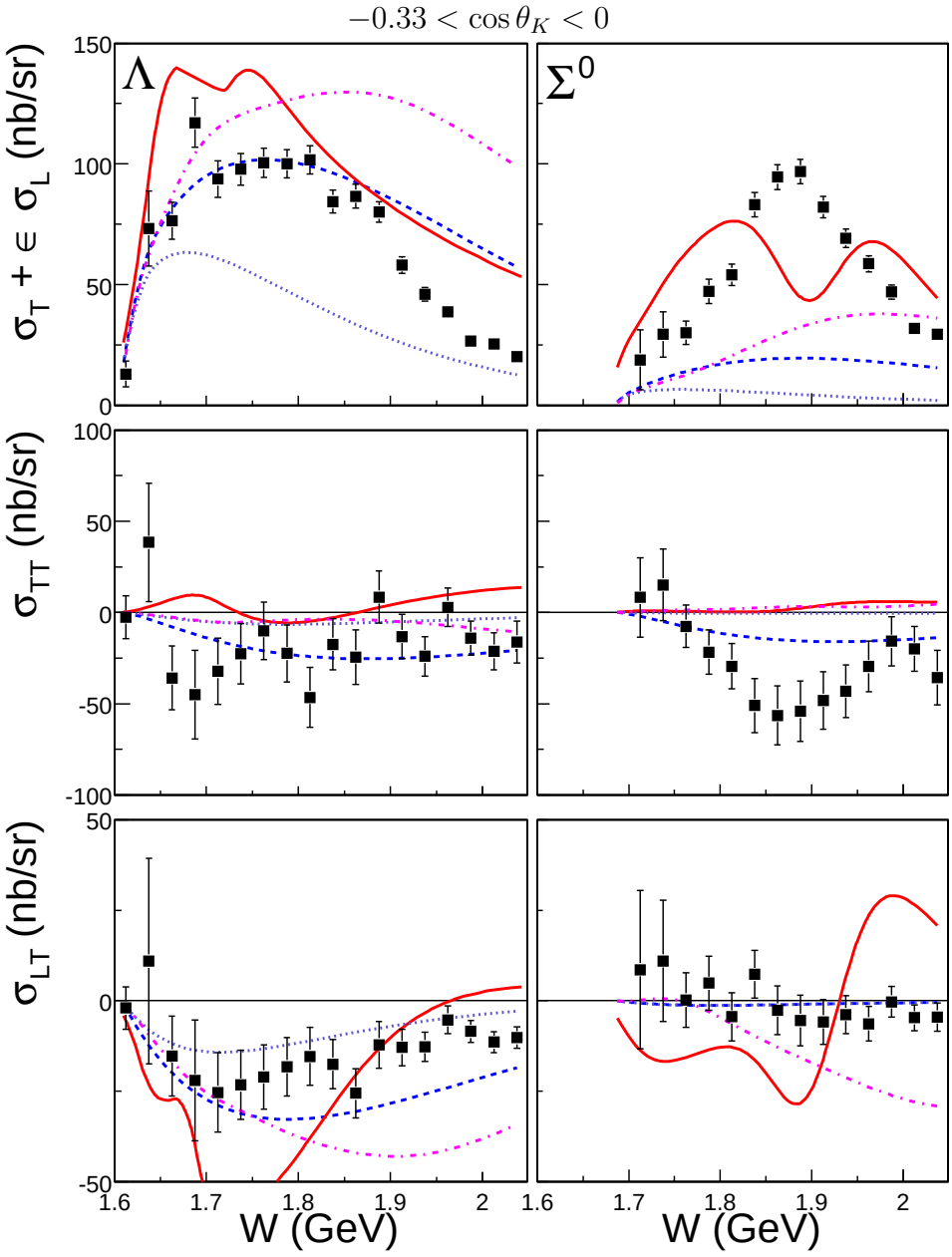

Figure 5.6: The response functions versus W for Λ and Σ^0 electroproduction in the left and right columns, respectively, for $-0.33 < \cos\theta_K < 0$. and $0.5 < Q^2 < 0.9\,(\mathrm{GeV/c})^2$. See Figure 5.3 for a description of the curves.

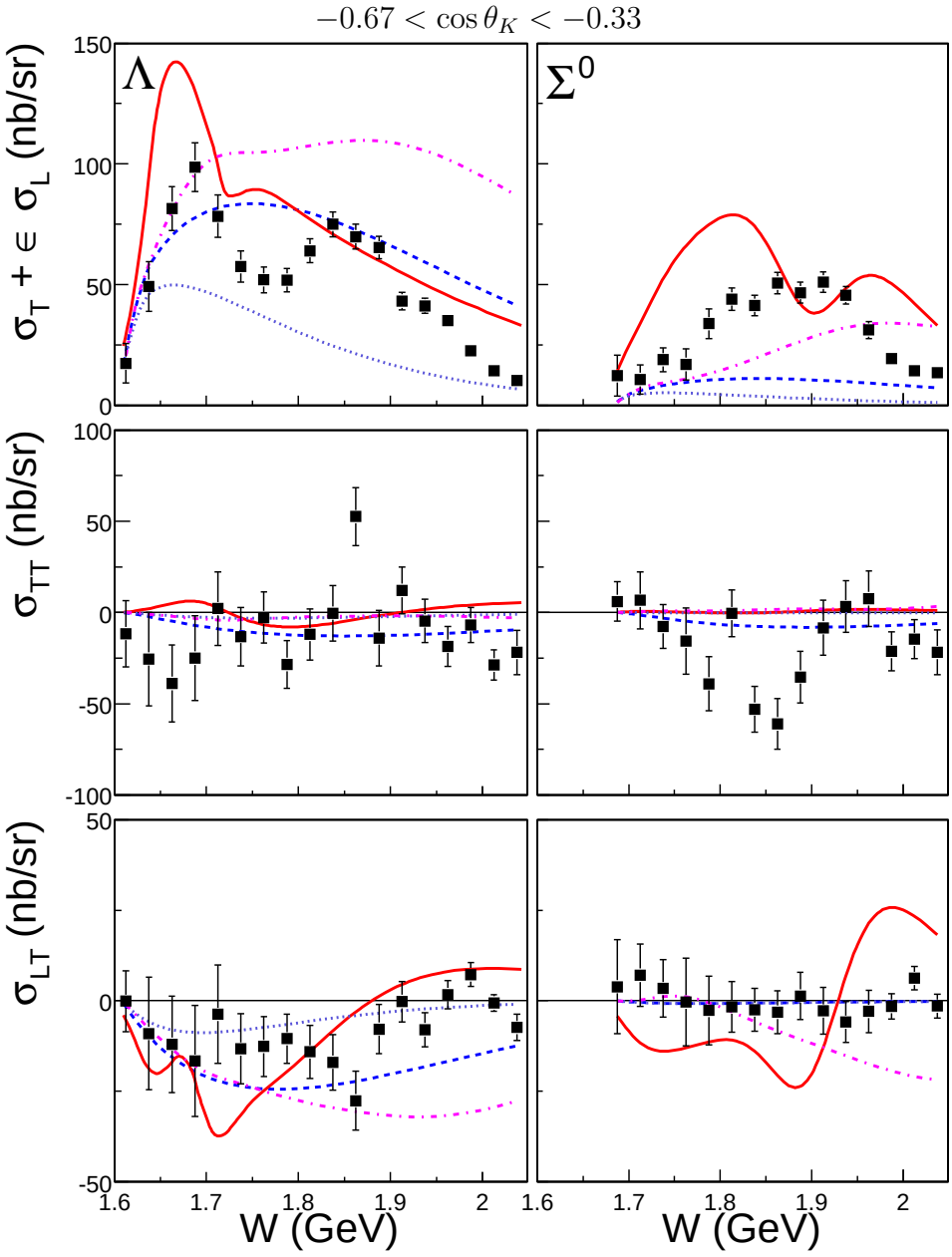

Figure 5.7: The response functions versus W for Λ and Σ^0 electroproduction in the left and right columns, respectively, for $-0.67 < \cos\theta_K < -0.33$ and $0.5 < Q^2 < 0.9\,(\mathrm{GeV/c})^2$. See Figure 5.3 for a description of the curves.

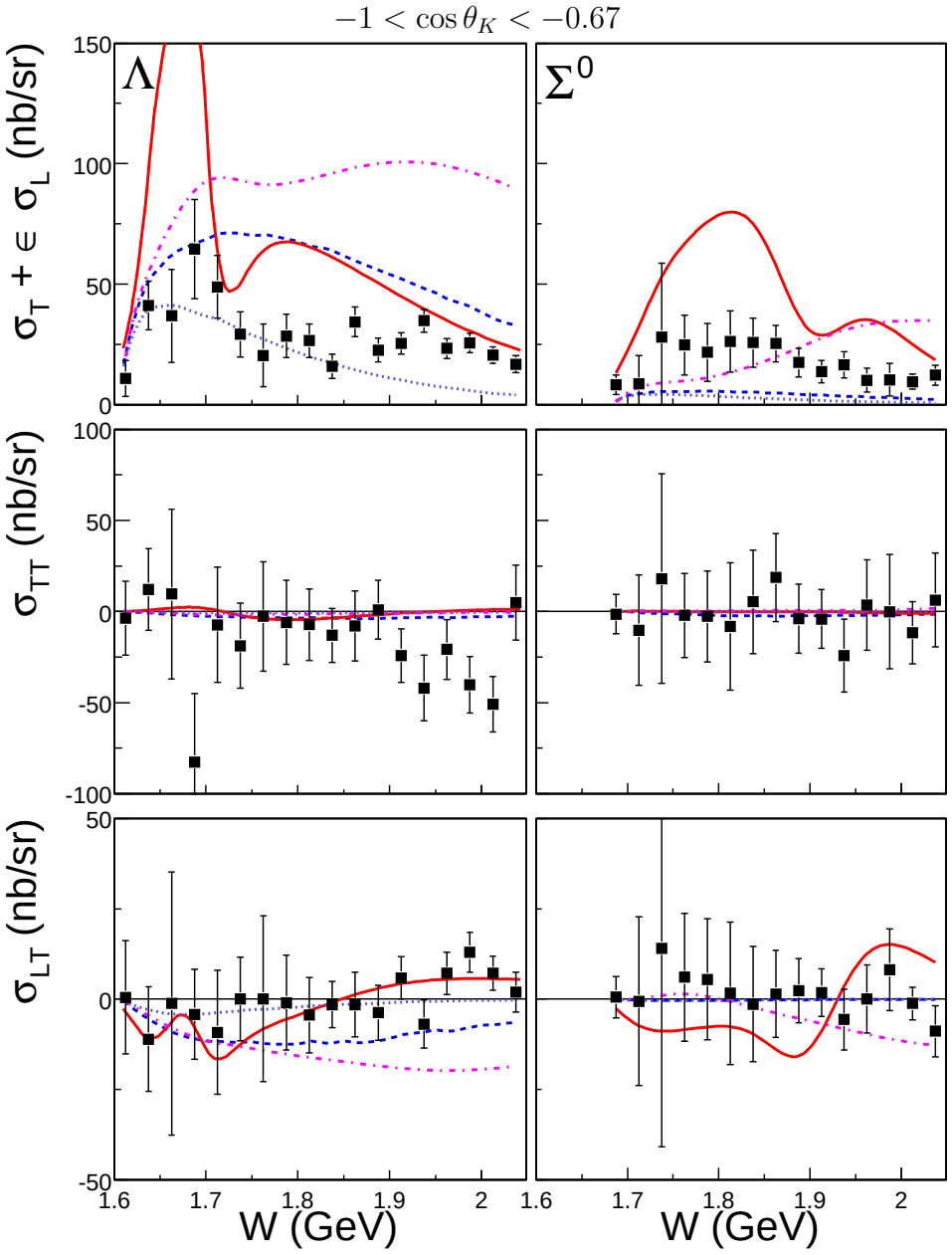

Figure 5.8: The response functions versus W for Λ and Σ^0 electroproduction in the left and right columns, respectively, for $-1 < \cos\theta_K < -0.67$ and $0.5 < Q^2 < 0.9\,(\mathrm{GeV/c})^2$. See Figure 5.3 for a description of the curves.

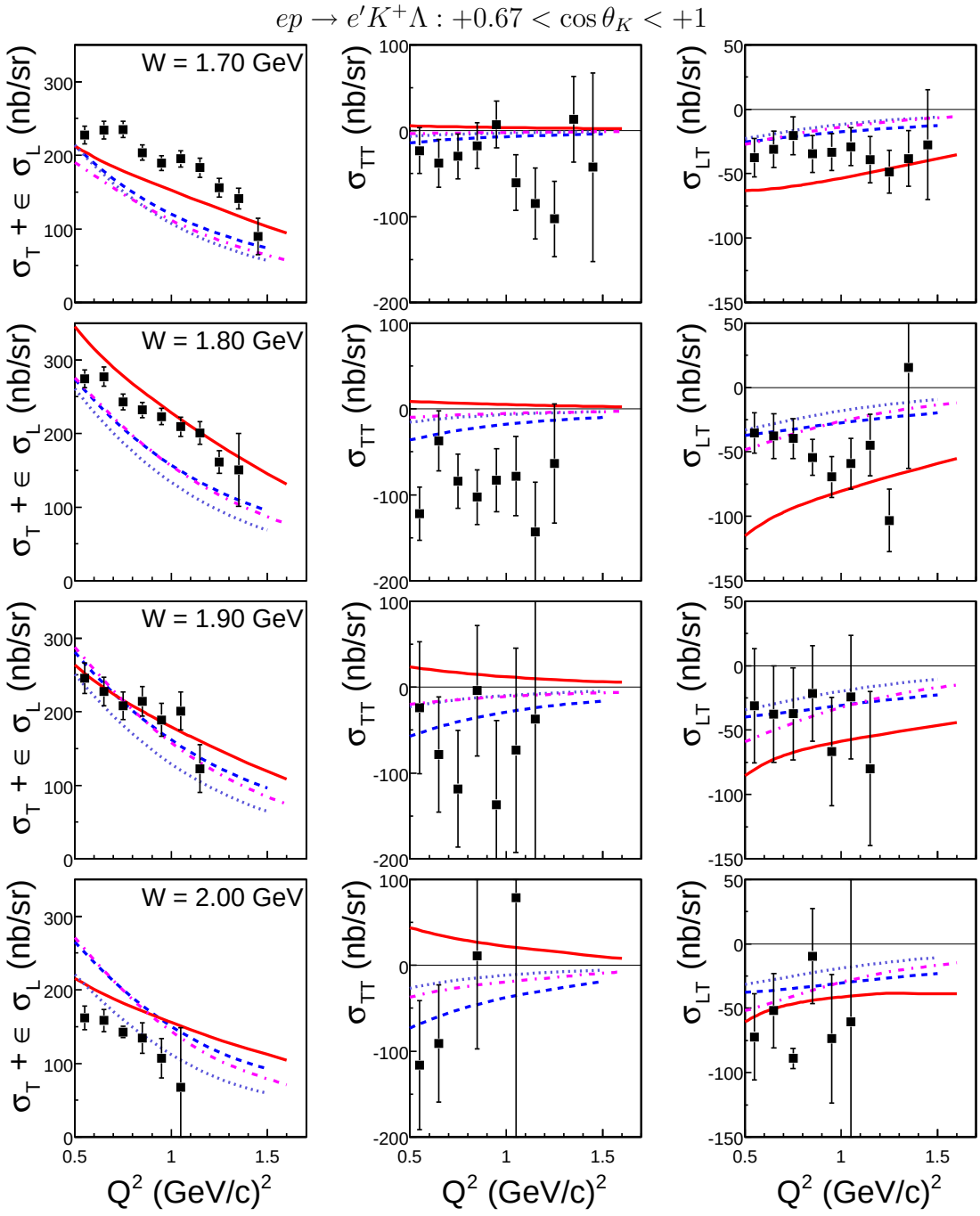

Figure 5.9: The response functions of Λ electroproduction versus Q^2 for $0.67 < \cos\theta_K < 1$, and 100 MeV wide bins in W. The theoretical curves are from the Bennhold [24] (solid, red), Janssen [73] (dot-dashed, magenta), and Guidal [20] (dashed, blue) calculations. The Guidal calculation excluding K^* exchange [72] (dotted, blue) is shown as well.

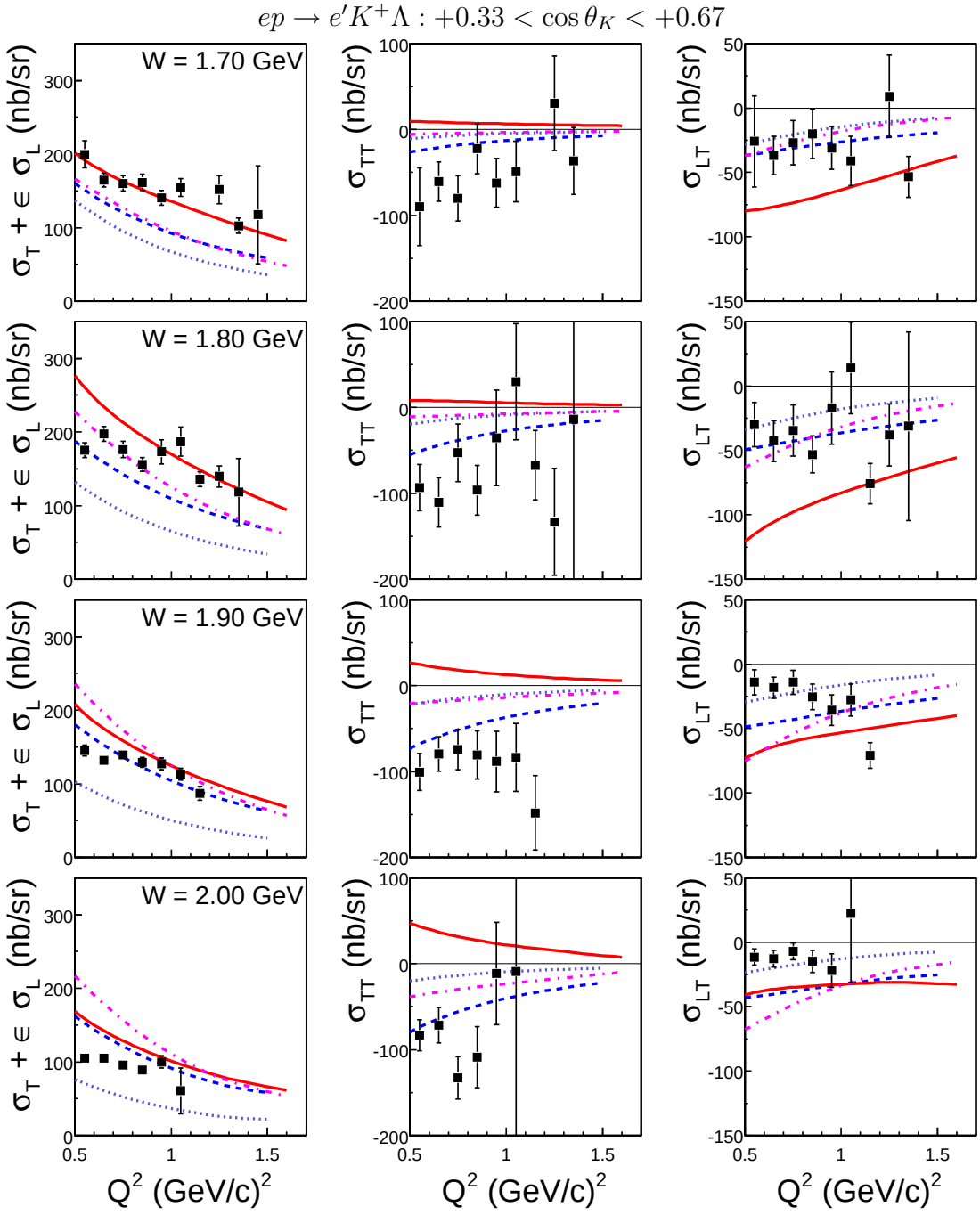

Figure 5.10: The response functions of Λ electroproduction versus Q^2 for $0.33 < \cos\theta_K < 0.67$ and 100 MeV wide bins in W. The curves are described in Figure 5.9.

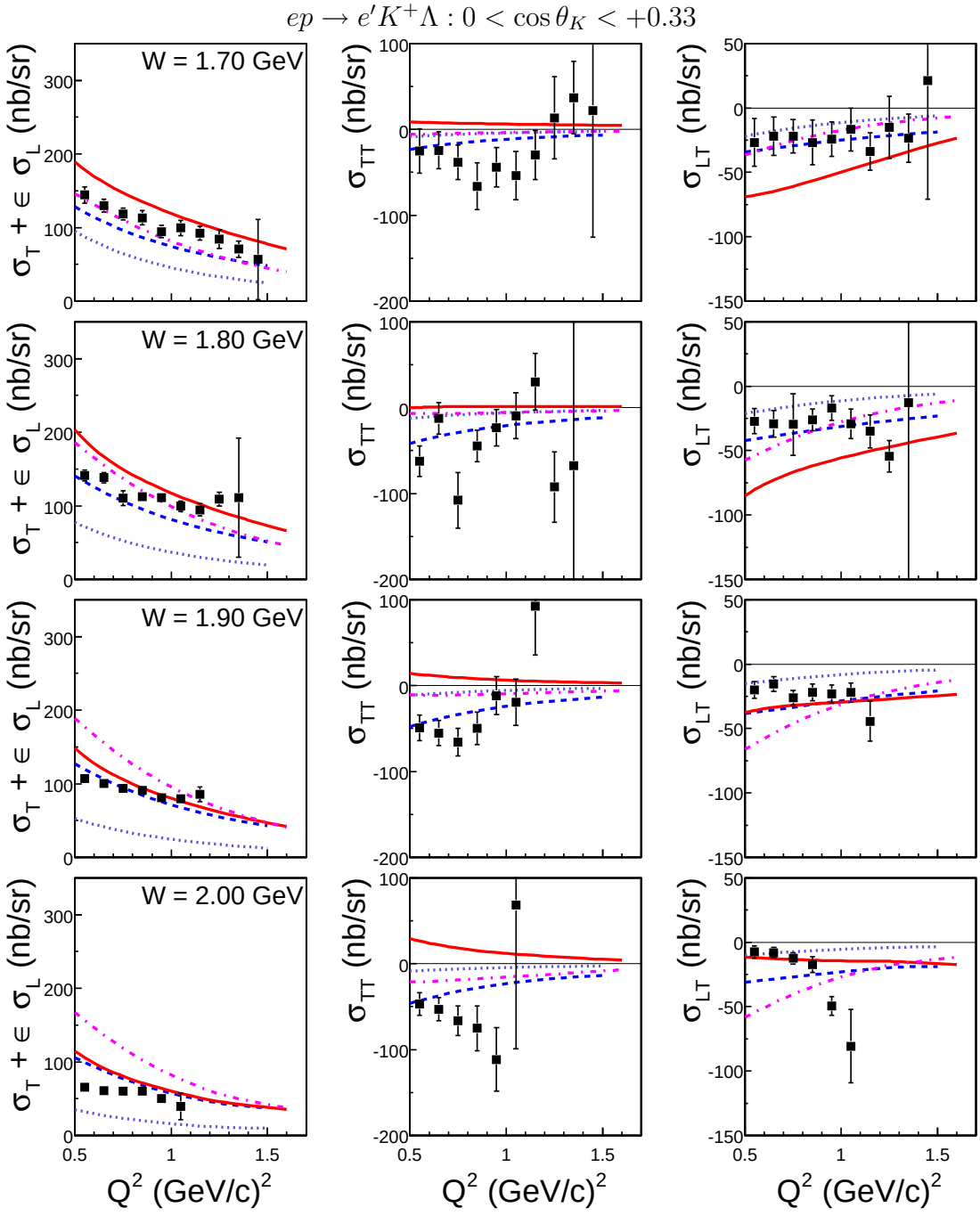

Figure 5.11: The response functions of Λ electroproduction versus Q^2 for $0 < \cos\theta_K < 0.33$ and 100 MeV wide bins in W. The curves are described in Figure 5.9.

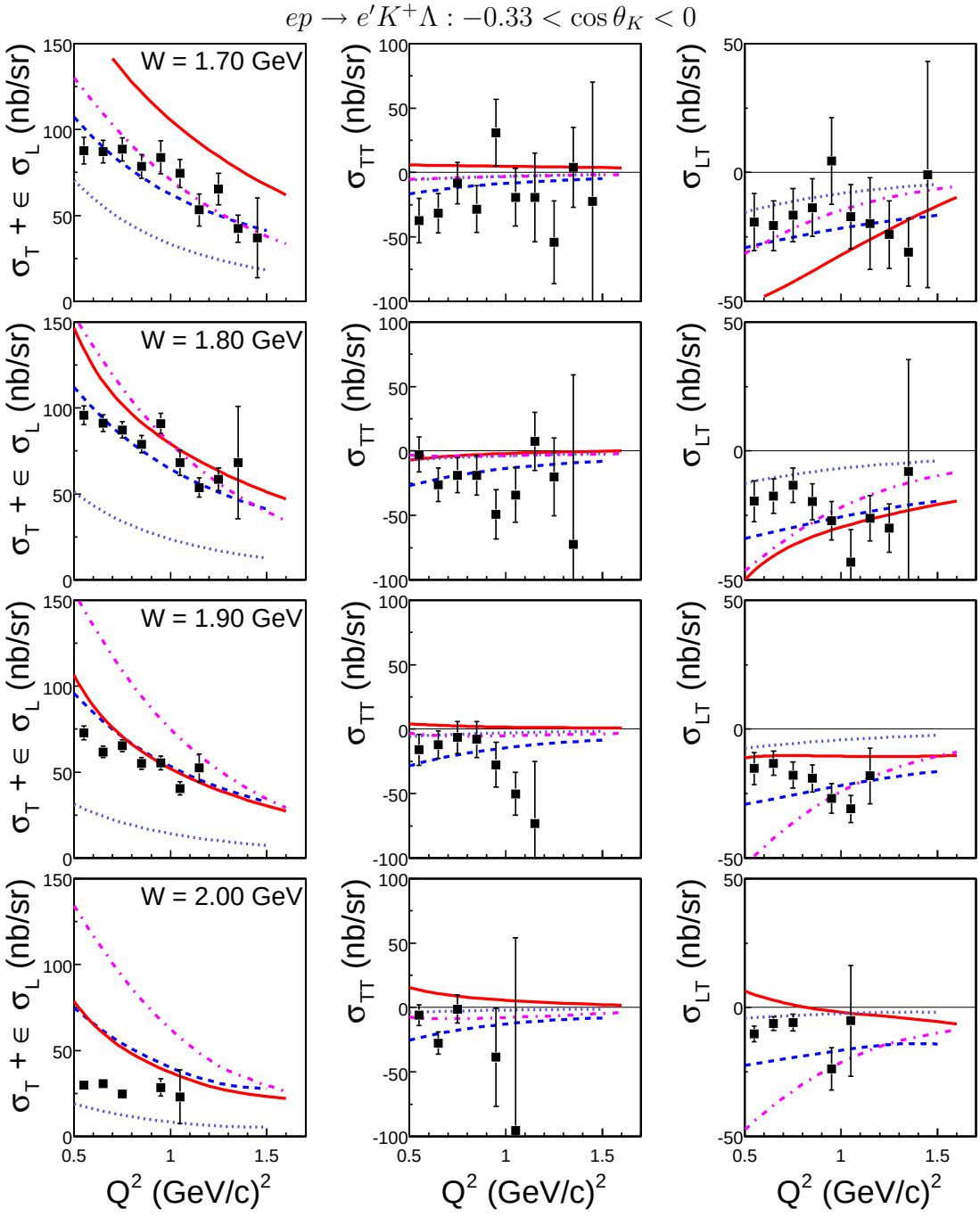

Figure 5.12: The response functions of Λ electroproduction versus Q^2 for $-0.33 < \cos\theta_K < 0$ and 100 MeV wide bins in W. The curves are described in Figure 5.9.

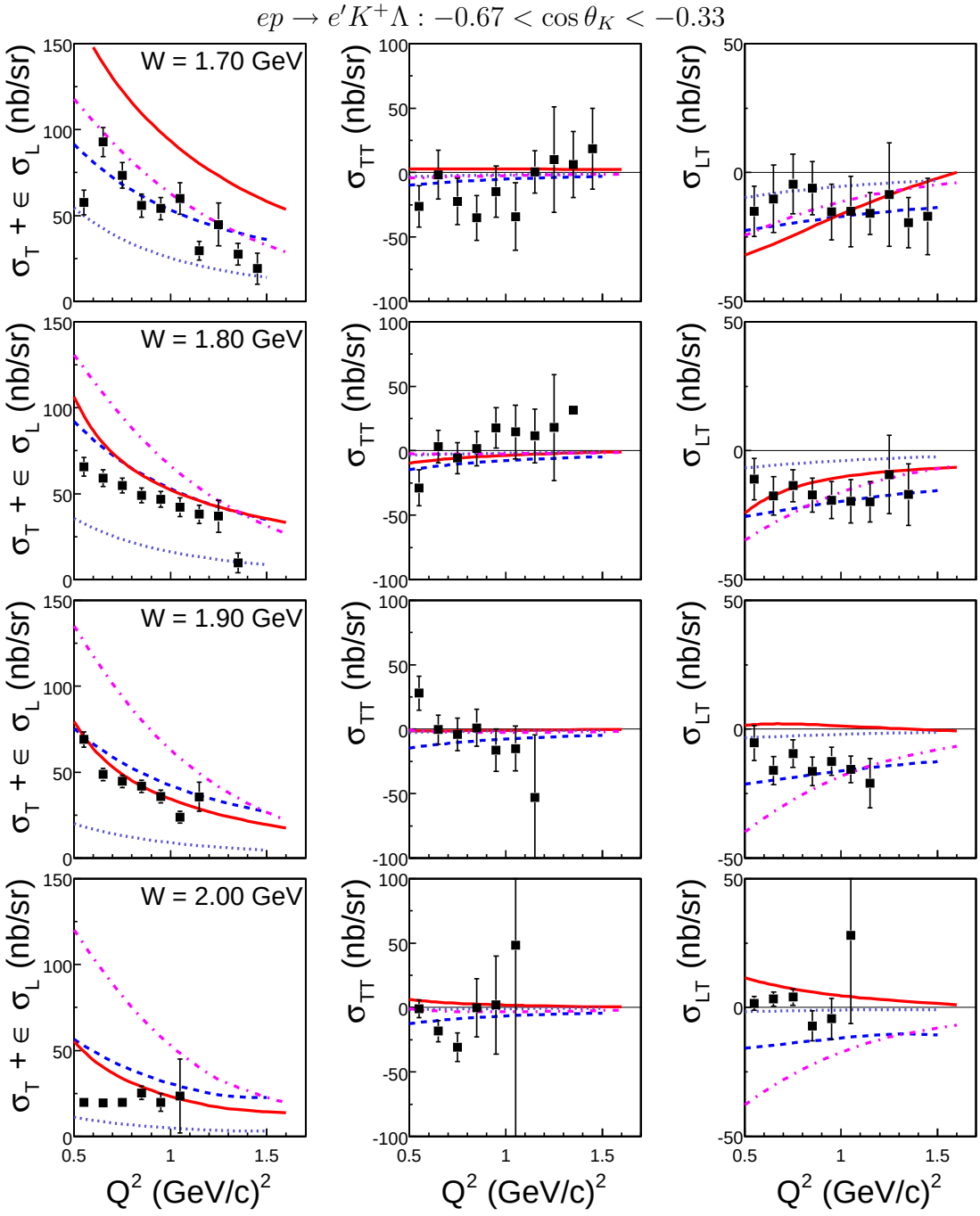

Figure 5.13: The response functions of Λ electroproduction versus Q^2 for $-0.67 < \cos\theta_K < -0.33$ and 100 MeV wide bins in W. The curves are described in Figure 5.9.

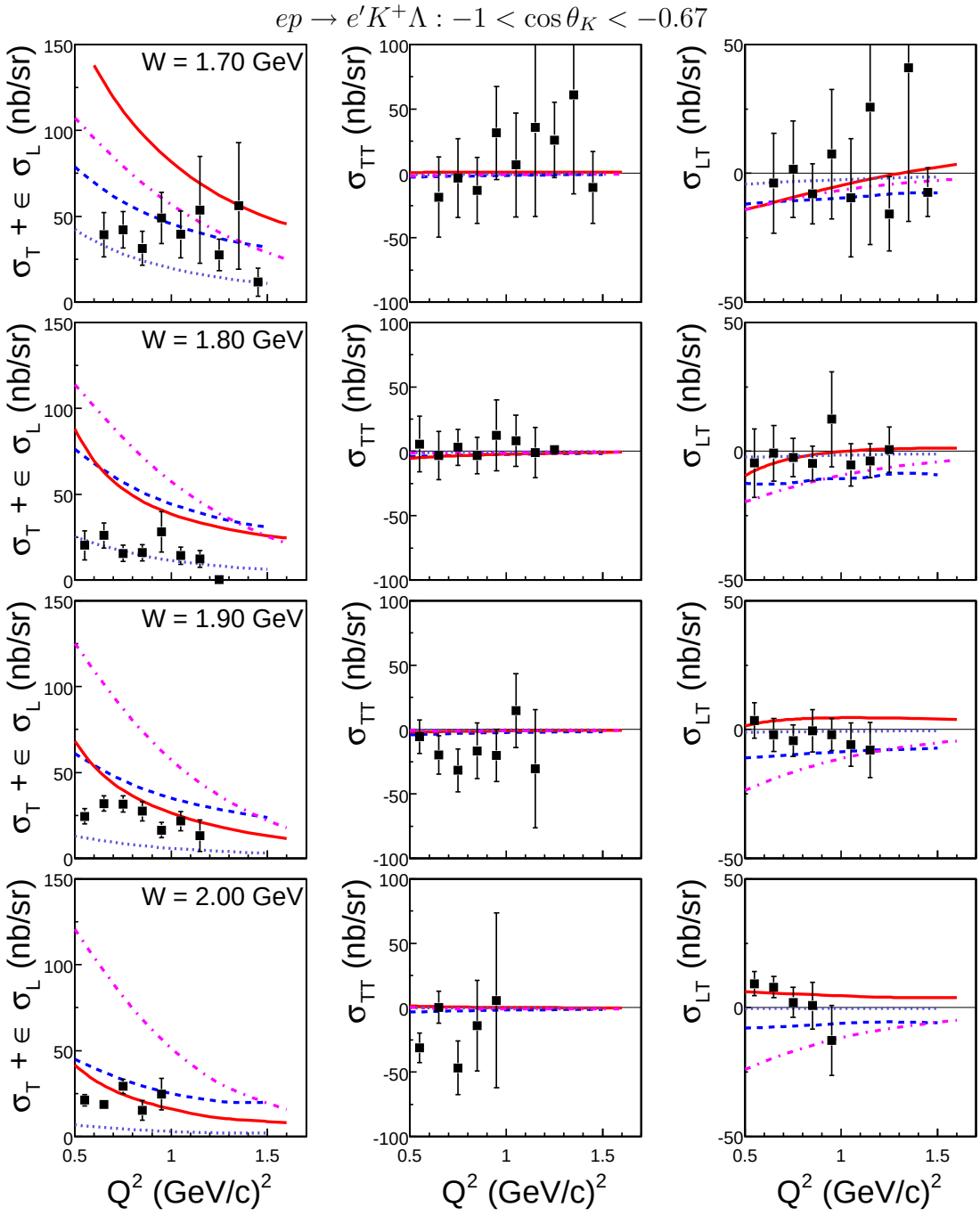

Figure 5.14: The response functions of Λ electroproduction versus Q^2 for $-1 < \cos\theta_K < -0.67$ and 100 MeV wide bins in W. The curves are described in Figure 5.9.

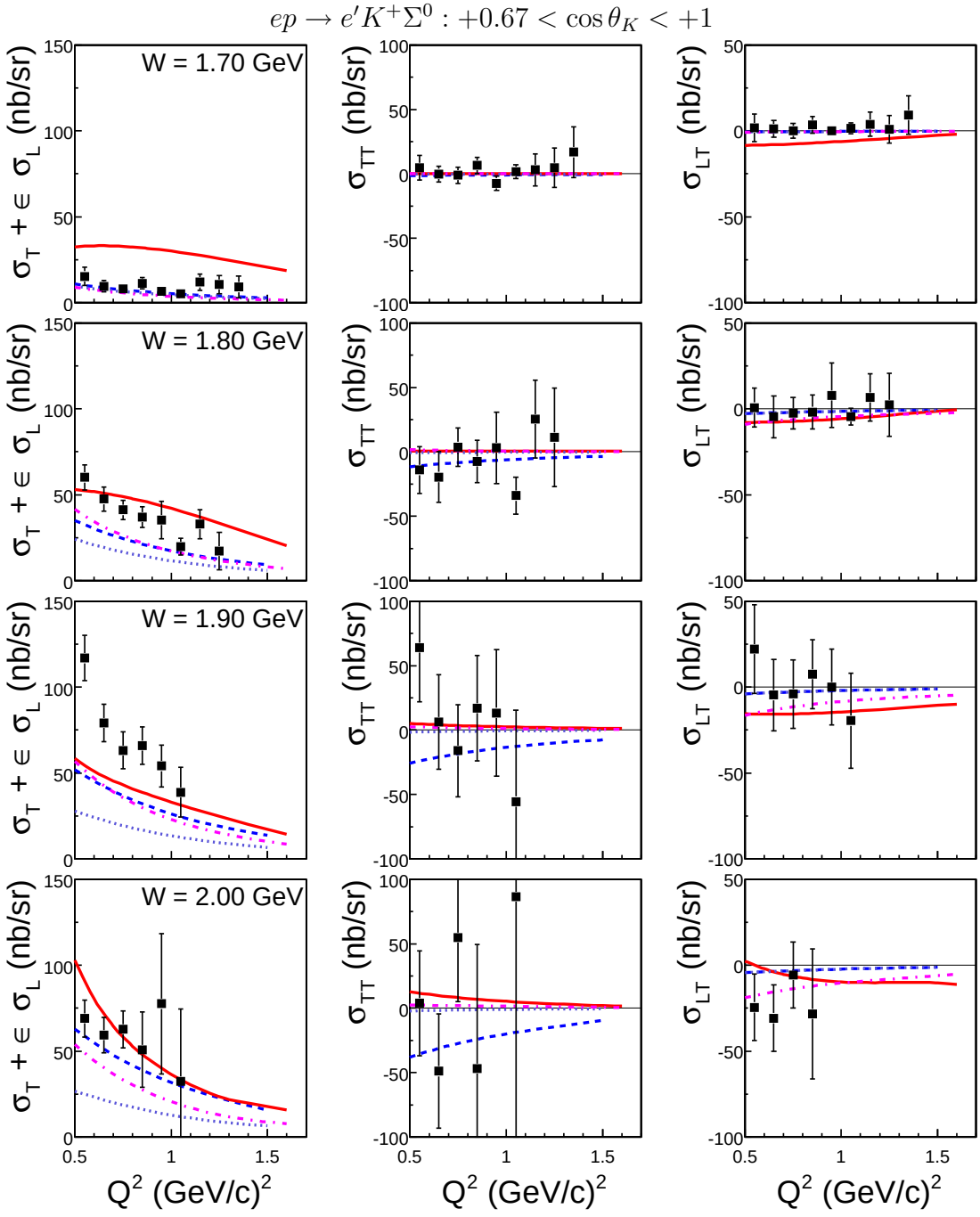

Figure 5.15: The response functions of Σ^0 electroproduction versus Q^2 for $0.67 < \cos\theta_K < 1$, and 100 MeV wide bins in W. The curves are described in Figure 5.9.

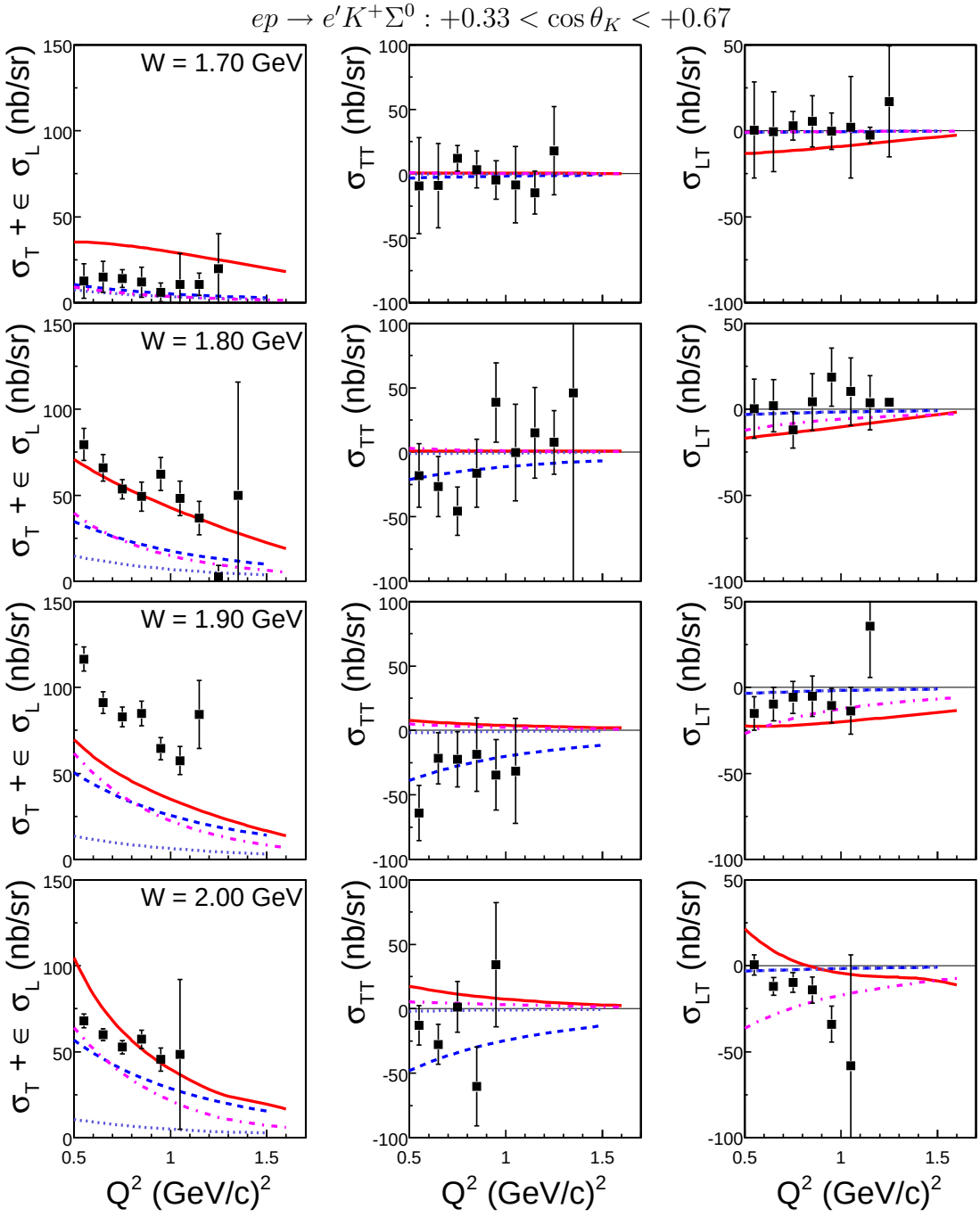

Figure 5.16: The response functions of Σ^0 electroproduction versus Q^2 for $0.33 < \cos\theta_K < 0.67$ and 100 MeV wide bins in W. The curves are described in Figure 5.9.

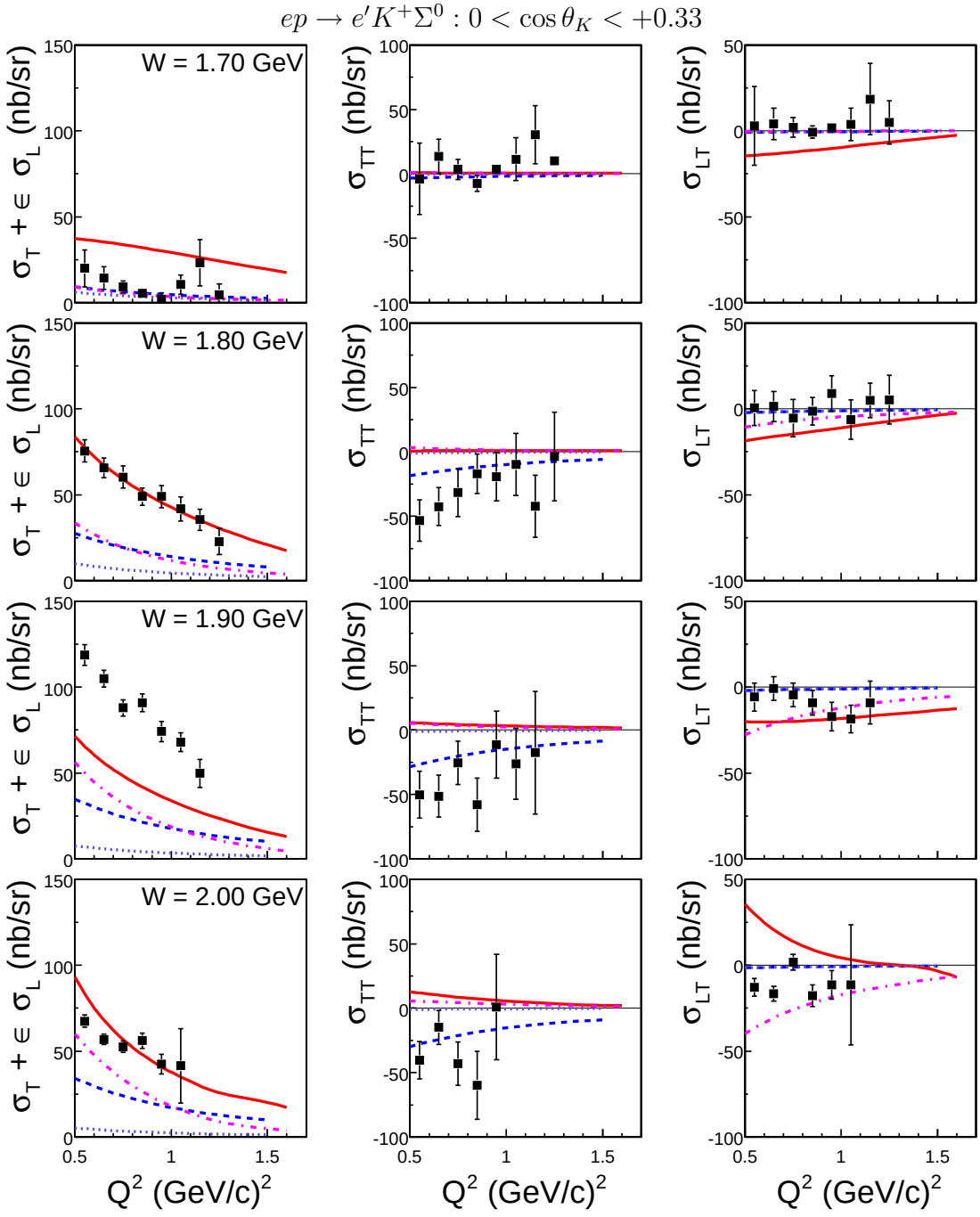

Figure 5.17: The response functions of Σ^0 electroproduction versus Q^2 for $0 < \cos\theta_K < 0.33$ and 100 MeV wide bins in W. The curves are described in Figure 5.9.

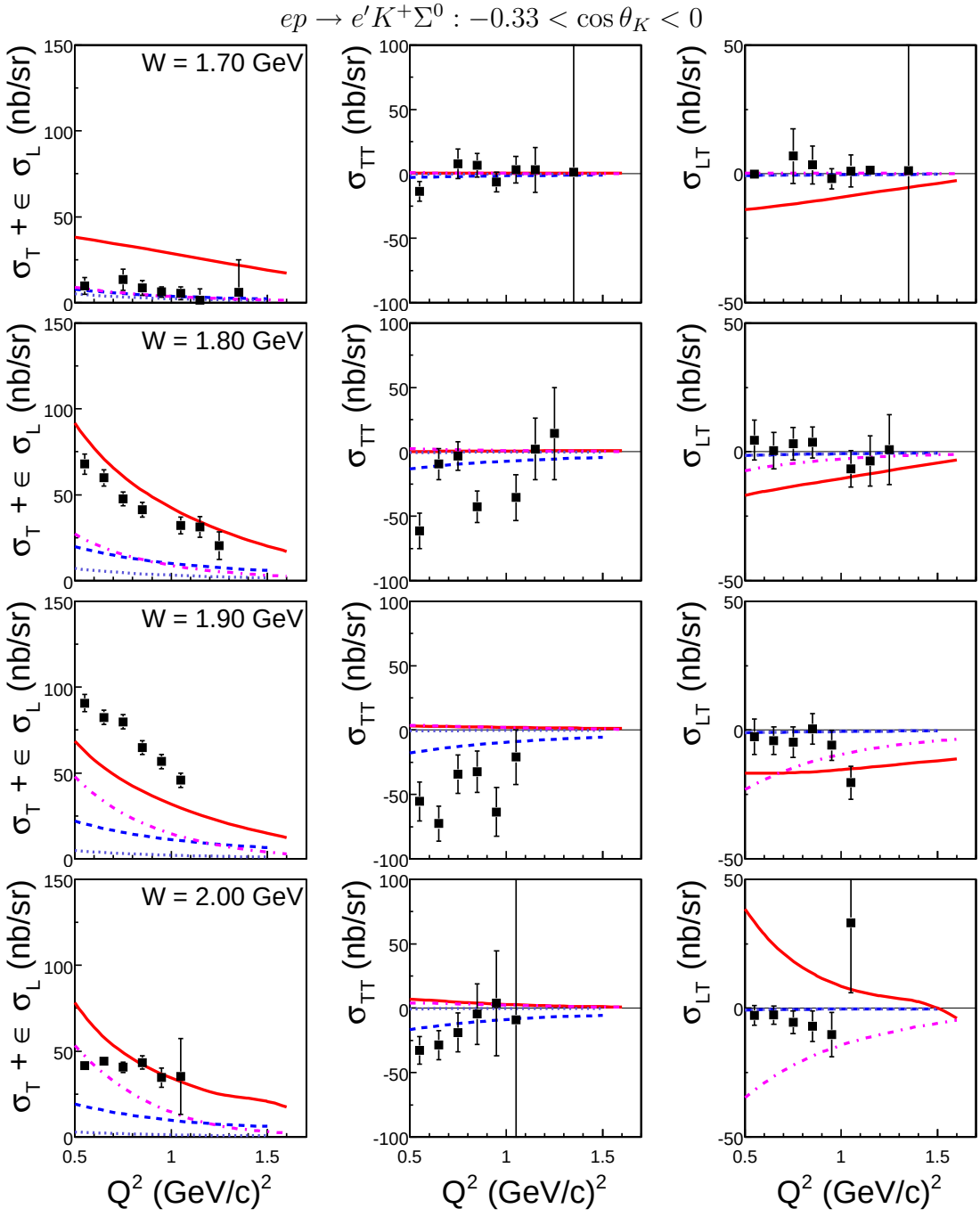

Figure 5.18: The response functions of Σ^0 electroproduction versus Q^2 for $-0.33 < \cos\theta_K < 0$ and 100 MeV wide bins in W. The curves are described in Figure 5.9.

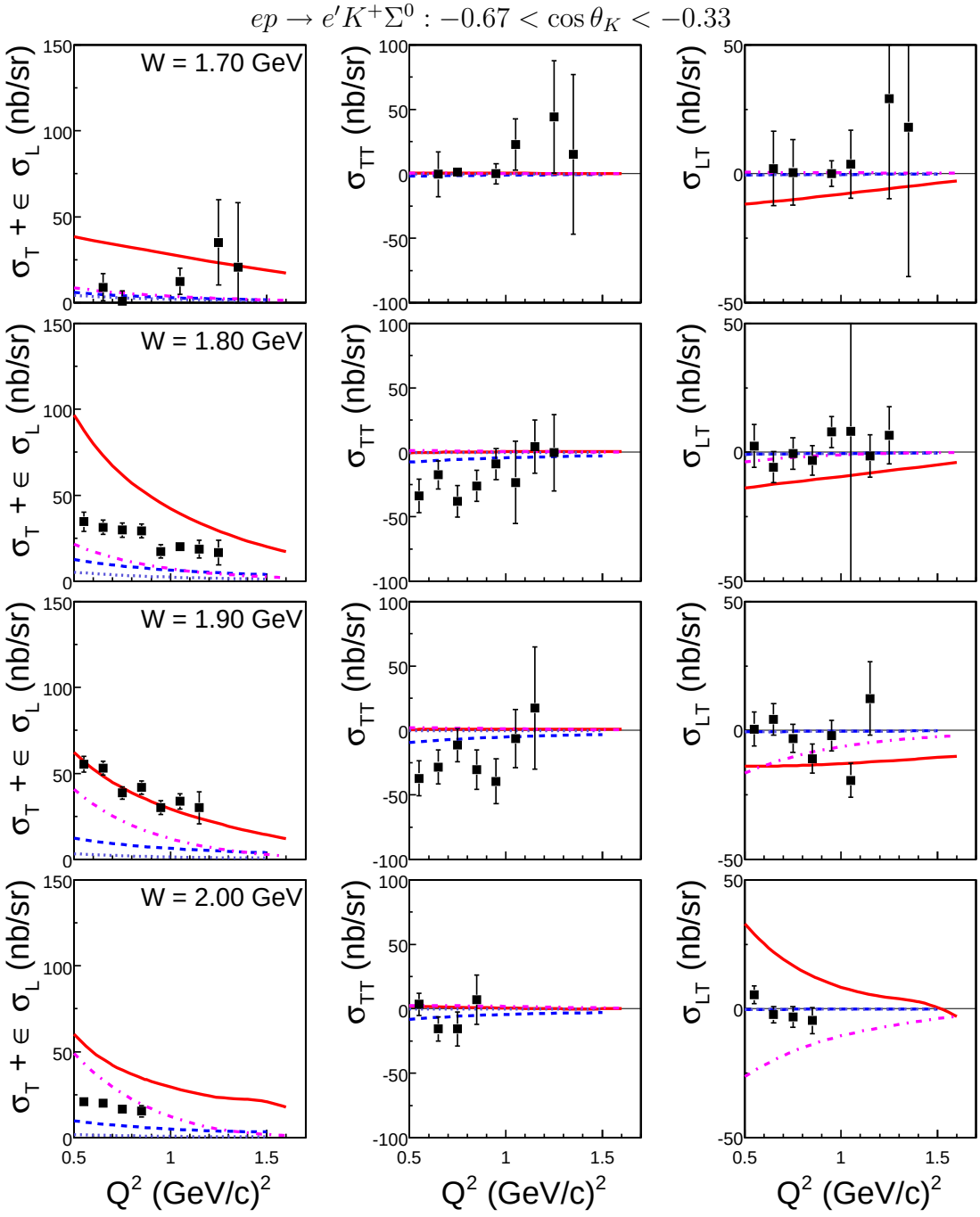

Figure 5.19: The response functions of Σ^0 electroproduction versus Q^2 for $-0.67 < \cos\theta_K < -0.33$ and 100 MeV wide bins in W. The curves are described in Figure 5.9.

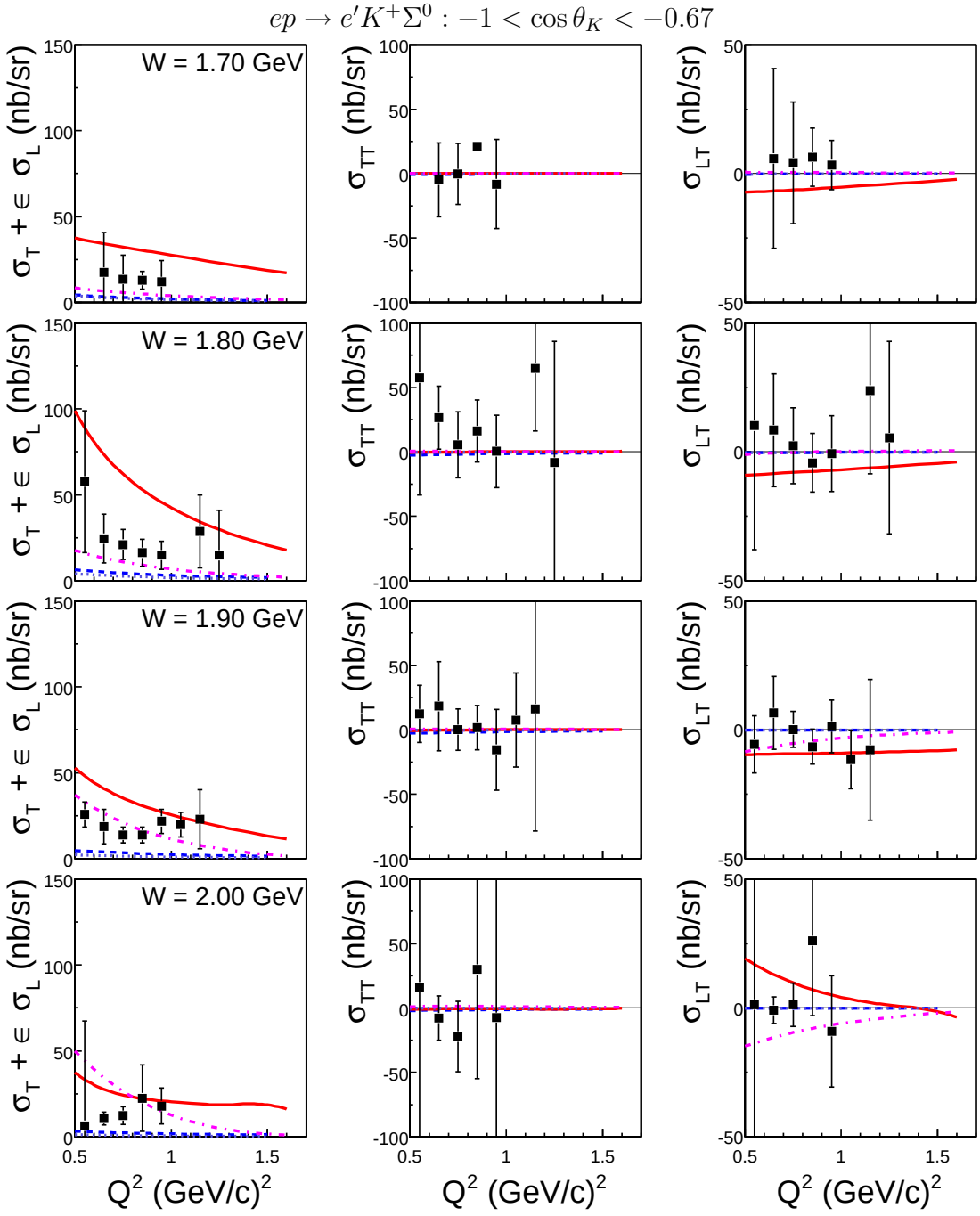

Figure 5.20: The response functions of Σ^0 electroproduction versus Q^2 for $-1 < \cos\theta_K < -0.67$ and 100 MeV wide bins in W. The curves are described in Figure 5.9.

5.5 Summary

Overall, the calculations compared with the new data presented in this thesis, while describing qualitatively the rise and fall of the unseparated differential cross-section, fail to explain the response functions at a quantitative level. In addition, several features in the W dependence of the Λ and Σ^0 electroproduction response functions and their implications, have been discussed.

Chapter 6

Conclusions

This experiment measured the $K^+ \Lambda$ and $K^+ \Sigma^0$ electroproduction reactions with unprecedented angular coverage in the center-of-momentum frame, taking advantage of the large acceptance of the CLAS detector at Jefferson Laboratory. Using a 2.567 GeV continuous electron beam, a large dataset spanning W continuously from threshold to 2.0 GeV and Q^2 from 0.5 to 1.5 $(\mathrm{GeV/c})^2$ was collected. Due to the large angular acceptance the differential cross-section $\sigma_T + \epsilon\sigma_L$, as well as the σ_{TT} and σ_{LT} response functions, could be extracted across this kinematic region for the production of the two hyperons.

For the $K^+ \Lambda$ final state, we measure values for the σ_{LT} and σ_{TT} response functions comparable in size to $\sigma_T + \epsilon\sigma_L$. We thus conclude that couplings to both the longitudinal and transverse polarization states of the virtual photon play an important part in Λ electroproduction, consistent with prior measurements and the current theoretical understanding. However, the Q^2 and $\cos\theta_K$ distributions of the cross-sections show significant discrepancies between the predicted and observed magnitudes of the $\sigma_T + \epsilon\sigma_L$ term, especially in the forward direction and across many W bins. We speculate that this might be due to a poor estimation of the σ_L response function in present models. In the backward direction, the $K^+ \Lambda$ final state's W dependence contains a large "bump" around $W = 1.9$ GeV. While a similar structure, seen in a recent photo-production measurement [8], was claimed to be a missing resonance state [9], we believe other interpretations of the structure are likely to be correct. In particular, a comparison to a Regge-model calculation [20] suggests the key feature in the W distribution is not the "bump" at $W = 1.9$ GeV, but instead the depleted region near $W = 1.75$ GeV.

In the $K^+ \Sigma^0$ final state a number of observations are also made. First, the magnitude of Σ^0 production is vastly underestimated by the existing models. Next, the σ_{LT} interference term is consistent with zero across the kinematic range while σ_{TT} is large, suggesting the Σ^0 couples most strongly to the transverse component of the virtual photon's polarization. Third, large variations of $(\sigma_T + \epsilon\sigma_L)$ and σ_{TT} with W point to a large s-channel resonant contribution to the production process. Since the $K^+ \Sigma^0$ state can couple to both N^* and Δ^* resonances, and a similar structure

is not seen in the $K^+\,\Lambda$ channel, this feature is likely due to a Δ^* resonance with a mass near $1900\,\mathrm{MeV/c^2}$. Previous partial-wave analyses of $\pi^+ p$ scattering implicates a $P_{33}(1920)$ state which had been found to couple strongly to $K\Sigma$ states [74]. This state was not included in the model calculations used for comparison to the present results.

The results of this measurement provide severe constraints on models built to calculate and study hyperon electroproduction. This, in turn, will contribute to the effort to better understand QCD in this low energy, non-perturbative region.

Bibliography

[1] W. Melnitchouk et al. Baryon resonances from a novel fat-link fermion action. *Nucl. Phys. Proc. Suppl.*, 109:96–100, 2002.

[2] J.M. Zanotti et al. Spin-3/2 baryons in lattice QCD. 2002.

[3] R. A. Adelseck, C. Bennhold, and L. E. Wright. Kaon photoproduction operator for use in nuclear physics. *Phys. Rev.*, C32:1681–1692, 1985.

[4] R. A. Adelseck and L. E. Wright. Electromagnetic production of kaons. *Phys. Rev.*, C38:1965–1967, 1988.

[5] R. A. Adelseck and B. Saghai. Kaon photoproduction: Data consistency, coupling constants, and polarization observables. *Phys. Rev.*, C42:108–127, 1990.

[6] R. A. Williams, C. R. Ji, and S. R. Cotanch. Hyperon electroproduction in a crossing and duality constrained model. *Phys. Rev.*, C46:1617–1635, 1992.

[7] J. C. David, C. Fayard, G. H. Lamot, and B. Saghai. Electromagnetic production of associated strangeness. *Phys. Rev.*, C53:2613–2637, 1996.

[8] M. Q. Tran et al. Measurement of $\gamma p \to K^+\Lambda$ and $\gamma p \to K^+\Sigma^0$ at photon energies up to 2-GeV. *Phys. Lett.*, B445:20–26, 1998.

[9] T. Mart and C. Bennhold. Evidence for a missing nucleon resonance in kaon photoproduction. *Phys. Rev.*, C61:012201, 2000.

[10] S. Capstick and W. Roberts. Strange decays of nonstrange baryons. *Phys. Rev.*, D58:074011, 1998.

[11] A. S. Raskin and T. W. Donnelly. Polarization in coincidence electron scattering from nuclei. *Ann. Phys.*, 191:78, 1989.

[12] C. W. Akerlof, W. W. Ash, K. Berkelman, and C.A. Lichtenstein. Measurement of the pion form factor. *Phys. Rev.*, 163(5):1482–1497, 1967.

[13] R. C. E. Devenish and D. H. Lyth. Single π^+ electroproduction at W approximately 2-GeV and the pion form-factor. *Phys. Rev.*, D5:47, 1972.

[14] G. Knochlein, D. Drechsel, and L. Tiator. Photoproduction and electroproduction of eta mesons. *Z. Phys.*, A352:327–343, 1995.

[15] C. N. Brown et al. Coincidence measurements of single K^+ electroproduction. *Phys. Rev. Lett.*, 28:1086–1089, 1972.

[16] T. Azemoon et al. Production of hyperons by virtual photons. *Nucl. Phys.*, B95:77, 1975.

[17] C. J. Bebek et al. Scalar - transverse separation of electroproduced $K^+\Lambda$ and $K^+\Sigma^0$ final states. *Phys. Rev.*, D15:3082, 1977.

[18] P. Brauel et al. Electroproduction of $\pi^+ n$, $\pi^- p$ and $K^+\Lambda, K^+\Sigma^0$ final states above the resonance region. *Zeit. Phys.*, C3:101, 1979.

[19] G. Niculescu, R.M. Mohring, et al. Longitudinal and transverse cross sections in the $H_1(e, e'K^+)\Lambda$ reaction. *Phys. Rev. Lett.*, 81:1805–1808, 1998.

[20] M. Guidal, J. M. Laget, and M. Vanderhaeghen. Electroproduction of strangeness above the resonance region. *Phys. Rev.*, C61:025204, 2000.

[21] C. J. Bebek et al. Electroproduction of K^+ mesons in the forward direction. (talk). *Phys. Rev. Lett.*, 32:21–24, 1974.

[22] P. Feller, D. Menze, U. Opara, W. Schulz, and W. J. Schwille. Photoproduction of $K^+\Lambda^0$ and $K^+\Sigma^0$ from hydrogen at constant momentum transfer t between 1.05 and 2.2 GeV. *Nucl. Phys.*, B39:413–420, 1972.

[23] G.N. Fleming. Recoupling effects in the isobar model. I. General formalism for three-pion scattering. *Phys. Rev.*, 135(2B):B551–560, July 1964.

[24] C. Bennhold, H. Haberzettl, and T. Mart. A new resonance in $K^+\Lambda$ electroproduction: The $D_{13}(1895)$ and its electromagnetic form factors. 1999. An extension to the model was provided; private communication.

[25] S. Janssen, J. Ryckebusch, W. Van Nespen, D. Debruyne, and T. Van Cauteren. The role of hyperon resonances in $p(\gamma, K^+)\Lambda$ processes. *Eur. Phys. J.*, A11:105–111, 2001.

[26] T. Feuster and U. Mosel. A unitary model for meson nucleon scattering. *Phys. Rev.*, C58:457–488, 1998.

[27] Wen-Tai Chiang, F. Tabakin, T. S. H. Lee, and B. Saghai. Coupled-channel study of $\gamma p \to K^+\Lambda$. *Phys. Lett.*, B517:101–108, 2001.

[28] M. Guidal, J. M. Laget, and M. Vanderhaeghen. Pion and kaon photoproduction at high energies: Forward and intermediate angles. *Nucl. Phys.*, A627:645–678, 1997.

[29] F. X. Lee, T. Mart, C. Bennhold, and L. E. Wright. Quasifree kaon photoproduction on nuclei. *Nucl. Phys.*, A695:237–272, 2001.

[30] S. Janssen, J. Ryckebusch, D. Debruyne, and T. Van Cauteren. Kaon photoproduction: Background contributions, form factors, and missing resonances. *Phys. Rev.*, C65:015201, 2001.

[31] H. Haberzettl, C. Bennhold, and T. Mart. Gauge - invariant description of photoproduction and electroproduction of mesons with extended nucleons applied to kaon production. *Nucl. Phys.*, A684:475–477, 2001.

[32] B. Saghai. From known to undiscovered resonances. 2001.

[33] S. Janssen, J. Ryckebusch, D. Debruyne, and T. Van Cauteren. Σ photoproduction in the resonance region. *Phys. Rev.*, C66:035202, 2002.

[34] Stijn Janssen. *Strangeness Production on the Nucleon.* PhD thesis, Universiteit Gent, 2002.

[35] T. Regge. Introduction to complex orbital momenta. *Nuovo Cim.*, 14:951, 1959.

[36] H.A. Grunder. CEBAF commissioning and future plans. In *Particle Accelerator Conference 1995*, pages 1–3, May 1995.

[37] B.M. Dunham, P. Hartmann, H. Liu, B.M. Poelker, J.S. Price, P.M. Rutt, W.J. Schneider, and C.K. Sinclair. Advances in DC photocathode electron guns. JLAB-ACP 1998-02, Jefferson Laboratory, 1998.

[38] S. Gagnon. Jefferson Lab site tour. http://education.jlab.org/sitetour, Jefferson Laboratory, 2002.

[39] B.M. Dunham. Jefferson Lab, a status report. ACC 1996-01, Jefferson Laboratory, 1996.

[40] G. A. Krafft, J.-C. Denard, R. W. Dickson, R. Kazimi, V. A. Lebedev, and M. G. Tiefenback. Measuring and controlling energy spread in CEBAF. 2000.

[41] C.E. Reece. Achieving 800 kW CW beam power and continuing energy improvements in CEBAF. In *LINAC 1998*, pages 448–450, 1998.

[42] B. Mecking et al. The CEBAF large acceptance spectrometer. To be submitted to Nuclear Instruments and Methods in Physics Research A.

[43] R. Ursic, R. Flood, C. Piller, E. Strong, and L. Turlington. 1 nA beam position monitoring system. In *Particle Accelerator Conference 1997*, pages 2131–2133, May 1997.

[44] A. Freyberger. Electron beam profile measurement. http://claspc1.jlab.org/PROCEDURES/electron_beam_profile_scan, December 2001. CLAS Shift documentation.

[45] A. Freyberger. Beamline scalers troubleshooting guide. http://claspc1.jlab.org/TSG/beamline_scalers, November 2000. CLAS Shift documentation.

[46] R. Bradford and R.A. Schumacher. Liquid H_2 density in the g1c CLAS cryotarget. CLAS-NOTE 2002-003, Jefferson Laboratory, 2002.

[47] M.D. Mestayer et al. The CLAS drift chamber system. *Nuclear Instruments and Methods in Physics Research A*, 449:81 – 111, 2000.

[48] G. Adams et al. The CLAS Čerenkov detector. *Nuclear Instruments and Methods in Physics Research A*, 465:414 – 427, 2001.

[49] E. Smith et al. The time-of-flight system for CLAS. *Nuclear Instruments and Methods in Physics Research A*, 432:265 – 298, 1999.

[50] M. Amarian, G. Asryan, K. Beard, et al. The CLAS forward electromagnetic calorimeter. *Nuclear Instruments and Methods in Physics Research A*, 460:239 – 265, 2001.

[51] J.S.H. Ross, K.D. Smith, A.J. Street, et al. Development in the design of the superconducting toroidal magnet for the continuous electron beam acclerator facility (CEBAF) large acceptance spectrometer. CLAS-NOTE 1992-015, Jefferson Laboratory, 1992.

[52] D. Lawrence and M. Mestayer. CLAS drift chamber calibration: Software and procedures. CLAS-NOTE 1999-018, Jefferson Laboratory, 1999.

[53] V. Burkert. e1b/c run-period status reports. http://clasweb.jlab.org/e1/e1b_web.html, 1999.

[54] J.J. Manak, E.S. Smith, S. McAleer, and S. Barrow. e1, g1, and g6 Data processing procedures. CLAS-NOTE 1999-016, Jefferson Laboratory, 1999.

[55] B.B. Niczyporuk. Track fitting in an inhomogeneous magnetic field. CEBAF-PR 1991-004, Jefferson Laboratory, 1991.

[56] John William Clark McNabb. *Photoproduction of Λ and Σ^0 Hyperons off Protons in the Nucleon Resonance Region using CLAS at Jefferson Lab.* PhD thesis, Carnegie Mellon University, 2002.

[57] K. Y. Kim, H. Denizli, J. A. Mueller, and S. A. Dytman. General momentum correction form for CLAS: A study of momentum corrections for the prod 1-9 cooking of e1c data. CLAS-NOTE 2001-018, Jefferson Laboratory, 2001.

[58] A. Vlassov. CLAS Čerenkov detector efficiency based on the e1b run-period (1999). http://www.jlab.org/ vlassov/cc/cc_e1b_eff/e1b_1500.html, 1999.

[59] K.S. Egiyan. Determination of the electron energy cut due to the CLAS EC threshold. CLAS-NOTE 1999-007, Jefferson Laboratory, 1999.

[60] C. Smith and K. Joo. Single π° electroproduction in the $\Delta(1232)$ resonance from e1a data. CLAS-ANALYSIS-NOTE 2001-008, University of Virginia, 2001.

[61] D. E. Groom et al. Review of particle physics. *Eur. Phys. J.*, C15:1–878, 2000.

[62] Richard Thompson. *η Electroproduction in the Region of the Isospin 1/2, Spin 1/2 1535MeV Baryon Resonance*. PhD thesis, University of Pittsburgh, 2000.

[63] R. Ent et al. Radiative corrections for (e,e' p) reactions at GeV energies. *Phys. Rev.*, C64:054610, 2001.

[64] Philip R. Bevington and D. Keith Robinson. *Data Reduction and Error Analysis for the Physical Sciences*. McGraw-Hill, second edition, 1992.

[65] Stephen Andrew Wood. *An Experimental Study of Inclusive Pion Double Charge Exchange Reactions in the Delta Resonance Region*. PhD thesis, Massachusetts Institute of Technology, 1983.

[66] G.J. Feldman and R.D. Cousins. A unified approach to the classical statistical analysis of small signals. *Phys. Rev.*, D57:3873–3889, 1998.

[67] CERN. *GEANT – Detector Description and Simulation Tool*, it/asd W5013 edition, 1995.

[68] S. Kuhn. Email to the eg1 group. An idea for evaluating systematic errors when tightening cuts.

[69] Gabriel Niculescu. Private communcation.

[70] T. Mart and C. Bennhold. Kaon and hyperon form factors in kaon electroproduction on the nucleon. *Nucl. Phys.*, A639:237–246, 1998.

[71] R. A. Williams, C. R. Ji, and S. R. Cotanch. Crossing and duality consistent study of Λ, Σ^0, and $\Lambda(1405)$ production by kaon photoproduction and radiative capture. *Phys. Rev.*, C43:452–455, 1991.

[72] Michel Guidal. Only K-exchange (no K^*) was permitted in the Regge calculation. Private communication.

[73] Stijn Janssen. Strangeness production on the nucleon, 2002.

[74] D. J. Candlin et al. An energy dependent partial wave analysis of $\pi^+ p$ to $K^+\Sigma^+$ between threshold and 2.35-GeV. *Nucl. Phys.*, B238:477, 1984.

[75] K. Hagiwara et al. Review of particle physics. *Phys. Rev.*, D66:010001, 2002.

[76] R. Feuerbach, J. McNabb, M. Mestayer, R. Schumacher, and A. Skabelin. Drift chamber alignment, version 0.1. CLAS-NOTE 1998-002, Jefferson Laboratory, 1998.

[77] James Mueller. Private communication. A tracking code error was present where the more forward wires were preferentially picked when constructing tracks.

Appendix A

Λ Electroproduction Response Functions

This chapter contains the final values for the extracted $\sigma_T + \epsilon\sigma_L$, σ_{TT} and σ_{LT} terms of the $ep \to e'K^+\Lambda$ reaction, with an incident 2.567 GeV electron beam. The results for the three primary binnings of the data are each presented in the same format. The first four columns provide the location of the center of the kinematic bin. The next six columns contain the fitted values of the response functions, with their associated uncertainty. The quoted uncertainties include the estimated point-to-point systematic errors, but not the 3.3% scale factor due to the uncertainty on the absolute value of the integrated luminosity. Bins for which the structure functions could not be extracted are excluded from the listing. When using these results, please keep in mind that all three result sets were determined from the same data; they are not three independent measurements.

The values are given in GeV and $(\mathrm{GeV/c})^2$ for W and Q^2, respectively, and in nb/sr for the structure functions and their quoted uncertainty.

A.1 Response Functions for Narrow Cos(θ_K) Bins

The results are given for bins with full-widths of 100 MeV in W, 0.40 $(\mathrm{GeV/c})^2$ in Q^2, and 1/5 in $\cos\theta_K$.

# W	Q2	eps	CosTh	SigU	err	SigTT	err	SigLT	err
1.700	0.70	0.660	-0.700	86.7	7.4	-7.4	7.5	-15.1	17.2
1.700	0.70	0.660	-0.500	83.2	5.6	-20.4	5.1	-48.8	13.3
1.700	0.70	0.660	-0.300	98.2	5.3	-12.7	5.3	-8.9	12.7
1.700	0.70	0.660	-0.100	112.4	5.7	-29.1	5.6	-35.9	13.7
1.700	0.70	0.660	0.100	132.0	6.0	-32.7	6.2	-38.9	14.7
1.700	0.70	0.660	0.300	163.1	10.1	-33.7	12.3	-42.7	25.4
1.700	0.70	0.660	0.500	186.3	7.9	-43.3	7.9	-65.4	19.6
1.700	0.70	0.660	0.700	235.0	12.6	-21.5	14.3	-10.0	29.8
1.700	0.70	0.660	0.900	275.6	9.4	-39.5	8.6	-24.9	22.4

1.800	0.70	0.570	-0.900	6.6	105.7	0.9	87.7	2.6	291.1
1.800	0.70	0.570	-0.700	45.2	3.5	-10.1	3.8	-9.0	9.8
1.800	0.70	0.570	-0.500	66.5	3.8	-14.2	4.0	-3.5	10.6
1.800	0.70	0.570	-0.300	85.6	4.0	-19.8	3.9	-25.7	10.9
1.800	0.70	0.570	-0.100	106.5	5.4	-29.4	6.3	-11.3	14.3
1.800	0.70	0.570	0.100	135.0	5.8	-34.7	5.7	-25.1	15.9
1.800	0.70	0.570	0.300	148.4	7.4	-37.7	8.0	-67.6	20.0
1.800	0.70	0.570	0.500	206.9	9.4	-28.3	12.9	-23.8	28.9
1.800	0.70	0.570	0.700	238.2	16.3	-49.1	27.8	-78.9	61.3
1.800	0.70	0.570	0.900	301.1	10.2	-54.6	10.3	-89.8	27.9
1.900	0.70	0.460	-0.900	34.4	7.7	2.9	9.6	-16.7	25.5
1.900	0.70	0.460	-0.700	52.3	2.9	-0.0	3.5	-19.8	9.9
1.900	0.70	0.460	-0.500	57.6	2.9	-13.5	3.9	19.9	9.9
1.900	0.70	0.460	-0.300	55.8	2.5	-11.7	3.2	-2.5	8.5
1.900	0.70	0.460	-0.100	73.4	3.2	-22.6	3.8	-13.5	10.6
1.900	0.70	0.460	0.100	96.9	3.6	-24.0	4.0	-45.9	12.0
1.900	0.70	0.460	0.300	116.7	4.1	-18.8	4.7	-74.2	13.9
1.900	0.70	0.460	0.500	142.9	5.1	-17.8	6.3	-63.1	17.6
1.900	0.70	0.460	0.700	191.4	12.7	-19.0	20.9	-75.8	45.3
1.900	0.70	0.460	0.900	226.3	10.2	-111.8	14.0	-179.6	35.5
2.000	0.70	0.329	-0.900	24.8	4.4	6.2	6.9	-20.2	20.8
2.000	0.70	0.329	-0.700	30.8	1.8	9.8	2.7	-24.6	8.6
2.000	0.70	0.329	-0.500	20.8	1.3	-0.8	1.9	-17.5	6.2
2.000	0.70	0.329	-0.300	20.6	1.3	-4.5	2.0	-12.6	6.0
2.000	0.70	0.329	-0.100	34.5	1.6	-10.2	2.5	-12.5	7.7
2.000	0.70	0.329	0.100	54.5	2.2	-12.4	3.2	-44.2	10.5
2.000	0.70	0.329	0.300	76.2	2.7	-13.0	3.8	-71.8	13.0
2.000	0.70	0.329	0.500	99.8	3.7	-11.2	5.3	-86.5	17.3
2.000	0.70	0.329	0.700	139.3	5.9	-9.0	10.3	-86.5	28.3
2.000	0.70	0.329	0.900	172.5	15.9	-90.2	33.0	-172.9	78.9
1.700	1.10	0.517	-0.900	28.9	18.6	-11.0	27.0	-27.9	46.8
1.700	1.10	0.517	-0.700	56.3	6.2	-21.1	7.8	-11.5	19.4
1.700	1.10	0.517	-0.500	54.0	5.2	-21.3	7.1	7.6	17.5
1.700	1.10	0.517	-0.300	63.8	5.0	-8.1	5.8	-25.0	14.8
1.700	1.10	0.517	-0.100	76.8	6.3	-24.1	8.1	-20.6	19.0
1.700	1.10	0.517	0.100	103.1	7.9	-29.1	11.0	-37.8	25.1
1.700	1.10	0.517	0.300	114.9	10.0	-23.5	14.0	-15.2	30.6
1.700	1.10	0.517	0.500	143.2	9.1	-35.9	12.6	-39.8	28.6
1.700	1.10	0.517	0.700	176.3	10.9	-52.6	13.6	-101.3	31.8
1.700	1.10	0.517	0.900	204.5	8.4	-29.2	9.6	-12.6	25.5
1.800	1.10	0.413	-0.900	9.4	5.9	2.8	9.6	5.5	23.0
1.800	1.10	0.413	-0.700	31.0	3.5	-6.2	4.9	0.3	13.2
1.800	1.10	0.413	-0.500	47.4	3.7	-27.0	5.4	29.6	14.2
1.800	1.10	0.413	-0.300	56.7	3.5	-22.0	4.4	-35.6	13.4
1.800	1.10	0.413	-0.100	83.2	4.6	-28.6	6.1	-34.5	17.3
1.800	1.10	0.413	0.100	101.0	5.2	-28.0	7.0	-11.2	19.7
1.800	1.10	0.413	0.300	138.5	6.7	-31.6	9.3	-23.3	25.0
1.800	1.10	0.413	0.500	165.2	13.0	-19.3	22.4	0.5	51.5
1.800	1.10	0.413	0.700	202.3	16.3	-17.0	28.1	-22.5	61.9
1.800	1.10	0.413	0.900	225.6	9.5	-70.3	12.4	-72.7	35.9

1.900	1.10	0.290	-0.900	18.5	7.7	-7.1	14.1	2.6	39.7
1.900	1.10	0.290	-0.700	31.9	3.5	-12.7	5.3	-34.6	18.7
1.900	1.10	0.290	-0.500	31.4	3.1	-13.7	5.3	-21.7	16.5
1.900	1.10	0.290	-0.300	37.9	2.9	-21.2	4.7	-25.9	16.1
1.900	1.10	0.290	-0.100	55.0	3.4	-26.2	5.4	-43.4	18.2
1.900	1.10	0.290	0.100	79.8	4.5	-25.7	7.1	-24.4	24.1
1.900	1.10	0.290	0.300	90.0	5.1	-20.8	8.4	-7.5	27.5
1.900	1.10	0.290	0.500	114.3	6.8	-34.4	12.2	-116.3	36.4
1.900	1.10	0.290	0.700	147.7	14.1	-14.5	31.7	-48.9	80.6

A.2 Response Functions for Narrow W Bins

The results are given for bins with full-widths of 25 MeV in W, 0.40 $(\mathrm{GeV/c})^2$ in Q^2, and 1/3 in $\cos\theta_K$.

# W	Q2	eps	CosTh	SigU	err	SigTT	err	SigLT	err
1.613	0.70	0.724	-0.833	10.9	7.5	0.8	9.9	-3.7	20.3
1.613	0.70	0.724	-0.500	17.4	8.2	-0.2	5.3	-11.6	18.2
1.613	0.70	0.724	-0.167	13.0	5.3	-3.1	3.7	-2.5	11.7
1.613	0.70	0.724	0.167	10.1	3.4	-1.6	3.5	4.5	7.8
1.613	0.70	0.724	0.500	10.9	4.6	-1.0	5.4	4.8	11.5
1.613	0.70	0.724	0.833	15.5	3.7	-3.5	2.9	2.8	8.4
1.637	0.70	0.707	-0.833	41.1	10.0	-17.2	9.3	12.1	22.4
1.637	0.70	0.707	-0.500	49.2	10.3	-14.1	10.0	-25.5	25.7
1.637	0.70	0.707	-0.167	73.2	15.6	17.0	18.2	38.5	32.5
1.637	0.70	0.707	0.167	48.1	11.4	-6.4	13.1	-17.0	27.0
1.637	0.70	0.707	0.500	65.5	19.3	12.3	20.5	42.0	27.6
1.637	0.70	0.707	0.833	59.7	5.9	-5.4	5.1	-10.1	12.9
1.663	0.70	0.689	-0.833	36.9	19.3	-1.9	23.8	9.6	46.6
1.663	0.70	0.689	-0.500	81.6	9.1	-18.4	8.7	-38.9	21.0
1.663	0.70	0.689	-0.167	76.5	7.7	-23.3	7.2	-35.9	17.5
1.663	0.70	0.689	0.167	107.3	9.2	-22.7	9.2	-29.2	21.0
1.663	0.70	0.689	0.500	128.4	12.7	-25.3	12.4	-71.0	28.0
1.663	0.70	0.689	0.833	150.5	9.0	-15.8	7.9	-5.3	20.5
1.688	0.70	0.670	-0.500	98.7	10.1	-24.9	10.2	-25.0	23.3
1.688	0.70	0.670	-0.167	117.1	10.2	-33.0	11.1	-45.0	24.3
1.688	0.70	0.670	0.167	129.6	9.1	-43.0	10.1	-32.8	22.6
1.688	0.70	0.670	0.500	170.9	10.5	-49.9	10.7	-86.3	25.9
1.688	0.70	0.670	0.833	225.3	11.5	-32.6	10.6	11.6	26.7
1.712	0.70	0.650	-0.833	48.9	13.1	-13.5	11.7	-7.3	31.6
1.712	0.70	0.650	-0.500	78.3	8.7	-5.5	9.3	2.1	20.2
1.712	0.70	0.650	-0.167	93.8	7.6	-37.1	7.5	-32.2	18.1
1.712	0.70	0.650	0.167	159.5	14.9	-27.2	19.5	-55.6	39.0
1.712	0.70	0.650	0.500	201.0	12.1	-58.3	13.1	-71.5	29.8
1.712	0.70	0.650	0.833	289.1	12.6	-76.7	11.5	-21.6	30.6
1.738	0.70	0.629	-0.833	29.2	9.4	0.1	8.1	-18.7	23.4
1.738	0.70	0.629	-0.500	57.5	6.4	-19.0	6.8	-13.2	16.0
1.738	0.70	0.629	-0.167	97.8	6.5	-33.3	6.7	-22.7	16.6
1.738	0.70	0.629	0.167	170.1	10.0	-38.7	11.5	-32.8	26.0
1.738	0.70	0.629	0.500	214.7	12.9	-74.3	15.7	-131.1	35.6
1.738	0.70	0.629	0.833	329.6	15.0	-69.5	12.9	-78.5	37.4
1.762	0.70	0.606	-0.833	20.4	13.0	0.2	16.4	-2.7	30.0
1.762	0.70	0.606	-0.500	52.0	5.4	-17.6	5.9	-2.8	14.0
1.762	0.70	0.606	-0.167	100.4	6.1	-29.4	6.3	-10.0	15.7
1.762	0.70	0.606	0.167	149.4	7.7	-36.2	7.7	-54.4	19.9
1.762	0.70	0.606	0.500	199.1	14.7	-69.1	19.1	-101.1	41.2
1.762	0.70	0.606	0.833	321.2	13.5	-50.4	13.0	-75.6	34.7
1.788	0.70	0.583	-0.833	28.5	9.0	-1.3	9.7	-6.0	23.0
1.788	0.70	0.583	-0.500	51.9	4.9	-14.3	5.0	-28.5	13.2
1.788	0.70	0.583	-0.167	100.1	5.8	-24.7	6.0	-22.4	15.6

1.788	0.70	0.583	0.500	220.1	17.2	-13.2	24.1	-5.1	49.3
1.788	0.70	0.583	0.833	289.9	14.7	-72.9	11.9	-109.9	39.6
1.812	0.70	0.558	-0.833	26.6	7.0	-5.8	7.9	-7.2	19.6
1.812	0.70	0.558	-0.500	64.0	5.0	-18.6	5.6	-12.0	14.0
1.812	0.70	0.558	-0.167	101.7	5.8	-20.2	6.1	-46.6	16.4
1.812	0.70	0.558	0.167	153.5	13.4	-41.2	17.8	-34.4	34.8
1.812	0.70	0.558	0.500	182.4	10.4	-34.8	13.4	-43.6	30.7
1.812	0.70	0.558	0.833	241.2	10.9	-82.8	10.7	-172.7	30.8
1.837	0.70	0.532	-0.833	15.9	5.0	-1.9	5.0	-13.1	14.8
1.837	0.70	0.532	-0.500	75.0	5.1	-21.7	6.0	-0.4	15.2
1.837	0.70	0.532	-0.167	84.4	4.7	-22.4	5.3	-17.4	14.0
1.837	0.70	0.532	0.167	135.2	6.7	-31.8	7.8	-18.5	19.6
1.837	0.70	0.532	0.500	175.8	8.8	-40.4	10.4	-97.5	25.7
1.837	0.70	0.532	0.833	241.9	12.4	-71.6	13.9	-111.5	36.7
1.863	0.70	0.504	-0.833	34.4	6.2	-1.9	7.3	-7.8	19.2
1.863	0.70	0.504	-0.500	69.9	5.1	-34.0	6.6	52.6	15.9
1.863	0.70	0.504	-0.167	86.6	4.9	-31.4	5.5	-24.4	15.0
1.863	0.70	0.504	0.167	122.1	5.7	-29.8	6.6	-53.2	17.9
1.863	0.70	0.504	0.500	161.4	8.0	-29.7	9.9	-79.0	25.4
1.863	0.70	0.504	0.833	247.2	15.3	-50.5	22.4	-112.6	49.9
1.887	0.70	0.475	-0.833	22.6	5.0	-4.4	6.4	1.0	16.1
1.887	0.70	0.475	-0.500	65.3	4.6	-9.3	5.8	-14.0	15.2
1.887	0.70	0.475	-0.167	80.1	4.3	-14.4	5.4	8.5	14.3
1.887	0.70	0.475	0.167	109.3	5.3	-28.3	6.4	-42.1	17.8
1.887	0.70	0.475	0.500	151.9	7.1	-21.9	8.5	-98.5	24.6
1.887	0.70	0.475	0.833	252.1	21.6	-46.4	35.2	-75.5	74.2
1.913	0.70	0.445	-0.833	25.4	4.5	6.7	5.2	-24.2	14.7
1.913	0.70	0.445	-0.500	43.2	3.6	-0.3	4.9	12.1	12.7
1.913	0.70	0.445	-0.167	58.2	3.4	-14.7	4.4	-13.1	12.1
1.913	0.70	0.445	0.167	97.3	4.7	-17.5	5.8	-58.7	16.8
1.913	0.70	0.445	0.500	127.6	6.3	-12.7	8.0	-105.3	22.2
1.913	0.70	0.445	0.833	208.3	20.7	-67.3	35.0	-103.4	74.2
1.938	0.70	0.414	-0.833	34.8	4.8	-7.4	6.1	-42.0	18.0
1.938	0.70	0.414	-0.500	41.2	3.1	-8.6	4.3	-4.6	11.9
1.938	0.70	0.414	-0.167	46.0	2.9	-13.7	3.7	-24.0	10.8
1.938	0.70	0.414	0.167	81.9	4.0	-10.6	5.0	-41.5	15.1
1.938	0.70	0.414	0.500	129.4	5.8	-10.5	7.8	-75.1	22.1
1.938	0.70	0.414	0.833	224.3	19.4	-31.9	34.1	-28.9	75.2
1.962	0.70	0.381	-0.833	23.3	4.1	7.3	5.7	-20.8	16.4
1.962	0.70	0.381	-0.500	35.2	2.7	1.7	3.8	-18.5	10.9
1.962	0.70	0.381	-0.167	38.8	2.5	-5.4	3.8	2.8	10.5
1.962	0.70	0.381	0.167	67.1	3.6	-12.4	4.7	-40.8	14.7
1.962	0.70	0.381	0.500	111.6	5.2	-21.6	6.9	-102.0	21.3
1.962	0.70	0.381	0.833	177.5	18.0	-85.9	34.7	-166.7	80.7
1.988	0.70	0.347	-0.833	25.6	4.0	12.5	5.8	-40.1	15.5
1.988	0.70	0.347	-0.500	22.7	2.1	7.0	3.4	-6.8	9.6
1.988	0.70	0.347	-0.167	26.6	2.1	-8.2	3.2	-14.1	9.4
1.988	0.70	0.347	0.167	63.8	3.2	-13.2	4.6	-48.3	14.6
1.988	0.70	0.347	0.500	108.2	5.0	-7.7	7.1	-97.2	22.4
1.988	0.70	0.347	0.833	150.8	17.3	-67.0	34.3	-174.9	78.4

1.613	1.10	0.594	-0.833	15.1	7.4	11.7	8.2	5.9	11.3
1.613	1.10	0.594	-0.500	6.2	4.0	-1.7	6.0	0.9	14.0
1.613	1.10	0.594	-0.167	10.2	4.8	2.7	5.2	3.5	11.1
1.613	1.10	0.594	0.833	10.5	4.2	2.6	4.5	-2.8	11.2
1.637	1.10	0.573	-0.833	30.3	12.5	2.1	14.6	28.5	25.2
1.637	1.10	0.573	-0.500	20.2	6.0	-7.4	5.7	-3.9	16.3
1.637	1.10	0.573	-0.167	40.6	10.1	-8.3	11.8	4.8	27.2
1.637	1.10	0.573	0.167	38.3	13.8	-5.1	19.3	-1.9	37.0
1.637	1.10	0.573	0.500	34.8	6.5	-16.4	7.0	11.2	16.9
1.637	1.10	0.573	0.833	46.5	5.7	-8.2	5.4	-11.6	15.2
1.663	1.10	0.552	-0.833	29.8	11.7	-5.1	16.9	5.7	38.9
1.663	1.10	0.552	-0.500	38.9	8.6	-12.6	12.3	-11.8	28.3
1.663	1.10	0.552	-0.167	61.5	12.0	4.5	18.2	9.4	39.6
1.663	1.10	0.552	0.167	75.5	10.6	-17.0	14.1	-30.4	30.6
1.663	1.10	0.552	0.500	79.5	12.4	-13.2	15.1	-20.1	30.4
1.663	1.10	0.552	0.833	97.8	8.4	-30.4	9.5	1.9	24.6
1.688	1.10	0.529	-0.500	48.2	6.8	-28.7	7.3	-13.7	19.8
1.688	1.10	0.529	-0.167	95.3	15.2	22.5	19.9	27.5	34.4
1.688	1.10	0.529	0.167	94.5	11.5	-33.4	17.8	-69.9	40.9
1.688	1.10	0.529	0.500	133.8	11.3	-39.6	13.5	-70.3	34.1
1.688	1.10	0.529	0.833	172.5	11.7	-25.3	11.8	-69.1	33.8
1.712	1.10	0.505	-0.833	33.6	14.1	-0.3	23.0	-3.8	53.0
1.712	1.10	0.505	-0.500	49.5	7.1	-20.0	7.7	-14.4	21.9
1.712	1.10	0.505	-0.167	64.0	8.2	-37.4	11.2	-32.6	27.1
1.712	1.10	0.505	0.167	98.7	10.5	-32.0	14.1	-26.5	31.4
1.712	1.10	0.505	0.500	155.9	12.5	-42.7	16.7	-59.7	39.0
1.712	1.10	0.505	0.833	232.7	13.1	-52.7	15.7	7.8	40.6
1.738	1.10	0.480	-0.833	14.8	6.0	-0.7	8.0	12.8	20.4
1.738	1.10	0.480	-0.500	39.9	6.0	-14.8	7.5	-7.8	20.4
1.738	1.10	0.480	-0.167	70.4	6.9	-26.8	9.1	-10.1	23.0
1.738	1.10	0.480	0.167	101.3	9.0	-56.5	11.5	-49.5	29.3
1.738	1.10	0.480	0.500	187.0	15.8	-56.6	24.0	-26.3	55.0
1.738	1.10	0.480	0.833	238.0	13.3	-56.4	14.4	-85.2	43.4
1.762	1.10	0.454	-0.833	17.6	8.5	-4.6	14.1	-9.7	34.1
1.762	1.10	0.454	-0.500	36.7	5.6	-13.1	6.7	-0.2	19.5
1.762	1.10	0.454	-0.167	73.6	6.9	-29.8	8.9	-23.8	24.2
1.762	1.10	0.454	0.167	118.1	9.6	-45.0	13.6	-0.1	34.2
1.762	1.10	0.454	0.500	179.5	19.1	-30.1	29.3	-4.2	64.2
1.762	1.10	0.454	0.833	238.6	14.1	-85.4	15.7	-157.9	48.3
1.788	1.10	0.427	-0.833	14.9	7.0	4.3	9.1	8.5	21.4
1.788	1.10	0.427	-0.500	40.1	5.5	-17.9	7.6	7.4	20.1
1.788	1.10	0.427	-0.167	77.1	6.3	-28.2	8.0	-37.6	23.2
1.788	1.10	0.427	0.167	120.2	8.6	-13.3	12.0	5.5	29.7
1.788	1.10	0.427	0.500	178.5	19.2	-14.9	33.2	-37.4	72.4
1.788	1.10	0.427	0.833	182.8	11.5	-74.0	15.2	-18.8	41.2
1.812	1.10	0.399	-0.833	14.7	5.7	-8.7	8.5	6.2	22.6
1.812	1.10	0.399	-0.500	36.7	6.8	-22.9	8.5	-31.6	0.0
1.812	1.10	0.399	-0.167	61.7	5.2	-32.6	7.0	-35.1	20.5
1.812	1.10	0.399	0.167	100.3	7.7	-49.9	11.1	24.4	30.5
1.812	1.10	0.399	0.500	159.3	17.6	-18.1	31.4	-29.3	71.3
1.812	1.10	0.399	0.833	199.7	13.1	-87.6	18.6	-133.8	50.5

1.837	1.10	0.369	-0.833	19.5	8.9	3.0	14.2	24.4	35.7
1.837	1.10	0.369	-0.500	42.2	5.5	-30.4	8.7	35.6	23.4
1.837	1.10	0.369	-0.167	66.7	5.6	-32.9	8.3	-5.2	23.6
1.837	1.10	0.369	0.167	98.6	7.0	-23.8	10.3	-35.2	29.6
1.837	1.10	0.369	0.500	128.1	10.7	-56.8	16.9	-118.2	44.4
1.837	1.10	0.369	0.833	174.5	14.6	-65.8	24.2	-120.8	60.7
1.863	1.10	0.338	-0.833	18.8	5.7	2.7	9.3	-16.7	26.6
1.863	1.10	0.338	-0.500	32.7	4.7	-20.6	7.4	-7.1	21.9
1.863	1.10	0.338	-0.167	61.1	5.6	-28.7	8.6	-14.5	26.3
1.863	1.10	0.338	0.167	99.6	7.0	-31.1	10.9	-17.2	32.4
1.863	1.10	0.338	0.500	123.9	12.6	-44.2	23.4	-76.3	58.6
1.863	1.10	0.338	0.833	203.8	29.2	-39.6	59.6	-66.1	135.0
1.887	1.10	0.306	-0.833	18.1	7.1	-2.9	9.7	-15.7	38.4
1.887	1.10	0.306	-0.500	30.9	4.7	-21.6	7.9	-6.7	22.7
1.887	1.10	0.306	-0.167	54.2	5.0	-38.8	7.6	-46.7	25.7
1.887	1.10	0.306	0.167	76.3	6.7	-33.0	11.6	30.3	34.6
1.887	1.10	0.306	0.500	103.0	9.7	-24.3	18.4	-109.4	52.6
1.887	1.10	0.306	0.833	146.3	23.0	-74.9	50.7	-200.3	123.0
1.613	1.50	0.449	-0.500	12.1	12.9	3.8	19.7	3.4	38.1
1.613	1.50	0.449	-0.167	18.2	57.4	4.2	185.7	-5.5	472.9
1.613	1.50	0.449	0.167	8.3	6.7	4.6	9.3	7.5	19.6
1.613	1.50	0.449	0.500	6.3	91.0	0.1	213.8	1.2	318.3
1.613	1.50	0.449	0.833	5.5	6.0	-2.2	8.4	0.5	22.5
1.637	1.50	0.425	-0.833	9.6	5.4	-3.9	7.8	17.0	20.1
1.637	1.50	0.425	-0.167	10.1	8.8	-0.6	8.2	-12.1	27.8
1.637	1.50	0.425	0.167	23.6	17.7	9.6	26.1	36.6	56.3
1.637	1.50	0.425	0.500	59.3	67.2	39.4	99.9	-3.6	135.6
1.637	1.50	0.425	0.833	20.8	7.5	1.5	9.8	-0.4	28.2

A.3 Response Functions for Narrow Q^2 Bins

The results are given for bins with full-widths of 100 MeV in W, 0.10 $(\mathrm{GeV/c})^2$ in Q^2, and 1/3 in $\cos\theta_K$.

# W	Q2	eps	CosTh	SigU	err	SigTT	err	SigLT	err
1.700	0.55	0.710	-0.500	57.7	7.2	-23.4	6.3	-26.0	16.0
1.700	0.55	0.710	-0.167	87.8	7.8	-30.0	7.1	-37.3	17.3
1.700	0.55	0.710	0.167	144.4	10.9	-41.7	11.9	-25.0	25.7
1.700	0.55	0.710	0.500	199.7	18.6	-40.3	22.7	-89.9	45.3
1.700	0.55	0.710	0.833	227.5	12.1	-58.6	9.6	-23.1	26.8
1.800	0.55	0.626	-0.833	20.2	8.4	-6.5	9.3	5.7	21.6
1.800	0.55	0.626	-0.500	65.7	5.5	-15.7	5.6	-28.7	13.9
1.800	0.55	0.626	-0.167	95.7	5.4	-27.8	5.6	-2.8	13.6
1.800	0.55	0.626	0.167	141.2	7.1	-38.8	6.9	-62.4	17.7
1.800	0.55	0.626	0.500	175.4	10.2	-42.5	12.0	-93.4	27.0
1.800	0.55	0.626	0.833	274.4	12.2	-50.3	11.0	-121.9	30.8
1.900	0.55	0.522	-0.833	24.5	4.5	4.5	5.4	-5.5	13.0
1.900	0.55	0.522	-0.500	69.0	4.4	-6.7	5.4	27.9	13.2
1.900	0.55	0.522	-0.167	72.9	4.1	-19.3	4.9	-16.0	12.2
1.900	0.55	0.522	0.167	106.8	4.9	-25.2	5.2	-49.2	14.9
1.900	0.55	0.522	0.500	145.1	7.2	-17.6	7.7	-100.5	21.5
1.900	0.55	0.522	0.833	245.4	20.7	-39.3	35.1	-24.1	76.8
2.000	0.55	0.396	-0.833	21.1	3.3	9.8	4.4	-31.1	11.6
2.000	0.55	0.396	-0.500	19.8	1.7	1.8	2.5	-0.9	6.9
2.000	0.55	0.396	-0.167	29.8	2.0	-10.8	2.9	-5.8	8.0
2.000	0.55	0.396	0.167	65.5	3.3	-8.0	4.4	-47.0	13.1
2.000	0.55	0.396	0.500	105.2	4.6	-12.1	6.0	-83.1	18.1
2.000	0.55	0.396	0.833	162.0	16.2	-75.9	31.7	-116.2	75.0
1.700	0.65	0.677	-0.833	39.4	12.8	-5.8	12.8	-18.4	31.2
1.700	0.65	0.677	-0.500	92.8	8.6	-15.3	8.6	-1.5	19.0
1.700	0.65	0.677	-0.167	87.1	6.5	-31.1	6.4	-31.6	15.4
1.700	0.65	0.677	0.167	130.0	8.8	-33.0	9.8	-24.2	21.5
1.700	0.65	0.677	0.500	164.7	9.1	-55.4	9.8	-60.4	22.9
1.700	0.65	0.677	0.833	234.1	12.0	-46.9	9.4	-37.8	27.8
1.800	0.65	0.589	-0.833	26.0	7.2	-1.0	7.8	-3.2	18.8
1.800	0.65	0.589	-0.500	59.2	4.8	-23.9	5.4	3.2	12.8
1.800	0.65	0.589	-0.167	91.1	4.9	-24.0	4.9	-26.2	12.9
1.800	0.65	0.589	0.167	138.3	7.2	-40.1	7.6	-12.7	18.3
1.800	0.65	0.589	0.500	197.5	10.0	-58.4	11.6	-110.3	28.6
1.800	0.65	0.589	0.833	277.3	12.9	-51.6	12.8	-37.0	34.9
1.900	0.65	0.481	-0.833	31.9	4.5	-2.5	5.4	-19.7	14.9
1.900	0.65	0.481	-0.500	48.6	3.5	-19.2	4.5	-0.3	11.3
1.900	0.65	0.481	-0.167	61.8	3.3	-15.8	4.0	-12.1	10.7
1.900	0.65	0.481	0.167	100.1	4.4	-18.4	4.9	-55.2	14.5
1.900	0.65	0.481	0.500	132.0	6.2	-21.6	6.9	-79.3	20.1
1.900	0.65	0.481	0.833	227.5	19.2	-44.8	31.5	-78.5	66.9
2.000	0.65	0.352	-0.833	18.6	2.7	7.8	4.2	0.3	12.4

2.000	0.65	0.352	-0.500	19.6	1.8	3.2	2.9	-18.3	8.3
2.000	0.65	0.352	-0.167	30.6	1.9	-6.0	2.8	-27.7	8.6
2.000	0.65	0.352	0.167	61.2	3.0	-7.8	4.2	-53.0	13.3
2.000	0.65	0.352	0.500	105.2	4.6	-12.4	6.8	-71.4	20.5
2.000	0.65	0.352	0.833	158.3	15.3	-50.6	29.6	-90.8	68.2
1.700	0.75	0.643	-0.833	42.1	10.6	2.3	12.9	-3.6	30.5
1.700	0.75	0.643	-0.500	73.5	7.5	-6.4	7.9	-22.4	17.9
1.700	0.75	0.643	-0.167	88.5	6.7	-24.0	7.1	-8.3	16.0
1.700	0.75	0.643	0.167	118.7	8.1	-31.9	8.9	-38.3	19.8
1.700	0.75	0.643	0.500	160.2	10.6	-39.2	11.7	-80.2	26.4
1.700	0.75	0.643	0.833	235.1	10.8	-29.9	10.1	-29.7	26.1
1.800	0.75	0.551	-0.833	15.6	4.7	-3.2	5.7	3.1	14.1
1.800	0.75	0.551	-0.500	54.8	4.3	-17.8	4.7	-5.7	12.0
1.800	0.75	0.551	-0.167	87.3	4.8	-17.4	5.1	-18.8	13.6
1.800	0.75	0.551	0.167	110.3	9.9	-38.9	18.1	-107.8	32.4
1.800	0.75	0.551	0.500	176.3	10.9	-45.3	15.2	-52.7	33.6
1.800	0.75	0.551	0.833	242.7	10.8	-51.8	11.8	-84.0	31.5
1.900	0.75	0.439	-0.833	31.7	4.7	-4.8	5.4	-31.7	16.7
1.900	0.75	0.439	-0.500	44.6	3.6	-10.6	4.8	-4.1	12.7
1.900	0.75	0.439	-0.167	65.5	3.5	-20.1	4.5	-6.4	12.4
1.900	0.75	0.439	0.167	93.4	4.6	-29.3	5.2	-65.9	16.2
1.900	0.75	0.439	0.500	139.5	6.4	-15.8	8.4	-74.3	23.5
1.900	0.75	0.439	0.833	208.0	18.6	-42.1	31.9	-118.3	68.1
2.000	0.75	0.307	-0.833	29.1	4.1	1.9	6.5	-46.7	20.9
2.000	0.75	0.307	-0.500	19.8	2.2	3.6	3.5	-30.9	11.1
2.000	0.75	0.307	-0.167	24.7	2.1	-5.2	3.6	-1.3	10.9
2.000	0.75	0.307	0.167	60.2	3.4	-11.2	5.0	-66.4	17.4
2.000	0.75	0.307	0.500	95.9	4.9	-6.3	7.3	-132.7	24.6
1.700	0.85	0.608	-0.833	31.4	9.8	-11.2	8.3	-13.2	25.7
1.700	0.85	0.608	-0.500	55.9	6.7	-8.5	7.4	-35.1	17.5
1.700	0.85	0.608	-0.167	78.7	6.8	-19.0	8.0	-28.3	18.3
1.700	0.85	0.608	0.167	113.3	9.5	-37.4	12.5	-66.1	27.3
1.700	0.85	0.608	0.500	161.5	11.2	-28.1	13.7	-22.4	28.9
1.700	0.85	0.608	0.833	203.6	10.4	-48.5	10.2	-17.4	26.7
1.800	0.85	0.513	-0.833	16.0	4.6	-5.8	5.4	-3.1	14.2
1.800	0.85	0.513	-0.500	49.1	4.4	-21.4	5.3	1.7	13.2
1.800	0.85	0.513	-0.167	79.0	5.0	-24.5	5.6	-18.8	15.4
1.800	0.85	0.513	0.167	112.2	6.0	-32.4	6.8	-44.4	18.3
1.800	0.85	0.513	0.500	155.7	9.4	-66.2	11.5	-96.4	28.9
1.800	0.85	0.513	0.833	232.0	10.5	-67.5	11.2	-102.6	31.9
1.900	0.85	0.397	-0.833	27.4	5.5	-0.6	7.8	-16.5	21.6
1.900	0.85	0.397	-0.500	41.8	3.6	-17.2	5.2	1.1	14.1
1.900	0.85	0.397	-0.167	55.0	3.5	-20.1	5.0	-8.0	13.9
1.900	0.85	0.397	0.167	91.1	4.8	-23.2	6.3	-49.6	19.0
1.900	0.85	0.397	0.500	129.3	6.9	-26.8	9.5	-80.6	28.1
1.900	0.85	0.397	0.833	214.1	20.1	-22.8	35.2	-4.0	75.8
2.000	0.85	0.262	-0.833	15.2	5.8	0.6	11.1	-13.9	35.1
2.000	0.85	0.262	-0.500	25.4	3.8	-5.8	7.2	-0.3	22.6
2.000	0.85	0.262	0.167	60.3	4.3	-14.1	7.5	-75.0	26.1

2.000	0.85	0.262	0.500	88.9	6.0	-12.1	10.4	-108.6	35.5
2.000	0.85	0.262	0.833	134.5	20.5	-7.8	45.4	10.9	108.4
1.700	0.95	0.573	-0.833	49.0	14.9	10.1	18.7	31.4	36.2
1.700	0.95	0.573	-0.500	54.1	6.5	-20.5	8.0	-14.8	19.9
1.700	0.95	0.573	-0.167	83.8	9.5	6.1	12.5	30.9	25.9
1.700	0.95	0.573	0.167	94.7	8.2	-32.5	9.9	-44.0	22.9
1.700	0.95	0.573	0.500	140.8	10.0	-41.6	12.3	-62.3	28.4
1.700	0.95	0.573	0.833	189.5	10.0	-44.6	10.8	7.1	27.3
1.800	0.95	0.473	-0.833	28.1	11.7	14.8	15.6	12.5	27.6
1.800	0.95	0.473	-0.500	46.8	4.7	-22.6	6.1	17.8	15.6
1.800	0.95	0.473	-0.167	91.0	5.8	-31.9	6.4	-49.1	19.1
1.800	0.95	0.473	0.167	111.0	6.4	-20.0	8.1	-23.2	21.3
1.800	0.95	0.473	0.500	173.0	16.1	-20.0	23.8	-35.4	55.4
1.800	0.95	0.473	0.833	223.1	11.2	-82.0	13.3	-82.9	36.8
1.900	0.95	0.355	-0.833	16.5	4.5	-1.9	6.3	-20.1	20.3
1.900	0.95	0.355	-0.500	35.8	3.7	-12.2	5.6	-16.1	16.4
1.900	0.95	0.355	-0.167	55.4	4.0	-26.4	5.8	-27.6	17.5
1.900	0.95	0.355	0.167	80.8	5.0	-22.7	7.2	-11.6	22.1
1.900	0.95	0.355	0.500	127.2	8.0	-35.0	12.2	-88.4	35.1
1.900	0.95	0.355	0.833	189.0	22.1	-65.4	43.0	-136.6	97.7
1.700	1.05	0.536	-0.833	39.4	13.5	-12.0	17.9	6.6	40.2
1.700	1.05	0.536	-0.500	59.9	9.1	-19.3	10.7	-34.0	26.1
1.700	1.05	0.536	-0.167	74.4	8.2	-22.0	9.7	-19.1	22.5
1.700	1.05	0.536	0.167	99.5	10.4	-21.5	12.9	-53.7	28.2
1.700	1.05	0.536	0.500	154.4	11.9	-52.7	14.8	-49.0	35.3
1.700	1.05	0.536	0.833	195.1	11.2	-37.3	11.6	-60.4	32.4
1.800	1.05	0.433	-0.833	14.2	5.1	-5.9	7.4	8.2	19.7
1.800	1.05	0.433	-0.500	42.1	5.4	-21.8	7.6	14.6	20.8
1.800	1.05	0.433	0.167	99.6	7.2	-32.7	10.3	-9.4	26.8
1.800	1.05	0.433	0.500	186.8	19.6	15.5	32.0	29.9	67.7
1.800	1.05	0.433	0.833	209.3	13.1	-65.9	17.6	-78.1	46.2
1.900	1.05	0.312	-0.833	21.7	5.7	-5.2	9.3	14.7	28.6
1.900	1.05	0.312	-0.500	23.7	3.4	-14.1	5.7	-14.9	17.4
1.900	1.05	0.312	0.167	79.5	5.4	-20.0	8.2	-19.4	27.0
1.900	1.05	0.312	0.500	113.1	8.0	-25.1	13.8	-83.7	39.6
1.900	1.05	0.312	0.833	200.9	25.9	-22.0	53.0	-73.4	119.1
1.700	1.15	0.498	-0.833	53.7	31.2	31.5	43.7	35.6	68.9
1.700	1.15	0.498	-0.500	29.6	5.5	-19.4	6.7	0.7	16.5
1.700	1.15	0.498	-0.167	53.2	9.3	-24.1	14.5	-19.4	34.4
1.700	1.15	0.498	0.167	92.3	9.3	-41.2	11.9	-29.6	28.9
1.700	1.15	0.498	0.833	183.1	13.1	-47.8	14.6	-84.9	41.3
1.800	1.15	0.392	-0.833	12.3	4.9	-3.8	6.3	-1.0	19.7
1.800	1.15	0.392	-0.500	38.0	5.2	-20.6	7.5	11.5	20.9
1.800	1.15	0.392	-0.167	53.7	5.6	-27.2	8.4	7.4	22.5
1.800	1.15	0.392	0.167	94.7	8.2	-36.6	12.3	30.1	32.9
1.800	1.15	0.392	0.500	135.7	9.9	-79.4	14.9	-67.4	40.4
1.800	1.15	0.392	0.833	200.6	15.5	-46.7	23.0	-143.2	58.1

1.700	1.25	0.460	-0.833	27.5	9.1	-18.2	12.4	26.0	29.4
1.700	1.25	0.460	-0.500	44.9	12.5	-9.9	17.3	10.1	40.9
1.700	1.25	0.460	-0.167	65.4	9.3	-27.9	11.3	-54.0	32.2
1.700	1.25	0.460	0.167	84.2	12.6	-17.4	20.8	13.5	47.9
1.700	1.25	0.460	0.500	151.6	19.1	10.6	27.5	30.5	54.9
1.700	1.25	0.460	0.833	155.9	12.9	-56.3	14.4	-102.7	44.0
1.800	1.25	0.351	-0.500	36.9	9.2	-9.0	15.6	18.0	41.0
1.800	1.25	0.351	-0.167	58.6	6.6	-29.1	9.6	-20.1	30.1
1.800	1.25	0.351	0.167	109.1	9.2	-53.0	12.7	-92.4	40.9
1.800	1.25	0.351	0.500	139.6	14.4	-37.0	24.9	-133.2	62.1
1.800	1.25	0.351	0.833	161.3	15.6	-100.5	24.8	-63.5	69.4
1.700	1.35	0.421	-0.833	56.1	36.7	44.8	54.4	61.1	77.0
1.700	1.35	0.421	-0.500	27.6	6.3	-21.2	8.9	6.3	25.7
1.700	1.35	0.421	-0.167	42.4	7.8	-33.8	12.0	4.0	31.1
1.700	1.35	0.421	0.167	70.7	10.9	-25.7	17.0	37.0	42.2
1.700	1.35	0.421	0.500	102.6	10.4	-58.4	14.5	-36.6	39.0
1.700	1.35	0.421	0.833	141.2	14.3	-41.8	19.9	13.3	49.6

Appendix B

Σ^0 Electroproduction Response Functions

This chapter contains the final values for the extracted $\sigma_T + \epsilon\sigma_L$, σ_{TT} and σ_{LT} terms of the $ep \to e'K^+\Sigma^0$ reaction, with an incident 2.567 GeV electron beam. The results for the three primary binnings of the data are each presented in the same format. The first four columns provide the location of the center of the kinematic bin. The next six columns contain the fitted values of the response functions, with their associated uncertainty. The quoted uncertainties include the estimated point-to-point systematic errors, but not the 3.3% scale factor due to the uncertainty on the absolute value of the integrated luminosity. Bins for which the structure functions could not be extracted are excluded from the listing. When using these results, please keep in mind that the sets of results for the different binnings were determined from the same data; they are not three independent measurements.

The values are given in GeV, $(\mathrm{GeV/c})^2$ for W, Q^2, respectively, and in nb/sr for the structure functions and their quoted uncertainty.

B.1 Response Functions for Narrow Cos(θ_K) Bins

The results are given for bins with full-widths of 100 MeV in W, 0.40 $(\mathrm{GeV/c})^2$ in Q^2, and 1/5 in $\cos\theta_K$.

# W	Q2	eps	CosTh	SigU	err	SigTT	err	SigLT	err
1.700	0.70	0.660	-0.900	10.3	7.0	3.9	6.1	-2.0	18.0
1.700	0.70	0.660	-0.700	14.1	9.7	11.0	10.2	11.3	11.8
1.700	0.70	0.660	-0.500	10.1	5.3	5.7	6.9	-2.4	12.0
1.700	0.70	0.660	-0.300	9.5	3.7	6.2	4.4	5.8	7.2
1.700	0.70	0.660	-0.100	9.4	3.6	1.5	4.9	1.5	9.4
1.700	0.70	0.660	0.100	9.6	2.4	1.1	2.5	-5.0	5.7
1.700	0.70	0.660	0.300	10.6	2.4	3.6	2.7	5.5	5.1
1.700	0.70	0.660	0.500	18.1	4.1	11.2	4.5	17.3	6.4
1.700	0.70	0.660	0.700	10.8	3.2	-0.2	3.2	-0.0	7.1

1.700	0.70	0.660	0.900	10.3	1.7	1.9	1.7	4.1	3.6
1.800	0.70	0.570	-0.700	17.9	2.8	-1.8	3.2	-13.1	7.5
1.800	0.70	0.570	-0.500	42.3	3.3	-0.8	3.1	-29.1	8.9
1.800	0.70	0.570	-0.300	49.7	3.1	0.9	2.8	-32.3	8.3
1.800	0.70	0.570	-0.100	63.0	3.6	5.4	3.7	-18.3	9.6
1.800	0.70	0.570	0.100	67.2	3.8	2.3	3.8	-40.1	10.1
1.800	0.70	0.570	0.300	70.5	4.5	-6.7	5.5	-35.8	12.4
1.800	0.70	0.570	0.500	69.2	6.8	0.2	10.3	-14.9	21.8
1.800	0.70	0.570	0.700	56.0	6.5	-6.5	10.4	-23.2	22.2
1.800	0.70	0.570	0.900	50.5	4.2	1.0	4.8	6.8	10.4
1.900	0.70	0.460	-0.700	30.8	2.6	-4.9	3.6	18.8	9.2
1.900	0.70	0.460	-0.500	49.8	2.8	3.8	3.4	-39.7	9.4
1.900	0.70	0.460	-0.300	70.2	3.0	3.3	3.4	-53.4	10.1
1.900	0.70	0.460	-0.100	91.6	3.7	-8.3	4.2	-49.5	12.8
1.900	0.70	0.460	0.100	101.2	3.8	-2.2	4.5	-37.6	13.0
1.900	0.70	0.460	0.300	107.6	4.1	-8.0	5.0	-38.8	13.8
1.900	0.70	0.460	0.500	92.5	4.2	-11.8	5.6	-32.2	14.5
1.900	0.70	0.460	0.700	95.4	7.5	12.6	11.6	33.4	25.5
1.900	0.70	0.460	0.900	74.7	9.1	-2.3	14.5	18.4	28.9
2.000	0.70	0.329	-0.700	8.3	1.8	6.8	3.3	-18.9	8.6
2.000	0.70	0.329	-0.500	21.4	1.5	-0.1	2.4	-6.5	7.2
2.000	0.70	0.329	-0.300	33.0	1.8	-5.4	2.7	-19.4	8.4
2.000	0.70	0.329	-0.100	49.1	2.1	-5.1	3.3	-28.3	10.2
2.000	0.70	0.329	0.100	59.8	2.4	-12.7	3.8	-22.3	11.6
2.000	0.70	0.329	0.300	60.3	2.4	-8.0	3.6	-36.9	11.5
2.000	0.70	0.329	0.500	73.4	3.0	-2.9	4.8	2.6	14.2
2.000	0.70	0.329	0.700	59.3	4.5	-20.0	8.0	-25.8	20.0
1.700	1.10	0.517	-0.500	7.1	4.3	1.6	4.9	10.1	11.9
1.700	1.10	0.517	-0.300	5.7	3.2	1.1	5.3	-1.0	11.5
1.700	1.10	0.517	-0.100	7.7	3.4	4.0	4.3	10.4	8.1
1.700	1.10	0.517	0.100	7.8	4.2	2.0	5.8	-0.5	10.8
1.700	1.10	0.517	0.300	12.9	4.1	7.9	5.3	10.4	8.8
1.700	1.10	0.517	0.500	8.4	3.2	3.8	4.1	-0.2	8.1
1.700	1.10	0.517	0.700	8.1	4.6	1.9	6.2	-3.7	10.1
1.700	1.10	0.517	0.900	8.8	1.9	2.4	2.2	-1.5	5.3
1.800	1.10	0.413	-0.900	13.7	8.5	-0.0	12.4	16.3	24.7
1.800	1.10	0.413	-0.700	12.7	2.9	-1.3	3.9	-6.4	10.5
1.800	1.10	0.413	-0.500	17.4	2.7	5.5	3.8	-13.8	9.8
1.800	1.10	0.413	-0.300	30.8	2.9	0.5	4.1	-28.4	11.1
1.800	1.10	0.413	-0.100	40.5	3.5	3.0	5.1	-24.7	12.9
1.800	1.10	0.413	0.100	38.4	4.0	-1.8	5.9	-20.5	14.2
1.800	1.10	0.413	0.300	51.2	6.1	15.8	9.5	7.3	19.5
1.800	1.10	0.413	0.500	49.3	6.6	7.6	11.1	6.6	25.0
1.800	1.10	0.413	0.700	33.9	6.5	14.8	11.5	16.8	23.8
1.800	1.10	0.413	0.900	31.0	4.7	-3.9	6.5	-13.1	15.7
1.900	1.10	0.290	-0.900	19.8	10.2	-11.3	14.2	-21.9	52.0
1.900	1.10	0.290	-0.700	15.6	3.2	-2.5	5.6	-13.4	17.1
1.900	1.10	0.290	-0.500	32.1	3.2	-4.5	5.5	-26.1	17.7
1.900	1.10	0.290	-0.300	37.7	3.0	-7.7	5.1	-28.4	16.2
1.900	1.10	0.290	-0.100	60.8	4.0	-10.5	6.4	-64.7	21.9

1.900	1.10	0.290	0.100	72.1	4.6	-15.5	7.6	-22.4	24.8
1.900	1.10	0.290	0.300	72.2	4.7	-14.5	8.0	-56.4	25.4
1.900	1.10	0.290	0.500	84.4	8.9	25.9	15.1	114.3	43.9
1.900	1.10	0.290	0.700	49.6	8.4	-2.0	18.0	-18.7	45.9

B.2 Response Functions for Narrow W Bins

The results are given for bins with full-widths of 25 MeV in W, 0.40 $(\mathrm{GeV/c})^2$ in Q^2, and 1/3 in $\cos\theta_K$.

# W	Q2	eps	CosTh	SigU	err	SigTT	err	SigLT	err
1.688	0.70	0.670	-0.833	8.4	4.0	0.9	3.8	-1.4	10.9
1.688	0.70	0.670	-0.500	12.3	8.5	5.8	8.7	6.1	10.7
1.688	0.70	0.670	-0.167	7.1	25.5	1.1	61.0	-2.0	136.8
1.688	0.70	0.670	0.167	17.4	12.9	4.9	12.7	-5.9	22.3
1.688	0.70	0.670	0.500	8.3	7.4	4.4	7.7	3.3	11.5
1.688	0.70	0.670	0.833	6.3	3.2	-1.2	3.2	1.5	7.5
1.712	0.70	0.650	-0.833	8.6	11.8	-0.8	16.0	-10.2	30.3
1.712	0.70	0.650	-0.167	18.8	12.4	12.6	14.9	8.3	21.8
1.712	0.70	0.650	0.167	20.8	10.9	8.3	14.3	11.8	27.0
1.712	0.70	0.650	0.500	27.1	18.0	8.3	23.7	5.1	39.1
1.712	0.70	0.650	0.833	21.6	5.5	8.0	5.7	3.2	10.1
1.738	0.70	0.629	-0.833	28.1	30.6	20.2	38.4	18.1	57.6
1.738	0.70	0.629	-0.500	18.9	5.0	4.9	5.5	-7.7	12.1
1.738	0.70	0.629	-0.167	29.4	9.4	15.8	11.7	15.1	19.6
1.738	0.70	0.629	0.167	28.4	6.6	12.9	7.9	10.0	16.0
1.738	0.70	0.629	0.500	38.7	8.3	23.8	10.7	30.9	18.4
1.738	0.70	0.629	0.833	23.5	5.4	4.1	4.4	-2.0	11.4
1.762	0.70	0.606	-0.833	24.8	12.4	8.5	12.7	-2.1	23.1
1.762	0.70	0.606	-0.500	16.9	6.5	-0.5	8.7	-15.7	18.1
1.762	0.70	0.606	-0.167	30.0	4.8	0.3	5.4	-7.5	11.6
1.762	0.70	0.606	0.167	47.5	8.3	13.9	10.8	-2.9	21.7
1.762	0.70	0.606	0.500	36.9	6.4	-1.7	10.7	-31.5	23.4
1.762	0.70	0.606	0.833	37.2	7.2	9.7	7.9	0.4	15.0
1.788	0.70	0.583	-0.833	21.7	12.0	7.5	12.3	-2.6	24.9
1.788	0.70	0.583	-0.500	33.8	6.1	-3.6	7.0	-39.1	14.9
1.788	0.70	0.583	-0.167	47.2	5.0	6.6	5.5	-21.7	12.2
1.788	0.70	0.583	0.167	58.5	6.9	9.4	8.8	-17.4	17.3
1.788	0.70	0.583	0.500	57.2	8.3	-1.0	12.5	1.2	27.4
1.788	0.70	0.583	0.833	48.0	6.1	-0.8	7.6	27.8	17.1
1.812	0.70	0.558	-0.833	26.2	12.7	2.2	15.0	-8.2	34.9
1.812	0.70	0.558	-0.500	44.0	4.6	-2.2	5.3	-0.5	12.8
1.812	0.70	0.558	-0.167	54.1	4.5	-5.8	5.0	-29.5	12.5
1.812	0.70	0.558	0.167	76.3	7.7	-5.4	9.3	-43.3	21.9
1.812	0.70	0.558	0.500	74.2	11.7	-6.5	18.8	-39.3	40.0
1.812	0.70	0.558	0.833	43.2	8.6	-14.3	13.2	-19.8	28.2
1.837	0.70	0.532	-0.833	25.7	10.1	-1.8	12.5	5.3	28.4
1.837	0.70	0.532	-0.500	41.4	4.3	-3.2	4.7	-52.9	12.5
1.837	0.70	0.532	-0.167	83.1	5.1	9.3	5.2	-51.0	14.8
1.837	0.70	0.532	0.167	94.1	5.8	-8.6	6.2	-63.8	17.2
1.837	0.70	0.532	0.500	92.4	9.1	4.7	12.2	-20.0	25.2
1.837	0.70	0.532	0.833	66.4	8.1	-2.9	11.8	12.1	26.5
1.863	0.70	0.504	-0.833	25.4	7.6	1.8	9.8	18.7	24.2
1.863	0.70	0.504	-0.500	50.6	4.4	-3.9	4.8	-61.1	13.8
1.863	0.70	0.504	-0.167	94.6	5.2	-3.2	5.5	-56.4	16.1

1.863	0.70	0.504	0.167	108.7	6.0	6.0	6.7	-55.5	18.7
1.863	0.70	0.504	0.500	99.4	8.5	-29.4	12.4	-54.6	29.9
1.863	0.70	0.504	0.833	57.1	11.0	-23.1	19.0	-53.0	40.8
1.887	0.70	0.475	-0.833	17.5	5.9	2.7	7.5	-3.9	19.0
1.887	0.70	0.475	-0.500	46.7	4.3	1.5	5.5	-35.3	14.2
1.887	0.70	0.475	-0.167	96.8	5.0	-6.5	5.9	-54.1	16.5
1.887	0.70	0.475	0.167	113.7	5.8	-8.1	6.7	-72.2	19.4
1.887	0.70	0.475	0.500	106.9	6.6	-12.4	8.8	-50.7	22.9
1.887	0.70	0.475	0.833	103.5	13.5	13.0	21.6	21.8	44.7
1.913	0.70	0.445	-0.833	13.7	4.6	2.1	5.8	-4.1	16.2
1.913	0.70	0.445	-0.500	51.0	4.2	-3.2	5.7	-8.4	15.0
1.913	0.70	0.445	-0.167	82.1	4.5	-6.6	5.4	-48.2	15.8
1.913	0.70	0.445	0.167	99.5	5.2	-8.7	6.7	-42.6	18.2
1.913	0.70	0.445	0.500	91.3	6.1	4.9	8.4	-14.0	20.6
1.913	0.70	0.445	0.833	108.5	14.3	21.9	22.1	64.9	43.9
1.938	0.70	0.414	-0.500	45.6	3.7	-6.4	5.2	3.2	14.1
1.938	0.70	0.414	-0.167	69.1	3.8	-4.1	4.8	-43.1	14.5
1.938	0.70	0.414	0.167	89.9	4.5	-1.1	6.2	-16.0	17.3
1.938	0.70	0.414	0.500	79.4	5.2	-9.6	7.5	5.8	19.3
1.938	0.70	0.414	0.833	66.1	10.3	-12.4	17.3	22.7	38.2
1.962	0.70	0.381	-0.833	10.1	5.0	0.0	9.2	3.5	24.8
1.962	0.70	0.381	-0.500	31.2	3.5	-3.0	5.7	7.6	15.2
1.962	0.70	0.381	-0.167	58.6	3.4	-6.5	4.7	-29.6	13.9
1.962	0.70	0.381	0.167	73.1	4.0	-12.8	5.6	-28.0	16.4
1.962	0.70	0.381	0.500	69.6	4.2	-4.7	6.1	-35.6	17.1
1.962	0.70	0.381	0.833	71.8	11.2	-4.7	20.1	21.6	43.8
1.988	0.70	0.347	-0.833	10.3	6.8	7.9	11.7	-0.1	31.3
1.988	0.70	0.347	-0.500	19.4	2.4	-1.5	3.6	-21.3	10.7
1.988	0.70	0.347	-0.167	46.9	3.0	-0.3	4.4	-15.7	13.5
1.988	0.70	0.347	0.167	60.5	3.3	-13.2	4.7	-52.5	15.0
1.988	0.70	0.347	0.500	67.5	4.2	-2.8	6.7	11.4	18.7
1.988	0.70	0.347	0.833	65.9	11.2	-30.1	21.1	-23.4	48.9
1.688	1.10	0.529	-0.500	7.5	5.6	5.8	6.3	3.4	13.0
1.688	1.10	0.529	-0.167	4.3	10.7	-0.4	13.6	-2.6	16.8
1.688	1.10	0.529	0.500	7.2	6.1	4.8	7.2	3.9	16.3
1.688	1.10	0.529	0.833	4.7	5.5	5.2	5.2	-2.0	17.1
1.712	1.10	0.505	-0.500	6.7	8.4	1.4	15.0	-1.3	31.6
1.712	1.10	0.505	0.167	14.1	7.3	8.9	10.1	8.6	17.4
1.712	1.10	0.505	0.500	31.4	33.1	29.3	43.0	19.9	49.0
1.712	1.10	0.505	0.833	13.5	4.7	8.7	5.9	6.0	10.5
1.738	1.10	0.480	-0.500	9.2	7.9	1.1	15.0	-4.6	33.7
1.738	1.10	0.480	-0.167	16.3	8.8	3.2	12.8	9.0	25.7
1.738	1.10	0.480	0.167	23.1	9.2	8.4	12.1	27.7	26.5
1.738	1.10	0.480	0.833	19.0	5.0	0.7	5.9	-14.2	14.1
1.762	1.10	0.454	-0.833	15.4	11.9	6.2	18.5	-1.4	36.3
1.762	1.10	0.454	-0.500	18.5	7.1	11.1	10.0	-4.8	22.3
1.762	1.10	0.454	-0.167	25.3	6.8	12.7	9.8	16.7	20.2
1.762	1.10	0.454	0.500	39.6	10.3	22.9	15.9	41.9	30.5
1.762	1.10	0.454	0.833	29.2	10.1	8.9	13.1	13.4	23.8
1.788	1.10	0.427	-0.833	17.1	12.0	-3.0	18.5	2.4	45.8

1.788	1.10	0.427	-0.500	13.4	4.8	4.8	6.7	-7.5	17.1
1.788	1.10	0.427	-0.167	21.4	4.8	-0.8	6.5	-25.9	18.1
1.788	1.10	0.427	0.167	36.6	6.8	11.6	9.8	20.8	23.0
1.788	1.10	0.427	0.500	30.9	9.0	5.2	14.2	8.5	28.9
1.788	1.10	0.427	0.833	17.7	8.0	0.6	12.4	-7.7	25.6
1.812	1.10	0.399	-0.833	14.9	12.9	2.4	21.2	-8.6	42.3
1.812	1.10	0.399	-0.500	18.1	4.4	5.8	6.3	-11.0	16.8
1.812	1.10	0.399	-0.167	32.9	4.5	-5.7	6.2	-31.0	17.1
1.812	1.10	0.399	0.167	58.0	8.8	7.8	13.0	32.2	28.7
1.812	1.10	0.399	0.500	37.0	8.9	5.2	16.7	-31.1	37.4
1.812	1.10	0.399	0.833	34.6	9.7	4.4	15.3	-38.9	31.4
1.837	1.10	0.369	-0.833	16.8	8.5	-1.0	14.9	-1.5	39.8
1.837	1.10	0.369	-0.500	30.5	5.6	1.2	8.2	-19.3	23.7
1.837	1.10	0.369	-0.167	48.0	5.5	-4.6	8.4	-17.4	23.6
1.837	1.10	0.369	0.167	46.7	5.6	-1.8	8.2	-72.5	23.5
1.837	1.10	0.369	0.500	48.9	11.2	7.2	20.4	-28.0	45.0
1.837	1.10	0.369	0.833	45.2	16.4	18.9	26.9	38.5	52.5
1.863	1.10	0.338	-0.833	15.4	7.3	-9.3	12.7	10.2	38.0
1.863	1.10	0.338	-0.500	29.5	5.5	1.0	8.7	-12.7	25.1
1.863	1.10	0.338	-0.167	36.6	4.7	-8.7	7.3	-32.3	21.6
1.863	1.10	0.338	0.167	66.2	7.3	-15.4	12.0	26.3	34.0
1.863	1.10	0.338	0.500	49.9	9.5	-5.9	17.1	3.3	44.3
1.887	1.10	0.306	-0.833	16.2	9.1	-4.4	14.8	0.8	48.4
1.887	1.10	0.306	-0.500	23.6	4.9	0.1	7.6	-16.4	24.8
1.887	1.10	0.306	-0.167	57.1	5.7	-21.0	9.1	-36.1	28.9
1.887	1.10	0.306	0.167	71.3	7.1	-9.2	11.3	-64.4	36.8
1.887	1.10	0.306	0.500	66.1	11.2	2.6	21.4	-27.1	52.0
1.887	1.10	0.306	0.833	58.3	17.4	30.1	32.4	105.5	66.0

B.3 Response Functions for Narrow Q^2 Bins

The results are given for bins with full-widths of 100 MeV in W, 0.10 $(\mathrm{GeV/c})^2$ in Q^2, and 1/3 in $\cos\theta_K$.

# W	Q2	eps	CosTh	SigU	err	SigTT	err	SigLT	err
1.700	0.55	0.710	0.167	20.0	10.7	4.7	14.7	-3.9	27.8
1.700	0.55	0.710	0.500	12.7	10.0	0.7	18.0	-9.3	37.3
1.700	0.55	0.710	0.833	15.3	5.3	2.9	5.2	4.7	9.7
1.800	0.55	0.626	-0.833	57.8	41.3	14.4	33.6	57.7	91.3
1.800	0.55	0.626	-0.500	34.6	5.6	3.5	5.8	-33.8	13.0
1.800	0.55	0.626	-0.167	67.8	5.9	6.4	5.4	-61.4	13.7
1.800	0.55	0.626	0.167	75.5	6.5	0.8	7.1	-53.2	16.0
1.800	0.55	0.626	0.500	79.5	9.4	0.6	12.0	-18.1	24.6
1.800	0.55	0.626	0.833	60.1	7.3	1.1	7.9	-14.1	18.1
1.900	0.55	0.522	-0.833	25.8	7.3	-7.1	8.8	12.5	22.1
1.900	0.55	0.522	-0.500	55.3	4.5	0.7	5.3	-37.1	13.5
1.900	0.55	0.522	-0.167	90.7	5.0	-3.3	5.5	-55.4	15.2
1.900	0.55	0.522	0.167	118.7	6.0	-7.3	6.5	-50.1	18.2

1.900	0.55	0.522	0.500	116.5	7.1	-19.1	7.7	-64.1	21.3
1.900	0.55	0.522	0.833	116.9	13.2	28.0	20.4	64.1	42.0
2.000	0.55	0.396	-0.500	20.9	2.2	5.6	3.3	3.5	8.7
2.000	0.55	0.396	-0.167	41.6	2.7	-3.0	3.6	-32.7	10.6
2.000	0.55	0.396	0.167	67.4	3.6	-13.5	4.9	-40.3	14.4
2.000	0.55	0.396	0.500	68.0	3.9	0.6	5.6	-12.7	15.2
2.000	0.55	0.396	0.833	69.0	10.7	-25.7	18.4	3.8	40.6
1.700	0.65	0.677	-0.833	17.5	23.3	8.9	23.1	-4.8	28.6
1.700	0.65	0.677	-0.500	9.0	7.9	3.1	9.6	-0.4	17.5
1.700	0.65	0.677	0.167	14.3	6.6	6.3	6.1	13.5	13.3
1.700	0.65	0.677	0.500	15.0	9.0	-0.7	15.4	-9.2	32.5
1.700	0.65	0.677	0.833	9.6	3.3	1.8	3.2	-0.0	6.1
1.800	0.65	0.589	-0.833	24.5	14.2	11.5	16.0	26.5	24.5
1.800	0.65	0.589	-0.500	31.3	4.2	-7.9	4.4	-17.5	11.0
1.800	0.65	0.589	-0.167	59.9	4.7	0.5	5.2	-9.5	12.1
1.800	0.65	0.589	0.167	65.7	5.6	2.0	6.4	-42.5	14.7
1.800	0.65	0.589	0.500	66.0	7.8	2.9	11.2	-26.6	23.4
1.800	0.65	0.589	0.833	47.5	7.0	-6.2	8.9	-19.5	19.5
1.900	0.65	0.481	-0.833	18.6	9.9	7.8	11.8	18.4	34.6
1.900	0.65	0.481	-0.500	53.0	4.1	5.1	5.1	-28.4	13.1
1.900	0.65	0.481	-0.167	82.4	4.2	-4.9	4.5	-72.6	13.7
1.900	0.65	0.481	0.167	104.9	5.0	-0.9	5.7	-51.2	16.2
1.900	0.65	0.481	0.500	91.2	6.2	-11.6	8.2	-21.6	19.8
1.900	0.65	0.481	0.833	79.2	10.9	-5.5	17.4	6.2	36.8
2.000	0.65	0.352	-0.833	10.6	3.8	-0.9	5.3	-7.8	17.2
2.000	0.65	0.352	-0.500	20.0	2.1	-2.2	3.2	-15.6	9.4
2.000	0.65	0.352	-0.167	44.1	2.5	-2.5	3.6	-28.5	11.3
2.000	0.65	0.352	0.167	56.9	3.0	-16.1	4.5	-14.9	13.2
2.000	0.65	0.352	0.500	60.0	3.5	-11.7	5.3	-27.7	15.5
2.000	0.65	0.352	0.833	59.4	10.3	-30.0	19.7	-48.9	44.3
1.700	0.75	0.643	-0.833	13.4	14.2	6.2	16.3	-0.3	23.8
1.700	0.75	0.643	-0.167	13.4	6.1	10.0	7.3	7.8	11.4
1.700	0.75	0.643	0.167	9.3	3.4	3.0	3.9	3.5	7.9
1.700	0.75	0.643	0.500	14.0	5.2	4.4	5.7	12.1	10.0
1.700	0.75	0.643	0.833	8.1	2.8	0.1	2.9	-1.1	6.4
1.800	0.75	0.551	-0.833	21.1	8.8	3.1	11.2	5.4	25.6
1.800	0.75	0.551	-0.500	29.7	4.3	-0.7	4.7	-38.1	12.2
1.800	0.75	0.551	-0.167	47.6	4.1	4.1	4.8	-3.3	11.1
1.800	0.75	0.551	0.167	60.4	6.6	-7.2	8.3	-31.6	18.5
1.800	0.75	0.551	0.500	53.6	5.6	-15.6	8.1	-45.5	18.7
1.800	0.75	0.551	0.833	41.2	5.5	-3.3	7.0	3.7	15.0
1.900	0.75	0.439	-0.833	13.8	4.6	0.2	6.3	0.2	16.2
1.900	0.75	0.439	-0.500	38.7	3.6	-3.5	4.8	-11.4	12.8
1.900	0.75	0.439	-0.167	79.8	4.2	-5.3	5.2	-34.4	14.9
1.900	0.75	0.439	0.167	87.9	4.7	-5.2	6.1	-25.3	16.9
1.900	0.75	0.439	0.500	82.9	5.7	-6.5	8.4	-22.4	21.3
1.900	0.75	0.439	0.833	63.2	10.8	-4.5	17.7	-16.0	35.7
2.000	0.75	0.307	-0.833	12.4	5.1	1.0	9.4	-22.1	27.5
2.000	0.75	0.307	-0.500	16.7	2.5	-2.8	4.5	-15.6	13.2

2.000	0.75	0.307	-0.167	40.6	2.9	-4.9	4.9	-18.9	15.1
2.000	0.75	0.307	0.167	52.5	3.3	1.7	5.2	-43.1	16.8
2.000	0.75	0.307	0.500	52.7	3.8	-8.7	6.5	1.5	19.6
2.000	0.75	0.307	0.833	62.8	10.8	-5.1	21.4	54.8	49.7
1.700	0.85	0.608	-0.167	8.7	4.3	4.9	5.2	6.6	9.2
1.700	0.85	0.608	0.500	12.0	8.8	7.7	10.6	3.3	14.3
1.700	0.85	0.608	0.833	11.3	3.2	4.9	3.5	6.6	6.3
1.800	0.85	0.513	-0.833	16.2	7.9	-5.3	9.2	16.2	24.2
1.800	0.85	0.513	-0.500	29.3	4.0	-3.9	4.6	-26.1	12.1
1.800	0.85	0.513	-0.167	41.3	4.2	4.6	4.8	-42.7	12.3
1.800	0.85	0.513	0.167	49.0	5.0	-1.6	6.4	-17.0	15.2
1.800	0.85	0.513	0.500	49.3	8.5	5.4	13.2	-16.2	26.5
1.800	0.85	0.513	0.833	37.0	6.0	-2.3	7.9	-7.6	16.5
1.900	0.85	0.397	-0.833	13.8	4.5	-6.9	6.4	1.7	17.1
1.900	0.85	0.397	-0.500	41.8	3.8	-11.5	5.4	-30.5	15.3
1.900	0.85	0.397	-0.167	64.9	4.1	0.4	5.6	-32.3	16.0
1.900	0.85	0.397	0.167	90.8	5.2	-9.5	6.8	-57.9	20.7
1.900	0.85	0.397	0.500	84.8	7.1	-5.4	11.2	-18.7	28.4
1.900	0.85	0.397	0.833	65.9	11.0	8.0	19.0	17.0	40.9
2.000	0.85	0.262	-0.833	22.5	19.3	21.2	35.6	29.9	84.6
2.000	0.85	0.262	-0.500	15.4	3.2	-3.7	6.2	7.1	19.1
2.000	0.85	0.262	-0.167	43.4	3.9	-5.7	7.3	-4.4	23.5
2.000	0.85	0.262	0.167	56.1	4.4	-14.4	7.6	-59.7	26.4
2.000	0.85	0.262	0.500	57.2	5.2	-11.5	9.5	-60.3	30.5
2.000	0.85	0.262	0.833	50.9	22.0	-23.1	46.5	-46.9	96.5
1.700	0.95	0.573	-0.833	12.1	12.2	4.6	7.1	-8.0	34.6
1.700	0.95	0.573	0.500	6.0	5.4	-0.4	8.0	-4.9	14.8
1.700	0.95	0.573	0.833	6.7	2.1	0.0	2.0	-7.3	5.5
1.800	0.95	0.473	-0.833	14.9	8.1	-0.8	12.4	0.4	27.9
1.800	0.95	0.473	-0.500	17.4	3.9	9.3	5.1	-9.1	12.1
1.800	0.95	0.473	0.167	49.0	6.4	10.5	8.8	-19.3	18.8
1.800	0.95	0.473	0.500	62.4	9.7	22.0	14.3	38.7	30.9
1.800	0.95	0.473	0.833	35.3	10.9	9.3	15.9	3.2	27.7
1.900	0.95	0.355	-0.833	21.7	6.9	1.3	10.5	-15.4	31.3
1.900	0.95	0.355	-0.500	30.1	3.9	-2.0	6.0	-39.5	17.5
1.900	0.95	0.355	-0.167	56.7	4.3	-5.8	6.0	-63.6	18.8
1.900	0.95	0.355	0.167	74.2	5.8	-16.8	8.5	-11.3	25.8
1.900	0.95	0.355	0.500	64.5	6.4	-10.3	10.3	-34.4	27.4
1.900	0.95	0.355	0.833	54.1	12.2	0.0	22.6	13.3	49.1
1.700	1.05	0.536	-0.833	21.8	17.0	0.1	0.1	-40.3	32.3
1.700	1.05	0.536	-0.167	5.3	3.7	1.4	4.9	3.2	10.2
1.700	1.05	0.536	0.167	10.6	5.6	4.8	7.3	11.4	16.6
1.700	1.05	0.536	0.500	10.7	17.9	2.6	23.0	-8.4	29.5
1.700	1.05	0.536	0.833	5.2	2.2	1.8	2.4	1.6	5.2
1.800	1.05	0.433	-0.500	20.2	0.0	9.1	73.2	-23.4	31.9
1.800	1.05	0.433	-0.167	32.2	4.8	-7.3	6.4	-35.5	17.7
1.800	1.05	0.433	0.167	41.8	7.0	-7.0	10.4	-9.9	24.1
1.800	1.05	0.433	0.500	48.2	10.1	11.5	17.5	-0.1	37.5

1.900	1.05	0.312	-0.833	19.9	7.2	-10.5	12.5	7.5	36.5
1.900	1.05	0.312	-0.500	33.7	4.4	-17.5	7.3	-6.3	22.6
1.900	1.05	0.312	-0.167	45.8	4.2	-18.4	7.1	-21.0	21.3
1.900	1.05	0.312	0.167	68.0	5.5	-16.9	8.9	-26.2	27.5
1.900	1.05	0.312	0.500	57.4	8.2	-12.3	15.2	-31.4	40.7
1.900	1.05	0.312	0.833	38.8	14.5	-17.7	30.7	-55.5	70.8
1.700	1.15	0.498	-0.500	18.8	97.5	4.4	299.6	2.0	734.6
1.700	1.15	0.498	0.167	23.1	13.5	22.6	17.0	30.3	22.6
1.700	1.15	0.498	0.833	11.9	4.8	4.7	5.7	3.1	12.4
1.800	1.15	0.392	-0.500	18.6	5.1	-1.5	7.9	4.5	20.7
1.800	1.15	0.392	-0.167	31.3	6.1	-3.7	9.3	2.2	23.8
1.800	1.15	0.392	0.167	35.5	6.1	5.2	9.7	-42.1	24.0
1.800	1.15	0.392	0.500	36.6	9.7	4.1	15.1	15.2	35.2
1.800	1.15	0.392	0.833	32.9	8.4	6.9	13.2	25.3	30.1
1.700	1.25	0.460	-0.500	35.1	24.8	33.8	33.5	44.1	43.6
1.700	1.25	0.460	0.500	19.9	20.1	19.8	27.9	17.9	34.2
1.700	1.25	0.460	0.833	10.6	5.2	1.1	6.8	4.8	15.4
1.800	1.25	0.351	-0.833	14.8	26.1	5.3	38.4	-8.1	94.1
1.800	1.25	0.351	-0.500	16.7	7.1	6.5	11.4	-0.2	29.6
1.800	1.25	0.351	-0.167	20.3	8.0	0.8	13.9	14.3	35.8
1.800	1.25	0.351	0.167	22.8	7.7	5.2	14.5	-3.6	34.5
1.800	1.25	0.351	0.833	17.2	10.9	2.3	18.9	11.1	38.2
1.700	1.35	0.421	-0.833	132.1	0.0	170.8	0.0	156.9	1569.1
1.700	1.35	0.421	-0.500	20.7	37.4	19.8	53.0	15.2	62.0
1.700	1.35	0.421	-0.167	6.0	19.1	1.3	65.2	1.2	169.5

Appendix C

Drift Chamber Alignment

Abstract

We have analyzed CLAS data taken with the main torus turned off as a source of straight tracks, and determined a set of alignment parameters to specify the orientation and location of the 18 drift chamber packages. The technique converged for the electron run 8935, but failed for multiple reasons when applied to a later photon run. The resulting alignment, used from 1998 to at least the end of 2001, is presented. Ideas for how to improve upon it in future efforts are also given.

C.1 Overview of the Alignment Technique

C.1.1 Introduction

Our goal is to determine the relative wire-to-wire positions in each CLAS drift chamber (DC), and the chamber-to-chamber positions relative to each other and to the target. It is important to determine the wire positions accurately because we have seen that for a misalignment of a few millimeters, the momentum resolution can be degraded by a factor of two or more. The precision to which the wire positions must be known is governed by the desired momentum resolution. The specified design momentum resolution was $\delta p/p \leq 0.5\%$ for a $p = 1\,\mathrm{GeV/c}$ particle [47]. Since the deviation of a track from a straight line (sagitta) goes as $\xi \propto \frac{B}{p}$, we get

$$\frac{dp}{d\xi} = \frac{p^2}{\xi_1 p_1 (B/B_1)}$$

at the reference point (ξ_1, p_1, B_1). With a 50% magnetic field, the sagitta for a 1 GeV track near $\theta = 30^\circ$ is 16 cm, yielding a $\frac{dp}{d\xi} \sim 0.62\%/\mathrm{mm}$. This suggests that it is necessary to know the hit positions along a track with a maximum uncertainty of 0.8 mm. The local position resolution of the drift chambers is on the order of 200 μm by design.

It must be kept in mind that an offset of the geometry has a consistent effect on the measured momentum of tracks in that sector, ie. it is not a source of uncorrelated error. We will refer to the relative wire-to-wire positioning inside a single drift chamber as the internal chamber geometry. It is assumed to be fixed, and is computed from direct conversions of the design drawings and databases for the drift chambers. The external geometry is then the position and orientation of the individual drift chambers in the CLAS detector.

Using data taken with the main torus magnetic field off, straight tracks can be used to study the alignment of the drift chambers without the momentum fit and the magnetic field masking the mis-alignments. The ideal conditions for collecting straight track data for DC alignment would be with all magnets off and a narrow incoming beam. The closest we can come to these conditions, however, is either to use a narrow ($\sigma_b < 0.5$mm) electron beam with the mini-toroid magnet on to protect DC Region One, or to use a wide ($\sigma_b \sim 3$cm) photon beam with all magnets off. Data of both types have been collected and analyzed. The current (as of 17-Dec-2001) best-determination of the geometry (r3_3tor2r1nom_req1_tre.map, Oct1998) was determined with electron Run 8935. There have been problems with the analysis and use of the photon data which will be discussed below.

C.1.2 Assumptions

The initial assumptions were:

- The internal drift chamber geometry[1] is fixed.
- Distortions of the drift chamber shape, such as twists and wire sag due to gravity, are not important at the level of this analysis.
- The Region One drift chambers have the best relative (sector-to-sector) alignment since they were constructed as a single unit, with a claimed sector-to-sector accuracy of about 0.2 mm.

A special x_vs_t calibration was not performed for these runs, which probably leads to some of the very wide residual distributions for Region Two. Region Two, which is located between the magnetic coils, was calibrated for non-zero magnetic field runs and the quality of the extrapolation of the x_vs_t function to B=0 is potentially poor.

C.1.3 Technique

The positions and directions of the individual sense wires within a single drift chamber unit (a given region and sector) are assumed to be fixed relative to each other -

[1]The relative positions and directions of the individual sense wires inside a single drift chamber sector and region.

the chambers are assumed to be rigid bodies. The overall geometry can then be characterized by 6 parameters: a set of offsets (d_X, d_Y, d_Z) and rotations (rot_X, rot_Y, rot_Z) of the chambers from their design position and orientation.

Using only the DC hit information, we only have access to the position and orientation of a drift chamber relative to the others in the same sector. The sector-to-sector relative alignment was taken into account by aligning the Region Two and Region Three drift chambers to the Region One chambers, since the Region One drift chambers were assembled into a single unit with tolerances of about 200 μm.

For the first pass, Region One was used as the reference drift chambers. The straight tracks were fit at the *time-based* level to the reference drift-chamber region (Region One), and at the *hit-based* level to the un-aligned regions (Region Two and Region Three). Then, the geometrical parameters for Region Two were permitted to float in order to minimize for the hits in that region:

$$\chi^2 = \sum_{tracks} \sum_{hits} \frac{(|D_{track,hit}| - |D_{hit}|)^2}{\sigma^2_{track,hit} + \sigma^2_{hit}} \tag{C.1}$$

where $D_{track,hit}$ is the calculated distance-of-closest approach of the track to the hit wire, D_{hit} is the drift distance returned by the x_vs_t function for that wire, $\sigma_{track,hit}$ is the uncertainty on the track position at that hit (by propagating the error matrix for the track to the hit), and σ_{hit} is the time-based resolution of the hit. The distances $D_{track,hit}$ and D_{hit} are signed according to the supposed side of the wire the track is on: $D_{track,hit}$ according to the fitted track, and D_{hit} as determined by the left-right ambiguity resolution performed over the superlayer. As the drift chamber geometry is modified by the fit, $D_{track,hit}$ is recalculated for each hit and track as the wire positions change. The **spatial residual** for a hit is $(D_{track,hit} - D_{hit})$, and is what will be examined later to determine the quality of the alignment.

After equation C.1 has reached a stable minimum for Region Two, the next step is to align Region Three. The method here is similar, with this time the tracks being fit at the *time-based* level to both Region One and Two, and at the *hit-based* level to Region Three. Equation C.1 is then minimized by varying the geometrical parameters for Region Three.

C.1.4 Track Selection and fitting Criteria

To have the minimization procedure converge to a stable result we found it necessary to:

- Select only those tracks with no more than one missing hit per superlayer per track.
- Reduce the geometric offset parameters to those accessible via the axial wires (d_X, d_Z, rot_Y).

- De-weight the stereo superlayer hits when determining the track parameters (which is performed before the alignment minimization).
- Select only those tracks containing hits within 3cm (!!) of the fitted track position.

C.2 Alignment Analysis with Electron Run 8935 (Oct1998)

The initial CLAS geometry was the "ideal" design geometry. An optical survey of the chambers completed on October 31, 1997 produced the first set of offsets and is called the SURVEY geometry [76]. The SURVEY offsets provided the starting geometry for the straight-track alignment analysis, and are listed in Table C.3.

The DC geometric offsets used for PROD-1-9 E1 and G1A,B cooking were determined using the *empty target* B=0 Run 8935, with the CLAS_PARMS directory and DC x_vs_t calibration as it was as of 9-Sep-1998. Between 18k and 29k tracks per sector were used, depending upon the sector. The tracks were first selected with the standard CLAS tracking code, but after multiplying the σ's of the *stereo* superlayers by 100, thus deweighting them in the fit. This was done so that only the *axial* superlayers, which would later be used in the alignment fit, contributed strongly to the track parameter fit. Then, the selected tracks were fit with σ-multipliers for superlayers {1-6} of {100, 1, 4000, 4000, 7000, 7000} respectively, to fit the tracks to Region One. The overall effect was that the selected tracks were now locked in place by the Region One axial layers. Next, the projection of these tracks into Region Two were used with Eqn. C.1 to align Region Two. The tracks were then re-fit to both Region One and Two, using σ-multipliers of {100, 1, 1, 100, 4000, 4000}. Again Eqn. C.1 was minimized, this time to align Region Three. The final deviations of the 3 free offsets from their survey values can be found in Table C.1.

To evaluate the uncertainty on these alignment parameters, we looked at their stability over multiple minimization trials, starting at different locations in the parameter space. For both Region 2 and Region 3 we found that for all sectors, δrot_Y was stable to within 0.0001 rad, and the shifts δd_X and δd_Z were stable to within 0.02 cm.

The quality of the alignment, and most importantly the change in the quality, is seen by looking at the residual distributions for the layers. These distributions were produced using Run 8936, which had a *full target* and B=0. The residual vs. layer plots for the starting survey geometry can be found Figures C.1, C.2, and C.3. The distributions are broken down into large and small angle portions, since over a limited range of the detector the offset parameters are highly correlated. Within each given angular range, all the cells in a given layers are summed over. In the past we have found alignment offset solutions that appear to correct the residual distribution for the small angle tracks, while making the distribution for the large

	δd_X(cm)	δd_Z(cm)	δrot_Y(rad)
Reg: 2 Sec: 1	0.1216	0.0048	-0.0001
Reg: 2 Sec: 2	0.0652	-0.0020	-0.0007
Reg: 2 Sec: 3	-0.0282	0.1022	-0.0004
Reg: 2 Sec: 4	0.0548	-0.0047	-0.0007
Reg: 2 Sec: 5	-0.0745	0.0206	0.0005
Reg: 2 Sec: 6	0.0685	-0.0727	-0.0001
Reg: 3 Sec: 1	-0.1905	0.2342	0.0009
Reg: 3 Sec: 2	-0.2145	0.2759	0.0004
Reg: 3 Sec: 3	-0.1717	0.3123	0.0003
Reg: 3 Sec: 4	-0.0216	-0.2412	-0.0007
Reg: 3 Sec: 5	-0.2997	0.1280	0.0010
Reg: 3 Sec: 6	-0.0156	-0.0332	0.0007
Uncertainty:	0.0200	0.0200	0.0001

Table C.1: Deviations of the final fit parameters from the Survey offsets as determined from Run 8935. The uncertainty is the stability of the fit over multiple minimization trials.

angle tracks much worse. As can be seen in the graphs, as one moves from one Region to the next (boundaries are at layers 13 and 19), often a jump in the center of the distribution can be seen (for example, in C.1, Sector 1). These sharp jumps are caused by chamber misalignments, while the wider distributions (as can be seen in C.2, Sector 4 large angle or any of the large angle plots) can be caused by a combination of the misalignment and a poor x_vs_t calibration. As was stated earlier, the x_vs_t calibration in Region Two was extrapolated to B=0 and is of questionable quality. Also, the behavior of the distributions for the small and large tracks can be quite different, hence we display their behavior separately.

After the alignment procedure, the sharp shifts in the distributions centers are, for the most part, removed, as can be seen in Figures C.4, C.5, and C.6. The width of the residual distribution is still abnormally large for some of the Region Two chambers, probably due to the extrapolation of the x_vs_t function to B=0. The final alignment offset parameters for the Oct1998 alignment can be found in Table C.4.

A more quantitative determination of the effect of the alignment procedure can be made. We compared the SURVEY and Oct1998 geometries by looking at the residual distributions summed over the axial superlayers. Again, separate distributions were collected for low angle ($15 < \theta < 25°$) and high angle ($55 < \theta < 65°$) ranges. These distributions were then fitted to a double-Gaussian function, and the results are summarized in Table C.2. The parameters P2, and P3 are the primary peak center and width; and similarly are P5, and P6 for the secondary peak. While the distributions are clearly more centered after the alignment, it appears that there is

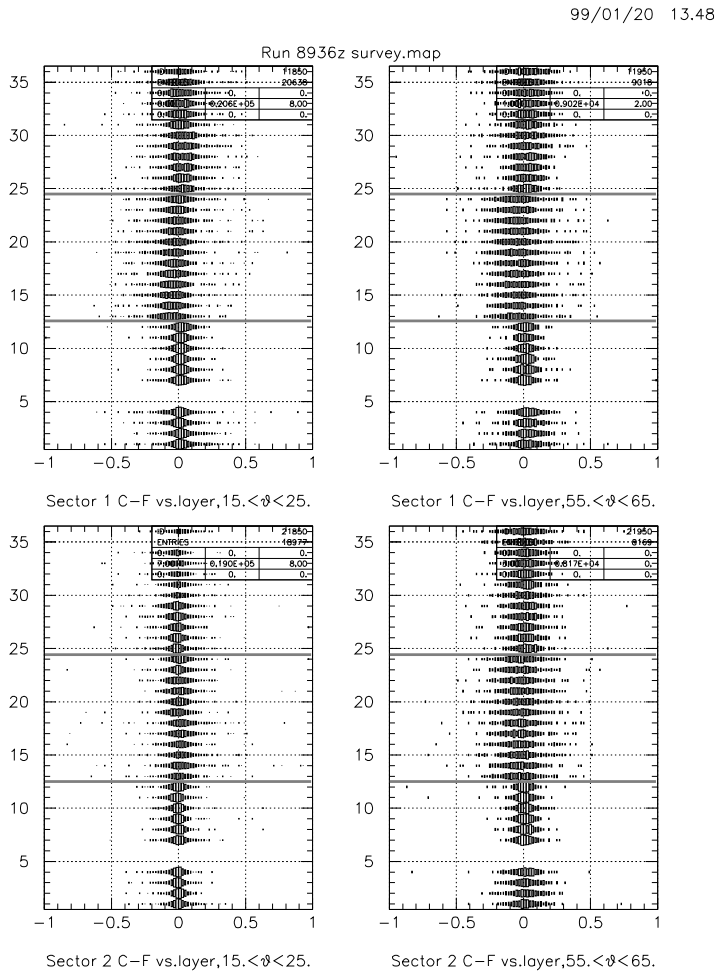

Figure C.1: Sectors 1(top) and 2(bottom), spatial residual(cm) (horizontal axis) vs. layer (vertical axis) with the Survey Geometry for Run 8936(B=0), fitting to all layers. The left column contains low angle (electron) and the right large angle (proton) tracks. Layers 1 to 12 are in Region One, Layers 13-24 are in Region Two, and Layers 25-36 are in Region Three. Layers 5 and 6 do not physically exist.

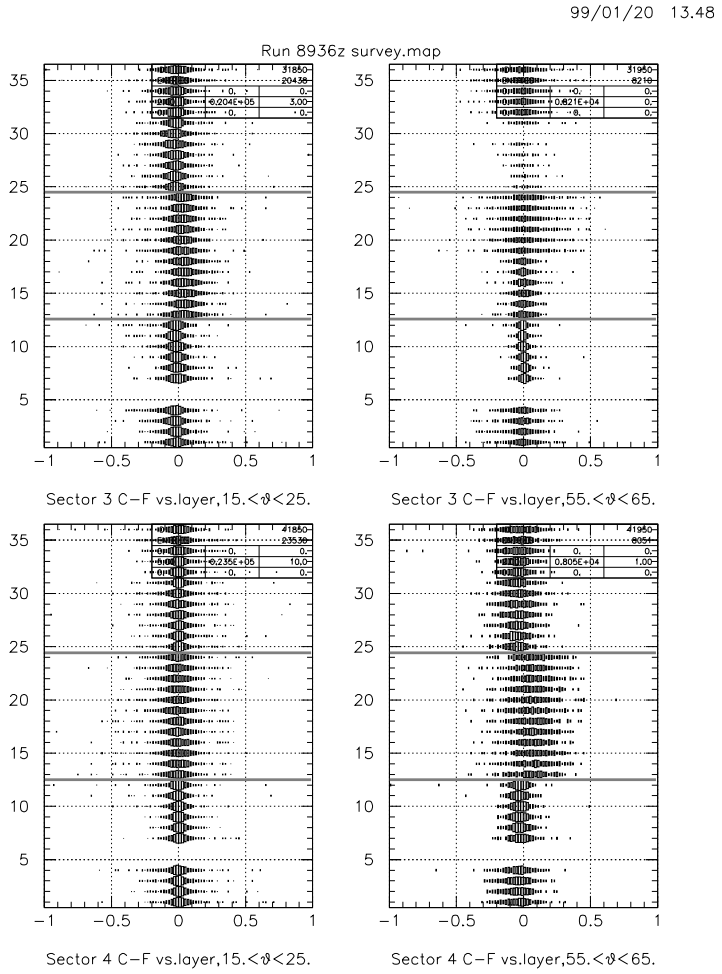

Figure C.2: Sectors 3(top) and 4(bottom). See caption for Figure C.1.

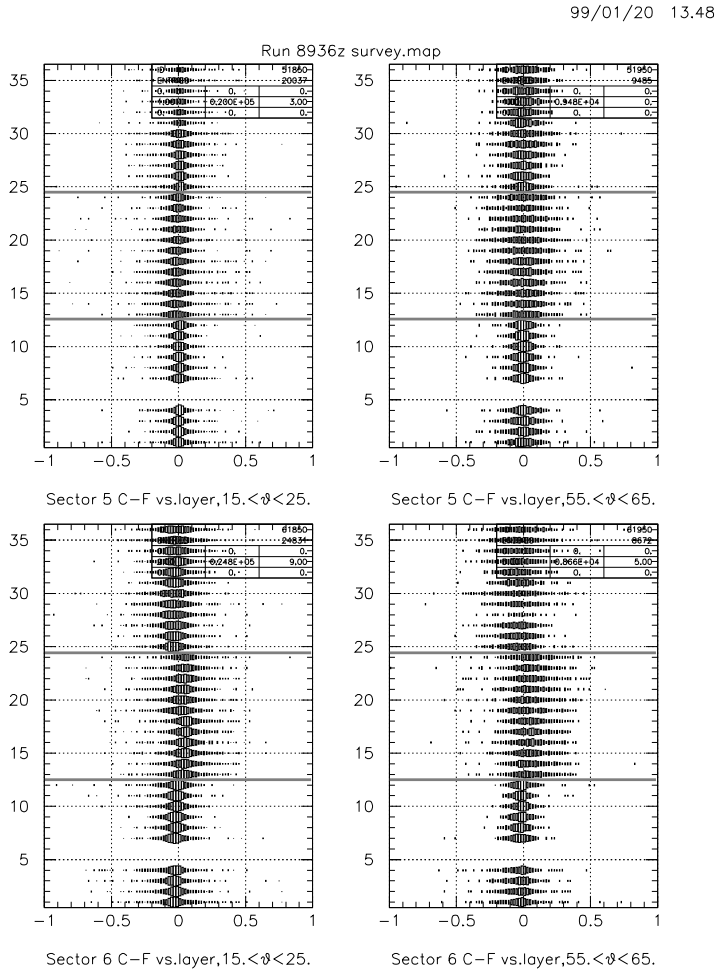

Figure C.3: Sectors 5(top) and 6(bottom). See caption for Figure C.1.

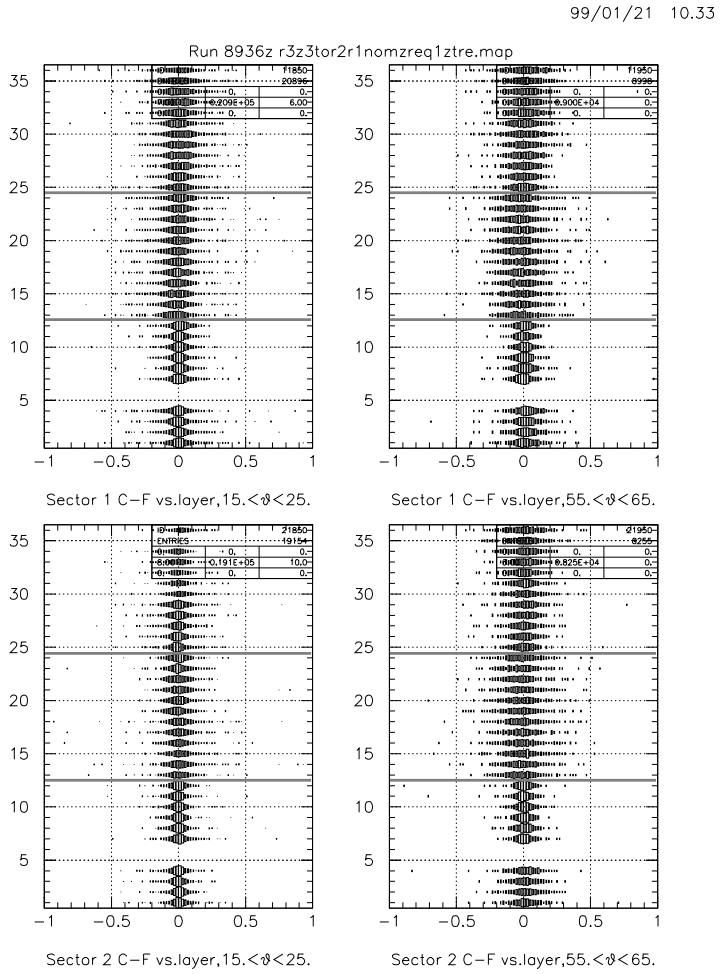

Figure C.4: Sectors 1(top) and 2(bottom), residual vs. layer with the Oct1998 Geometry for Run 8936(B=0), fitting to all layers. This figure is to be compared with Figure C.1.

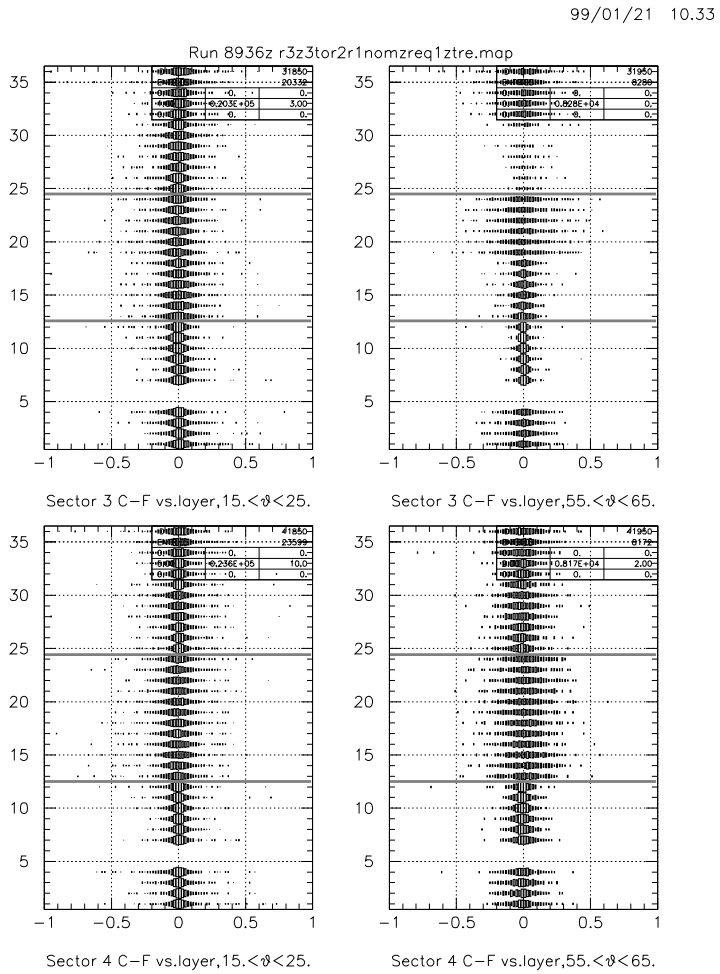

Figure C.5: Sectors 3(top) and 4(bottom), residual vs. layer with the Oct1998 Geometry for Run 8936(B=0). This figure is to be compared with Figure C.2.

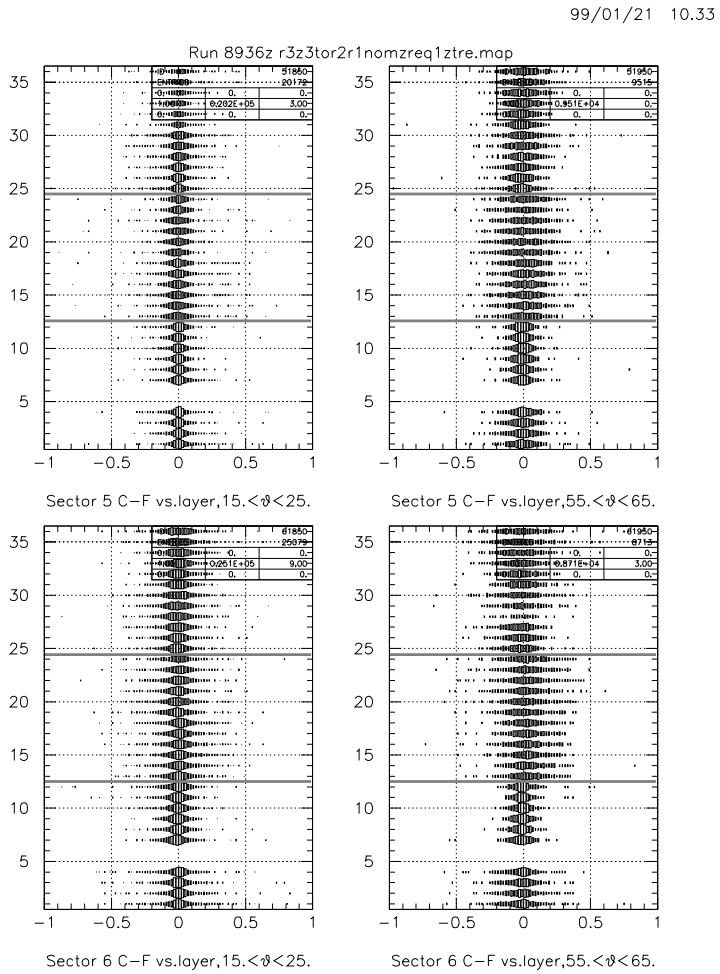

Figure C.6: Sectors 5(top) and 6(bottom), residual vs. layer with the Oct1998 Geometry for Run 8936(B=0). This figure is to be compared with Figure C.3.

still some room for improvement (see large angle Sectors 4 and 5 in Figures C.17 and C.19). While the widths of the distributions changed negligibly, the centroids of the primary peak, which had deviated by up to 650μm from zero, now lie within 200μm of zero, and on average are less than 150μm distant.

		Small Angle			Large Angle		
Sector	SL	$\lvert\overline{x_{survey}}\rvert$ (μm)	$\lvert\overline{x_{oct98}}\rvert$ (μm)	σ diff(%)	$\lvert\overline{x_{survey}}\rvert$ (μm)	$\lvert\overline{x_{oct98}}\rvert$ (μm)	σ diff(%)
1	2	152	32	-6	136	35	-3
	3	438	132	-9	470	177	-2
	5	303	85	2	249	54	5
2	2	37	5	-7	105	56	-6
	3	134	32	-8	263	141	-3
	5	116	48	5	174	90	-6
3	2	168	18	-5	8	7	-6
	3	393	3	-8	81	12	-23
	5	262	11	-2	124	35	2
4	2	10	26	-8	275	86	-20
	3	29	54	-4	750	194	-23
	5	21	42	-2	436	114	-7
5	2	67	6	-6	10	58	-7
	3	184	61	-7	74	173	4
	5	137	27	-2	39	92	35
6	2	198	59	-9	149	76	-16
	3	417	54	-13	283	142	-7
	5	349	78	-12	356	121	-16
Average		190	43	-6	221	92	-6

Table C.2: The fit parameters for the residual distributions summed over each the axial superlayer for the SURVEY and Oct1998 DC geometries. Shown are the magnitudes of the position (ideally at 0) of the primary peak fitted position ($|\overline{X}|$) for the two geometries, and percentage change of the peak width. Note that not only do the average positions get closer to 0, but the range of values also decreases significantly. These were extracted from Figures C.8-C.19.

C.3 Alignment Analysis with Photon Run 19583

A great deal of effort was put into attempting to extract a DC geometry for the Photon run 19583, taken August 1999. This run had the potential to be very useful since:

1. some Region 3 sectors of the Drift Chambers had recently been moved while being repaired;

2. the mini-toroid was not installed, so it was a true "B=0" run;

3. the target was empty, providing hard constraints on the tracks having to come from the target walls.

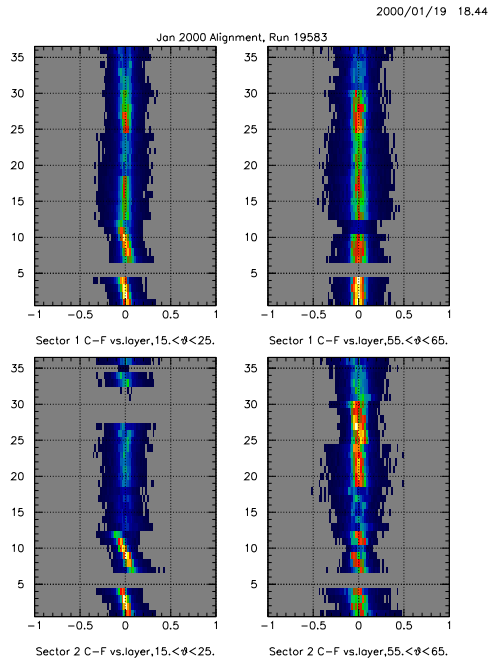

Figure C.7: The residual distribution seen for Sectors 1 and 2 from the Photon run. The very strong layer dependence of the residual in Region 1 at small angles was evident in all sectors and persisted regardless of which layers were used in the fit, causing the analysis to fail.

Unfortunately, there were some problems that made this run unusable. First, it had a two-charged track trigger, but with low energy thresholds so that the data was dominated by the production of low energy e^+e^-pairs, which normally would have been swept away by the magnetic field. The low energy tracks multiple-scattered more than the higher energy hadrons (greater than 500 MeV). Secondly, the drift-time calibration of this run was very problematic, probably due to the previous issue. Lastly, we observed a layer-dependence to the track residuals in Region 1 that was not seen in any of the other data sets. This effect can be seen in the lower part of the left-hand panels of Figure C.7. It is believed that this effect was due to a bug in the tracking code [77]. Another analysis using the now corrected version of the tracking library might succeed.

C.4 Future Work

While we had success in improving upon the SURVEY drift chamber alignment, as has been shown in the residual distribution, there is still room for improvement. Most importantly, the chambers have been physically moved during repairs to the Region 3 drift chambers and a new software alignment has not been determined since then. Some ways to improve the current understanding of the drift chamber geometry are:

1. Improve the internal DC geometry, taking into account gravitational wire sag (at most ˜150μm for 2m wire);
2. Better select high energy electrons/hadrons via $\frac{dE}{dx}$ in the EC(small angle) or TOF(very large angle) detectors;
3. Use data taken with a thin target of precisely known (x,y,z) position relative to the cryostat/R1, to supply a constraint on the track vertex position and be able to better position Region 1 inside the magnetic field.

Of course, understanding the drift chamber alignment is only a part of the issue of improving the momentum resolution of CLAS. Of equal or greater importance is to understand the magnetic field generated by the main torus. Work to parameterize the effect on the measured momentum due to both residual misalignment and magnetic field issues has been done by others [57].

C.5 Conclusion

We were able to analyze and use the electron run 8935 to improve the measurement of the alignment of the CLAS drift chambers. This alignment was then used for the cooking of e1b/c data with PROD-1-9 and all subsequent data sets to date. Another analysis was attempted after repairs were performed on the drift chambers, but failed due to the poor quality of the data and a bug in the tracking software. The alignment analysis can and should be repeated after every removal and re-placement of the drift chambers. We believe that the technique used here would work as well or better if applied to more recent field-off calibration runs.

C.6 The Programs

C.6.1 user_align – Track reconstruction

Two programs were used to do the alignment procedure. The first is a specialized user package called user_align to be used with the standard RECSIS tracking/reconstruction software. It is available under CVS at calib/dc_cal/user_align. The

tracking software [55] had to be modified to permit the fitting of the zero-magnetic field data, removing the optimization of the track momentum from the fit, as well as related entries in the covariance matrix. These changes have been implemented into the standard tracking code (trk package). Other than just fitting the tracks, user_align can also:

- keep only events that contain 2 or more opposite sector tracks for electron runs (defeated with align_photon_run TCL variable);
- determine for empty target runs which target wall the tracks came from, so that it can be used as a vertex constraint in the track fitting (see align_vert_cut, trk_VXconstr, target_wall, dstmwall, upstmwall, dstmlen, and upstmlen TCL variables);
- create an NTUPLE containing hit and track information.

A sample TCL file with information as to how to use these switches can be found below.

Sample TCL file

```
#
# init file for RECSIS
#

#  load in  Tcl procedures, first check to see
#  if the user is working
#  from the stand recsis_proc.tcl or has their own

if { {[}file exists ../../tcl/recsis_proc.tcl{]} } {
    source ../../tcl/recsis_proc.tcl
} else {
    source $env(RECSIS)/tcl/recsis_proc.tcl
}

# define packages

turnoff ALL
global_section off

# set ltagger_do and lst_do = -1 for photon running
set ltagger_do  0;
set lst_do      0;
set lrf_do     -1;
set lcall_do   -1;
set ltof_do    -1;
set lcc_do     -1;
set legn_do    -1;
```

```
set lec1_do    -1;
set llac_do    -1;
set ltrk_do    -1;
set lusr1_do   -1;
set lusr0_do   -1;
set lhbid_do   -1;
set lseb_do     0;

inputfile clas_008935.A00
setc chist_filename all_layer_fit.hbook
outputfile all_layer_fit.out
setc log_file_name all_layer_fit.log

# Set the magnetic field type to 5, specifying
# that no B-field present. This is not exactly true
# for electron running, where the minitorus is present,
# but is needed to get the right switches used in
# ana_trfit.
# Besides, we don't know what the momentum of a
# particle is, so tracking it through a B-field is
# not of much use.
# Uncomment next line to force B-field=0
#set trk_magtyp 5;

set trk_print(1) 1;

#level of analysis 0: raw  2: hbt 4: tbt
set trk_level 4;

# Tbt stuff realistic curve for drift time to
# drift distance. Probably no longer needed
set dc_xvst_choice 2;

#For the ALIGNMENT, we want to be able to modify the
# SIGMA's for the track fitting
# by default, these are all = 1.
# Default running conditions
set dc_mult_Sigma(1) 1.
set dc_mult_Sigma(2) 1.
set dc_mult_Sigma(3) 1.
set dc_mult_Sigma(4) 1.
set dc_mult_Sigma(5) 1.
set dc_mult_Sigma(6) 1.

# Fit to AXIAL layers only strongly
#set dc_mult_Sigma(1) 100.
#set dc_mult_Sigma(2) 1.
#set dc_mult_Sigma(3) 1.
#set dc_mult_Sigma(4) 100.
#set dc_mult_Sigma(5) 1.
#set dc_mult_Sigma(6) 100.
```

```
# Fit to Region 1 Axial layers only strongly
#set dc_mult_Sigma(1) 100.
#set dc_mult_Sigma(2) 1.
#set dc_mult_Sigma(3) 4000.
#set dc_mult_Sigma(4) 4000.
#set dc_mult_Sigma(5) 7000.
#set dc_mult_Sigma(6) 7000.

# Fit to Region 1+2 Axial layers only strongly
#set dc_mult_Sigma(1) 100.
#set dc_mult_Sigma(2) 1.
#set dc_mult_Sigma(3) 4000.
#set dc_mult_Sigma(4) 4000.
#set dc_mult_Sigma(5) 7000.
#set dc_mult_Sigma(6) 7000.
# DO VERTEX-Constrained FIT -{}- empty target runs only!!!
#  align_vert_cut = 0 don't change target wall
#                   1 change target wall to either
#                     upstm or dwnstm, depending upon
#                     which has more tracks around.
#set align_vert_cut 1;
#
#  trk_VXconstr = 0  no vertex constraint on track
#                 1 or 3   constraint due to thin
#                          beam size
#                 2 or 3   constraint due to thin
#                          target (transverse to beam)
#set trk_VXconstr   2;
#
#  target_wall  =   length (thickness) of target
#                   along Z (beam direction)
#set target_wall   0.5;
#  beam_spot =  NOT USED
#set beam_spot     0.5;
#
#  dstmwall , upstmwall  = Z(cm) location of the
#                          downstream and upstream
#                          target walls. Determine
#                          location from 3-track Vertices
#set dstmwall
#set upstmwall
#
#  dstmlen, upstmlen  = distance in Z from the
#                       target-wall center the track
#                       vertex can be in order to count
#                       as a track from that wall.
#set dstmlen       0.5;
#set upstmlen      0.5;
#
# Be sure to set the TARGET POSITIONS appropriately!!!
#set TargetPos(1)   0.099920;
```

```
#set TargetPos(2)  -0.580300;

# tell FPACK not to stop if it thinks you are running
#  out of time
fpack char‘"{}timestop -999999999char‘"{}

# do not send events to event display
set lscat $false;
set ldisplay_all $false;

# tell recsis to pause or go
#set nevt_to_skip 10000
go 300000
setc rec_prompt char‘"{}align_recsis> char‘"{}
exit_pend
```

C.6.2 alignndc – Intra-sector Alignment

The program alignndc, available under CVS at calib/dc_cal/alignndc, takes the tracks from a BOS file created with user_align and performs the actual minimization of C.1 with trial DC geometries. It uses the downhill simplex method to find the minimum. The options for it are:

```
>alignndc -h

Usage:

 alignndc -o<results> {[}-options{]} <file>
    -o<results>     final fitted file of form used by dc\_map
     <file>         cooked file containing B=0 tracks to be used.

Options : (default)
    -i<offsets>     offset file of form used by dc\_map
    -s<sector>      list of sectors to fit coherently.
    -n<\#events>     number of events to process. 0 for all (1000)
    -j<\#events>     number of events to skip/jump over (0)
    -d<dim \#>       dimension to fit (z,x,roty,rotx,y,rotz) (123 = z x roty)
    -l<layertype>   1 for axial, 2 for stereo, 3 for both (1)
    -rf<RegionPat>  which region group to move and fit together (2)
    -M<sl><maxhole> max number of permitted holes in sl (1,2,2,2,2,2)
    -w<reg><float>  factor that sigma has been multiplied by (1.,1.,1.)
    -D              debugging output flag.
    -W              turn on term weights by cos(theta) distribution.
    -P<float>       Maximum \%difference between best and worst chi2.(0.000020)
```

It can accept the initial geometry offsets from either a text file in the dc_map format, or from the Map/CalDB, and it will write the output in the dc_map format to the ¡results¿ file. The input datafile of tracks ¡file¿, generated by user_align, must

contain the following BOS banks: HEAD, TBTR, TBER, and TBLA. To select which chambers to align, use the -s and -rf options; if the sector is 0, then all of Region One will be moved about as a unit (keeping it "intact"), otherwise select only one sector. Multiple Regions can be selected with -rf, and the same offsets will be applied to them. The -M option specifies the maximum number of missing hit wires for that superlayer. Also, the σ-multiplier that was used for tracking should be specified on a Region-by-Region basis with -w (for example, if Region Two was fit with a multiplier of 4000, the option would be -w24000.). The -l option specifies which superlayers will be used in the minimization.

The -W option probably should NOT be used without studying its implementation in code. It permits the user to change the weight of a track in the fit as a function of theta, to emphasize the larger angle tracks. The statistical propriety of this technique as implemented is dubious.

An example of using aligndc to align Region Two sector 2 to Region One with the (dX, dY, rotY) parameters, accounting for the σ multiplier of 4000. for Region Two, using only the *axial* superlayers, permitting a maximum number of holes per superlayer of (4,1,2,6,6,6) is:

```
> aligndc -s2 -rf2 -w24000. -d123 -l1
   -M14 -M21 -M32 -M46 -M56 -M66
   -isurvey.map -ofit_sector2-output1.map r1_8935ax.filter
```

C.7 Geometrical Offsets

The parameter offsets for the Survey and final Oct1998 Geometries.

DC Geometry for run	2	**(Survey, survey.map)**				
	dX(cm)	dY(cm)	dZ(cm)	rotX(rad)	rotY(rad)	rotZ(rad)
Toroid align (xyz)	0.1310	0.0030	0.0330	0.0000	0.0000	0.0040
DC reg:1 sec:1	0.0660	-0.0940	-0.1400	-0.0008	0.0001	-0.0042
DC reg:1 sec:2	-0.0480	-0.1040	-0.1400	-0.0005	-0.0007	-0.0042
DC reg:1 sec:3	-0.1140	-0.0100	-0.1400	0.0003	-0.0008	-0.0042
DC reg:1 sec:4	-0.0660	0.0940	-0.1400	0.0008	-0.0001	-0.0042
DC reg:1 sec:5	0.0480	0.1040	-0.1400	0.0005	0.0007	-0.0042
DC reg:1 sec:6	0.1140	0.0100	-0.1400	-0.0003	0.0008	-0.0042
DC reg:2 sec:1	0.9630	0.0790	-0.1530	0.0001	-0.0001	0.0029
DC reg:2 sec:2	0.8730	0.0840	-0.1710	0.0003	-0.0001	0.0030
DC reg:2 sec:3	0.8680	-0.2160	-0.2010	-0.0003	-0.0005	0.0049
DC reg:2 sec:4	0.9300	-0.0010	-0.2170	-0.0002	-0.0007	0.0043
DC reg:2 sec:5	0.9990	0.0380	-0.2870	-0.0007	-0.0005	0.0033
DC reg:2 sec:6	0.9940	0.0410	-0.1590	0.0005	0.0003	0.0036
DC reg:3 sec:1	1.3550	-1.0950	-0.2750	0.0017	0.0007	0.0035
DC reg:3 sec:2	0.9150	0.1660	-0.1450	-0.0003	0.0007	0.0023
DC reg:3 sec:3	1.0320	0.5740	-0.1130	0.0000	0.0001	0.0038
DC reg:3 sec:4	1.1840	1.0640	0.5230	-0.0004	0.0004	0.0038
DC reg:3 sec:5	1.4150	-0.0970	0.1180	-0.0003	0.0009	0.0053
DC reg:3 sec:6	1.5750	-0.3810	0.2790	0.0001	0.0006	0.0041

Table C.3: DC Geometry offsets as determined by the Survey group at Jefferson Lab. [76]

DC Geometry for run	10	**(Oct1998, r3_3tor2r1nom_req1_tre.map)**				
	dX(cm)	dY(cm)	dZ(cm)	rotX(rad)	rotY(rad)	rotZ(rad)
Toroid align (xyz)	0.1310	0.0030	0.0330	0.0000	0.0000	0.0040
DC reg:1 sec:1	0.0660	-0.0940	-0.1400	-0.0008	0.0001	-0.0042
DC reg:1 sec:2	-0.0480	-0.1040	-0.1400	-0.0005	-0.0007	-0.0042
DC reg:1 sec:3	-0.1140	-0.0100	-0.1400	0.0003	-0.0008	-0.0042
DC reg:1 sec:4	-0.0660	0.0940	-0.1400	0.0008	-0.0001	-0.0042
DC reg:1 sec:5	0.0480	0.1040	-0.1400	0.0005	0.0007	-0.0042
DC reg:1 sec:6	0.1140	0.0100	-0.1400	-0.0003	0.0008	-0.0042
DC reg:2 sec:1	1.0846	0.0786	-0.1482	0.0001	-0.0002	0.0029
DC reg:2 sec:2	0.9382	0.0838	-0.1730	0.0003	-0.0008	0.0030
DC reg:2 sec:3	0.8398	-0.2159	-0.0988	-0.0003	-0.0009	0.0049
DC reg:2 sec:4	0.9848	-0.0013	-0.2217	-0.0002	-0.0014	0.0043
DC reg:2 sec:5	0.9245	0.0382	-0.2664	-0.0007	0.0000	0.0033
DC reg:2 sec:6	1.0625	0.0407	-0.2317	0.0005	0.0002	0.0036
DC reg:3 sec:1	1.1645	-1.0939	-0.0408	0.0017	0.0016	0.0035
DC reg:3 sec:2	0.7005	0.1664	0.1309	-0.0003	0.0011	0.0023
DC reg:3 sec:3	0.8603	0.5746	0.1993	-0.0000	0.0004	0.0038
DC reg:3 sec:4	1.1624	1.0643	0.2818	-0.0004	-0.0003	0.0038
DC reg:3 sec:5	1.1153	-0.0956	0.2460	-0.0003	0.0019	0.0053
DC reg:3 sec:6	1.5594	-0.3809	0.2458	0.0001	0.0013	0.0041

Table C.4: DC Geometry offsets for the October 1998 analysis of Run 8935 (r3_3tor2r1nom_req1_tre.map).

C.8 Summed over Superlayer Results

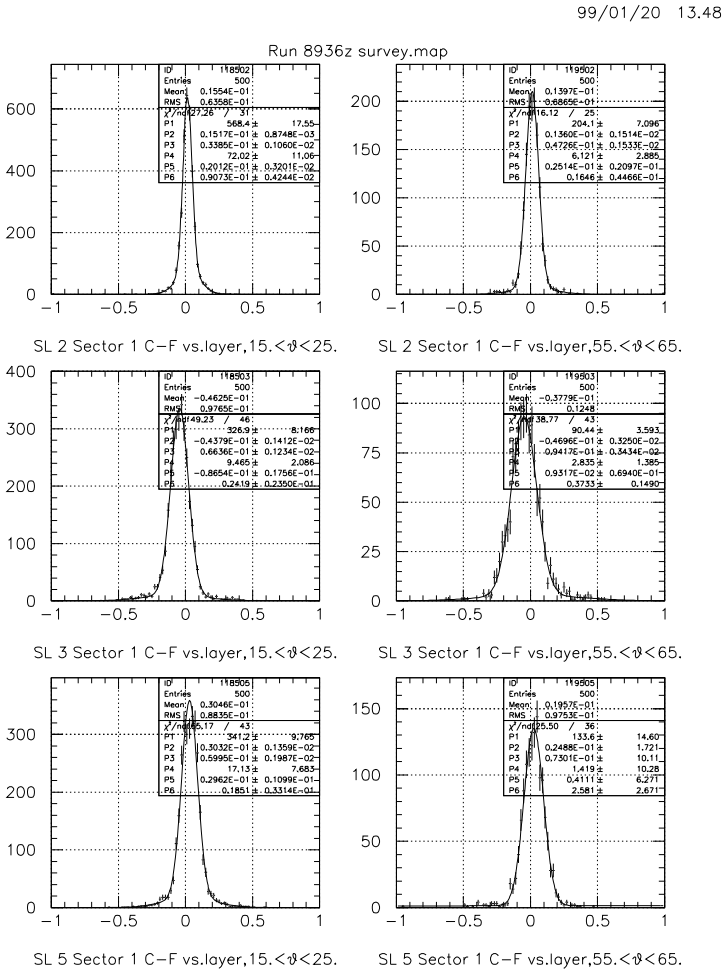

Figure C.8: Sector 1 spatial residual distributions for the Survey Geometry, summed over the *axial* superlayers in each region.

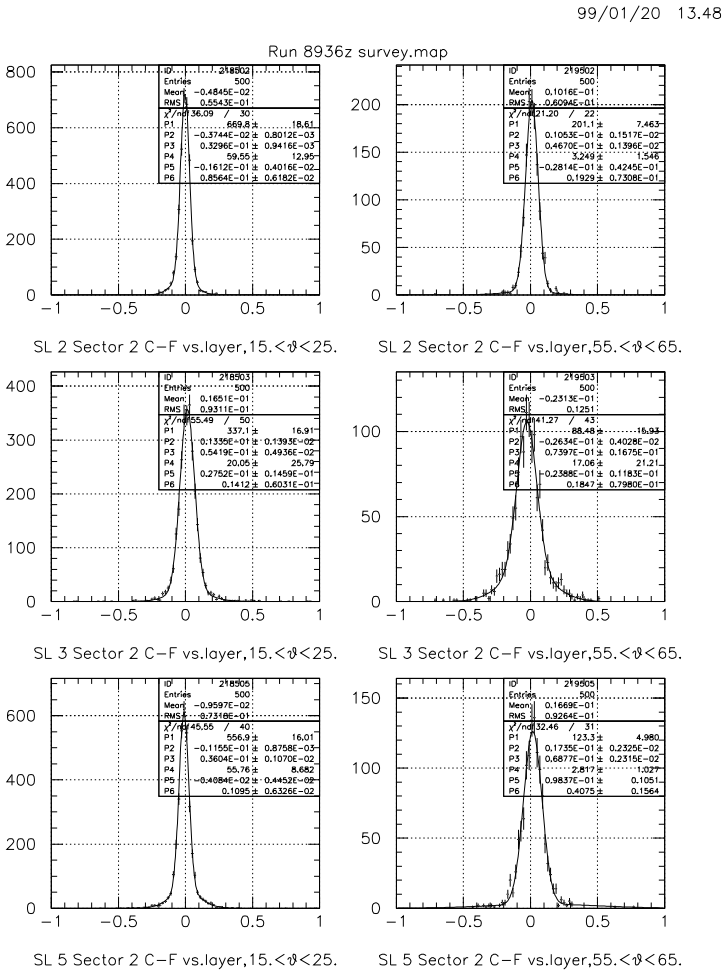

Figure C.9: Sector 2 spatial residual distributions for the Survey Geometry, summed over the *axial* superlayers in each region.

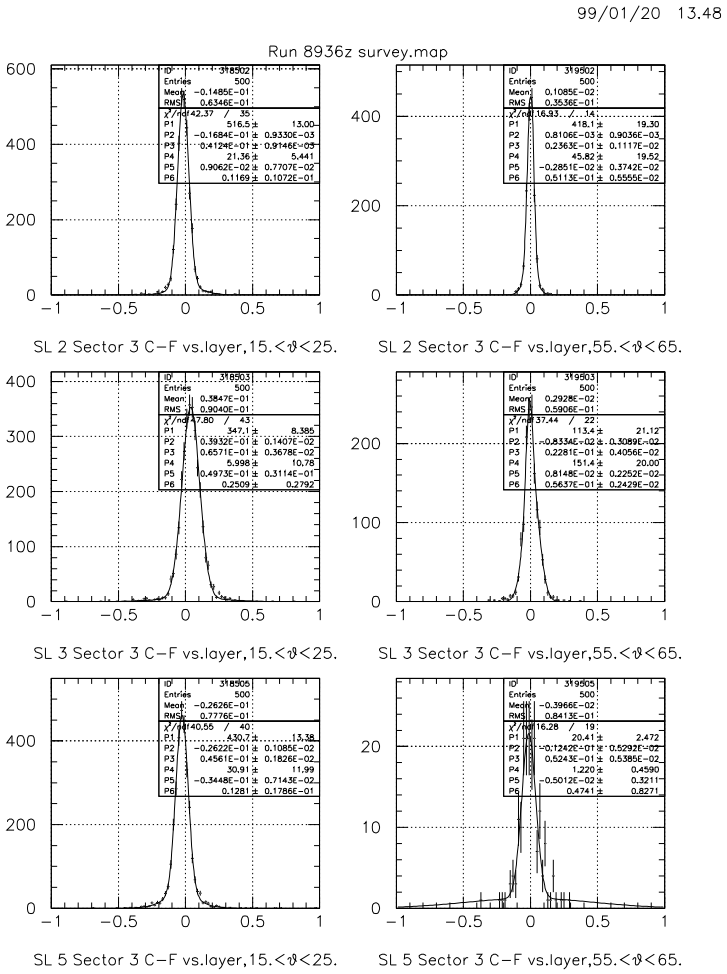

Figure C.10: Sector 3 spatial residual distributions for the Survey Geometry, summed over the *axial* superlayers in each region.

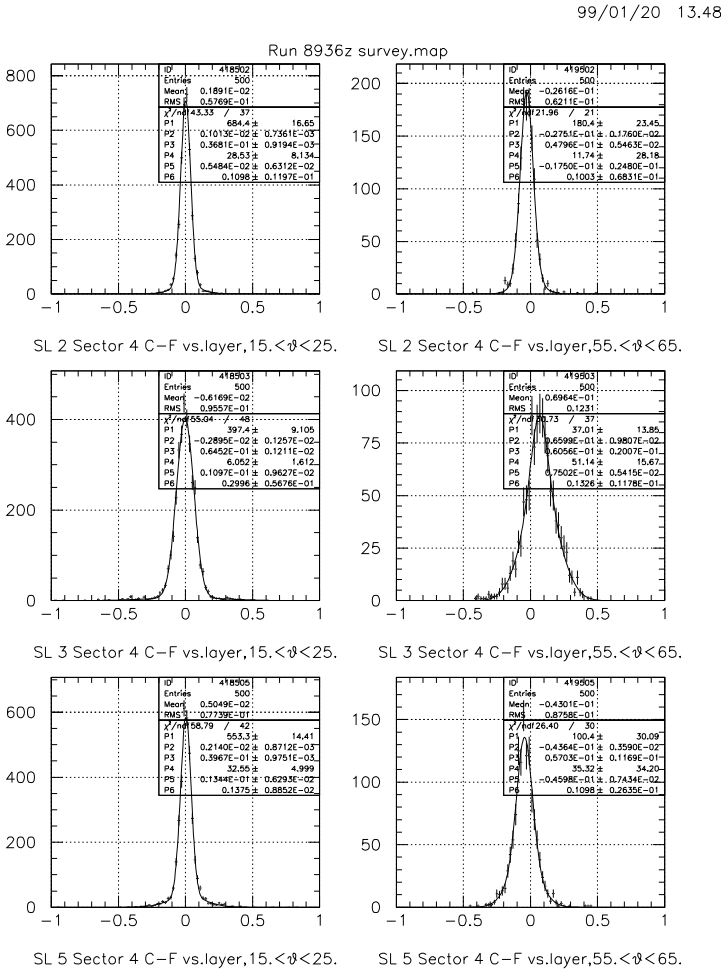

Figure C.11: Sector 4 spatial residual distributions for the Survey Geometry, summed over the *axial* superlayers in each region.

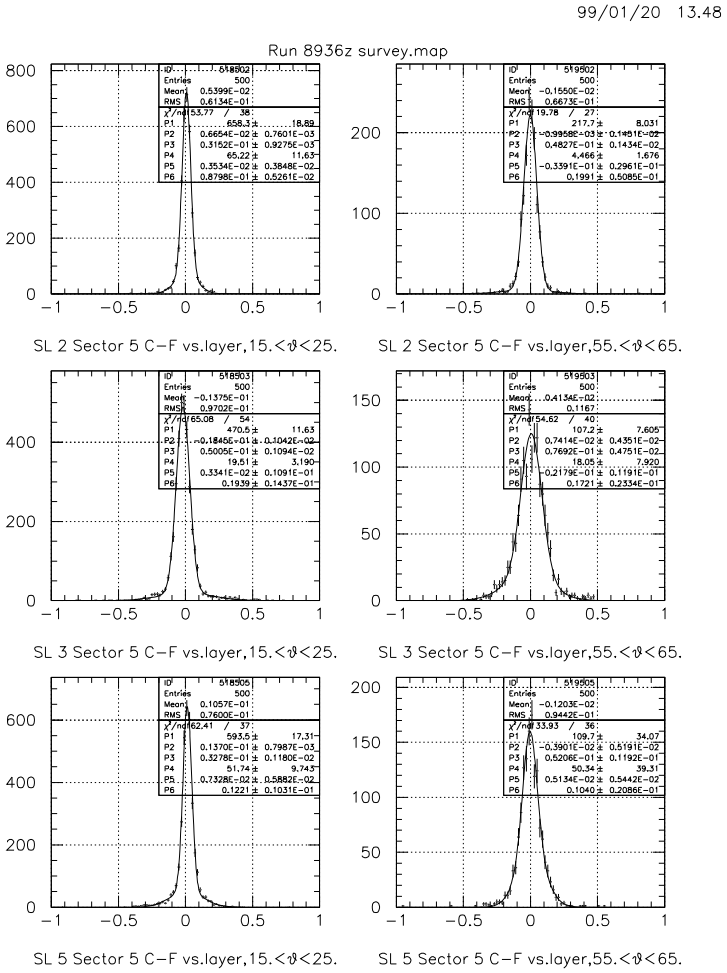

Figure C.12: Sector 5 spatial residual distributions for the Survey Geometry, summed over the *axial* superlayers in each region.

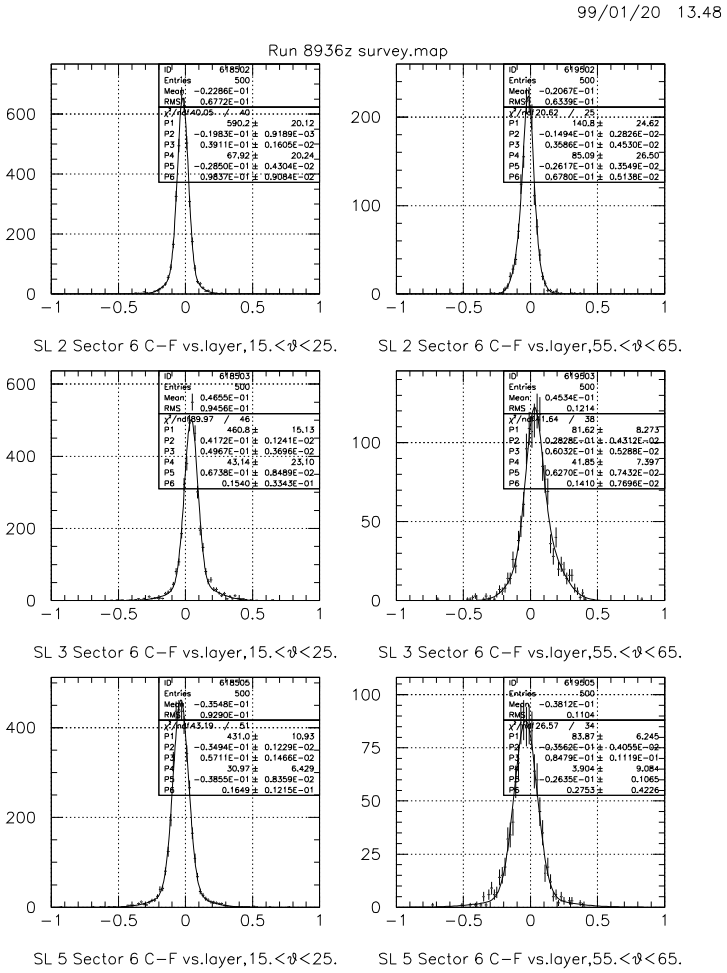

Figure C.13: Sector 6 spatial residual distributions for the Survey Geometry, summed over the *axial* superlayers in each region.

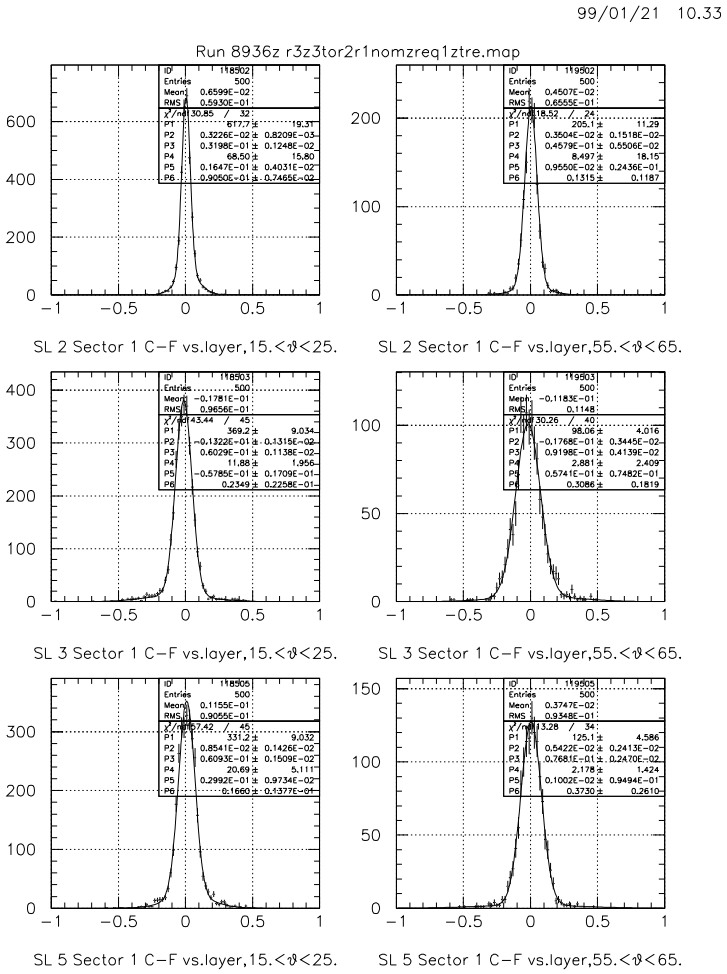

Figure C.14: Sector 1 spatial residual distributions for the Oct1998 Geometry, summed over the *axial* superlayers in each region.

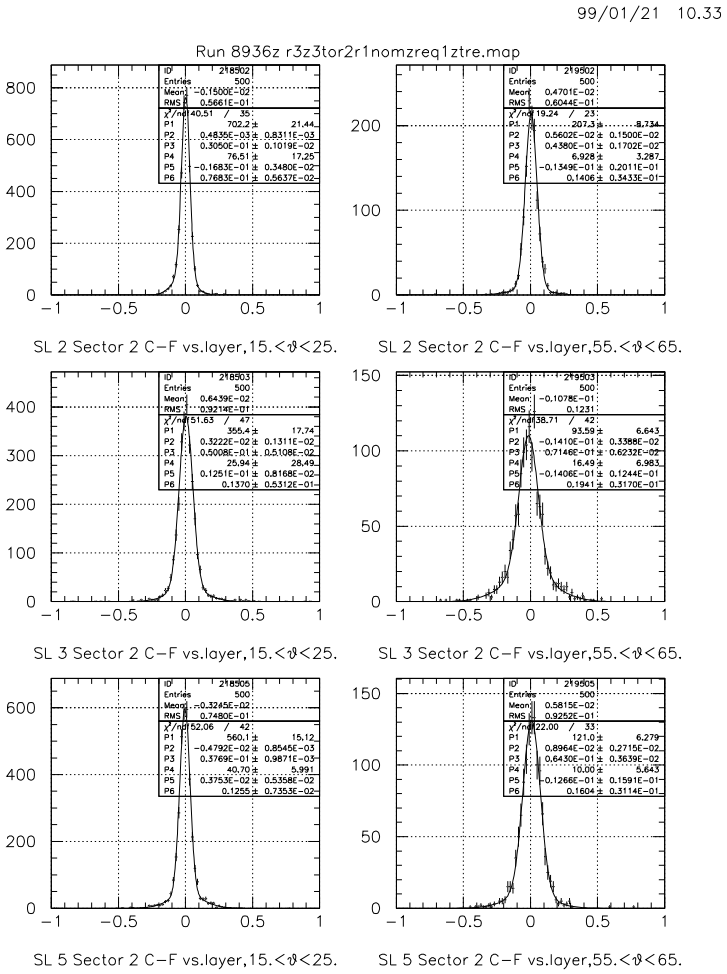

Figure C.15: Sector 2 spatial residual distributions for the Oct1998 Geometry, summed over the *axial* superlayers in each region.

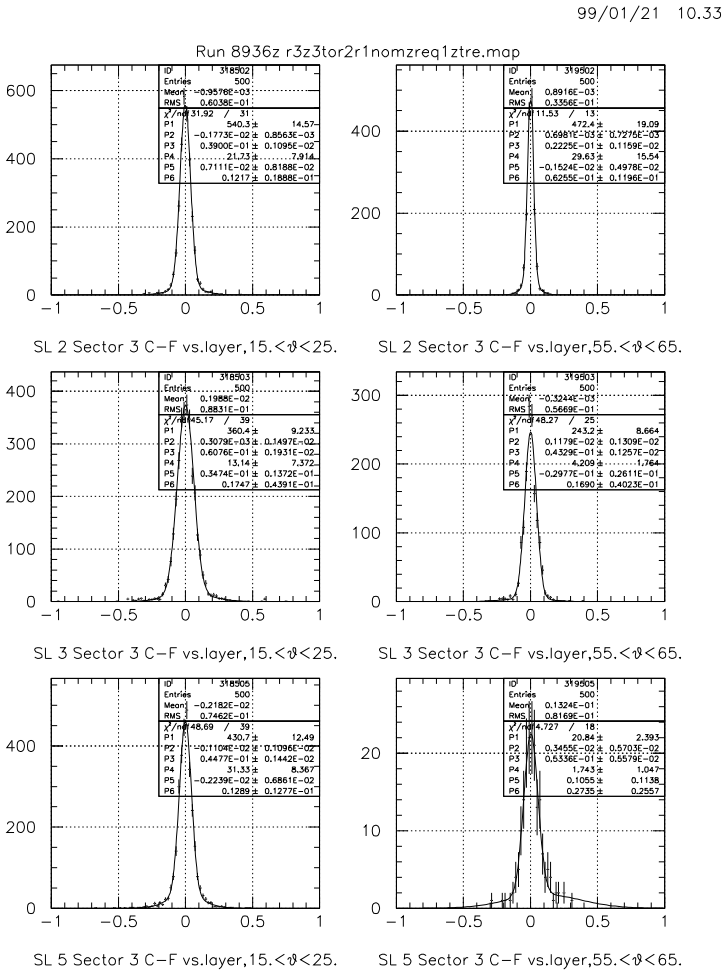

Figure C.16: Sector 3 spatial residual distributions for the Oct1998 Geometry, summed over the *axial* superlayers in each region.

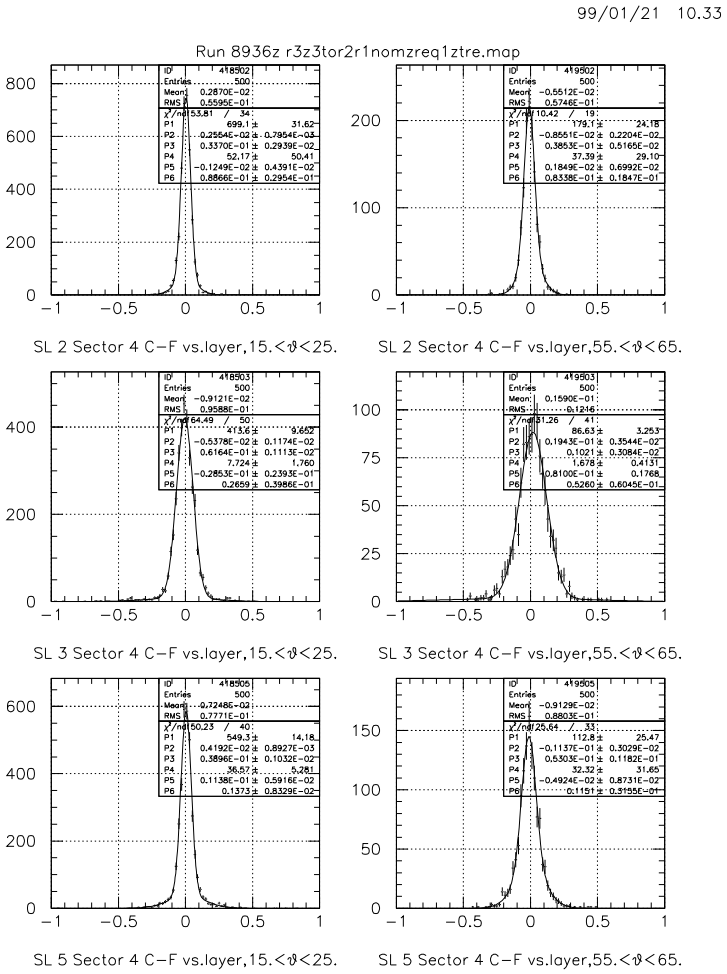

Figure C.17: Sector 4 spatial residual distributions for the Oct1998 Geometry, summed over the *axial* superlayers in each region.

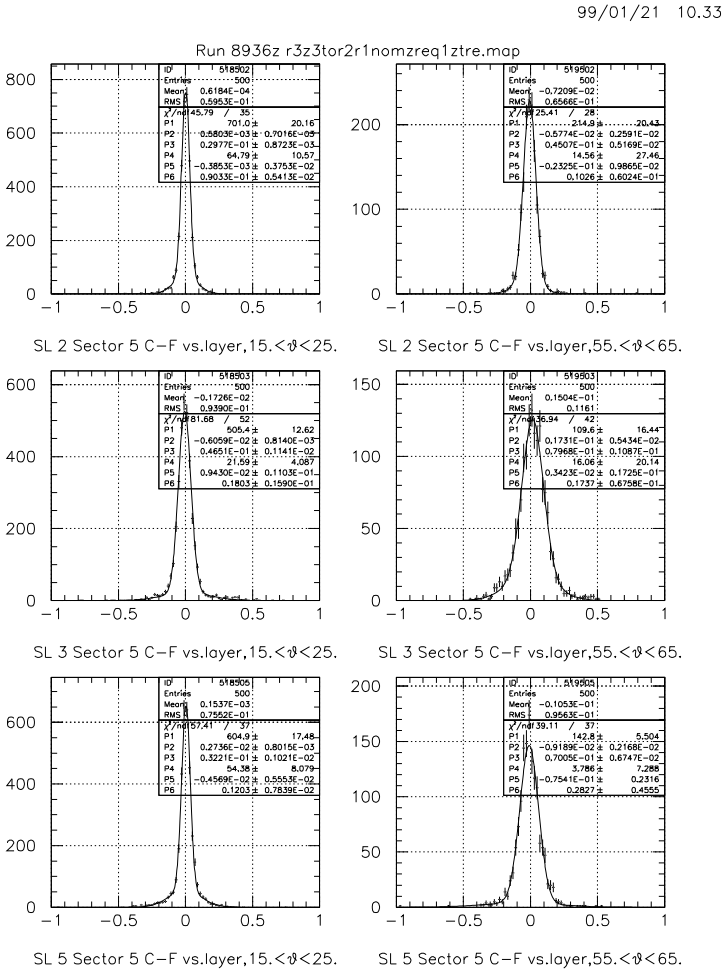

Figure C.18: Sector 5 spatial residual distributions for the Oct1998 Geometry, summed over the *axial* superlayers in each region.

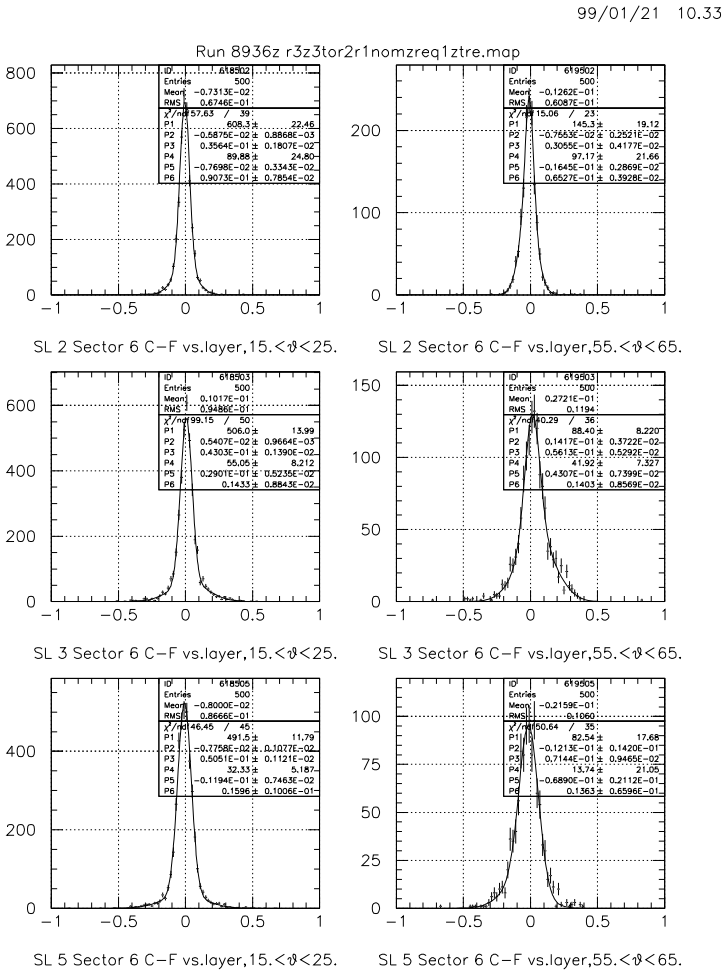

Figure C.19: Sector 6 spatial residual distributions for the Oct1998 Geometry, summed over the *axial* superlayers in each region.